Numerical simulation of the wind flow around a tall building and its dynamic response to wind excitation

Julia Revuz

Supervisors: Dr. David Hargreaves and Dr. John Owen

Department of Civil Engineering, Faculty of Engineering,

University of Nottingham

Thesis submitted to the University of Nottingham

for the degree of Doctor of Philosophy

April 2011

Abstract

Wind action is particularly important for tall buildings, both in providing a significant contribution to the dynamic overall loading on the structure and by affecting its serviceability. Whereas low and medium-rise buildings are fairly rigid, tall structures are characterized by a greater flexibility and a lower natural frequency, which is more likely to be in the frequency range of wind gusts. In addition, wake effects, such as vortex shedding, can become a significant problem for flexible structures when the vortex shedding frequency is close to the natural frequency of the building.

The aim of the present thesis is to assess the validity of commercial CFD codes for modelling the wind flow around a high-rise building, including the consideration of the coupled dynamic response of the building to turbulent wind loading. Three intermediate objectives are set.

The first is to develop a tool to couple fluid and structure in a sequential manner. The equations for the air flow are solved using the commercial CFD program ANSYS-Fluent. The response of the structure is found from solving the structural response with a modal approach, the response in each vibration mode being treated as a SDOF problem. This fluid-structure interaction tool is applied to model a 180 m building, allowed to move in the across wind direction. The second objective is to investigate and find a method to generate fully turbulent inflow for LES in order to reproduce an accurate wind spectrum. The chosen method is tested and validated in an empty fetch. Ultimately, both tools are brought together and applied to model a 180 m building, which is allowed to bend in the along wind and across wind directions. Finally, the third intermediate objective

brings together the tools developed in the first and second intermediate objective to model the dynamic response of a 180 m building to dynamic wind loading, within a turbulent inflow, using LES.

Acknowledgements

This thesis would not have been possible without the support, in various ways, of a number of people. First of all, I am deeply grateful to my main supervisor, Dr David Hargreaves, for his endless patience and knowledge sharing. I would also like to thank Dr John Owen for his support and his ability to make me see the bigger picture and not get lost in the details. I would also like to thank Dr Herve Morvan for always taking interest in my work and adding an external perspective to the project.

I would also like to thank Dr Zhengtong Xie for his collaboration on the turbulent inflow generation method used for this research.

In my daily work, I have to thank Bruce Kakimpa for all the fruitful discussions about everything related to CFD, but not only: politics was definitely a favourite topic of conversation whenever we had had enough of CFD, or Gambit had exhausted all of our energy!

I am deeply grateful to my family for the support and encouragement I received throughout my studies.

As for the writing-up, I would like to thank Rachel Thomas, for taking the time to proof read most of my thesis, and helping me make the text much clearer.

Finally, what made these three years such a great experience on every possible level is definitely working in a multicultural environment alongside some amazing people in the department. So, a huge thanks to my friends Jeff, Meinard, Paloma, Diego, Fangfang, Riccardo, Andy, Kawran...

Contents

List of Figures

List of Tables

PAGINATED
BLANK PAGES
ARE SCANNED AS
FOUND IN
ORIGINAL
THESIS

NO
INFORMATION
MISSING

Notations

f_{vs}	Frequency of vortex shedding	s^{-1}
f_n	Natural frequency of the building	s^{-1}
g_x	Along wind displacement of the structure	m
g_y	Across wind displacement of the structure	m
h	Height of the building	m
k	Turbulent kinetic energy	$m^2\ s^{-2}$
L_i^j	Length scales of turbulence ($i = u,\ v,\ v$ and $j = x,\ y,\ z$)	m
Re	Reynolds number	
St	Strouhal number	
u	Longitudinal component of the wind speed	$m\ s^{-1}$
$\overline{u}$	Mean longitudinal component of the wind speed	$m\ s^{-1}$
u'	Fluctuating longitudinal component of the wind speed	$m\ s^{-1}$
u_x, u_y, u_z	Components of the velocity of the wind in Chapter 6	$m\ s^{-1}$
u_*	Friction velocity	$m\ s^{-1}$
u_{ref}	Reference wind speed	$m\ s^{-1}$
v	Horizontal component of the wind speed	$m\ s^{-1}$
v'	Fluctuating horizontal component of the wind speed	$m\ s^{-1}$
w	Vertical component of the wind speed	$m\ s^{-1}$
w'	Fluctuating vertical component of the wind speed	$m\ s^{-1}$
y	Structure displacement	m
z_0	Roughness length	m
z_g	Gradient height	m
z_{ref}	Reference height	m

ϵ	Turbulent dissipation rate (fluid)	$m^2\ s^{-3}$
κ	Von Karman constant	
μ	Air dynamic viscosity	$m^2\ s^{-2}$
ν	Air kinematic viscosity	$m^2\ s^{-1}$
ξ	Structural damping ratio	
ρ	Air density	$kg\ m^{-3}$
σ_u, σ_v, σ_w	Components of the standard deviation of the wind speed	$m\ s^-1$
τ_{ij}	Shear stresses in the ABL	$kg\ m^{-1}\ s^{-2}$
ϕ_n	Mode shapes in the along-wind direction of the structure	
ψ_n	Mode shapes in the across-wind direction of the structure	
ω	Specific dissipation rate (k-ω turbulence model)	s^{-1}

Chapter 1

Introduction

1.1 Context

Computational Wind Engineering

The Wind Engineering Society defines Wind Engineering as a multidisciplinary subject concerned with the effects of wind on the natural and built environment. This includes investigation of pollutant dispersion and pedestrian comfort assessment, but also most important for the present work: the study of the wind loads on buildings and the aerodynamic phenomena caused by the interaction of the air-flow and the surface structures.

Computational Wind Engineering (CWE) is the application of Computational Fluid Dynamic (CFD) techniques to wind engineering and aims to predict the wind loads on buildings and the air flow around them. CWE only became feasible twenty years ago with the rapid increase of computer speed and memory capacities. Even so, for many years, computer resources have not allowed complex calculations, being restricted to steady-state RANS (Reynolds Averaged Navier Stokes) turbulence modelling. In the last five years, transient simulations using Large Eddy Simulation (LES), applied to large grids, have demonstrated that CWE can reach a good level of accuracy and potentially compete with wind-tunnel studies.

There has always been a clear predominance of wind-tunnel based studies over computer-based work for assessing wind loads on buildings. Besides, codes of practise are mainly based on wind-tunnel studies. In fact, wind engineering still remains one application area that requires experiment-based studies despite the actual tendency in building design towards virtual prototyping. In other words, engineers tend to keep most of the design steps on computers, from architect design to the last stage before laying the first stone on the building site. There are several reasons why it would be consistent to further develop numerical tools so that CWE becomes competitive with wind-tunnels. In fact, CWE inherently overcomes some of the limitations encountered by wind-tunnels. The first example is that wind-tunnel studies are less flexible and limited in terms of the configurations that can be tested: a major design change is far more costly for a wind-tunnel based study than for a computer based study. The second reason is that CWE offers the advantage of full-scale simulation where wind-tunnels are limited to scale models and hence face scale effects. A third reason is that CWE is not limited in terms of the outputs: data is not only available at particular locations but everywhere within the computational domain.

Tall Buildings

The focus on tall buildings is not recent and began in the late 19th century in the United State – the Monadnock building in Chicago was built in 1891 and was one the first skyscrapers with 16 storeys. Later, the Empire State building and the Chrysler building, 443 and 319 meters high respectively, were built in the 1920-1930s in New York and set the then standard for high-rise structures. The construction of tall buildings was in response to real economic needs, due to the constantly increasing population and economic activities. Nowadays, the economic need is still a powerful driver for building tall structures. In addition, in the context of environmentally friendly construction, tall buildings are seen as a sustainable choice, as they help concentrating activities by offering large office and accommodation spaces on limited footprints, they can help to limit the urban expansion. As a consequence, tall buildings also assist in reducing the

carbon footprint by reducing transport across a sprawling metropolis.

The design of tall buildings faces two main challenges that CWE can help to answer. On the one hand, the combination of tall buildings and dense urban environment significantly reinforces aeroelastic phenomena, such as wake effects and buffeting (to be defined in section 2), which then considerably modifies and complicates the wind loading problem. In fact, the wake effects play an important role for the buildings located downstream of the structure that caused them. As a result, the flow field around tall buildings presents particular features that need to be carefully studied, especially near the ground where strong downward flows can perturb the environment for pedestrians and also in the wake, downstream of the structure. On the other hand, whereas low and medium-rise buildings are fairly rigid, tall structures are inevitably more flexible. This makes them more sensitive to wind loading excitation and implies a significant dynamic response. Therefore, tall buildings involve the association of complex flow fields modified by aerodynamic phenomena, and hence a substantial dynamic response that may have an influence back on the fluid flow.

If many researches have worked on the numerical simulation of the dynamic response of tall buildings, and others have been interested in the key features of the flow field around tall buildings, both interests have not often been combined. Consequently, it is of main importance to develop numerical tools for studying the flow field around high-rise buildings accounting for their dynamic response. It is believed that existing commercial CFD codes offer a sufficiently advanced and flexible basis to address the challenges involved in modelling the flow field around tall buildings including the effects of their dynamic response.

1.2 Aims and Objectives

The aim of the present work is to assess the ability of commercial CFD codes for modelling the wind flow around a high-rise building – including the consideration of the coupled dynamic response of the building to turbulent wind loading – by bringing to-

gether existing tools. This should establish a framework for modelling building response to wind loading within a turbulent atmospheric boundary layer.

The main objectives of the present work are:

1. To develop and evaluate a numerical tool in order to account for the dynamic response of the building to wind loading, and to assess the coupling of the building motion and the wind flow.

2. To develop a suitable method for generating turbulent inflow for unsteady LES simulations and to assess the use of LES combined with the method for turbulent inflow in the modelling of wind flow around tall buildings.

3. To combine and evaluate the performances of the combination of 2) the coupling of the dynamic response of the tall building with the modelling of the wind flow, and 3) the technique for producing turbulent inflow, in an unsteady LES simulation.

Summary of chapters

Chapter 1 introduces the thesis with a very general background of the history of the tall buildings and wind engineering, and sets the main goal of this work with associated intermediate objectives.

Chapter 2 introduces the field of wind engineering and presents the important features of the flow around buildings and the main characteristics of the Atmospheric Boundary Layer, as well as the general method to study the building response.

Chapter 3 presents a literature review of the application of CFD to wind engineering problems, mainly focusing on turbulence modelling.

Chapter 4 presents the results of an investigation of the optimal dimensions of the computational domain to use to numerically study the flow around tall buildings. The main conclusion is that the computational domain can be greatly reduced from the general guidelines, which were derived for low to mid-rise buildings. The chapter suggests new guidelines for the size of the computational domains to be applied to tall buildings.

Chapter 5 develops the method that has been determined to couple fluid and structure using an existing CFD code. This method is then applied to a cantilever, which is allowed to move in the transversal direction. "Lock-in" phenomenon was found to happen for reduced velocity of about 1.1.

Chapter 6 presents the investigation and the optimisation of a method to generate turbulent inflow for LES. The generator is applied to an empty fetch test case in order to verify and validate the approach.

Chapter 7 presents the results of a study combining the main two tools developed in Chapters 5 and 6 in order to meet the main objective of this work.

Chapter 8 finally summarizes the main findings of this thesis and suggests some further recommendations.

Chapter 2

Introduction to Wind Engineering

2.1 The Atmospheric Boundary Layer

2.1.1 Introduction

From a wind engineering point of view, the region of the Earth's atmosphere of interest is the Atmospheric Boundary Layer (ABL), which can cover the lowest kilometre or so of the atmosphere.

Garrat (1992) defines the ABL as the part of "the Earth's surface where the effects of the surface, such as friction, heating, and cooling, are felt directly on a time scale of less than a day, and in which significant fluxes of momentum, heat or matter are carried by turbulent motions on a scale of the order of the depth of the boundary layer or less".

Two main layers can be distinguished in the ABL (Figure 2.1):

- the inner region called the Surface Layer, mainly influenced by the surface features. The Surface layer is composed of the Interfacial layer, and the Inertial sub-layer. The Inertial sub-layer allows the transition between the inner region and the outer region.

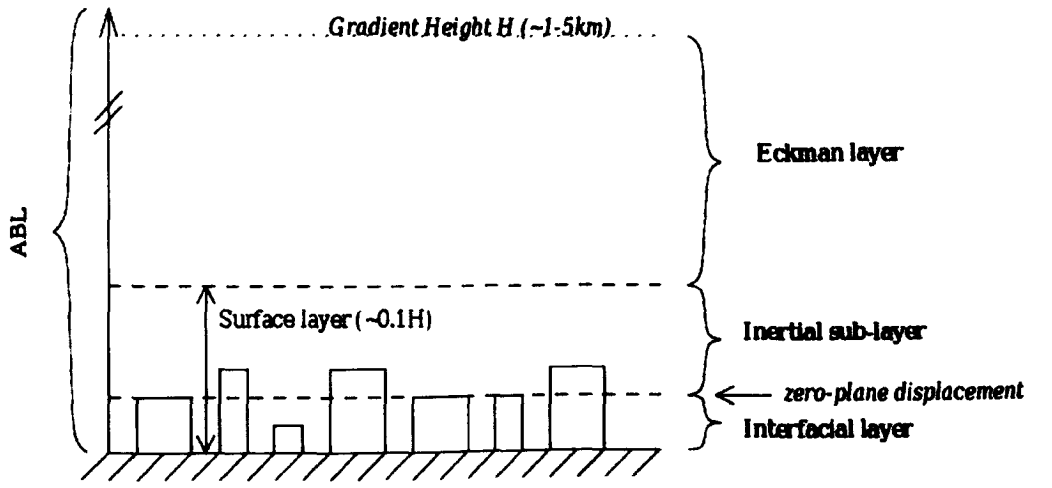

Figure 2.1: Composition of the ABL: The Surface layer composed of the Interfacial layer, and the Inertial sublayer; and the Eckman layer.

- the outer region, also called the Eckman Layer, where the dominant factor is the Earth's rotation.

The *turbulent shear stress* or Reynolds stress, defined in section 2.1.4, varies with the height through the ABL as follows: it is equal to zero at the ground level, reaches a maximum at the top of the interfacial layer, and then decreases to vanish at the top of the boundary layer, where the velocity reaches the gradient velocity, V_g.

The *Interfacial layer* covers approximately four fifths of the average building height. There is no general direction for the wind flow within this layer but many local directions, due to the buildings locations creating channels for the wind flow. Consequently, the overall net flow is zero, which is why the depth of the interfacial layer is often called the *zero-plane displacement height* and denoted z_d. The zero plane displacement height strongly depends on the surface roughness: in urban areas, where structures contribute to a significant increase in surface roughness, this depth is important. In open country, where the Interfacial layer is not significant, the Eckman layer is predominant.

Wind motion in the *Eckman layer* is determined by the pressure force due to the static pressure field, and by the Coriolis force from the Earth's rotation. The former acts normal to the isobars and the latter acts normal to the wind direction (Cook, 1992). In other words, within that layer the pressure gradient effects and the Coriolis effects are

the two dominant phenomena.

The overall depth of the ABL depends on the atmospheric conditions but generally varies between a few hundreds metres to several kilometres, depending on the location. Depending on the influence of the thermal effects, the ABL will be considered unstable, neutral, or stable.

Let us first define the lapse rate: it is the rate of temperature decrease with height of a parcel of air in the ABL. Under adiabatic conditions (where no heat is exchanged) and for an unsaturated mass of air, the lapse rate is the Dry Adiabatic Lapse Rate (DALR), and the three states of the ABL can be characterized relatively to the DALR, as shown in Figure 2.2 (a), neutral, stable or unstable.

In order to illustrate what happens in each case, consider a mass of warm air near the surface; as this air is warmer, it rises, and the low pressure causes the mass of air to expand in an adiabatic cooling process. If the mass of air does not cool down to the level of the surrounding air, then it will continue to rise, creating large convection cells, causing the boundary layer to be thick with large scale turbulent eddies. This situation is considered unstable and is likely to occur on warm days, where the decrease of temperature is not as steep as in DALR conditions as illustrated in Figure 2.2(a). However, if the adiabatic cooling process brings the mass of air to thermal equilibrium with the surrounding air, then the air will stop rising, and the boundary layer is then considered stable, this typically occurs when the ground is colder, for example on cool nights. Finally, if there are strong winds causing sufficient mixing to maintain thermal equilibrium through the adiabatic cooling process, then the ABL is considered to be neutral. This last case is the most important in wind engineering applications, as it is the state of the ABL with strong winds and high turbulence levels. The displacement of a mass of air in a neutral ABL is illustrated in Figure 2.2 (b). (Simiu and Scanlan, 1986; Burton et al., 2002)

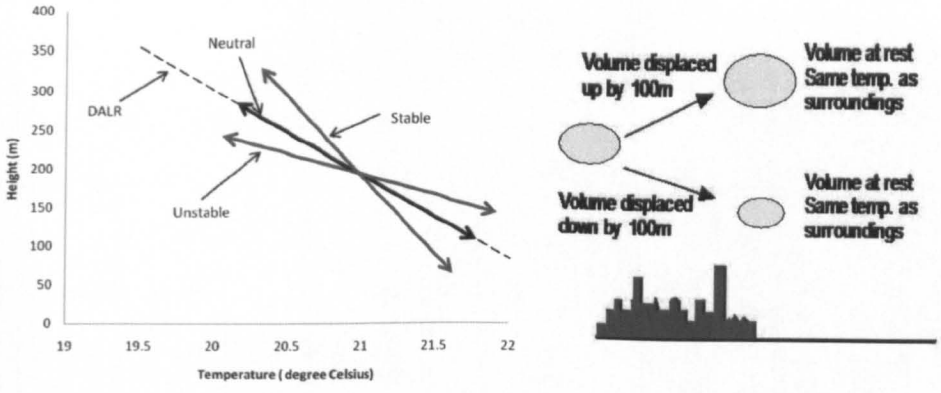

(a) (b)

Figure 2.2: Lapse rates for a stable, neutral and unstable ABL (a) and illustration of the displacement of a mass of air in a neutral ABL (after Dyrbye and Hansen (1997)).

2.1.2 Basic assumptions

Two main assumptions need to be made to simplify the resolution of the ABL motion.

Firstly, in the present work, the ABL is considered neutrally stable, that is, heat convection is neglected compared to mechanical turbulence. The mechanical turbulence produces enough mixing to swamp movements due to the thermal effects. This assumption can be made as structural engineers are mainly concerned with the effects of strong winds, with high Reynolds numbers, hence high turbulence levels.

In addition, incompressibility is assumed for the wind flow.

2.1.3 Governing equations

The governing equations for the wind motion within the neutrally stable ABL are as follows

$$\frac{\partial u}{\partial t} + (u\frac{\partial u}{\partial x} + v\frac{\partial u}{\partial y} + w\frac{\partial u}{\partial z}) + \frac{1}{\rho}\frac{\partial p}{\partial x} = fV + \frac{1}{\rho}\frac{\partial \tau_u}{\partial z} \tag{2.1.1}$$

$$\frac{\partial v}{\partial t} + (u\frac{\partial v}{\partial x} + v\frac{\partial v}{\partial y} + w\frac{\partial v}{\partial z}) + \frac{1}{\rho}\frac{\partial p}{\partial y} = -fU + \frac{1}{\rho}\frac{\partial \tau_v}{\partial z} \tag{2.1.2}$$

$$\frac{\partial w}{\partial t} + (u\frac{\partial w}{\partial x} + v\frac{\partial w}{\partial y} + w\frac{\partial w}{\partial z}) + \frac{1}{\rho}\frac{\partial p}{\partial z} + g = -\frac{1}{\rho}\frac{\partial \tau_w}{\partial z} \tag{2.1.3}$$

$$\rho(\frac{\partial u}{\partial x} + \frac{\partial v}{\partial y} + \frac{\partial w}{\partial z}) = 0 \tag{2.1.4}$$

where u, v, w are the velocity components along the x, y, z axes respectively, where x is the along-wind axis, y the cross-wind axis, and z the vertical axis. ρ is the air density, p the pressure, g the acceleration of gravity, and τ_u, τ_v and τ_w are the shear stresses. The first terms on the right-hand side in Equations 2.1.1 and 2.1.2 express the Coriolis force acting on the air flow caused by the Earth's rotation. The Coriolis parameter, f, is given by

$$f = 2\Omega \sin|\lambda| \tag{2.1.5}$$

where Ω is the angular velocity of the Earth's rotation, and λ the latitude. The last terms of equations (2.1.1)-(2.1.2) express the viscous stresses, the terms τ_u and τ_v and τ_w are the shear stresses, to be defined.

In the ABL, the following simplifications can be made:

1. In Equation 2.1.3, assuming a low vertical acceleration, the predominant terms are the vertical gradient of pressure and the gravity effects.

2. In urban area, the surface layer reaches a few hundred meters and is assumed to be fully turbulent and close enough to the surface to neglect the Coriolis effects (Simiu and Scanlan, 1986). As a result, the terms in f of Equations 2.1.1 and 2.1.2, fU and fV are neglected.

3. In Equation 2.1.4, compressibility effects expressed by $\partial\rho/\partial t$ can be neglected in the ABL according to the second main assumption made for the wind flow.

Applying these assumptions leads to the following set of equations:

$$\frac{\partial u}{\partial t} + (u\frac{\partial u}{\partial x} + v\frac{\partial u}{\partial y} + w\frac{\partial u}{\partial z}) + \frac{1}{\rho}\frac{\partial p}{\partial x} = \frac{1}{\rho}\frac{\partial \tau_u}{\partial z} \tag{2.1.6}$$

$$\frac{\partial v}{\partial t} + (u\frac{\partial v}{\partial x} + v\frac{\partial v}{\partial y} + w\frac{\partial v}{\partial z}) + \frac{1}{\rho}\frac{\partial p}{\partial y} = \frac{1}{\rho}\frac{\partial \tau_v}{\partial z} \tag{2.1.7}$$

$$\frac{1}{\rho}\frac{\partial p}{\partial z} + g = 0 \tag{2.1.8}$$

$$\frac{\partial u}{\partial x} + \frac{\partial v}{\partial y} + \frac{\partial w}{\partial z} = 0 \tag{2.1.9}$$

The shear stresses τ_u and τ_v remain undefined in Equations (2.1.6) and (2.1.7) respectively. They can be written as functions of the viscosity μ as follows, based on the assumption that the viscous stresses are proportional to the rates of deformation for a Newtonian fluid:

$$\tau_u = \mu \left(\frac{\partial u}{\partial z} + \frac{\partial w}{\partial x} \right) \tag{2.1.10}$$

$$\tau_v = \mu \left(\frac{\partial v}{\partial z} + \frac{\partial w}{\partial y} \right) \tag{2.1.11}$$

From differentiating Equation 2.1.8 with respect to x and y, it follows that the vertical variation of the horizontal pressure gradient depends on the horizontal density gradients. Assuming that the horizontal density gradients are negligible, it follows that the horizontal pressure gradient does not vary with height (Simiu and Scanlan, 1986). As a consequence of the horizontal pressure gradient constant with height being only partly balanced by the Coriolis force (at least below the gradient height), the growth of the boundary layer that occurs on flat plates for example, is counteracted in the case of the ABL and the horizontal homogeneity is maintained. In other words, in the absence of any obstruction, the ABL does not vary in the along-wind direction, which is confirmed by full scale observations of the ABL (Simiu and Scanlan, 1986).

2.1.4 Mean velocity and roughness height

Above the ABL, the wind is not affected by the Earth's surface and flows with the gradient velocity, which is the velocity at the top of the ABL, Figure 2.1. The height at which the velocity reaches the gradient velocity is called the gradient height. Through the ABL, the velocity varies from zero at the ground level to the gradient velocity at the top.

Under the assumption of a neutrally stable ABL, the two variables that affect the ABL

are the surface roughness and the Coriolis force, Equation (2.1.5). The height of the ABL can be estimated as a function of f, the Coriolis parameter.

$$h_g = \frac{u_*}{6f} \tag{2.1.12}$$

where u_*, the friction velocity, is defined as:

$$u_* = \sqrt{\frac{\tau_w}{\rho}} \tag{2.1.13}$$

where τ_w is the wall shear stress, and ρ the fluid density.

For the region that is not directly affected by roughness elements, namely the inertial sublayer, two main models have been proposed to describe the vertical variations of the velocity.

The first modelling of the ABL assumed from a power law:

$$\overline{u}(z) = u_{\text{ref}} \left(\frac{z}{z_{\text{ref}}} \right)^{\alpha} \tag{2.1.14}$$

where $\overline{u}(z)$ is the mean velocity at height z, u_{ref} is the velocity at a reference height z_{ref}, and α is a factor dependent upon the roughness and the stability of the terrain. This model shows good agreement with the upper region of the ABL but fails to accurately predict the velocity in the lower region. To overcome this drawback, a model based on a logarithmic law has been developed and has been widely used. The following equation shows an example of such a logarithmic law for neutrally stable ABL:

$$\overline{u}(z) = \frac{u_*}{\kappa} \ln \left(\frac{z - z_d}{z_0} \right) \tag{2.1.15}$$

where κ is the Von Karman constant (usually $\kappa \approx 0.4$), z_0 the roughness length, z_d the displacement height and u_* the friction velocity. The roughness length is related to the surface roughness, and is defined as the height where the wind speed would be equal to zero if the log-law wind speed profile were extrapolated (Garrat, 1992).

Table 2.1: Typical Surface Roughness Lengths (after Burton et al. (2002)).

Type of terrain	Roughness lengths z_0 in meters	z_d
Cities, forests	0.7	15 to 25
Suburbs, wooded countryside	0.3	5 to 10
Villages, countryside with trees and hedges	0.1	0 to 2
Open farmland, few trees and buildings	0.03	0
Flat grassy plains	0.01	0
Flat desert, rough sea	0.001	0

The roughness length z_0 plays a similar role to α in the power law. In addition to being scale dependant, log-law-based models give good approximations of the wind speed in lower regions. For these reasons, such models are of more interest when studying flow around buildings and will be adopted in future work. However, log-law wind profiles have been shown to estimate poorly the velocity in the high regions of the ABL; as a consequence, Harris and Deaves (1980) extended the log-law velocity profile, adding an empirically-based polynomial, making it valid up to the gradient height, h_g (defined in Equation (2.1.12)):

$$\overline{u}(z) = \frac{u_*}{\kappa}\left[\ln\left(\frac{z-z_d}{z_0}\right) + 5.75a - 1.88a^2 - 1.33a^3 + 0.25a^4\right] \tag{2.1.16}$$

where $a = (z - z_d)/z_g$. Roughness heights, as well as zero displacement heights are given in Table 2.1 for different types of terrain. Figure 2.3 shows the effects of the roughness height on the velocity profile for three different terrains.

Surface roughness has an influence on the velocity profile. Consider two terrains of different roughness height, a smoother and a rougher terrain. The wind flow will be slowed down more over the rougher terrain due to the larger surface shear stress. If a change in roughness length is now considered over a terrain as shown in Figure 2.4, the flow, initially in equilibrium, will reach a "new" equilibrium by the action of the Reynolds stress. That is, the momentum required to overcome the surface shear stress exactly balances the momentum supplied (Cook, 1992).

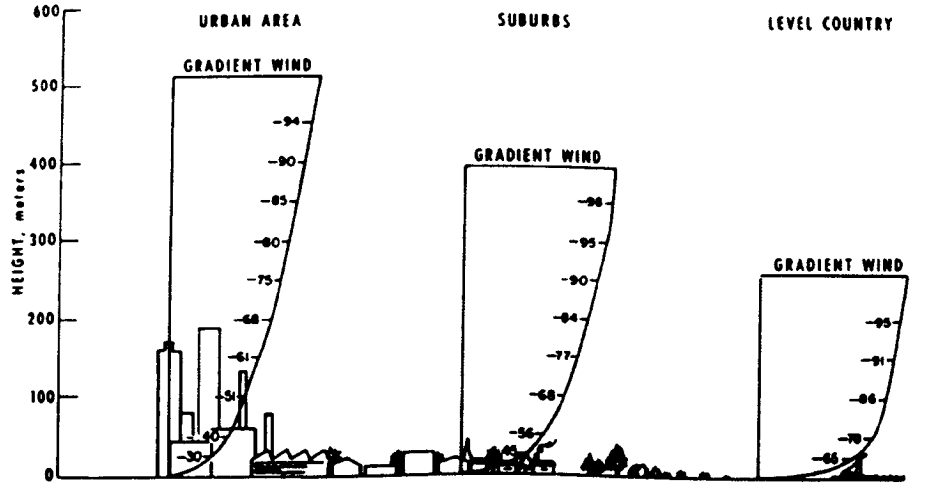

Figure 2.3: Roughness effects on the velocity profile, for three types of terrain (after Dyrbye and Hansen (1997)).

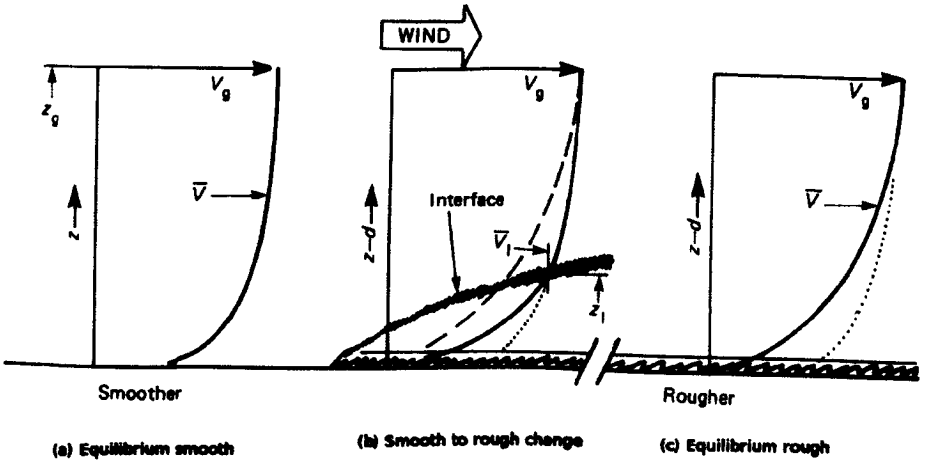

Figure 2.4: Effect of roughness change from smoother to rougher terrain on the velocity profile (V_g indicates the gradient velocity and z_g the gradient height) (after Cook (1992)).

2.1.5 Atmospheric turbulence

Vortex stretching and energy cascade

Visualization of turbulence shows rotational flow structures, called eddies. The rotational nature of turbulent flows can be characterized by the vorticity, which can be described as the curl of the velocity: $\vec{\omega} = \nabla \times \vec{u}$ [1], and is equal to twice the rate of rotation of the fluid (Pope, 2000). The largest turbulent eddies interact with the smaller ones and extract energy from the mean flow by a process called *vortex stretching*, illustrated in Figure 2.5. The larger eddies are dominated by inertia effects and viscous effects are negligible. It follows that the angular momentum is conserved and the vorticity increases, leading to vortex stretching: as shown in the figure, the vortex line increases in length but decreases in diameter, leading ultimately to the formation of smaller eddies. Thus, energy is transferred from large scales to smaller scales. Ultimately, the kinetic energy associated with the smallest eddies is dissipated and converted to thermal internal energy. The whole process is called the *energy cascade* (Versteeg and Malalasekera, 2007). The smallest scales are characterized by the Kolmogorov length scale, defined as:

$$\eta = \left(\frac{\nu^3}{\epsilon}\right)^{1/4} \tag{2.1.17}$$

where ν is the kinematic viscosity, and ϵ is the dissipation rate of the turbulent kinetic energy. The large scales, are characterized by the geometry. Sometimes, the smaller eddies can in turn contribute to larger eddies, i.e. transfer energy to the larger eddies; this process is known as backscatter.

As larger eddies are believed to be dominated by inertia effects and extract energy from the mean flow, their structure is *anisotropic* and influenced by the boundary conditions. In contrast, the smallest eddies that are principally affected by energy dissipation, behave in a more *isotropic* manner. The behaviour of smallest eddies can be considered more universal, less dependent on the boundary conditions (Kolmogorov, 1941).

[1] $\nabla \times \vec{u} = \left(\frac{\partial w}{\partial y} - \frac{\partial v}{\partial z}\right)\vec{x} + \left(\frac{\partial u}{\partial z} - \frac{\partial w}{\partial x}\right)\vec{v} + \left(\frac{\partial v}{\partial x} - \frac{\partial u}{\partial y}\right)\vec{z}$

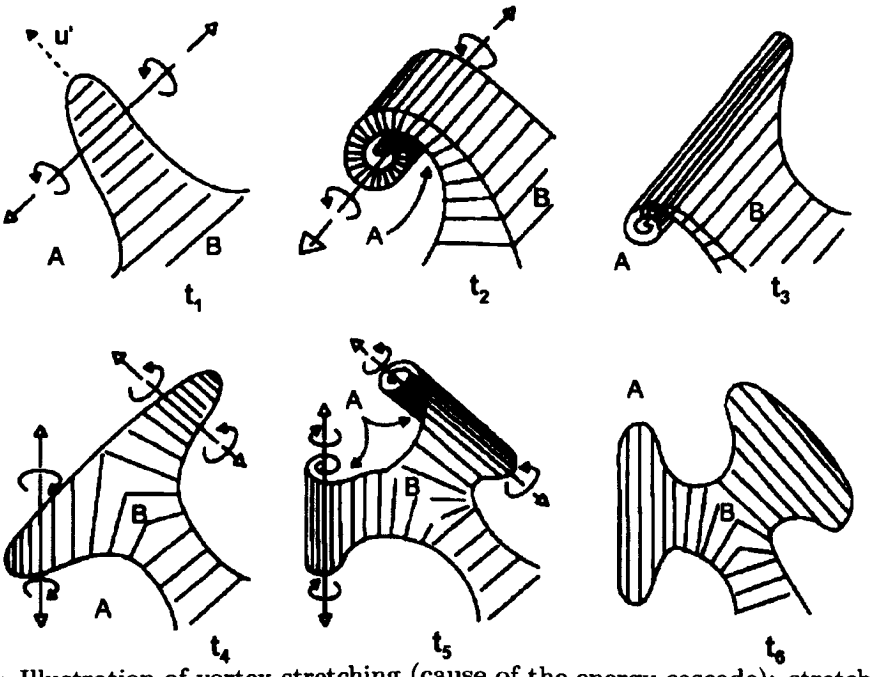

Figure 2.5: Illustration of vortex stretching (cause of the energy cascade): stretching of a vortex, to the point where two smaller vortices are formed (after Baldyga and Bourne (1984)).

Mathematical model and governing equations

The ABL is characterized by high Reynolds numbers (Re), which means that inertia effects dominate viscous effects. The Reynolds number is defined as:

$$Re = \frac{\overline{u}L}{\nu} \tag{2.1.18}$$

where $\overline{u}$ and L are characteristic velocity and length scale of the mean flow and ν is the kinematic viscosity defined as:

$$\nu = \mu/\rho \tag{2.1.19}$$

where μ is the dynamic viscosity and ρ the fluid density.

One method of describing turbulence is to consider the wind velocity to be written as the sum of mean components $\overline{u}$, $\overline{v}$, $\overline{w}$ and fluctuating components u', v', w'.

$$\begin{Bmatrix} u(t) \\ v(t) \\ w(t) \end{Bmatrix} = \begin{Bmatrix} \overline{u} + u'(t) \\ \overline{v} + v'(t) \\ \overline{w} + w'(t) \end{Bmatrix} \tag{2.1.20}$$

where $\frac{du'}{dt} = 0$, $\frac{dv'}{dt} = 0$ and $\frac{dw'}{dt} = 0$. The mean value in time of each fluctuating component equals zero by definition. Other variables, such as pressure, can be described similarly.

Writing the velocity as the sum of a mean and a fluctuating components leads to extra terms, known as the Reynolds stresses, $-\rho\overline{u_i' u_j'}$, in the Navier-Stokes Equations (2.1.6 and 2.1.7). The new set of equations is known as the Reynolds Averaged Navier-Stokes formulation (RANS):

$$\frac{\partial \overline{u}}{\partial t} + (\overline{u}\frac{\partial \overline{u}}{\partial x} + \overline{v}\frac{\partial \overline{u}}{\partial y} + \overline{w}\frac{\partial \overline{u}}{\partial z}) = -\frac{1}{\rho}\frac{\partial p}{\partial x} + \nu\frac{\partial^2 \overline{u}}{\partial x_j^2} - \frac{1}{\rho}\left(\frac{\partial \rho\overline{u'^2}}{\partial x} + \frac{\partial \rho\overline{u'v'}}{\partial y} + \frac{\partial \rho\overline{u'w'}}{\partial z}\right) \tag{2.1.21}$$

$$\frac{\partial \overline{v}}{\partial t} + (\overline{u}\frac{\partial \overline{u}}{\partial x} + \overline{u}\frac{\partial \overline{v}}{\partial y} + \overline{u}\frac{\partial \overline{w}}{\partial z}) = -\frac{1}{\rho}\frac{\partial p}{\partial y} + \nu\frac{\partial^2 \overline{v}}{\partial x_j^2} - \frac{1}{\rho}\left(\frac{\partial \rho\overline{u'v'}}{\partial x} + \frac{\partial \rho\overline{v'^2}}{\partial y} + \frac{\partial \rho\overline{v'w'}}{\partial z}\right) \tag{2.1.22}$$

$$\frac{\partial \overline{u}}{\partial x} + \frac{\partial \overline{v}}{\partial y} + \frac{\partial \overline{w}}{\partial z} = 0 \tag{2.1.23}$$

In total, six extra terms are added to the Navier-Stokes equations, namely three normal stresses: $\tau_{uu} = -\rho\overline{u'^2}$, $\tau_{vv} = -\rho\overline{v'^2}$, $\tau_{ww} = -\rho\overline{w'^2}$ and three shear stresses: $\tau_{uv} = -\rho\overline{u'v'}$, $\tau_{uw} = -\rho\overline{u'w'}$, $\tau_{vw} = -\rho\overline{v'w'}$. The fact that six extra terms are added while no extra equation is added to the system is called the *closure problem*. The next chapter details the turbulence models and how they have been proposed to solve this closure issue in order to numerically solve the equations for the flow.

2.1.6 Turbulence intensity, Reynolds stresses and length scales

Turbulence intensity and gust wind speed factor

Turbulence in the ABL can be quantified by the turbulence intensity:

$$I = \frac{\sqrt{1/3\,(\overline{u'u'} + \overline{v'v'} + \overline{w'w'})}}{U} \tag{2.1.24}$$

where $U = \sqrt{U_x^2 + U_y^2 + U_z^2}$. It gives a general idea of the level of turbulence in the boundary layer, but is not enough to characterize and define the turbulent structures as it treats the three velocity fluctuations with equal weight.

The turbulence in the wind can also be characterised by the gust wind speed factor, G, defined as:

$$G = \frac{U_{\text{gust}}}{\overline{U}_{\text{hourly}}}$$

It characterises the peak wind speed in a given time interval, over the mean hourly mean wind speed. It is a function of the turbulence intensity and it also depends on the duration of the gust: the larger the time interval, the smaller the gust factor is.

Reynolds stresses distribution in the ABL

The distribution of the Reynolds stresses in a boundary layer is plotted in Figure 2.6. Only the normal stresses and the shear stress $-\overline{u'w'}$ are plotted as the other shear stresses are assumed to be negligible (those stresses are identically zero if the mean flow is two-dimensional).

Full scale measurements have allowed expressions to be derived for the Reynolds stresses in the ABL; the following definition of the standard deviations of the velocity are taken from ESDU 85020 (1985, revised in 1990). The standard deviations are directly related to the normal Reynolds stresses by: $\tau_{uu} = -\rho\sigma_{uu}^2$, $\tau_{vv} = -\rho\sigma_{vv}^2$ and $\tau_{ww} = -\rho\sigma_{ww}^2$.

$$\frac{\sigma_u}{u_*} = \frac{7.5\,\eta(0.538 + 0.09\,\ln(z/z_0))^p}{1 + 0.156\,\ln(u_*/(f\,z_0))} \tag{2.1.25}$$

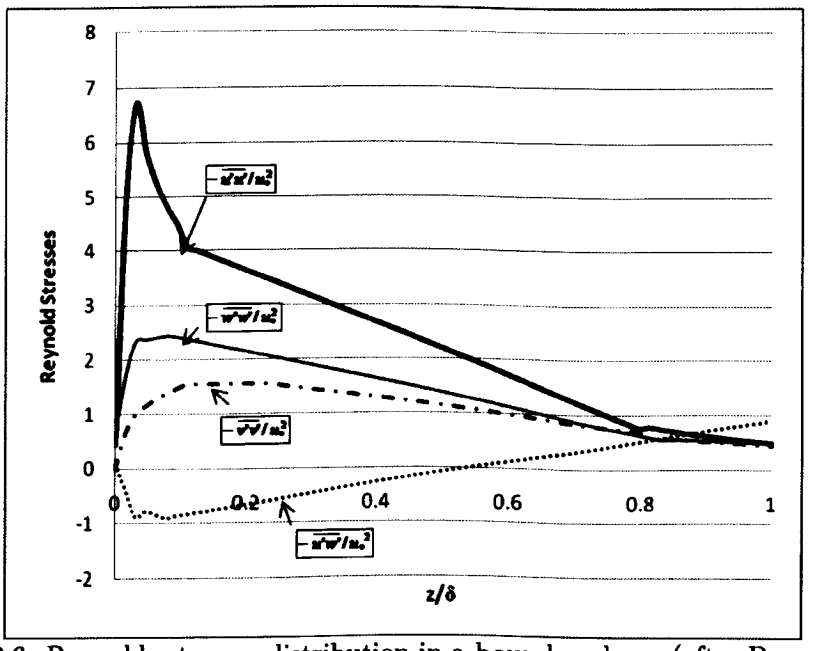

Figure 2.6: Reynolds stresses distribution in a boundary layer (after Pope (2000).

where

$$\eta = 1 - 6fz/u_*, \text{ and } p = \eta^{16}$$

and

$$\frac{\sigma_v}{\sigma_u} = 1 - 0.22\cos^4\left(\frac{\pi z}{2h}\right) \tag{2.1.26}$$

and

$$\frac{\sigma_w}{\sigma_u} = 1 - 0.45\cos^4\left(\frac{\pi z}{2h}\right) \tag{2.1.27}$$

Figure 2.7 shows a plot of the normal Reynolds stresses, as defined by ESDU. The shear stress has also been defined by ESDU as: $\tau_{uw} = -\rho\overline{uw} = \rho u_*^2(1 - z/h)^2$.

Length scales of the velocity fluctuations in the ABL

The average size of the eddies in the flow is characterized by the nine *integral length scales of turbulence*, for the three main directions, and for the longitudinal, transverse and vertical components of the fluctuating velocity. For example, the integral length scale in the x-direction associated with the longitudinal component of the velocity is

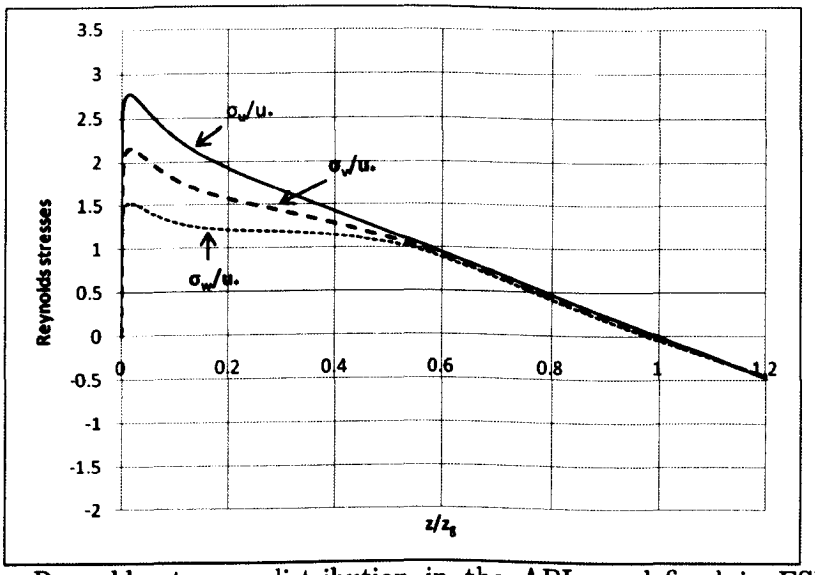

Figure 2.7: Reynolds stresses distribution in the ABL as defined in ESDU 85020 (1985, revised in 1990) for $z_0 = 0.01$ m.

defined as:

$$L_u^x = \frac{1}{\overline{u^2}} \int_0^\infty R_{uu}(x)dx \tag{2.1.28}$$

where R_{uu} is the cross-covariance function[2] of the longitudinal velocity component u. In the same manner, the integral length scales in the vertical (z) and horizontal (y) direction of the longitudinal component of the velocity are defined as:

$$L_u^z = \frac{1}{\overline{u^2}} \int_0^\infty R_{uu}(z)dz \tag{2.1.29}$$

$$L_u^y = \frac{1}{\overline{u^2}} \int_0^\infty R_{uu}(y)dy \tag{2.1.30}$$

Integral length scales in the x, y, z-directions are also defined for the other two components of the velocity[3], v and w.

The longitudinal integral length scales for an equilibrium boundary layer are defined in the technical report ESDU 85020 (1985, revised in 1990). The definition of these length scales are derived from the Von Karman spectrum for S_{uu}, defined in Equation (2.1.38).

[2] R_{uu} is defined is Appendix D.

[3] In this Chapter, the three components of the velocity are noted u, v and w. In Chapter 6, the notation u_x, u_y and u_z is used to be consistent with the indices used in the variables of the synthetic turbulent inflow generator.

$$L_u^x = \frac{A^{3/2}(\sigma_u/u_*)^3 z}{2.5K_z^{3/2}(1-z/h)^2(1+5.75z/h)} \tag{2.1.31}$$

where

$$A = 0.115\left[1+0.315(1-z/h)^6\right]^{2/3}$$

$$K_z = 0.19 - (0.19 - K_0)\exp -B(z/h)^N$$

$$K_0 = \frac{0.39}{R_0^{0.11}},\ B = 24R_0^{0.155}$$

and R_0 is the non-dimensional surface Rossby number:

$$R_0 = \frac{u_*}{fz_0}$$

The other longitudinal integral length scales (for the other two components of the velocity) are defined in ESDU 85020 (1985, revised in 1990):

$$\frac{L_v^x}{L_u^x} = 0.5\left(\frac{\sigma_v}{\sigma_u}\right)^3 \tag{2.1.32}$$

$$\frac{L_w^x}{L_u^x} = 0.5\left(\frac{\sigma_w}{\sigma_u}\right)^3 \tag{2.1.33}$$

The vertical and horizontal integral length scales were first defined by Counihan (1975) as being roughly: $L_u^z = 0.5\,L_u^x$, and $L_u^y = \frac{1}{3}L_u^x$, which was later refined by Duchêne-Marullaz (1980) and cited in Simiu and Scanlan (1986): $L_u^z = 6\sqrt{z}$, and $L_u^y = 0.2L_u^x$.

A later publication, ESDU 86010 (1986, revised in 2001) redefined the vertical and horizontal integral length scales based on more recent full scale measurements. They are

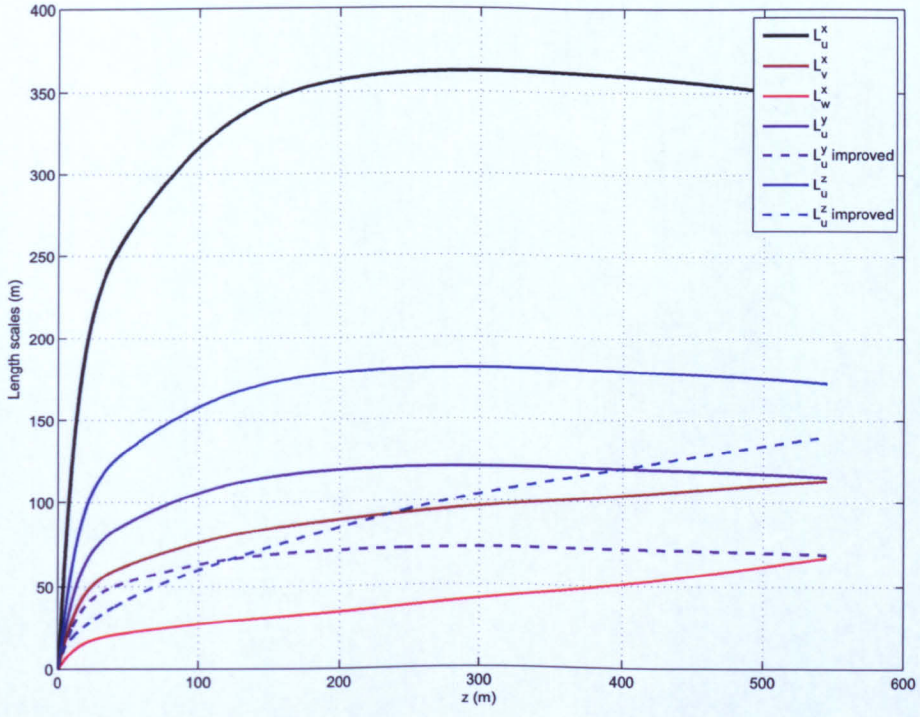

Figure 2.8: Integral length scales, $z_0 = 0.01\ m$, $\overline{u} = 10$ m/s at $z_{\text{ref}} = 10$ m (after ESDU 85020 (1985, revised in 1990)).

all expressed as a function of L_u^x:

$$\frac{L_u^z}{L_u^x} = 0.5\left(0.34\exp\left(-35(z/h)^{(1/7)}\right)\right) \tag{2.1.34}$$

$$\frac{L_u^y}{L_u^x} = 0.16 + 0.68\frac{L_u^z}{L_u^x} \tag{2.1.35}$$

$$\frac{L_v^y}{L_u^x} = 2\,\frac{L_u^y}{L_u^x}\frac{\sigma_v}{\sigma_u} \tag{2.1.36}$$

$$\frac{L_w^y}{L_u^x} = \frac{L_u^y}{L_u^x}\frac{\sigma_v}{\sigma_u} \tag{2.1.37}$$

The main integral length scales are plotted for a given roughness height, and a given mean velocity in Figure 2.8.

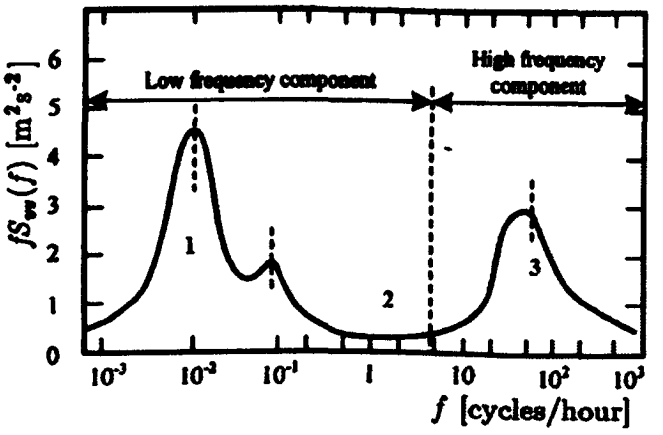

Figure 2.9: van der Hoven Spectrum of longitudinal wind speed (after Neammanee et al. (2007)).

2.1.7 Wind spectra

The van der Hoven spectrum

The van der Hoven wind spectrum characterizes the power spectral density of the wind on a large time scale for temperate latitudes. It was first presented by Panofsky and van der Hoven (1955) and then later developed by van der Hoven (1957). Figure 2.9 shows the power spectral density as a function of the frequency expressed in cycles/hour.

The van der Hoven spectrum highlights three main zones (Cook, 1992):

Zone (1) shows an important peak at a low frequency of 0.01 cycles/hour. It corresponds to the typical 4-day transit period of a fully developed weather system usually called the *macrometeorological peak.*

Zone (2) is the spectral gap [1-10 cycles/hour] where there are very few wind fluctuations, between the two majors peaks. The importance of this spectral gap is that it allows interactions between wind climate and boundary layer to be neglected, and thus be treated separately.

Zone (3) shows a second important peak, called the *micrometeorological peak*, occurs at higher frequencies [$\geq$ 10 cycles/hour] and is associated with the turbulence of the ABL.

A more recent work, presenting full scale long term wind speed monitoring, confirmed the existence of the spectral gap (Harris, 2008).

Since the fundamental frequencies of vibration of most buildings are higher than the lower end of the spectral gap, turbulence is most important in wind engineering. Therefore, when investigating wind loading on buildings, the focus is on the micrometeorological peak.

Spectra of longitudinal velocity fluctuations in the high frequencies range

A number of spectra have been proposed to describe wind turbulence in the high frequency range (upper part of the von der Hoven spectrum). However, the two which will be considered here are the von Karman and the Kaimal spectra. Both spectra respect the slope in $n^{5/3}$, corresponding to the energy cascade.

Firstly, the *von Karman spectrum* is based on the longitudinal fluctuations of the velocity and its normalised spectrum is defined as:

$$\frac{nS_u(n)}{\sigma_u^2} = \frac{4(\frac{nL_u^x}{\overline{u}})}{[1+70.8(\frac{nL_u^x}{\overline{u}})^2]^{5/6}} \tag{2.1.38}$$

where n is the frequency, $S_u(n)$ the spectral density, σ_u the standard deviation of the x-component of the velocity, L_u^x is the longitudinal integral scale of turbulence, and $\overline{u}$ is the mean velocity.

The second most commonly used spectrum (Burton et al., 2002, part 2), the Kaimal spectrum, is defined as:

$$\frac{nS_u(n)}{\sigma_u^2} = \frac{4(\frac{nL_{u1}^x}{\overline{u}})}{(1+6\frac{nL_u^x}{\overline{u}})^{5/3}} \tag{2.1.39}$$

where the length scale L_{u1}^x is related to the longitudinal length scale by $L_{u1}^x = 2.329\, L_u^x$ so that both spectra have the same high-frequency asymptotic limit (Burton et al., 2002).

While the von Karman spectrum is believed to give a good representation of the high frequency turbulence in wind tunnel modelling, the Kaimal spectrum tends to predict full scale measurements of the ABL better. Figure 2.10 shows a comparison of the Kaimal

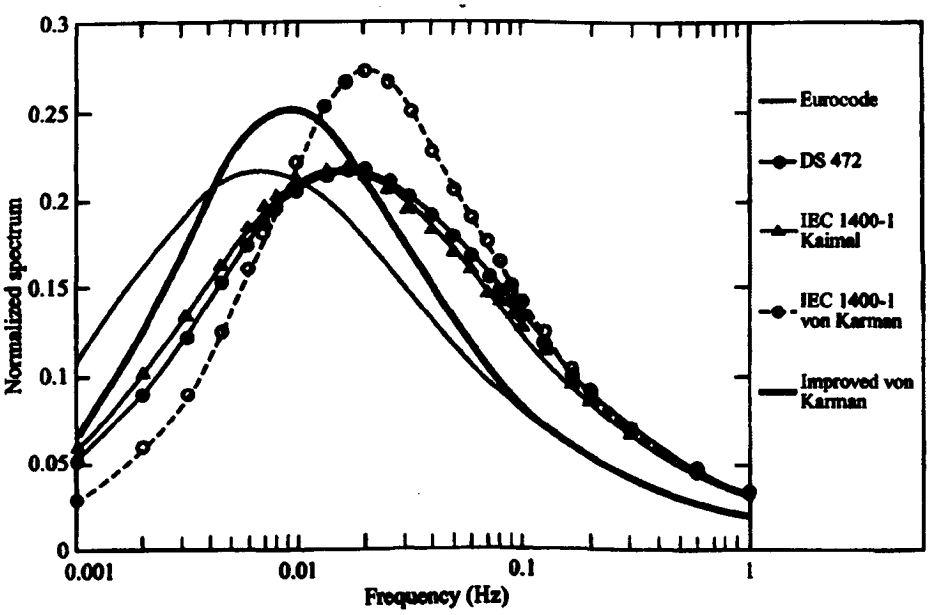

Figure 2.10: Wind spectra over rough terrain ($z_0 = 0.1$ m) at 10 m/s at $z = 30$ m (after Burton et al. (2002)).

and Von Karman normalised spectra of the wind velocity over a rough terrain; these spectra are plotted along side the spectra used in the Eurocode (European standard code of practise) and in the Danish Standards (DS).

Cross spectrum of longitudinal velocity fluctuations

This section presents results of correlations of wind speed between two points, $P_1(y_1, z_1)$ and $P_2(y_2, z_2)$, separated by a distance Δr. The degree of correlation between two points is expressed by the Coherence function and can be expressed as a decaying exponential function:

$$\mathrm{Coh}(r, n) = e^{-\hat{f}} \tag{2.1.40}$$

where

$$\hat{f} = \frac{n[C_z^2 (z_1 - z_2)^2 + C_y^2 (y_1 - y_2)^2]^{1/2}}{0.5\,[\overline{u}(z_1) + \overline{u}(z_2)]}$$

and the constants C_z and C_y are determined empirically and depend on the roughness height, and the mean velocity (Simiu and Scanlan, 1986). Figure 2.11 shows an example of equation (2.1.40) for a given velocity, on which depend the constants.

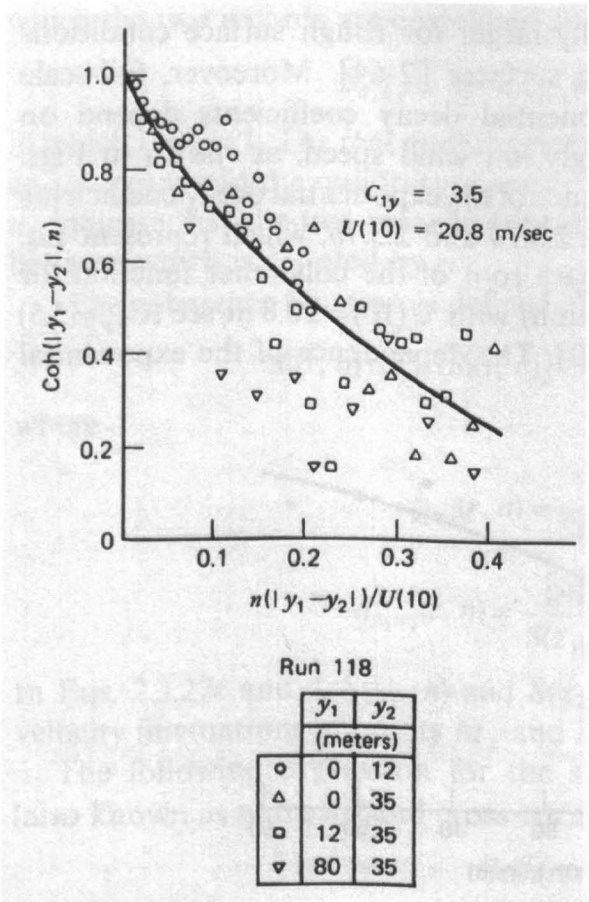

Figure 2.11: Coherence functions (after Simiu and Scanlan (1986)).

The cross spectrum $S^{cr}_{u_1u_2}$ can be deduced from the Coherence function:

$$||S^{cr}_{u_1u_2}|| = \mathrm{Coh}(r,n)\sqrt{S(z_1,n)S(z_2,n)}$$

where $S(z_1,n)$ and $S(z_2,n)$ are the spectra of the longitudinal velocity fluctuations at points P_1 and P_2.

2.2 Response of tall buildings to wind loading

2.2.1 Introduction: building aerodynamics

The domain of wind engineering is concerned with the interactions between the Atmospheric Boundary Layer and buildings, which are typically bluff-bodies. This study

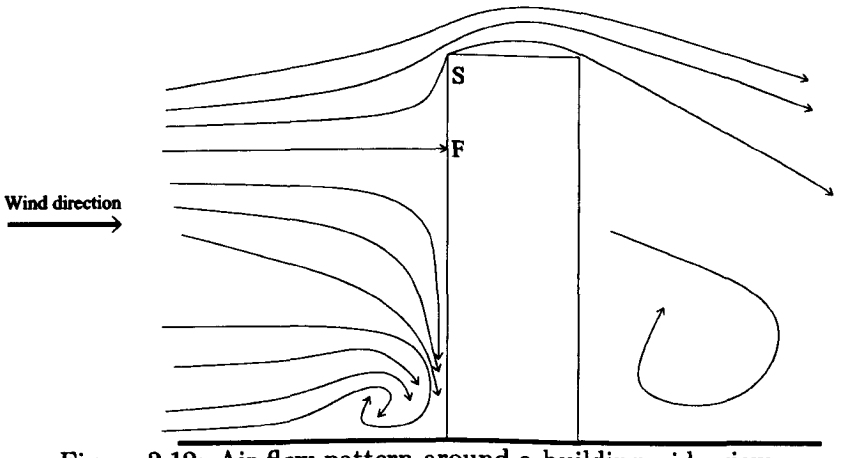

Figure 2.12: Air flow pattern around a building, side view.

focuses on tall buildings and the aerodynamics of these structures are presented in this section. The Council on Tall Buildings and Urban Habitat (CTBUH) keeps a record of all existing and future tall buildings and set the following criterion to enter their database: 14 or more storeys and over 50 meters.

Figure 2.12 represents the streamlines of the air flow around a building when the incident wind is normal to the building.

On the windward face of the building, at about two-thirds of the height, the flow comes to rest at the stagnation point (F), where the pressure is maximal. Below F, the flow goes down and allows recirculation vortices to develop near the ground. For tall buildings, this vortex creates high downward wind velocity that can severely affect the comfort of pedestrians walking around the structure.

Above F, the flow goes up to the top of the building. On the windward edge of the roof, the flow is separated (S), and a separation bubble appears. Reattachment can occur on the roof. Pressure distributions on the roof show high suction (negative pressures) near the windward edge. Pressures become less negative as the flow goes to the leeward edge. The leeward face is characterized by negative pressures that are relatively constant. In fact, the building is subjected, on average, to negative pressure on all its faces, except the windward face.

When seen from the top, the flow also separates at the right and left edges of the building.

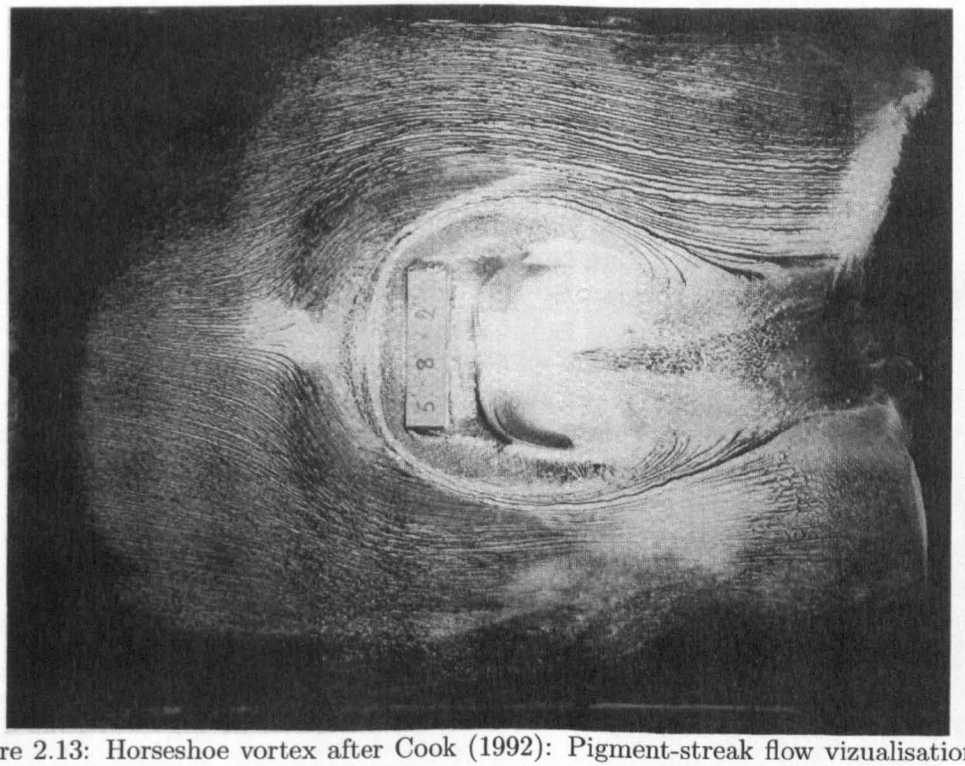

Figure 2.13: Horseshoe vortex after Cook (1992): Pigment-streak flow vizualisation of slab building model in boundary layer mean velocity profile.

Just after the edges, there is a formation of vortices. Then, the flow reattaches if the building is long enough in the along-wind direction. If the building is shorter, the flow does not reattach on the side of the building. The two branches of the flow that have been separated join in the wake, downstream of the structure. Recirculating vortices form near the base of the building, and the flow detaches and envelop these recirculating vortices. forming the horse-shoe vortex, Figure 2.13.

Just downstream of the structure, recirculating vortices develop and the flow can reattach through different patterns: studies on the flow behind a rectangular feature have shown that as the Reynolds number increases, the wake is first separated following a symmetrical pattern and then, for $Re > 30$, starts oscillating; this is called the vortex shedding (Cook, 1992). The symmetrical flow pattern and vortex shedding are illustrated in Figure 2.14. The Strouhal number St, non-dimensional, helps to characterise this phenomenon.

$$St = \frac{n_s D}{\overline{u}} \tag{2.2.1}$$

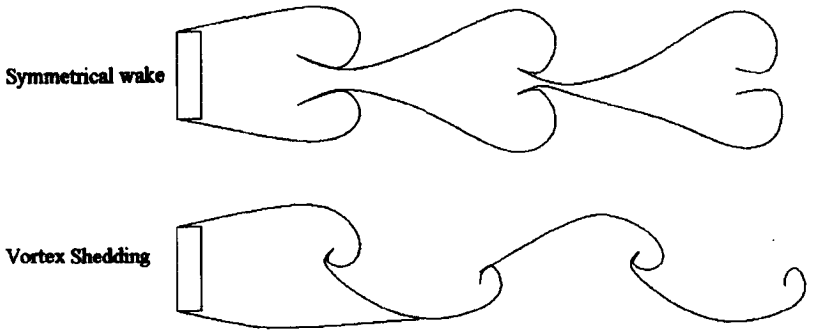

Figure 2.14: Symmetrical wake for $5 < Re < 40$ and Vortex shedding past a rectangular cylinder (laminar votex street for $40 < Re < 200$, view from the top.

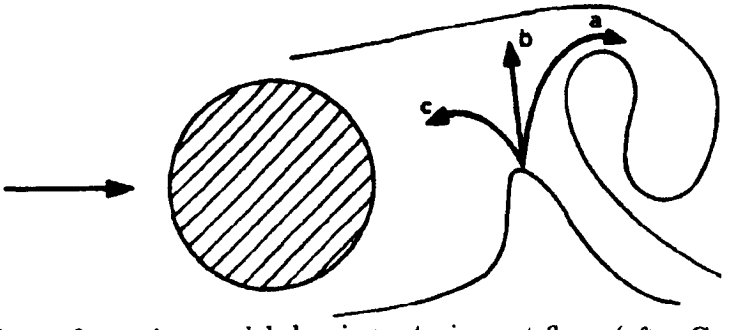

Figure 2.15: Vortex-formation model showing entrainment flows (after Gerrard (1966)).

with n_s being the frequency of a full cycle of vortex shedding, D a characteristic dimension of the body in the normal direction of the flow, and $\overline{u}$, the velocity of the oncoming wind flow. Okajima (1982) showed the dependence of the Strouhal number with the width to height ratio of rectangular cylinder as well as its dependence with the Reynolds number.

The formation of vortices in the wake has been extensively described by Gerrard (1966) for a circular cylinder and is illustrated in Figure 2.15. On this figure, the instantaneous flow line pattern shows how the flow is separated and two shear layers appear on both sides of the cylinder. The flow (a) is then entrained into the growing vortex, (b) goes into the developing shear layer and (c) is captured in the near wake region. Vortex shedding is therefore the result of the interaction of the two shear layers (Bearman, 1984).

The main difference in the flow around sharp-edged bluff-bodies and circular cylinders is the location of flow separation: for a circular cylinder, there is a critical Reynolds

number range, for which the two separation points on the sides of the cylinder are not fixed and oscillate between the front and the back of the cylinder. In the subcritical range, for $300 < Re < 3 \times 10^5$, the wake is completely turbulent, but the boundary layer separation is still laminar. In the critical range, $3 \times 10^5 < Re < 3.5 \times 10^5$, the separation is laminar on one side and turbulent on the other side but the boundary layer remain laminar. For higher Reynolds numbers, up until 1.5×10^6, the separation is turbulent, but the boundary layer is partly turbulent, partly laminar. For even higher Reynolds numbers, the boundary layer is completely turbulent at one side, and for $Re > 4 \times 10^6$, it is turbulent at two sides. This transition from laminar boundary layer with a laminar boundary layer separation to a turbulent boundary layer with turbulent boundary layer separation does not occur for a sharp-edged bluff-body, as separation must occur at the front edges of the structure.

Bearman (1984) pointed out that vortex shedding is likely to occur for structures with a high aspect ratio (height/width). Consequently, the excitation induced by vortex shedding is particularly important and will be detailed in section 2.2.2.

If the incident wind is not normal to the building, which is mostly the case, another aerodynamic feature is of importance: the delta-wing vortex. This conical vortex develops at upwind corners, when the flow separating from an edge has a component of velocity along the line of separation (Sachs, 1978). In the centre of these vortices, the suction is large, possibly leading to structural severe damage. Recirculating vortices develop along the edge, downstream the Delta-wing vortices, as shown in Figure 2.16.

2.2.2 Aeroelastic phenomena

The study of the flow around buildings shows that this is a fundamentally three-dimensional field: the air flow diverges in both cross-wind directions and in the vertical direction on the roof. This section aims to describe the main aeroelastic phenomena, vortex shedding, buffeting, and galloping excitations that can occur for structures.

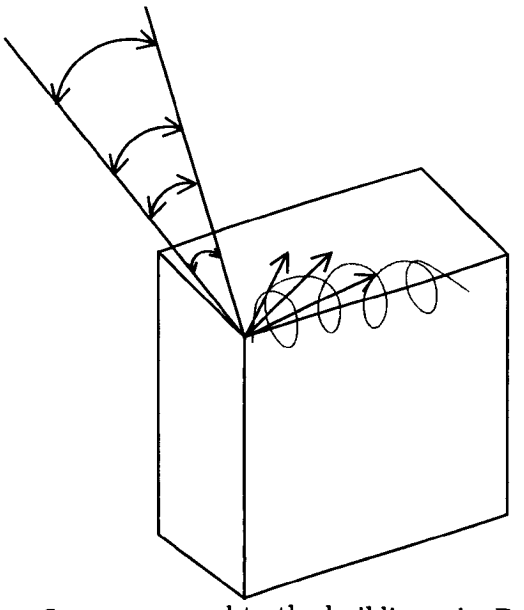

Figure 2.16: Incident flow not normal to the building: the Delta wing vortices.

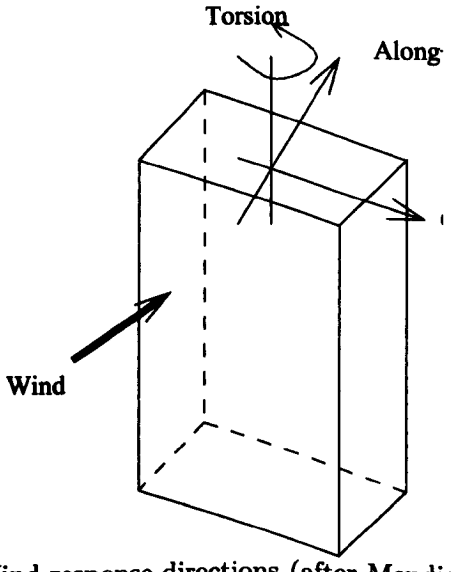

Figure 2.17: Wind response directions (after Mendis et al. (2007)).

Vortex shedding excitation of a flexible structure

The most important aerodynamic feature when studying flow around a building, especially tall buildings, is vortex shedding. Vortex shedding can induce oscillations in the direction transverse to that of the incident wind for flexible structures.

For bluff-bodies, the Strouhal number, St, depends on the structure shape and is approximately constant for high Reynolds numbers ($Re > 10^3$). As a consequence, knowing the natural frequency of the building f_n, as well as St and the across-wind dimension of the structure, D, leads to the definition of the *critical wind velocity* $u_c = \frac{f_n D}{St}$, for which the frequency of the vortex shedding equals the natural frequency of the building. This is only valid as long as the vortex shedding remains a regular (single frequency) phenomenon. In the super-critical range of Reynolds number ($3 \times 10^5 < Re < 3 \times 10^6$), the vortex shedding becomes random and is characterized by unsteady disorganised wake motion, and the vortex excitation becomes random. The amplitudes of the oscillations are lower than those seen at one of the natural frequencies of the building. Wind gusts make the occurrence of single-frequency vortex excitation more difficult because of its multi-directional and unsteady characteristics (Sachs, 1978; Simiu and Scanlan, 1986).

If the structure can move in response to the vortex shedding excitation, a major aeroelastic phenomenon can occur: the "lock-in". As the velocity increases, the frequency of vortex shedding f_{vs} increases proportionately to the shedding frequency of a static cylinder, given by the Strouhal number. When the vortex shedding frequency is close to the natural frequency f_n of the building in the transverse direction, the amplitude of the response increases, and the building oscillates at the vortex shedding frequency. As the velocity increases, the frequency of the vortex shedding is locked on to the natural frequency of the building, and the amplitude of the building response is maximal. At this point, the building "controls" the vortex shedding frequency, hence the "lock-in" phenomenon. If the velocity increases further, the amplitude of the oscillations drops, and at the upper end of this range, the vortex shedding frequency reverts to that of a static cylinder.

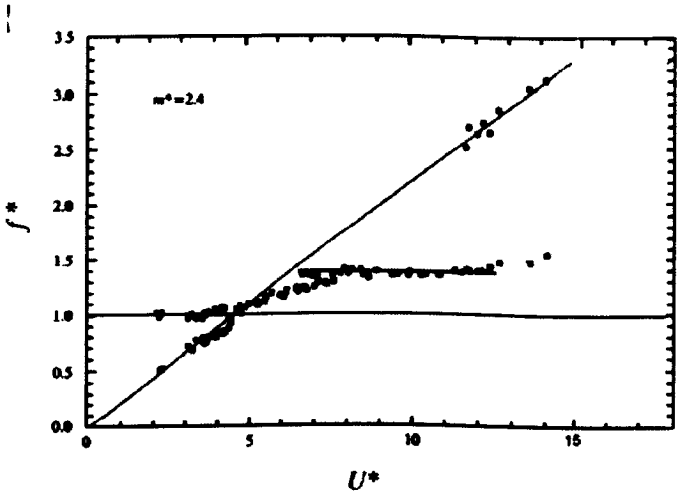

Figure 2.18: Free vibration of a cylinder: response frequency vs reduced flow speed, lock-in phenomenon identified for $f^* \approx 1.4$ (Williamson and Govardhan, 2008).

While there is an extensive literature about vortex induced vibrations of elastically mounted cylinders (Williamson and Govardhan, 2008), illustrating the lock-in phenomena, little has been done for more complex structures, such as a flexible cantilever. Figure 2.18 illustrates the response frequency versus the oncoming flow speed, and the lock-in phenomena is clearly identified: below the natural frequency of the building ($f^* < 1.0$), the building oscillates at the vortex shedding frequency with small amplitude, but as the flow speed increases, increasing the vortex shedding frequency, the frequency gets closer to the natural frequency of the building, and the cylinder starts controlling the vortex shedding frequency.

A wind-tunnel study of an oscillating tall building has been carried out by Fediw et al. (1995). It was found that for a velocity below the critical velocity (previously defined), the vortex formation is controlled by the building motion. It was confirmed that for a velocity close to the critical velocity, the natural shedding frequency coincides with the driving frequency and the largest shedding forces are observed. For velocities larger than the critical velocity, the motion effects are small and natural shedding is stronger. In addition, the local Strouhal number was found to decrease with height, probably due to the log-law velocity profile.

Buffeting excitations

Buffeting excitation of a building is caused by the combination of the velocity fluctuations of the oncoming wind flow and the turbulence shed in the wake of an upstream building. Buffeting creates along-wind loading on a building but the presence of three-dimensional excitations due to upstream buildings might also induce a torsional response. Tall buildings are more likely to undergo buffeting as their rather lower damping and light weight imply lower natural frequencies, that are more likely to be in the same range as the average frequency of occurrence of powerful gusts (Simiu and Scanlan, 1986). But even if the building's natural frequency does not lie in the range of the wind gusts, buffeting excitation can be caused by simply wake effects from neighbouring buildings. Regular vortex shedding might occur from neighbouring buildings and cause along-wind regular oscillating loading, possibly at a frequency close to the natural frequency of the building.

Within best-practise codes, extreme wind loads due to buffeting are predicted using gust factors, which are factors that characterize the fluctuating component of the wind velocity. However, it does not predict the dynamic response and it has been observed that this does not lead to accurate predictions when there are upstream buildings. When the dynamic response of a building is significant, wind tunnel tests are carried out either with an aeroelastic model, or a static combined to a high frequency force balance.

2.2.3 Structural dynamics

Unlike low and medium-rise buildings that are more or less stiff structures, tall buildings are more flexible and have lower natural frequencies, which makes them subject to vortex and gust excitation in addition to static deflections.

Nature of forces due to wind loading

For a *single-degree of freedom system (SDOF)*, the equation of motion is determined by equating the oscillating forces:

$$m\ddot{y} + c\dot{y} + ky = F(t) \tag{2.2.2}$$

where y is the displacement of the structure m the mass per unit span, c a viscous-type damping term, k the stiffness, and $F(t)$ the time-dependent force due to wind loading. The natural angular frequency of the system is given by $\omega_n = \sqrt{k/m}$ and the natural frequency by $f_n = \omega_n/(2\pi)$. The damping ratio is $\xi_n = c/(2\sqrt{km})$ where $2\sqrt{km}$ is the critical damping coefficient, above which the response is non-oscillatory.

The total dynamic response of a lightly damped structure to any excitation can be written as the superposition of the individual modal responses. The response in each mode is concentrated at a single frequency, called the modal frequency. Therefore, for analysing purposes, the whole structure is viewed as a set of independent single-degree of freedom systems, each corresponding to a single mode (Cook, 1992). Each modal response corresponds to:

(i) *A modal deflection*, which is the deflection at the position of maximum amplitude.

(ii) *A mode shape*, defined as the ratio of the local deflection and the modal deflection.

Usually, the first three modes appear in the dynamic response of a building. They are identified by peaks in the power spectral density of the acceleration response. The first two modes correspond to motion in the two principal horizontal directions, the third mode corresponds to the torsional response.

In wind engineering, as stated by Davenport (1995), the three sources of aerodynamic excitation causing dynamic response are:

1. Single-frequency excitation: forces caused by vortices shed in the wake of the structure, affecting primarily the resonant responses and occuring primarily in the cross-wind direction.
2. Random excitation: forces due to the turbulent fluctuations (or "gustiness") of the oncoming wind flow, causing both background and reso-

nant responses in the along-wind and cross-wind directions.

3. Forces induced by the motion of the structure, such as aerodynamic damping forces which control the resonant response amplitude.

Single-frequency vortex excitation

If any random excitation is artificially excluded and the sole response to a single frequency excitation is studied, $F(t)$ can be written as a simple sinusoidal function: the total force acting on the structure is defined as $F = F_0 \cos \omega t$.

The solution can then simply be expressed as the sum of the transient and steady-state solutions. The transient solution creates the decaying exponential envelope dependent on the initial disturbance, and the steady-state solution is a sinusoidal function, which is dependent on the excitation force. The steady-state response of a SDOF can be written as:

$$x(t) = F_0 H(\omega) \cos(\omega t - \phi)$$

where

$$\phi = \tan^{-1} \frac{2\xi_n(\omega/\omega_n)}{1 - (\omega/\omega_n)}$$

and $H(\omega)$ is the mechanical magnification factor (or structural admittance) and defined as:

$$H(\omega) = \frac{1}{k\sqrt{(1 - (\omega/\omega_n)^2)^2 + 4\xi_n^2(\omega/\omega_n)^2}} \tag{2.2.3}$$

The amplitude of the response is characterized by the amplification factor, which is the ratio between the amplitude of the response to the harmonic loading x_f and the amplitude of the response to a constant load x_0 (static load): x_f/x_0. The amplification factor decreases as the damping ratio increases[4].

If the frequency of the excitation force, f, reaches the natural frequency of the structure, f_n, the amplitude of the oscillating steady-state solution increases to a constant level, which can be dangerous for the structure, and resonance occurs. If the exciting frequency

[4]This will be illustrated in section 5.3.2 and in Figure 5.5.

does not approach the natural frequency, as in most cases, the steady-state solution is negligible.

Random excitation: turbulence in the oncoming wind flow

The dynamic response to a random frequency excitation, such as turbulent fluctuations in the oncoming wind flow, can no longer be expressed in terms of the oscillation amplitude and phase. Instead, a statistical approach is chosen, and was first introduced by Davenport (1961). The velocity fluctuations of the wind are characterized by their power spectral density (PSD) $S_u(n)$ (n is the frequency) of the wind spectrum, from which the PSD of F can be defined $S_f(n)$.

The response to this random excitation comprises the response to both the mean wind load, and the random component of the wind load. The former corresponds to the response to the dynamic head ($q = \frac{1}{2}\rho C_D \overline{V}^2$ where ρ is the air density, C_D the coefficient of drag and V the wind velocity) and the latter remains the sum of transient and steady-state components. However, the shape of the steady-state response is no longer sinusoidal, since it depends on a random parameter, the excitation force. As for the response to a simple oscillating excitation force, there will be a resonant response and a non-resonant response to random excitations.

The method developed by Davenport (1961) allows the response of the structure to the wind gusts to be determined in the frequency domain: the method is the wind loading chain. The wind is described in the frequency domain by the wind gust spectrum. The one used by Davenport is as follows:

$$\frac{nS_u(n)}{\sigma_u^2} = \frac{2}{3}\frac{nL_u^x/\overline{u}}{(1+(nL_u^x/\overline{u})^2)^{4/3}}$$

but in theory any spectrum model may be used, such as the one described in section 2.1.7. Only the spectrum of the longitudinal velocity is considered as it is where most of the energy is contained. The wind spectrum is then filtered by the aerodynamic admittance $X_a(n)$, which takes into the account the fact that the typical structure

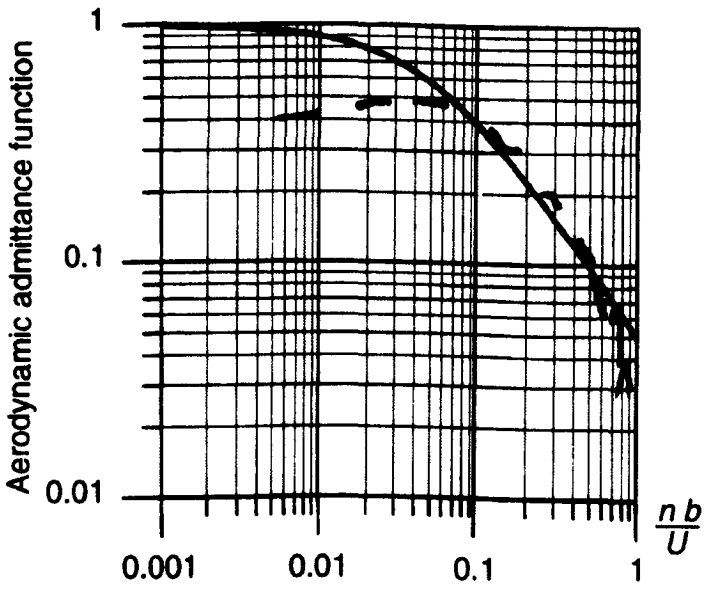

Figure 2.19: Aerodynamic admittance function (after Houghton and Carruthers (1976)).

is not point-like and velocity fluctuations approaching the windward face cannot be assumed to be uniform. This implies that the pressures acting on the building will generally not be correlated, especially at high frequencies. Effectively, that means that the aerodynamic admittance acts as a low-pass filter. An example of an aerodynamic admittance is shown in Figure 2.19. It can be observed that it is closed to 1 in the low frequencies and decreases as the frequency increases, this expresses that the large gusts that envelop the structure have more effect on the building than the smaller gusts (higher frequencies).

The aerodynamic admittance function then produces a force spectrum S_f, related to the velocity spectrum through the aerodynamic admittance:

$$\frac{S_f(n)}{\overline{F}^2} = 4|X_a(n)|^2 \frac{S_u(n)}{\overline{u}^2}$$

The response spectrum is then obtained by filtering the force spectrum with the structural admittance (similar to the structural admittance defined in Equation (2.2.3)). The response spectrum presents peaks corresponding to the background response at a lower frequency, and may also exhibit a peak at a higher frequency corresponding to the resonant response.

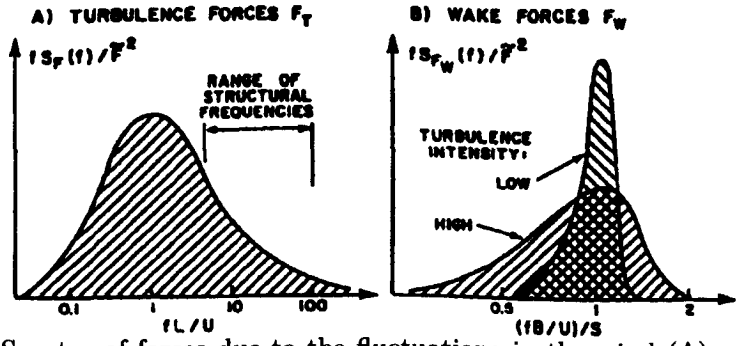

Figure 2.20: Spectra of forces due to the fluctuations in the wind (A), and spectra of forces due to vortices shed in the wake (B) (after Davenport (1995)).

Summary of wind forces acting on the building

To sum-up, the response of the structure is composed of the background response and the resonant response with a well defined frequency, generally higher than the peak for the background response. The background response consists of "an irregular and slowly varying component" and is larger in the along-wind direction than in the cross wind direction (Davenport, 1995).

The forces due to single frequency excitations (vortex shedding) and due to the fluctuations in the wind are presented in the domain frequency in Figure 2.20. In the case of forces due to the fluctuations in the oncoming flow (A), the spectra is quite broad, but shows a larger response at smaller reduced frequencies fL/U, hence at larger wind speeds U. In the case of wake forces, the peak of the spectra is much sharper and corresponds to the frequency of the vortices shed in the wake of the structure (related to the Strouhal number of the structure). It is interesting to note that when there is more turbulence intensity, which means more fluctuations in the wind, the forces spectra due to the wake gets broader. It appears that the fluctuations in the wind tend to damp the single-frequency vortex shedding excitation.

2.3 Summary and conclusions

This chapter introduced the field of wind engineering, and presented the important features of the flow around buildings, and the main characteristics of the Atmospheric

Boundary Layer, including the wind spectra and the integral length scales. This chapter also introduced building aerodynamics and the main characteristics of the dynamic response of buildings to wind loading, including the wind loading chain developed by Davenport. It is the object of the next chapter to present the models used in CFD to model the ABL and the flow around buildings.

Chapter 3

Literature Review of Computational Wind Engineering

3.1 Introduction on Computational Wind Engineering

3.1.1 CFD in wind engineering

Computational Fluid Dynamics (CFD) provides various tools to investigate complex fluid flows. The spatial domain is discretized into small cells to form a volume mesh. Numerical methods, such as the Finite Difference Method (FDM), Finite Volume Method (FVM) or the Finite Element Method (FEM) are then applied to reformulate the Navier-Stokes equations (2.1.1-2.1.4) as a series of algebraic equations. These equations are solved numerically over the domain, with specified boundary conditions to simulate the effects of the environment.

Soon after computers first became available they were used in the solution of partial differential equations and by the 1970s the use of computers to solve the equations governing fluid flow was under active investigation by researchers (Patankar and Spalding, 1972; Launder and Spalding, 1974). The application of CFD to wind engineering problems started in the 1980s, when a market for CFD emerged in a handful of engineering fields and several companies like Fluent, AEA Technology and Computational Dynam-

ics emerged to fulfil this need. Despite progress of Computational Wind Engineering (CWE) in this time, wind loading standards and building codes of practice still rely on wind tunnel studies for non-standard building designs. However the use of wind tunnels is associated with several limitations that CFD can potentially overcome. For example, it is not possible to fully model swirling flow impacts on structures and gust fronts in wind-tunnels. Furthermore, modelling of flow inside buildings or around bluff bodies in wind-tunnels is difficult due to Reynolds number limitations (Stathopoulos, 1997). CFD offers some flexibility that is maybe of a different nature than the flexibility offered by wind-tunnels. In addition to flexibility, it is possible with CFD to extract data everywhere in the domain. But perhaps the most prominent advantage of CFD in wind engineering is the fact that it can potentially be integrated into the virtual design process of a building.

However, despite these potential advantages of CFD, it has been the target of many critics from the wind engineering community, for whom CFD is a very young tool that cannot compare with wind tunnels and the level of expertise reached in wind tunnel testing. Some of these criticisms are based on the fact that on some occasions, CFD users have provided different solutions, sometimes simply wrong, to the same problem (often claiming to use the same models) (Richards and Quinn, 2002; Sabatino et al., 2010). Wind tunnel testing requires an experienced worker who knows the characteristics of the wind tunnel, the type of flow it can produce and the type of the flow that needs to be modelled. In the same way CFD requires an experienced user who knows what equations are solved, and how, and the details of the models used. Because wind tunnels have been used for much longer, very precise guidance exists; the same cannot be said about CFD, although there has been attempts to provide better and unified guidance for the application of CFD to wind engineering such as in Franke et al. (2004, 2007).

As recognized by Castro and Graham (1999), many of the models have been developed for very precise applications by researchers concentrating on modelling a particular flow, often in the aeronautics industry, concerned with flows around streamlined bodies. These CFD codes might be very good at predicting the flow for a certain application but would

fail to offer a more general code simply because they were not designed for a general use; this is true of most turbulent models, which have been designed for specific applications. Turbulence modelling is particularly important in CWE because unlike the aeronautics industry that models flows around streamlined bodies, CWE is concerned with flows around bluff bodies. For this reason, there is a need for assessing the performance of each of these models in CWE.

However over the past 10 years, much progress has been made in CFD for wind engineering problems, to the point where its use has been accepted for some applications. This includes predicting wind speeds in pedestrian areas, where CFD is considered a good substitute to wind tunnel testing, as reported by Bitsuamlak and Simiu (2010) at a recent symposium on CWE. Bitsuamlak and Simiu reviewed the areas in which CFD had proven its use, and among these, it was noted that CFD could be useful to predict global aerodynamic loads on structural elements, or could complement experimental data on flow generation. In short, far from being redundant in the field of wind engineering, or providing a complete alternative to traditional wind tunnel testing, CFD is best used in conjunction with wind tunnels to achieve a better understanding of wind flow around buildings and wind loads on structures.

It could be said that the major disadvantage of CFD in wind engineering is its apparent ease of use and approachability. However, CFD does requires very careful attention to the following aspects: the discretization of the domain (mesh), turbulence modelling and boundary conditions as stated by Castro and Graham (1999). The purpose of this chapter is to review the current state of the art in CWE, and more precisely in these three areas of interest.

3.1.2 CFD methodology

Four steps can be distinguished in the CFD process:

- Geometry: The domain and the structure within that domain are built at this step. Details on how the geometry of the domain and the structure should be

determined are given in the present Chapter.

- Meshing: At this key stage, the spatial domain is divided into Control Volumes (CV) to form a mesh (grid.) Guidelines for this are presented in section (3.1.4).

- Model set-up: Boundary conditions, turbulence model, material properties, solver settings, data output options, frequency of the output of the flow field, etc are chosen at this stage. This Chapter explains how the boundary conditions should be chosen in CWE. As the choice of the turbulence model is crucial, two sections are devoted to this issue: section 3.3 develops the methods for modelling turbulence using the Reynolds Averaged Navier-Stokes equations. Section 3.4 presents the Large Eddy Simulations (LES), which allows most of the turbulence length scales to be resolved.

- Solver: the CFD code discretizes the Navier-Stokes equations, and solves them over the discretized domain of interest. Details on the solver can be found in section 3.1.3.

- Analysis of results or post-processing where data such as velocity flow fields, vorticity and pressures are extracted on lines, planes, surfaces of the domain under investigation.

3.1.3 Discretization of the governing equations

Spatial discretization

Once the governing equations of the flow, the Navier-Stokes equations, have been determined (first defined in Equations 2.1.1-2.1.4), they need to be spatially discretized since

in general they cannot be solved analytically:

$$\frac{\partial u}{\partial t} + (u\frac{\partial u}{\partial x} + v\frac{\partial u}{\partial y} + w\frac{\partial u}{\partial z}) + \frac{1}{\rho}\frac{\partial p}{\partial x} = fV + \frac{1}{\rho}\frac{\partial \tau_u}{\partial z}$$

$$\frac{\partial v}{\partial t} + (u\frac{\partial v}{\partial x} + v\frac{\partial v}{\partial y} + w\frac{\partial v}{\partial z}) + \frac{1}{\rho}\frac{\partial p}{\partial y} = -fU + \frac{1}{\rho}\frac{\partial \tau_v}{\partial z}$$

$$\frac{\partial w}{\partial t} + (u\frac{\partial w}{\partial x} + v\frac{\partial w}{\partial y} + w\frac{\partial w}{\partial z}) + \frac{1}{\rho}\frac{\partial p}{\partial z} + g = -\frac{1}{\rho}\frac{\partial \tau_w}{\partial z}$$

$$\frac{\partial \rho u}{\partial x} + \frac{\partial \rho v}{\partial y} + \frac{\partial \rho w}{\partial z} = 0$$

That is, continuous equations must be written in a discrete form. The Navier-Stokes equations are discretized using discretization methods such as the Finite Difference Method (FDM), Finite Volume Method (FVM) or the Finite Element Method (FEM). The FVM is the most commonly used in CFD codes, partly because conservation of fluxes through a particular volume is easier to ensure with FVM, and FVM is more efficient in terms of CPU usage. ANSYS-Fluent, which is used for the present work, uses the FVM.

The Finite Volume Method can be described as follows: The spatial domain is divided into finite control volumes, as shown in Figure 3.1. The discretized formulation of the Navier-Stokes equations are then solved over the grid. The balance of mass, momentum and energy is ensured by solving the conservative form of the Navier-Stokes equations. The integral formulations of these equations are expressed in equation 3.1.1 for a variable ϕ.

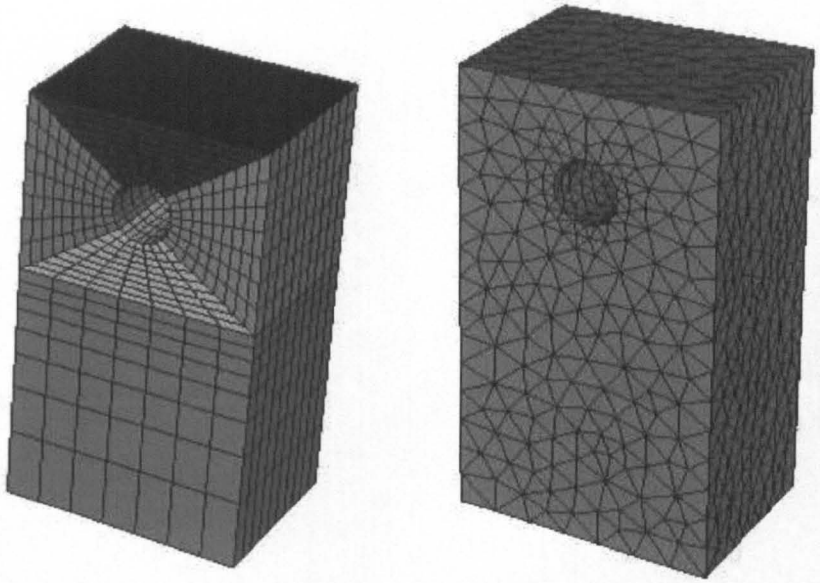

(a) (b)

Figure 3.1: Structured (a) and unstructured mesh (b). The structured mesh is composed exclusively of hexahedral elements, and the unstructured mesh is composed of tetrahedral elements.

$$\underbrace{\int_V \frac{\partial \rho\phi}{\partial t} dV}_{\text{Rate of change (transient)}} + \underbrace{\int_\Sigma \rho\phi\vec{v} \cdot d\vec{A}}_{\text{Net convective flux}} = \underbrace{\int_\Sigma \Gamma_\phi \nabla\phi \cdot d\vec{A}}_{\text{Net diffusive flux}} + \underbrace{\int_V S_\phi dV}_{\text{Source term}} \tag{3.1.1}$$

where V is the volume of the CV, Σ is the surface of the CV ρ is the fluid density, $\vec{v}$ is the velocity vector, $\vec{A}$ is the surface area vector, Γ_ϕ is the diffusion coefficient for ϕ, $\nabla\phi$ is the gradient of ϕ, and S_ϕ is the source of ϕ per unit volume.

For each CV, the rate at which a variable flows in through the boundaries is calculated and the rate of change of the variable is computed. A matrix is built with all variables in each cell. This matrix is solved by iteration. The process is stopped when the residual error reaches a pre-set value, which can be different for each variable.

The size of the grid cells must be carefully chosen. Generally, most cells are placed where the gradients of the flow variables are largest. A compromise must be found between

the number of cells of the mesh and the degree of accuracy that is required. On the one hand, a very fine mesh with a large cells number might require large CPU time to converge. In addition, it might also be difficult to converge because of oscillating features of the flow at small scales. On the other hand, a very coarse mesh might not provide accurate results by missing important features of the flow, such as a recirculation zone on a roof.

The convection and the diffusion terms in equations 3.1.1 require the values of ϕ at the surface of the control volume. However, since only the central values are stored by the CFD code, a scheme must be adopted to extrapolate the values on the boundaries. Most schemes uses the upstream cell's values to compute the face value ("upstream" is understood as upstream of the flow).

The simplest of these schemes is the *first-order upwind differencing scheme* which states that the value at the surface equals the value at the centre of the upstream cell. This method can be used when the expected level of accuracy is low. The *second-order upwind scheme* uses the cell-centered value ϕ and the gradient within the upstream cell $\Delta\phi$ to compute the face value ϕ_f:

$$\phi_f = \phi + \nabla\phi \cdot \vec{r} \tag{3.1.2}$$

where ϕ is the cell-centered value in the upstream cell, $\nabla\phi$ is the gradient in the upstream cell and $\vec{r}$ is the vector from the upstream cell centroid to the face centroid.

A third major scheme is called *QUICK* (Quadratic Upstream Interpolation for Convective Kinetics) and is a quadratic differencing method. The value at the surface of the cell n is computed using the values at the centres of the cell immediately upstream $(n-1)$, and the second cell upstream $(n-2)$. I can be written as follows:

$$\phi_f = \frac{1}{8}[A\phi_{D-1} + B\phi_U] + \frac{7}{8}[C\phi_{D-1} - D\phi_{D-2}] \tag{3.1.3}$$

where U stands for cell upstream of the surface, $D-1$ for the immediately downstream

cell and $D-2$ for the second cell downstream. A, B, C and D depend on the grid dimensions. The QUICK scheme can only be used when the grid is composed of quadrilateral and hexahedral cells as the above equation requires a unique upstream face and a unique downstream face.

Temporal discretization

For transient simulations, the rate of change of ϕ with respect to time, $\partial\rho\phi/\partial t$, must be taken into account and hence written in a discretized form. This can be done with an implicit first-order scheme, that is, ϕ_{n+1} is related to the value of ϕ_{n+1} in the neighbouring cells. If more accuracy is required, a second-order scheme can be adopted: The values at the current and at the previous time steps are combined to calculate the rate of change at the future time step. The choice of the time-step is crucial as it must be small enough to capture the important features of the flow, but not too small because a very small time step will require much more computational power without any increase in accuracy.

Temporal and spatial discretization are related through the Courant number:

$$C = \frac{u \times \Delta t}{\Delta x} \tag{3.1.4}$$

where u is the mean velocity of the flow, Δt is the time step, and Δx a characteristic grid size. The time step size is chosen such as $C < 1$. This means that the distance travelled by a particle of fluid during one time step should not be longer than the grid size.

Pressure-velocity coupling

Figure 3.2 summarizes the sequence of events followed by the CFD solver, for both segregated and coupled solvers.

In a *segregated solver*, the governing equations are solved sequentially. Firstly, the

momentum equations are solved with an assumed pressure gradient. The computed solution is then put into the continuity equation because the computed velocities from the momentum do not a priori satisfy the continuity equation, which leads to a corrected pressure. This corrected pressure is then put back into the momentum equations. This process is iterated until all the variables satisfy the momentum and the continuity equations. The other variables (velocity, mass flux) are then updated accounting for the new computed pressure. The scalar variables, such as turbulence quantities, are calculated afterwards. The whole process is repeated until all variables have converged, that is, the residuals of the variables have gone below a pre-fixed value. In addition to the residuals, forces, mass flux and various field variables at monitor points must be monitored to ensure that these have reached a stationary state, which means that the variables do not vary with time, or if they do, they vary in a consistent manner that can be predicted based on previous occurrences. One variant of this process is called the SIMPLE (Semi-Implicit Method for Pressure-Linked Equations) scheme.

The PISO (Pressure Implicit with Splitting of Operators) method is similar to SIMPLE but uses a second pressure correction equation before solving for the scalar variables. Versteeg and Malalasekera (2007) remarked that neither of these methods is superior in terms of accuracy. Their performance seems to be dependent on the application. However, PISO is recommended for transient simulations by the ANSYS-Fluent manual, and is, therefore, used in the present work.

For completeness, the *coupled pressure-velocity* method simultaneously solves the systems of momentum and pressure-based continuity equation. Consequently, the pressure correction equation is not necessary. Due to the strong coupling, the iteration time and memory requirements are increased compared with a segregated solver, but the convergence, when occurring, is improved.

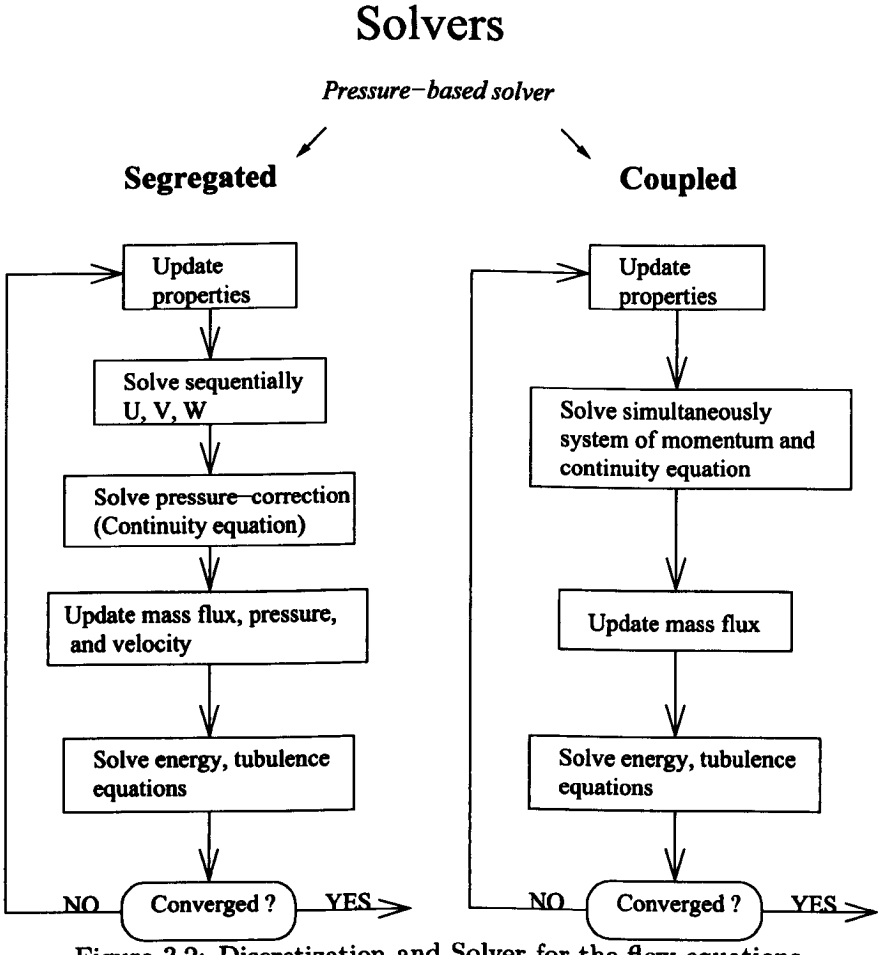

Figure 3.2: Discretization and Solver for the flow equations.

3.1.4 The computational grid

Structured and unstructured grids

A structured grid is defined as being composed of the regular repetition of an identifiable block (usually quadrilaterals in 2D, hexahedra in 3D), Figure 3.1a. Unstructured grids are characterized by irregular patterns as shown in Figure 3.1b; information on the location of the vertices and the connectivity to the neighbouring cells must be stored for each cell. For a very complex geometry, it is often easier to build an unstructured grid, while structured grids are limited to simple geometry and become either unfeasible or not optimal in terms of CPU time and accuracy for complex geometries. Practically, this means that for a structured grid, if the index of a node is known, the connectivity

information of this node is also known. While for an unstructured grid, a connectivity table detailing the connectivity for each node is needed. As far as most CFD codes are concerned (including ANSYS-Fluent), all grids are treated as unstructured. However, in some applications the physics of the flow requires the use of a structured grid. Besides, for a given geometry, a structured grid often involves a lot less nodes than an unstructured grid, which means that the computational time can be significantly reduced.

General guidelines for building the grid

Franke et al. (2004), published fairly general guidelines for good practise in CWE. Notably they specified how the computational grid should be defined: The grid should be fine enough to capture vortices and shear layers, grid stretching and compression should be avoided particularly where the gradients of values are large and numerical diffusion must be limited, so that, ideally, the line connecting the centres of two consecutive cells should be aligned with the flow, Figure 3.3. The numerical diffusion is related to the orthogonality of the mesh: a mesh is defined as orthogonal if, for each face within it, the face normal is parallel to the vector between the centres of the cells that the face connects. An example is a mesh of hexahedral cells whose faces are aligned with a Cartesian coordinate system. The second order differencing in Fluent tried to minimize this.

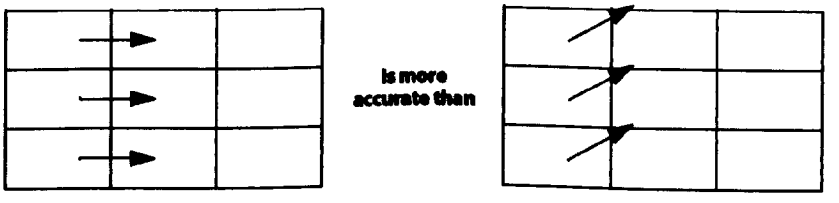

Figure 3.3: Numerical Diffusion.

In terms of an element hierarchy, hexahedra are known to introduce smaller truncation errors, so these elements are preferred to tetrahedra wherever it is feasible. Generally,

a fine mesh should be used in the regions of high gradients. Furthermore, the following criteria must be checked for a good quality mesh: the aspect ratio and the angle skewness, as illustrated in Figure 3.4. Both are used to check the quality of a mesh composed of hexahedra and tetrahedra (in 3D). The aspect ratio will naturally be far from 1 near the walls, as the boundary layer requires a finer grid in the direction normal to the wall (steep gradients) than parallel to it. The skewness is particularly important when using tetrahedra. A third quality criteria must be checked: the stretching ratio, which can be defined as the rate at which the cell size increases between two consecutive cells.

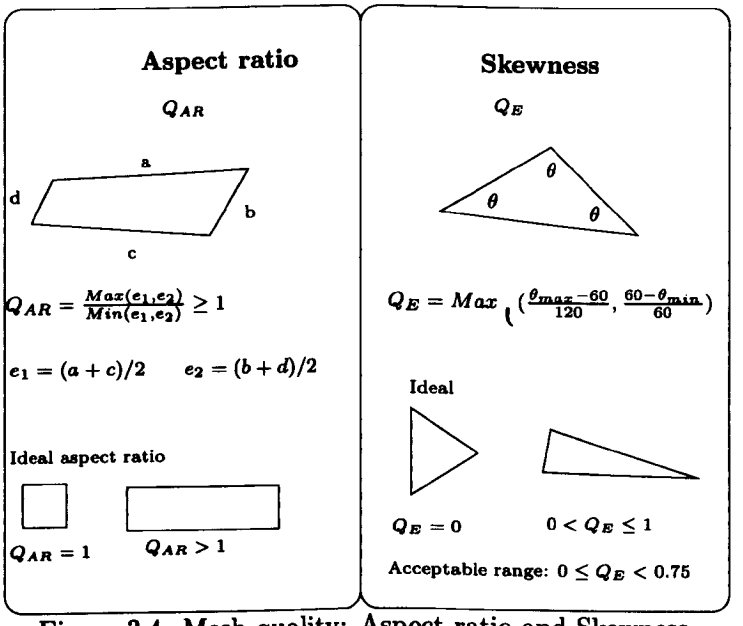

Figure 3.4: Mesh quality: Aspect ratio and Skewness.

Results are considered grid independent when the extrapolation of the results obtained with gradually refined meshes reach an asymptotic range. It is recommended to test at least three grids with increasing refinement. Grid independence is a major criterion for good-quality results.

2D and 3D grids

A three-dimensional grid is an obvious choice as all features of the flow can only be captured in a 3D domain. For example, vortex shedding is a transversal flow character-

istic and buffeting is caused by 3D wind excitation. The loss of these features of flow must be taken into consideration when a 2D grid is used. A 2D mesh is suitable for either; 1) coarse and quick runs; or 2) when a single phenomenon is to be observed; or 3) if certain parameters need to be tested with different values to assess their influence on one particular feature of the flow. It is generally not suitable when modelling turbulent structures arising from bluff body, as these are essentially 3D.

3.2 Introduction to turbulence modelling

Turbulence modelling is one of the main challenges when modelling wind flows within the ABL. Researchers have tried to improve numerical results by developing numerous turbulence models. They started with two-equation models, that were to be used in steady-state simulations, commensurate with the computer capacities then available. These models were then modified into several different versions in order to improve the characteristics of the predicted flow. However, most of these modified versions would in fact only improve one aspect of the flow, and would therefore be quite specific to a particular application (Castro and Graham, 1999). Consequently, as computer resources were increased, the use of two-equation turbulence models in academia was largely replaced by more computationally expensive models to solve most of the turbulence scales in a transient manner. Most prominent is the so-called Large Eddy Simulation (LES). Nowadays, although the focus in academia is on LES, two-equation turbulence models are still investigated as their robustness, simplicity and computational economy make them the primary choice for industrial applications (Hanjalić and Kenjereš, 2008).

It must be noted that Direct Numerical Simulations (DNS), in which the Navier-Stokes equations are solved without any turbulence modelling, cannot be considered in CWE. This is because the large 3D domains and high Reynolds numbers involved would require an amount of grid points that is beyond current computer capacity. Therefore, it is inconceivable that DNS be used for wind engineering purposes, unless a quantum leap in computing power is achieved.

3.3 RANS approach for turbulence modelling in wind engineering

Despite the obvious limitations of the RANS approach, it is instructive to describe some of the more commonly used models to provide context.

3.3.1 The k-ϵ turbulence model

The k-ϵ model is a two-equation turbulence model, based on the RANS (Reynolds Averaged Navier-Stokes) approach (see section 2.1.5 for RANS equations). In order to *close* the set of RANS equations, the k-ϵ model introduces two new variables: the turbulent kinetic energy k and the rate of dissipation of turbulent kinetic energy ϵ. These variables are defined as follows:

$$k = \frac{1}{2}(\overline{u'}^2 + \overline{v'}^2 + \overline{w'}^2) \tag{3.3.1}$$

$$\epsilon = \frac{\partial k}{\partial t} \tag{3.3.2}$$

The transport equations for k and ϵ are presented in equations below (Versteeg and Malalasekera, 2007):

$$\frac{\partial k}{\partial t} + \frac{\partial k u_i}{\partial x_i} = \frac{\partial}{\partial x_j}(\frac{\nu_t}{\sigma_k}\frac{\partial k}{\partial x_j}) + 2\nu_t S_{ij}.S_{ij} - \epsilon \tag{3.3.3}$$

$$\frac{\partial \epsilon}{\partial t} + \frac{\partial \epsilon u_i}{\partial x_i} = \frac{\partial}{\partial x_j}(\frac{\nu_t}{\sigma_\epsilon}\frac{\partial \epsilon}{\partial x_j}) + C_{1\epsilon}\frac{\epsilon}{k}2\nu_t S_{ij}.S_{ij} - C_{2\epsilon}\frac{\epsilon^2}{k} \tag{3.3.4}$$

The first terms of the right-hand side represent the effective diffusivity of k and ϵ, respectively (σ_k and σ_ϵ are the turbulent Prandtl numbers for k and ϵ), the second terms on the right-hand side of the equations express the rate of production of k or ϵ. The last terms on the right-hand side are the destruction rate of k and ϵ. where

$S_{ij} = \frac{1}{2}(\frac{\partial U_i}{\partial x_j} + \frac{\partial U_j}{\partial x_i})$ are the mean rates of deformation (strain-rate tensor),

$\nu_t = C_\mu \frac{k^2}{\epsilon}$ is the turbulent viscosity.

and the constants are taken as follows: $C_\mu = 0.09$, $\sigma_k = 1.00$, $C_{1\epsilon} = 1.44$, and $C_{2\epsilon} = 1.92$.

The Reynolds stresses are then computed following the **Boussinesq hypothesis**, which states that the Reynolds stresses $\overline{u_i' u_j'}$ are proportional to S_{ij}:

$$-\rho\overline{u_i' u_j'} = 2\mu_t S_{ij} - \frac{2}{3}\rho k \delta_{ij} \tag{3.3.5}$$

Near wall modelling

The near wall region is characterized by strong gradients, due to important viscous effects. When the mesh is not fine enough near the wall to resolve all the way down to the wall, the near wall region is modelled through the use of wall functions. One defines z^+ as the dimensionless wall unit,

$$z^+ = \frac{u^* z}{\nu}$$

and

$$u^+ = \frac{U}{u^*}$$

where u^* (defined in equation 2.1.13) is the wall friction velocity, z the distance fro; the wall to the first node, and ν is the kinematic viscosity, defined in equation 2.1.19. The wall functions are based on the idea that the near wall flow is composed of two main layers and a single intermediate layer:

1. Adjacent to the wall, for $z^+ < 30$, viscous effects are dominant. There is a linear relationship between the fluid velocity and the distance from the wall, $u^+ = z^+$. This region is called the *Laminar region* or viscous sub-layer.

2. Above the Laminar region, for $30 < z^+ < 500$, stands the *logarithmic layer*, in which turbulence dominates. The velocity follows a logarithmic law.

3. In between these two layers stands the buffer layer, in which turbulence and viscous effects are balanced.

A comprehensive work by Blocken et al. (2007) reviews the modelling of the flow near the wall using the k-ϵ turbulence model within the ABL. The general logarithmic law for the near wall flow is written as follows:

$$\frac{U}{u^*} = \frac{1}{\kappa} ln(\frac{u^* z}{\nu}) + B - \Delta B(k_S^+) \tag{3.3.6}$$

where U is the mean streamwise velocity, u^* is the friction velocity, κ is the von Karman constant, z is the coordinate in the wall normal direction, ν is the kinematic viscosity, B is the integration constant in the log-law, k_S^+ the dimensionless equivalent sand-grain roughness height defined by $k_S^+ = \frac{k_S u^*}{\nu}$, and ΔB is called the roughness function and its definition depends on the regime: aerodynamically smooth ($k_S^+ < 2.25$), transitional ($2.25 \leqslant k_S^+ < 90$) or fully rough ($k_S^+ > 90$).

The law of the wall is shown in Figure 3.5: the linear sublayer, buffer and logarithmic layers are shown along with the $z+$ associated limits.

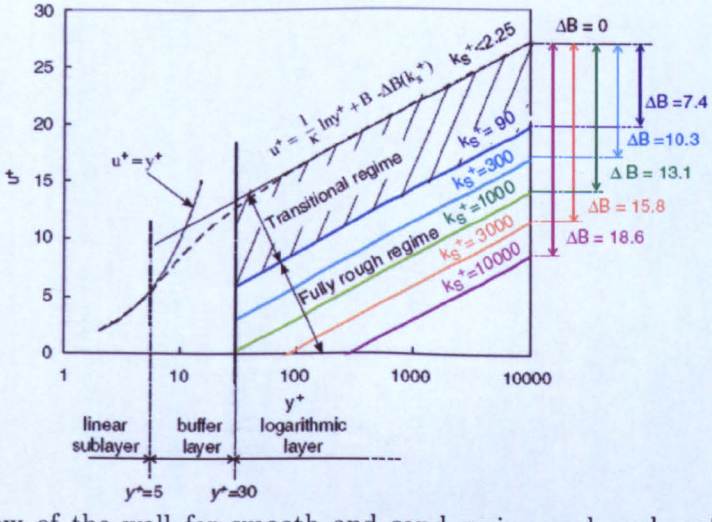

Figure 3.5: Law of the wall for smooth and sand-grain roughened surfaces with the dimensionless sand-grain roughness height k_S^+ as a parameter, $u^+ = U/u^*$ and ΔB is the roughness function, and y the distance normal to the wall (after Blocken et al. (2007)).

In order to implement equation 3.3.6 into a CFD code, U and y are replaced by their value at the centre of the first cell adjacent to the wall. Different CFD codes use slightly different definitions of the roughness height, hence the constant k_S^+ must be adjusted.

For example, equation 3.3.6 takes the following form in ANSYS-Fluent:

$$\frac{U_P}{u^*} = \frac{1}{\kappa} ln(\frac{u^* z_P}{\nu C_S k_S^+}) + 5.43 \tag{3.3.7}$$

where U_P and z_P are the velocity and the distance of the centroid of the adjacent cell from the wall, as shown in Figure 3.6. C_S is a constant equal to 0.5.

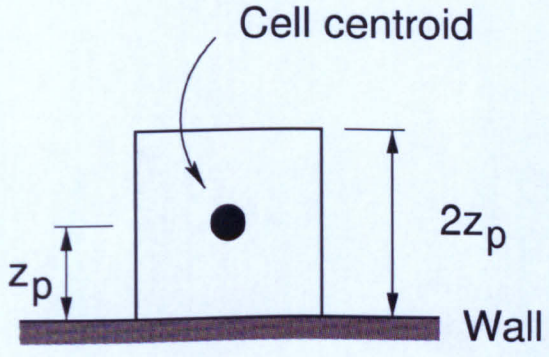

Figure 3.6: Adjacent cell to the wall, z_P in the Figure refers to y_P in Equation 3.3.7.

The relationship between k_S and the roughness length z_0 (that is more commonly used) in ANSYS-Fluent follows from the previous equations:

$$k_S = \frac{9.793 z_0}{C_S} \tag{3.3.8}$$

Application of the k-ϵ model to CWE

The standard k-ϵ turbulence model has been widely used in various applications for its efficiency. However, the standard version is not exempt from drawbacks in CWE. Early work has shown a major limitation: the standard k-ϵ turbulence model clearly over-predicts the turbulence kinetic energy, k, in the impinging region, i.e. around the frontal corners of the bluff bodies (Murakami and Mochida, 1995; Murakami, 1997, 1998). This leads to poor prediction of the flow on the roof, so that separation does not occur as it should (Richards and Quinn, 2002). In addition, the stagnation point on the windward face is not accurately predicted (Franke et al., 2004). The over-prediction of

turbulent kinetic energy is believed to be due to the use of Eddy Viscosity Modelling (Murakami, 1998). In order to reduce the over production of k in the impinging region, several research groups have proposed revised versions of the standard k-ϵ model. The most renowned of these models are the LK model by Kato and Launder (1993) and the MMK model by Murakiami, Mochida and Kondo (Murakami et al., 1994). The LK k-ϵ model helps to significantly reduce the production of k, but inconsistency in its mathematical formulation lead to the development of the MMK k-ϵ model. Details about these models and how they differ from the standard k-ϵ model can be found in table 3.1.

Std k-ϵ model	LK k-ϵ model	MMK k-ϵ model
$P_k = \nu_t S^2$	$P_k = \nu_t S\Omega$	$P_k = \nu_t S^2$
$\nu_t = C_\mu \frac{k^2}{\epsilon}$	idem	$\nu_t = C^*_\mu \frac{k^2}{\epsilon}$
$S = \sqrt{2S_{ij} \cdot S_{ij}}$	$\Omega = \sqrt{\frac{1}{2}(\frac{\partial U_i}{\partial x_j} - \frac{\partial U_j}{\partial x_i})^2}$	$C^*_\mu = C_\mu \frac{\Omega}{S} (\frac{\Omega}{S} < 1)$
		$C^*_\mu = C_\mu (\frac{\Omega}{S} \leq 1)$

Table 3.1: Standard and revised k-ϵ turbulence models (P_k = Rate of Production of k).

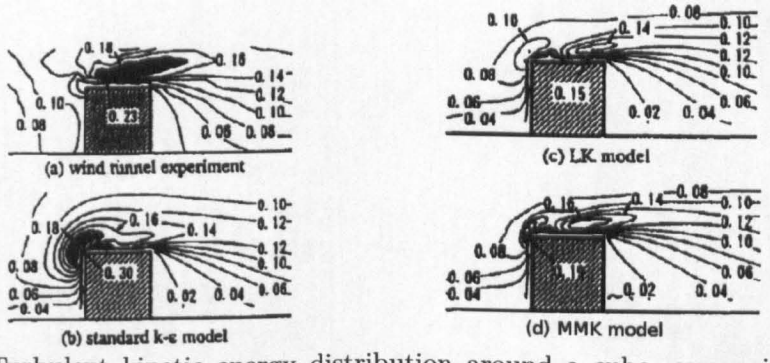

Figure 3.7: Turbulent kinetic energy distribution around a cube, comparison of the standard k-ϵ model with the revised LK and MMK turbulence models (after Murakami (1997)).

Figure 3.7 is extracted from the review of turbulence modelling conducted by Murakami (1997) and shows the improvements brought about by these revised models compared to the standard k-ϵ model. It can be seen from the comparison that the revised models do reduce the production of k around the frontal corner of the cube. However, the comparison of the numerical results with wind-tunnel outcomes highlights the lack of

accuracy of the turbulence models in the prediction of the reattachment length behind the cube. All revised k-ϵ models over-predicted the reattachment length behind the cube (Murakami, 1998), leading to incorrect pressure predictions.

Another modified version of the standard k-ϵ model must be mentioned here. The RNG k-ϵ model. It was developed in 1992 by Yakhot et al (Yakhot et al., 1992). In short, the model removes the effects of the smaller scales from the transport equations and expresses their effects in terms of larger scale motions and a modified viscosity (Versteeg and Malalasekera, 2007) in order to account for a wider range of motion scales. At first, this model was considered to be very promising because of the advanced mathematical techniques involved and was therefore investigated in CWE. However, this interest has rapidly decreased as research groups have noticed mixed results (Swaddiwudhipong and Khan, 2002; Hoxey et al., 2002; Mochida et al., 2002).

In 2002, Richards and Quinn (2002) reviewed the performance of the standard k-ϵ, the MMK k-ϵ and the RNG k-ϵ model for modelling the flow around a cube. They compared the numerical results obtained by other research groups to full-scale data recorded at the Silsoe cube, which is a 6-meter square cube installed at the Silsoe Research Institute in Bedford. The authors noticed that the MMK model predicts an excessive separation, whereas the standard k-ϵ model predicts no separation at all and the RNG k-ϵ model can predict a correct separation and an acceptable reattachment length. However, when the wind was applied at a 45° angle to the cube, none of these models were able to predict the correct pressure distribution on the cube, especially the negative pressure along the windward edges. It was concluded that none of the models were able to predict the correct turbulence levels, and that velocities are better predicted than the pressure distribution. More specifically all of the models under-predict the pressures on the roof.

3.3.2 The Menter SST k-ω turbulence model

The Menter k-ω turbulence model combines the k-ϵ model in the fully developed turbulent region and the Wilcox k-ω model in the near-wall region. The latter introduces

another variable in addition to k: the turbulent frequency $w = \frac{\epsilon}{k}$. The two transport equations for k and w for the SST k-ω model are written as follows, it combines both, the k-ϵ and k-ω models:

$$\frac{\partial k}{\partial t} + \frac{\partial k u_i}{\partial x_i} = \frac{\partial}{\partial x_j}(\nu + \frac{\nu_t}{\sigma_k})\frac{\partial k}{\partial x_j} + P_k - \beta^* k\omega \tag{3.3.9}$$

$$\frac{\partial \omega}{\partial t} + \frac{\partial \omega u_i}{\partial x_i} = \frac{\partial}{\partial x_j}(\nu + \frac{\nu_t}{\sigma_\omega})\frac{\partial k}{\partial x_j} + P_\omega - \beta_2 \omega^2 + C_{k\omega} \tag{3.3.10}$$

where the first terms on the right hand side of equations (3.3.9) and (3.3.10) represent the effective diffusivity of k and ω, respectively (σ_k and σ_ω are the turbulent Prandtl numbers for k and ω, details on their definitions in this case can be found in ANSYS (2009, 4-32,4-33)). The eddy viscosity, $\mu_t = \nu_t \rho$, is defined here as:

$$\mu_t = \frac{\rho k}{\omega} \frac{1}{\max[1/\alpha^*, (SF_2)/(a_1\omega)]}$$

where $S = ||S_{ij}||$, and α^* is a coefficient damping the turbulent viscosity (low Reynolds number correction) and is defined as

$$\alpha^* = \alpha^*_\infty \left(\frac{\alpha^*_0 + R_{e_t}/R_k}{1 + R_{e_t}/R_k} \right)$$

for which:

$$R_{e_t} = \frac{\rho k}{\mu \omega},\ R_k = 6 \text{ and } \alpha^*_0 = \frac{0.072}{3}$$

a_1 is a constant equal to 0.31 and F_2 is a function of k, μ, ω, and the distance to the wall [1].

The second terms on the right-hand side of equations (3.3.9) and (3.3.10) represent the production of k and ω, respectively. P_k, the production of turbulence kinetic energy can be defined as:

$$P_k = \min(P_{k_1}, 10\beta^* k\omega)$$

[1] Full definition of F_1 and F_2 can be found in ANSYS (2009, 4-33)

where:

$$P_{k_1} = -\overline{u_i' u_j'} \frac{\partial u_j}{\partial x_i}$$

and

$$\beta^* = \beta_i^* [1 + 1.5F(M_t)],\ \beta_i^* = 0.09^* (\frac{4/15 + (R_{e_t}/R_\beta)^4}{1 + (R_{e_t}/R_\beta}),\ R_\beta = 8$$

The production of ω is defined by

$$P_\omega = \frac{\alpha}{\mu_t} P_k$$

The third terms on the right hand side of each equation represent the dissipation of k and ω, respectively. For the dissipation of ω, the term β is not constant and depends on k and the distance to the first cell $y+$. The last term of the transport equation for ω, (3.3.10) is the cross diffusion term and represents how the two models are blended:

$$C_{k\omega} = 2(1 - F_1)\rho\sigma_{\omega,2} \frac{1}{\omega} \frac{\partial k}{\partial x_j} \frac{\partial \omega}{\partial x_j}$$

where F_1 is a function of k, μ is the distance to the wall and ω [1], and $\sigma_{\omega,2} = 1.168$.

The constants of the SST k-ω models, as implemented in ANSYS-Fluent are as follow: $\sigma_k = 1.176,\ \sigma_\omega = 2.0$.

This model has produced good approximation of the flow in several studies (Franke et al., 2004) at relatively low computer cost. However, it is not able to capture complex features of the wind turbulence as it remains a two-equation model which incorrectly portrays turbulence as isotropic.

Even if the revised k-ϵ turbulence models and the Menter k-ω model are able to overcome some of the drawbacks encountered by the standard k-ϵ model, this is due to ad-hoc modifications, which may solve one aspect of the flow but do not improve the general prediction of the flow around a building. This is partly due to the inherent principle of the two-equation turbulence models, which portrays turbulence as an isotropic phenomenon. It is also due to the fact that these models assume linearity between the

mean strains and the turbulence stresses. Another drawback of these models is the time averaging inherently present in the Reynolds decomposition of the velocity. As a result, another type of turbulence modelling, still based on the RANS formulation, is reviewed: the Reynolds Stress equation Model (RSM).

3.3.3 The Reynolds Stress Models (RSM)

While the standard k-ϵ model adds two extra transport equations for k and ϵ, the RSM adds seven extra transport equations: one for each of the six Reynolds stresses and one for the dissipation rate ϵ. Since RSM includes the anisotropic nature of the wind turbulence, the prediction of the wind flow around the bluff-body is generally improved compared to the k-ϵ models. The main physical process that needs to be modelled in the RSM formulation is the pressure-strain interaction term ϕ_{ij}, which is the main new physical process that appears in the turbulent kinetic energy equation (3.3.3). This term tends to reduce the anisotropy of the Reynolds stresses, i.e. to equalize the normal stresses. This causes damping of normal stresses due to the wall to be reduced in the near wall region.

In the same way as modified versions of the standard k-ϵ model have been developed, several authors have proposed improved versions of RSMs, with the focus being on the pressure-strain correlation term. The most notable of these revised RSMs are the SSG model presented by Speziale-Sarkar-Gatski (Speziale et al., 1991) and the FLT model formulated by Fu-Launder-Tselepidakis (Fu et al., 1987).

However, none of these RSMs are able to predict the reattachment on the roof. Furthermore, they all over-predict the reattachment length behind the building (Murakami, 1997). Other characteristics of the wind flow such as near wall stresses are not accurately reproduced by these RSMs. Considering the extra computer cost involved with the RSM and its modified versions, Reynolds Stress Models are not considered promising in CWE. (Murakami, 1997; Stathopoulos, 1997; Franke et al., 2004, 2007)

3.3.4 Boundary conditions for RANS-based models

In addition to the distance of the boundaries from the building, the effects of the environment are represented through the definition of the boundary conditions.

Inlet

At the inlet, a log-law or a power law velocity profile is specified. If using a RANS turbulence approach, the turbulent kinetic energy and the dissipation rate also need to be defined. Richards and Hoxey (1993) recommend the use of a log-law profile for the velocity at the inlet:

$$U = \frac{u_*}{\kappa} ln(\frac{z + z_0}{z_0})$$

, where

$$u_* = \frac{\kappa U_{ref}}{ln(\frac{z_{ref}+z_0}{z_0})}$$

and define the turbulent kinetic energy k and the dissipation rate ϵ as follows:

$$k = \frac{u_*^2}{\sqrt{C_\mu}} \tag{3.3.11}$$

$$\epsilon = \frac{u_*^3}{\kappa(z + z_0)} \tag{3.3.12}$$

where z_0 is the roughness length, u_* is the friction velocity defined in equation 2.1.13, κ is the Von Karman constant, and C_μ is a constant defined after equation 3.3.3.

Recent developments: The standard k-ϵ model has been the object of recent efforts to improve its use by redefining the inlet boundary conditions. Previously, a constant turbulent kinetic energy was specified at the inlet (Equation 3.3.11), as recommended by Richards and Hoxey (1993), but Yang et al. (2007, 2009) suggested varying k with height in order to more closely approximate wind tunnel and full scale measurements of the ABL. Their new formulation for k made the constant profile defined by Richards and Hoxey a special case of their new inflow boundary conditions. Later,

Gorle et al. (2009) further investigated this turbulent kinetic energy profile varying with height at the inlet by redefining the profile of the dissipation rate ϵ, as well as the constants of the turbulence model, C_μ and σ_ϵ according to the modification to k.

Top

Richards and Hoxey (1993) recommend applying a constant shear stress, $\tau = \rho u_*^2$ at the top boundary in the stream-wise direction to help to maintain the turbulent kinetic energy and the velocity profiles. This can be done by creating a cell thick layer at the top, defined as source of momentum. Above this layer, a symmetry condition is applied. Although the application of this shear stress at the top has often been neglected by CFD users using the k-ϵ turbulence model in CWE, Hargreaves and Wright (2007) have recently emphasised its importance. The authors have shown that the decay of the turbulent kinetic energy and the velocity can be reduced by applying a constant shear stress at the top boundary. They run a case with an empty domain (the geometry of the domain is displayed in figure 3.8, which also shows how the velocity profile is maintained along the fetch by the application of the shear stress at the top.

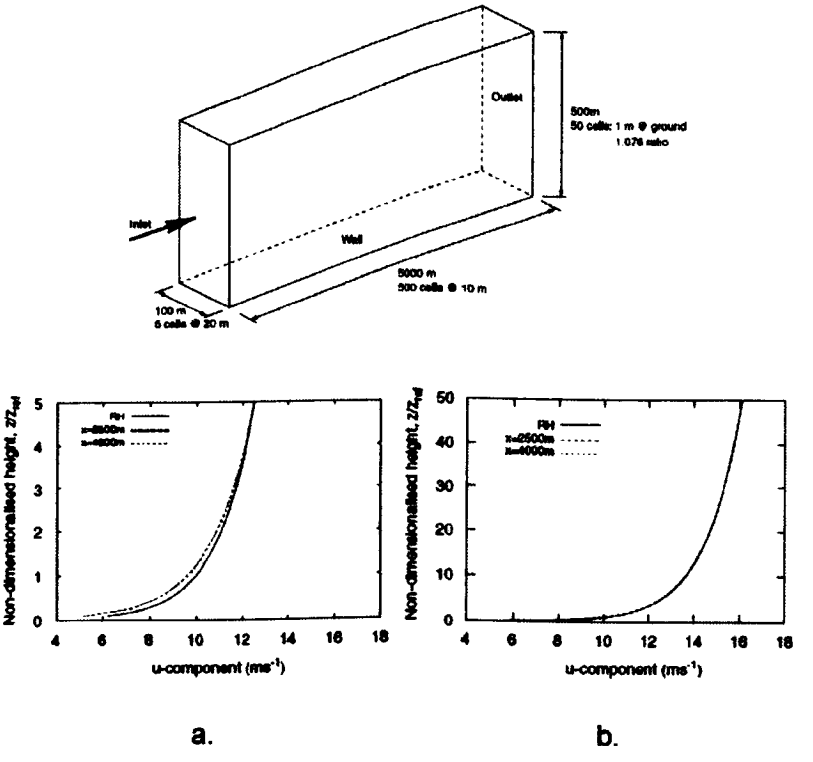

Figure 3.8: Geometry of the domain tested by Hargreaves and Wright (2007) a. Decay of the velocity profile with a simple symmetry condition at the top b. Decay of the velocity profile with a shear stress applied at the top, (RH stands for the work conducted by Richards and Hoxey (1993).

Lateral and outlet

A symmetry condition should be prescribed at the lateral boundaries in order to maintain the flow parallel to the sides. A symmetry condition effectively means that the normal velocities are set to zero and the values of all other properties just outside the solution domain are set to their values at the nearest node inside the domain (Versteeg and Malalasekera, 2007). The derivatives of all variables of the flow should vanish at the outlet, as specified by Richards and Hoxey (1993). A zero-pressure condition is then applied at the outlet.

3.3.5 URANS

A key reason why RANS models are less suited to predicting wind loads than other engineering problems is that the wind field is essentially unsteady. The incident wind is part of a naturally turbulent ABL as shown in section 2.1.5; flow around a building structure is dominated by local flow separation, reattachment and strong vortex structures; the wake region is often dominated by vortices shed from the building as seen in section 2.2. Consequently, even well defined flow regimes with symmetrical inlet conditions and a symmetrical structure can generate unsteady loading patterns such as wake switching (Prevezer et al., 2002). In these a steady RANS solution will not represent the true loading situation.

For this reason, RANS is sometimes used in an unsteady simulations, called URANS. URANS essentially introduces a temporal filter defined by the time step in the analysis such that the longer period flow features are captured by the simulation. Although this is often rightly criticised for lacking mathematical rigour (the RANS approach does intrinsically time average the variables), it has been used to produce significantly better estimates of wind pressure distributions that RANS models (Hanjalić and Kenjereš, 2008).

3.4 Large Eddy Simulation (LES)

3.4.1 Governing equations

LES is based on the idea that larger eddies are dependent on the geometry of the disturbance and smaller eddies have a more universal and isotropic behaviour. In chapter 2, the energy cascade (how the energy is dissipated from the large scales to the smaller scales), was presented. Since the larger scales interact with the main stream to extract energy, they depend on the flow field, and therefore, on the geometry and the boundary conditions.

In LES, the larger eddies, dependent on the geometry and the main flow, are resolved

directly in a time-dependent simulation, while the smaller eddies are modelled. A spatial filtering operation is used to distinguish the larger and the smaller eddies. This makes LES a **space averaging** method as opposed to the time-averaging turbulence models previously presented (RANS). The first step in LES consists of the filtering operation which filters out the eddies smaller than the cut-off width and only retains the larger eddies. The filtering of a variable ϕ can be expressed as follows:

$$\overline{\phi}(x,t) = \int_{Domain} \phi(x',t)G(x,x',\Delta)dx' \tag{3.4.1}$$

where $\overline{\phi}(x)$ is the filtered variable, the over-bar indicating spatial filtering, $\phi(x)$ is the unfiltered variable, G is the filtering function, and Δ is the cut-off width.

In commerical softwares, the cut-off width, Δ, is chosen to be of the same order as the grid size. Choosing a smaller cut-off width would be meaningless because any details concerning eddies smaller than the grid size are lost as only a single value of each flow variable is stored per grid cell (Versteeg and Malalasekera, 2007). The cut-off width is often taken to be $(\Delta x \Delta y \Delta z)^{1/3}$, where $\Delta x, \Delta y, \Delta z$ are the grid sizes for the X, Y and Z axes respectively.

After being filtered, the momentum equations are written as follows:

$$\frac{\partial \rho \overline{u}_i}{\partial t} + \frac{\partial \rho \overline{u}_i \overline{u}_j}{\partial x_j} = -\frac{\partial \overline{p}}{\partial x_i} - \frac{\partial \tau_{ij}}{\partial x_j} + \mu \,\mathrm{div}\,(\mathrm{grad}\,(\overline{u_i})) \tag{3.4.2}$$

where the interaction between the resolved scales (larger eddies) and the unresolved scales, also called Subgrid Scale eddies (SGS eddies), is contained within the subgrid-scale stress τ_{ij}, which can be written as follows, the prime indicating the unresolved scales:

$$\begin{aligned} \tau_{ij} &= \overline{\rho u_i u_j} - \rho \overline{u}_i \overline{u}_j \\ &= (\overline{\rho \overline{u}_i \overline{u}_j} - \rho \overline{u}_i \overline{u}_j) + (\overline{\rho \overline{u}_i u'_j} + \overline{\rho u'_i \overline{u}_j}) + (\overline{\rho u'_i u'_j}) \\ &= L_{ij} + C_{ij} + R_{ij} \end{aligned} \tag{3.4.3}$$

where

- L_{ij} are called the *Leonard stresses* and contain information on the resolved scales exclusively.
- C_{ij} are called the *Cross-stresses* and express the interaction between the resolved and unresolved scales.
- R_{ij} are also called the *LES Reynolds stresses* and are caused by convective moment transfer between the SGS eddies. They are similar to the Reynolds stresses in the RANS formulation and only involve unresolved eddies. As a result, they need to be modelled. The different implementations of LES differ in the modelling of these SGSs; a review of the most important approaches in CWE follows.

3.4.2 The key SGS models

The standard Smagorinsky-Lilly model, proposed by Smagorinsky (1963), was historically the first SGS model. The underlying idea of this SGS model is that the local SGS stresses R_{ij} are proportional to the local rate of strain of the resolved flow $\overline{S}_{ij}$, which is expressed as follows (Versteeg and Malalasekera, 2007):

$$R_{ij} = -\mu_{SGS}\left(\frac{\partial \overline{u}_i}{\partial x_j} + \frac{\partial \overline{u}_j}{\partial x_i}\right) + \frac{1}{3}R_{ii}\delta_{ij} \tag{3.4.4}$$

where the SGS eddy viscosity is defined as:

$$\mu_{SGS} = \rho L_s^2 |\overline{S}| \tag{3.4.5}$$

with $L_s = min(\kappa d, C_{SGS}\Delta)$, where κ is the von Karman constant, d is the distance to the closest wall, and C_{SGS} is a constant ($|\overline{S}| = \sqrt{2\overline{S}_{ij}\overline{S}_{ij}}$).

C_{SGS} is a constant in the standard Smagorinsky SGS model and has been optimized to values between 0.1 to 0.25 according to Murakami (1997). Swaddiwudhipong and Khan (2002) used the standard Smagorinsky SGS model for a 2D-simulation of the flow around

a building surface, using $C_{SGS} = 0.1$. They obtained a promising prediction of the flow, including accurate prediction of the vortex shedding. Nevertheless, a lot of the key features of the flow such as roof and side wall separation, and pressure distribution on the building were lost because it was a 2D simulation.

In fact, because wind flow around a bluff-body involves very different regions of homogeneous conditions, choosing a universal value for the constant is problematic. This implies the re-estimatation of the constant C_{SGS} for each considered flow field, which is not satisfactory. Furthermore, the standard SGS model has been proved to be overly dissipative. This may be due to the fact that the model only accounts for the energy cascade from large scales to smaller ones, and does not allow energy transfer from small to larger scales, also called *back scatter*. That is why other SGS models have been proposed, including a model where C_{SGS} is a function of time and space. One of the most prominent of these new models is the dynamic SGS model developed by Germano et al. (1991).

The dynamic Smagorinsky-Lilly model for the subgrid scale stress allows the constant C_{SGS} to be dynamically modified based on the characteristics of the resolved eddies. The dynamic procedure developed by Germano et al uses double filtering (Murakami, 1997):

$$C_{SGS} = -\frac{1}{2}\frac{L_{ij}M_{ij}}{M_{kl}^2} \tag{3.4.6}$$

where L_{ij} are the Leonard stresses, previously defined in equation 3.4.3, and

$$M_{ij} = \overline{\overline{\Delta^2}|\overline{S}|\overline{S}_{ij}} - \overline{\overline{\Delta^2}|\overline{S}|\overline{S}_{ij}} \tag{3.4.7}$$

Porte-Agel et al. (2000) suggested a further optimization of the dynamic Smagorinsky-Lilly model: The scale invariant assumption is relaxed in the near wall region. Near the wall, the length scales become comparable to the distance to the wall. This new SGS model was proven to perform better than the standard and the dynamic Smagorinsky-Lilly models.

Near wall modelling: In the LES formulation, it is assumed that the flow is going to be resolved close to the wall; for this reason the first node must be placed very close to the wall boundary, typically $y+ < 5$. However, it is possible to use wall functions if the application does not allow a very fine mesh next to the wall. Breuer et al. (2007) investigated wall models for LES in flow in plane channels; the underlying idea of the wall models being the concept of artificial viscosity. This requires the definitions of the distribution of the eddy viscosity in the outer layer and the thickness of the viscous sublayer. Other works, including those of Tessicini et al. (2006, 2007) have investigated the efficiency of near wall models for LES. These are effectively zonal hybrid RANS-LES models, and will be presented later.

Turbulent Inflow for LES: When using a k-ϵ turbulence model, the variables input at the inlet are either k and ϵ or other variables directly related to k and ϵ. Such simplified and time-averaged inlet conditions cannot be used for LES. It is very important to properly define a real turbulent wind inflow, namely a field of fluctuating velocities reflecting the characteristics of the turbulent flow within the real ABL when running LES. From the late nineties, when LES was first investigated in CWE, research groups pointed out the need for techniques to generate turbulent inflows (Murakami, 1997, 1998). Since then, several methods for producing velocity fluctuations at the inlet of the domain have arisen. A detailed review of the available methods have recently been published by Tabor and Baba-Ahmadi (2010). Four of them are presented here.

The simplest one but certainly the most costly is the method using a precursor simulation. The velocity field is stored at an appropriate downstream station of the precursor simulation in an empty domain with roughness elements on the ground. This field is then used as an inflow for the main simulation (Xie and Castro, 2008). This method has been developed in 1993 by Mochida et al. (1993) and later by Thomas and Williams (1999). The precursor simulation is as expensive as the main simulation. This makes the whole process very demanding in terms of computer storage capacity, memory and real time. However, the advantages of the method may justify such a cost. According

to Thomas and Williams (1999) it is the only method able to reproduce the coherent turbulent structures; it can also produce a wind spectrum that compared well with the von Karman spectrum. However, the huge cost involved by the precursor method means that it is not a viable option for practical industrial applications.

The second method of interest for the present work involves inverse Fourier transforms. Inverse Fourier transforms are applied to prescribed spectra to produce artificial turbulent inflows that respect given spatial and time correlations. This method was notably described and assessed by Lee et al. (1992). However, Klein et al. (2003) later noticed some disadvantages of the technique developed by Lee et al: it is both difficult to program, and the use of Fourier transforms restricts the application to Cartesian and equidistant meshes. Furthermore, it requires a 3D energy spectrum that is not easily obtainable experimentally. The major disadvantage appears to be the randomness in wave number space, that is, a realistic turbulence is only recovered after a long distance (Klein et al., 2003; Xie and Castro, 2008). For these reasons, Klein et al. (2003) developed another technique achieving the same goal and based on the method presented by Lee et al. (1992).

Klein et al proposed a technique that consists of filtering a set a random data using a Gaussian filter. The filter is applied to three sets of 3D random data ($2N_x \times N_y \times N_z$ with N_x, N_y and N_z are the time length scale and the two spatial length scales) to obtain a 2D turbulent inflow. Spatial and time correlation are ensured by a filter based on a Gaussian autocorrelation function.

Later, Xie and Castro (2008) modified the method in order to make it more economical and this is the fourth method. Instead of using three sets of 3D random data, their method only needs three sets of 2D random data ($N_y \times N_z$) and the time correlation is guaranteed by a second filter. The second major change is the form of the filter: Xie and Castro (2008) used a decaying exponential for defining the autocorrelation function. This technique has been implemented in the present work with one or two modifications, as described at length in Chapter 6.

Application of LES to CWE: Murakami (1997, 1998) reviewed a comprehensive comparison of the static and the dynamic Smagorinsky models, along with other dynamic SGS models. With regards to the computation, the author pointed out that one of the main advantages of the static SGS model is its stability. Although the dynamic SGS model does provide better numerical results, it is subject to stability problems due to the large fluctuations of C_{SGS}. As for the performance of the models: Where the static SGS model did not predict any back scatter, the dynamic model significantly over predicts it.

More generally, Murakami (1998) showed that the performance of the LES approach is excellent compared with turbulence models:

- Unlike the k-ϵ model and the Reynolds Stress Models, LES is able to predict the impinging area and the separated area of the wind flow around a bluff-body with excellent accuracy, even when the wind is not perpendicular to the structure.
- Unsteady phenomena, such as vortex shedding and other fluctuations are very well reproduced by LES.

A recent study, conducted by Huang et al. (2007), compares the k-ϵ model and LES in the modelling of the flow around a tall steel building. Since they compared their numerical results to outcomes of wind-tunnel studies, they modelled a 1:250 scale model: The domain featured a 73.55 cm high building. They used the *dynamic kinetic energy SGS model*, which is one of the dynamic SGS models implemented within ANSYS-Fluent. It is derived from the model developed by Kim and Menon (1997). It accounts for the transport of the subgrid-scale turbulence kinetic energy, k_{SGS}, that is defined in the following equation:

$$k_{SGS} = \frac{1}{2}(\overline{u_k^2} - \overline{u_k}^2) \tag{3.4.8}$$

A transport equation for k_{SGS} derived from the standard k equation is solved:

$$\frac{\partial \overline{k}_{SGS}}{\partial t} + \frac{\overline{u_j}\overline{k}_{SGS}}{\partial x_j} = -\tau_{ij}\frac{\overline{u}_i}{\partial x_j} - C_\epsilon \frac{k_{SGS}^{3/2}}{\Delta_f} + \frac{\partial}{\partial x_j}(\frac{\mu_t}{\sigma_k}\frac{\partial k_{SGS}}{\partial x_j}) \tag{3.4.9}$$

The subgrid-scale stresses are defined as follows:

$$\tau_{ij} - \frac{2}{3}k_{SGS}\delta_{ij} = -2C_k\sqrt{k_{SGS}}\Delta|S_{ij}| \tag{3.4.10}$$

Figure 3.9 presents the computational domain used by Huang et al. (2007) and some of their results in terms of mean velocity fields.

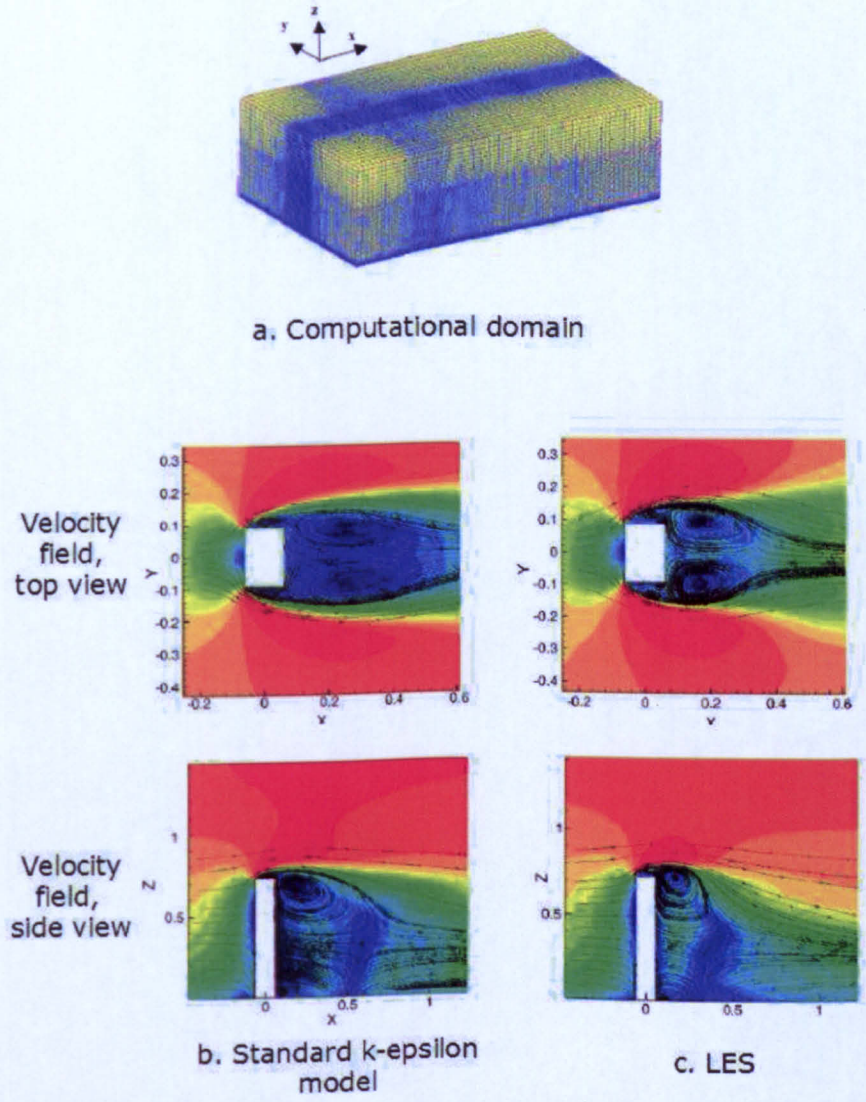

Figure 3.9: Comparison of the standard k-ϵ model and LES, wind flow around a tall building (after Huang et al. (2007)): (a) Computational domain, (b) and (c) Mean Velocity fields.

Comparing the flow field around the building, the authors showed that LES is able to reproduce irregular and complex details of the flow and the vortex around the corner of the building, which the k-ϵ turbulence model does not predict. The pressure distribution on the building predicted by LES were close to those from the wind-tunnel study.

Huang et al proved that LES can achieve prediction in good agreement with wind-tunnel results, which is very encouraging for the CFD. It is worthy of note that by modelling a scaled model, Huang et al. (2007) achieved much quicker simulations because a scaled model means a reduced Reynolds number, but also smaller turbulent length scales to model. However, they also did not make use of one the major advantage of CFD over wind-tunnel: The possibility for CFD to test full-scale buildings. As a consequence, LES must be further investigated in full-scale runs, and outcomes must be compared with data from full-scale monitoring of an existing building.

A more recent study by Lim et al. (2009) presents the results of a LES simulation of the flow around a cube. A precursor simulation was run to obtain a turbulent inflow to be used in the actual simulation. The resulting turbulent inflow was shown to possess accurate statistical properties, comparing well to ESDU data and experiments. The CFD results in terms of velocity profiles on the cube were compared with good agreement with experimental data. Pressure coefficient results are presented in Figure 3.10; they show very good agreement between experimental data and LES on the front, top and rear faces. Based on these findings, the authors predict a promising future of LES for modelling wind flow around an isolated building.

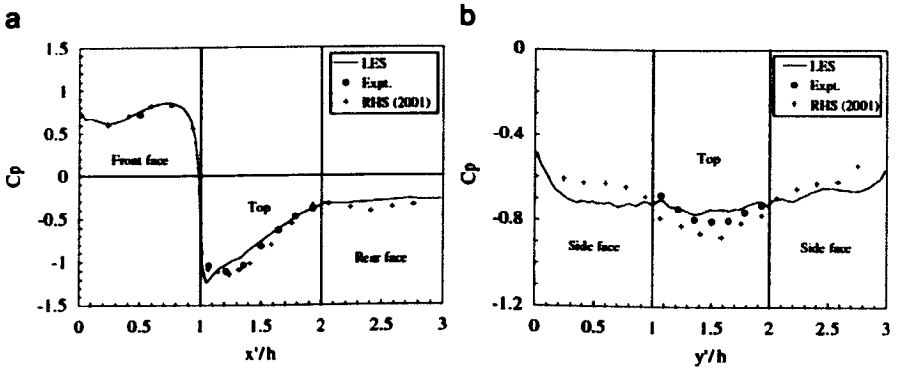

Figure 3.10: Results of pressure coefficient on a cube after Lim et al. (2009): comparison of LES, experimental data by Lim et al. and experimental data from Richards et al. (2001).

3.5 Hybrid RANS/LES models

Having presented the two ends of the spectrum of turbulence modelling, i.e. RANS and LES, this section presents the alternatives to RANS and LES that fall into the category of hybrid models. These models use URANS and LES in either a zonal or a seamless approach. In a zonal approach, the zones in which URANS and LES are used are well defined, generally the boundary layer is resolved by a URANS model, when the core region is resolved by LES.

The most famous of the seamless hybrid models is the DES model (Detached Eddy Simulation). This model effectively uses a RANS model in the near wall region in an unsteady manner (also called URANS) and the Subgrid Scale Model (SGS) in the outer LES region. The "seamless" switching between the approaches is done by changing the length scale. In the near wall region where RANS is used, the distance from the wall is used to set the length scale, while in the LES region the grid size is used (Hanjalić and Kenjereš, 2008).

A useful discussion is presented by Spalart (2001) when discussing meshing requirements

for DES. With reference to Figure 3.11 (a corruption of Spalarts original figure), Spalart defines a number of super regions: the Euler (ER), RANS and LES regions. The Euler region covers most of the domain and is never entered by turbulence and can therefore be covered by a fairly coarse, isotropic grid. Normal RANS gridding techniques are applied in the RANS region, especially in the viscous or near-wall sub-region (VR). Here the wall-normal dimension of the wall adjacent cell should be of an appropriate size for the particular law of the wall being implemented in the DES model. Wall-parallel dimensions are not such an issue. In the other RANS sub-region the outer region (OR), similar gridding techniques to the ER can be implemented, with cell sizes being too large for a switch to LES mode occurring. The switch does occur, however, in the focus region (FR) where a target grid spacing should be created which allows the LES turbulence model to be fully utilized. Cells should be isotropic in this region to maintain computational efficiency, because often the filter length scale is the cube root of the cell volume. Quite how large the FR should extend downstream is a matter for experience although the major turbulent structures of the wake should be captured in the FR. There then follows a departure region (DR) in which cells sizes smoothly transition from those in the FR to those in the ER.

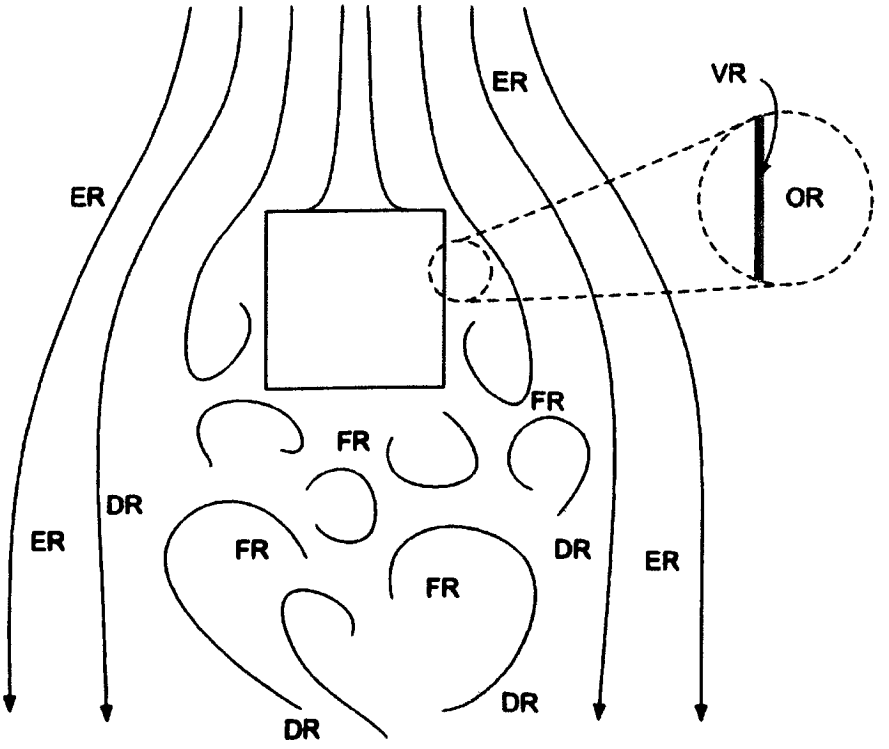

Figure 3.11: Flow regions in DES (modified version of a sketch by Spalart (2001)).

Originally, the RANS model used for DES was the one-equation model, the Spalart-Almaras model (details in Nikitin et al. (2000)), which was used in both regions. Later this was improved by using more advanced RANS based model, such as the SST k-ω (see section 3.3.2). In this formulation of the DES model, the dissipation term in Equation (3.3.9), which was equal to $\beta^* k\omega$ becomes $\beta^* k\omega F_{DES}$ where

$$F_{DES} = \max\left(L_t/(C_{DES}\,\Delta), 1\right)$$

C_{DES} is a calibration constant, equal to 0.61, Δ is the maximum local cell size, and $L_t = \frac{\sqrt{k}}{\beta^* \omega}$ the turbulent length scale of the RANS model. This expresses that the DES length scale L_{DES} is equal to the RANS length scale in the near wall region ($L_{DES} = L_t$), where $L_t < L_{DES}$. In the LES region, where the turbulent length scale is larger than the DES length scale, $L_{DES} = C_{DES}\Delta$. Effectively, the SST k-ω model is used in the boundary layer, while the LES formulation is applied in the separated regions. Hanjalić and Kenjereš (2008) noted that there is some degree of arbitrariness

in the DES model: The switching between two zones is determined by the size of the grid cells, even though the constant C_{DES} can be changed to tune the switching to the desired level. Despite this, DES is still a good alternative to LES, as it saves significant computing resources and time, while solving a lot more turbulent length scales than a simple RANS model.

Davidson and Peng (2003) have used this hybrid RANS-LES based on the k-ω turbulence model for predicting flow in a plane channel, Figure 3.12. They found that the mean flow was well predicted even with a coarse mesh. Some inconsistencies at the RANS-LES interface were also found. The major problem they noted was that the flow provided by the RANS region to the LES region did not have the proper spectral properties, or in other words LES was given poor information by RANS. This loss of information in the small scales (high frequency) was also observed by Tessicini et al. (2006). In order to solve this issue, Davidson and Peng suggested adding turbulent fluctuations to the mean quantities transferred from the RANS region to the LES region. They presented the results of such an approach in Davidson and Billson (2006). The authors actually implemented isotropic turbulent fluctuations, and then non-isotropic fluctuations. The isotropic fluctuations were found to be sufficient to greatly improve the flow prediction, as much as the non-isotropic fluctuations. However, it must be noted that the isotropic fluctuations are taken from a previous DNS simulation, which does not make this approach practical for a wide range of applications.

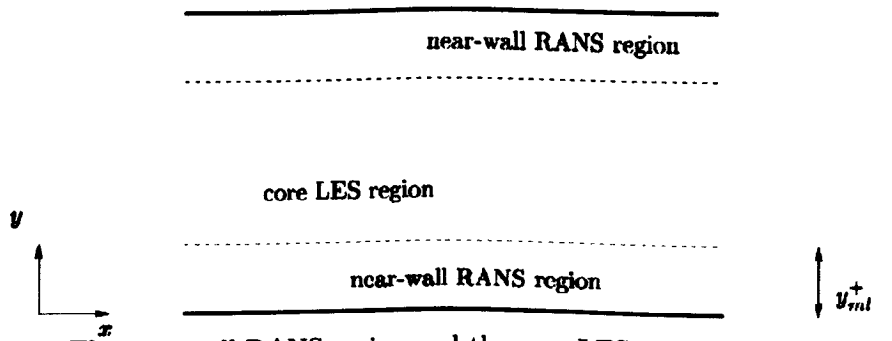

Figure 3.12: The near wall RANS region and the core LES region for modelling flow in a plane channel flow (after Davidson and Peng (2003)).

Tessicini et al. (2006, 2007) have presented results of a zonal hybrid RANS-LES model for high Reynolds numbers flow. The one equation RANS model they used for the near wall region represented a significant improvement from an analytically prescribed log-law wall function (Figure 3.13). The acceptable load on computing resources makes this method practical for industrial applications. It was also observed that the hybrid RANS-LES model applied to a relatively coarse mesh performed better than simple LES, which is consistent with the mesh refinement requirements for LES.

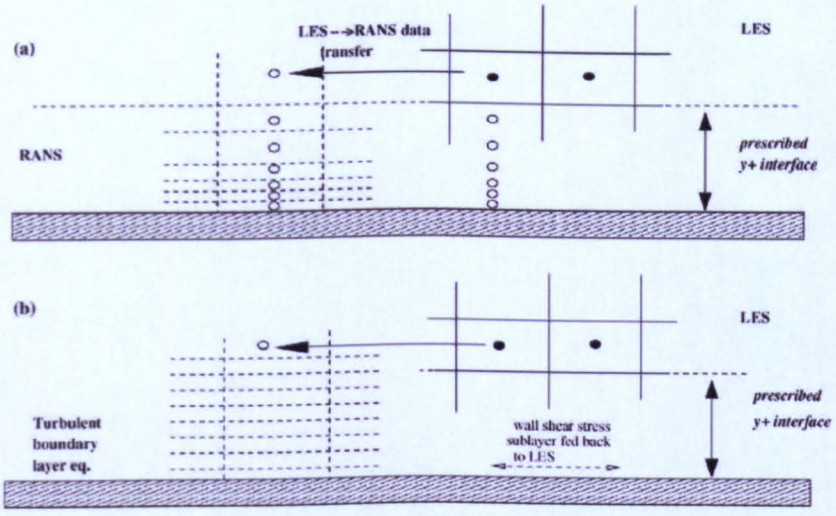

Figure 3.13: Illustration of the hybrid RANS-LES model in the near wall region (a) and the analytically defined logarithmic law of the wall (b) after Tessicini et al. (2006): hybrid RANS-LES showed better performance than the log-law at the wall.

Such hybrid models with a one-equation RANS model for the near wall region were also applied with success by Breuer et al. (2008); Temmerman et al. (2003). Temmerman et al. (2005) compared the use of one equation and two-equation RANS models for the near wall region, in association with LES. They concluded that the hybrid RANS-LES models showed potential. They noted that the models performed better when the RANS-LES interface was located further away from the wall, which indicates that the RANS model is more suited to predicting the near wall flow than LES. This can be explained by the fact that the mesh they used was probably too coarse for a pure LES simulation for which the mesh needs to be greatly refined near the wall ($y+ < 5$). For any coarser mesh, RANS can be expected to perform better than LES in the near wall region.

The same observation was made by Senocak et al. (2007): The hybrid RANS-LES model performed better in the prediction of the logarithmic profile in the near wall region than LES with dynamic Smagorinsky-Lilly SGS model. Senocak et al. suggested that this may be due to the fact that the RANS model, used in the hybrid model, takes the distance to the wall as length scale, and this can be shown analytically to give a log-law profile.

Hybrid RANS-LES models are very promising as they combine the accuracy of LES in the fully separated regions, and the robustness and flexibility of RANS based models in the boundary layers, saving significant computing power compared to LES by reducing the number of cells needed in the near wall region.

The good performance at acceptable computing cost of hybrid RANS-LES models are the reason why one of these models, the DES model, is used for the present work in some cases, and in particular for testing the fluid-structure interaction tool, as presented in Chapter 5.

3.6 Summary and conclusions

This chapter presented how CFD can be applied to wind engineering problems with a review of the models used in CWE, including the RANS turbulence models, as well as LES and the hybrid RANS/LES models. It was shown that RANS models can be used to obtained good approximations of the mean properties of the flow, despite some major limitations, notably in the prediction of recirculation regions. Hybrid RANS/LES models were shown to combine the advantages of RANS (relatively low computing resources needed) with those of LES (accuracy in the key regions, such as the wake). As a consequence, the hybrid RANS/LES DES model is used in the present work when possible.

The size of the computational domain was not discussed in this chapter as it is the object of the next chapter to investigate the current recommendations of domain sizes for modelling flow around tall buildings, and to challenge them.

Chapter 4

Size of the computational domain

4.1 Introduction

As the objective of this work is to study the flow around tall buildings, it was necessary to build numerous meshes in order to test the tools that were developed as part of this work. Religiously following the recommendations published by Franke et al. (2007) and Franke et al. (2004) generates particularly large domains. Such large domains are expensive in computational terms. Thus, it was decided to investigate smaller domain sizes and study the impact of this domain size reduction on the key flow variables. This way, it could be determined whether smaller domain sizes could be used while maintaining reasonable predictions of the flow.

4.2 Background

A key part of the modelling is the choice of the domain size and the positioning of the single tall building within that domain. Recent CFD studies have used Franke et al. (2004) as a starting point in determining the domain size. A later document (Franke et al., 2007) updates these recommendations but adds very little to the previous document in terms of the discussion about domain size. It does refer to a Verein Deutscher Ingenieure (VDI) publication which suggests that the blockage ratio should be less than 3%, based

largely on wind tunnel modelling experience.

There is considerable evidence of the recommendations published by Franke et al. (2007) and Franke et al. (2004) being adhered to by workers when modelling low–rise buildings. For example, Figure 4.1 is taken from Franke (2007) and shows the domain used by Wright and Easom (2003) to model the Silsoe cube, which is described in Hoxey et al. (2002). For such low–rise buildings, where $H \sim B \sim L$ (with B and L being the cross– and alongwind building dimensions respectively), these requirements produce domains that are both acceptable in physical and computational terms. By "acceptable in...computational terms", it is meant that the domain boundaries are not so distant from the building that the number of computational cells required to fill the domain to ensure a reasonable level of accuracy becomes too large.

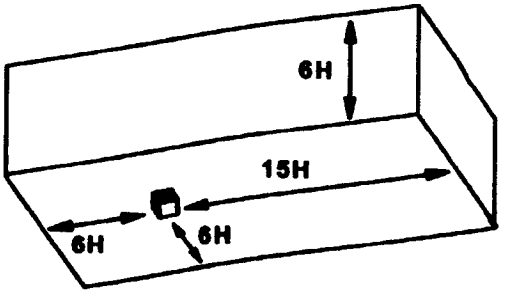

Figure 4.1: Computational domain taken from Franke (2007)

However, when the aspect ratio of the building changes and $H >> L, B$, as is the case for tall buildings, the domain size chosen by workers is open to more interpretation. There is a small, but increasing, body of work using CFD to model: 1) wind loads on; 2) pedestrian level comfort close to; and 3) rainfall around tall buildings. An analysis of this work is presented in Table 4.1, which includes the guidelines for comparison. Wherever possible, the length of the domain, l, is shown as a sum of three components: l_u, L and l_d, the upstream fetch, the building length in the alongwind direction and the downwind fetch, respectively. Similarly, the width of the domain, b, is broken into three components: b_d, B and b_g (most domains are symmetrical and so $b_d = b_g$, typically). The height of the domain, h, has only two components: H and h_s, the latter being the

Table 4.1: Domain sizes from relevant CFD modelling of tall buildings.

	Domain			Building
	l	b	h	H (m)
Sankaran and Paterson (1997)[a]	?	?	?	183
Watakabe et al. (2002)[b]	$28H$	$18H$	$25H$	31.2
Mochida et al. (2002)[c]	$10.8H$	$6.9H$	$5.6H$	0.16
Franke et al. (2004)	$5H + L + 15H$	$5H + B + 5H$	$H + 5H$	
So et al. (2005)[d]	$20H$	$10H$	$20H$	–
Huang et al. (2007)	$1.5H + L + 5.5H$	$2H + B + 2H$	$2H$	183
Tominaga et al. (2008)[e]	$? + L + 10H$	$5H + B + 5H$	$H + 5H$	–

[a] The building occupied the central $12 \times 12 \times 12$ cells of a $46 \times 42 \times 26$ grid.
[b] These are general guidelines, but the implication in the paper is that they are applicable for tall buildings.
[c] The domain size was constrained to be the same size as the wind tunnel used in the experiments of Ishihara and Hibi (1998). Here the aspect ratio, H/B was 2.
[d] A street canyon with tall buildings was modelled here, so it is only of passing relevance.
[e] H in this case is defined as the height between the fifth and sixth levels in the building, but the figures in the paper do not support this.

distance from the top of the building to the top of the domain. Due to the scarcity of reported work, cases with a single building, two buildings and arrays of buildings, one of which might be tall, are considered in the table. The overall impression from the literature is that very few tall buildings have been modelled by the academic community using CFD. Interestingly, the existing findings do not resemble the Franke et al. (2004) guidelines, with the exception of Tominaga et al. (2008). It should be noted some of the work presented in Table 4.1 predates the guidelines, but the impression remains.

This chapter sets out to determine the sensitivity of velocity fields and pressure coefficients to the size of the domain around a tall building. A similar study was carried out by Xiang and Wang (2008), but for low-rise buildings with a fixed domain height. Buccolieri and Di Sabatino (2007) looked at the influence of domain size on an array of buildings, effectively challenging the best practice guidelines of Franke et al. (2004) for the case of pollution dispersion in an array of buildings.

It is important to note that it is not the object of this work to study different mesh resolutions, turbulence models or boundary conditions, etc. Rather this work tests the effects of moving the boundaries by extending a small domain incrementally. The test

case described in Section 4.3 is for a 1:200 scale 180 m building, with a large aspect ratio. This work was motivated by the fact that the recommendations of Franke et al. (2004) produced very large domains for high rise buildings. This is largely due to H being used as the characteristic length scale upon which the dimensions of the domain are based. The resulting large domain implies a very large number of cells, which is expensive in terms of computing power and time. The underlying idea was, therefore, to generate new, practical recommendations for the size of the domain for tall buildings.

4.3 Case study

The computational work described in this paper was carried out using ANSYS Fluent, version 12.

4.3.1 Domains and meshes

The building chosen for this work is a 1:200 scale rectangular prism with full-scale dimensions of $H = 180$ m, $L = 10$ m and $B = 20$ m (0.9 m by 0.05 m by 0.1 m at scale). This prism is placed in a rectangular domain, the dimensions of which are varied. Four domains were created for the study:

Small whose dimensions respected a 3% blockage ratio (ratio of the front area of the building over the inlet area).

Medium which is an extension of the small domain, but only in the yz-plane, to create a 1.5% blockage ratio.

Medium 2 which has the same blockage ratio as the medium domain, but is extended upwind and downstream.

Large which was built according to the recommendations of Franke et al. (2007).

The dimensions of these four domains are summarized in Table 4.2 and shown schematically in Figure 4.2.

Table 4.2: Characteristics of the domains.

	Small	Medium	Medium 2	Large
Length, l	5B + L + 30B	5B + L + 30B	20B + L + 60B	45B + L + 108B
Width, b	8B + B + 8B	13B + B + 13B	13B + B + 13B	62B + B + 62B
Height, h	2H	2.5H	2.5H	5H
Ratio b/h	0.94	1.2	1.2	2.78
B.R.[a] in yz-plane	3%	1.50%	1.50%	0.15%
B.R. in y-dir.	6%	3.7%	3.7%	0.8%
B.R. in z-dir.	50%	40%	40%	20%
Cell count	1.2×10^6	1.5×10^6	2.1×10^6	5×10^6

[a] Blockage Ratio.

Since the aim of this work was to study the influence of the size of the domain on the flow field around the building and in the wake, the mesh adjacent to the building and in its wake remained the same throughout, so any differences in the wind flow will be due to a change in the size of the domain and not the mesh adjacent to the building. In fact, the small domain was extended by adding blocks around it, of increasing cell size, to create the required domain sizes. All the meshes consisted of hexahedral cells. The normal cell height next to the building was 5×10^{-4} m and the maximum cell size for the small, medium and medium 2 meshes was 0.06 m, while for the large domain, well away from the building, it was 0.18 m.

Figure 4.3(a) shows a close up of the surface mesh close to the foot of the building and highlights the growth of the cells in the boundary layer next to the building. A more distant view of the mesh is shown in Figure 4.3(b), which shows that the mesh was more refined in the wake region relative to more laterally distant regions of the domain.

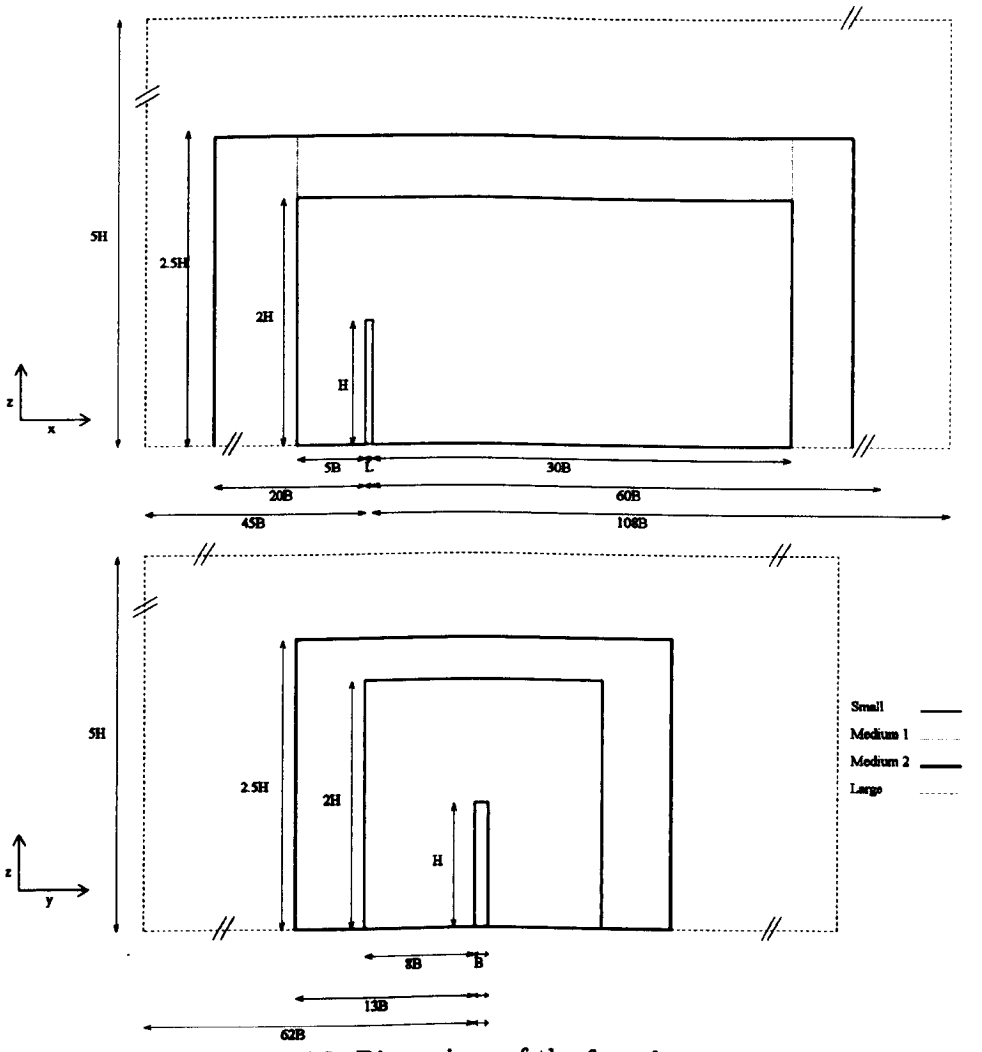

Figure 4.2: Dimensions of the four domains.

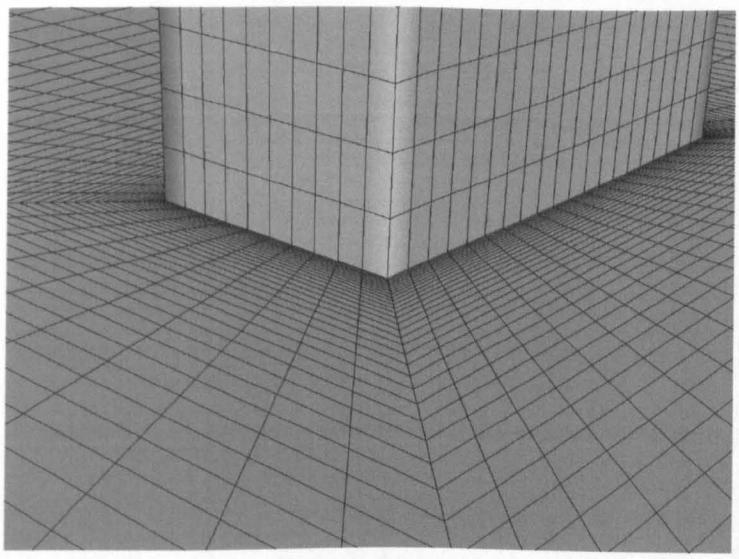

(a)

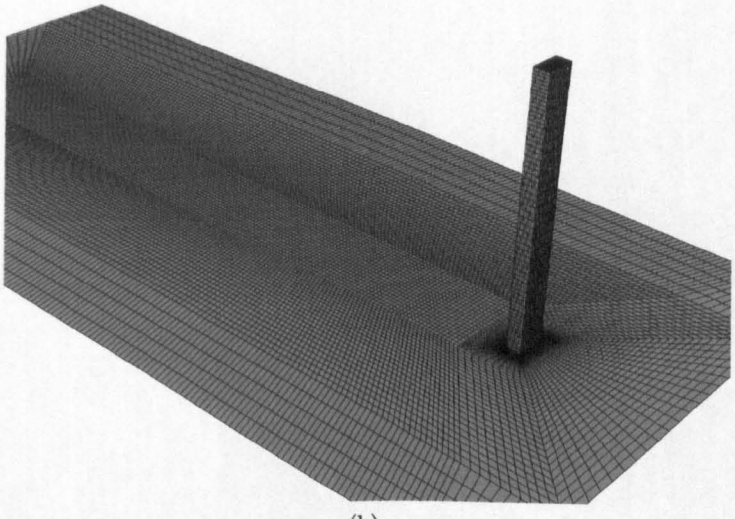

(b)

Figure 4.3: Surface meshes for the small domain showing (a) the region around the base of the building and (b) the building and wake region.

4.3.2 Turbulence model, boundary and initial Conditions

The turbulence is modelled by the RANS based model, the RNG k-ϵmodel, described in section 3.3, with standard wall functions ($y+$ values are maintained between 50 and 150 on the ground, and below 30 on the building).

At the upwind boundary, a velocity inlet was used and the following expressions for the alongwind component of velocity, U, the turbulent kinetic energy, k and its dissipation

rate, ϵ from Richards and Hoxey (1993) were used:

$$U(z) = \frac{u_\star}{\kappa} \ln\left(\frac{z + z_0}{z_0}\right), \tag{4.3.1}$$

$$k(z) = \frac{u_\star^2}{\sqrt{C_\mu}}, \tag{4.3.2}$$

$$\epsilon(z) = \frac{u_\star^3}{\kappa(z + z_0)}, \tag{4.3.3}$$

where κ is von Karman's constant and z_0 is the surface roughness length. Equation 4.3.1 is a standard representation of the velocity profile in the ABL. In the present work, $z_0 = 0.001$ m and $u_\star = 0.11$ ms^{-1}. No attempt, however, was made to modify the turbulent Schmidt number, σ_ϵ, as suggested by Richards and Hoxey (1993), because it is not clear how this could be incorporated in the RNG framework.

At the downwind boundary, a pressure outlet was used, with the relative pressure specified at 0 Pa and backflow conditions for k and ϵ set to those of the inlet. In all domains, however, backflow was not observed because the downwind boundary was sufficiently far from the building. The low– and high–y boundaries were set as symmetry conditions, as was the high-z boundary. A shear stress was not applied at the top boundary, as suggested by Richards and Hoxey (1993) because of the variable height of the domain between cases.

Equations 4.3.1 to 4.3.3 were used to specify the field variables throughout the domain as initial conditions at the start of the steady–state simulation.

4.3.3 Solver settings

As mentioned in Section 4.3.2, the solutions were steady–state. Second–order differencing was used for the momentum and turbulence equations and the convergence criteria were set to 10^{-4}. However, this was not the only test for convergence – the drag, lift and side forces as well as the moments acting on the building were monitored during the simulation and only when they achieved constant values were the simulations deemed to have converged.

4.4 Results and discussion

Figure 4.4 shows contour plots of the velocity magnitude at the mid–height of the building for the four domains. At first glance, they all present a very similar wake pattern, showing, as might be expected with a steady RANS simulation, a symmetrical wake. The free stream velocity appears to be higher for the small domain than for the three other domains. This is due to the proximity of the lateral boundaries to the building and is clearly a blockage issue. For the three other domains, the more distant lateral boundaries serve to reduce this effect.

Similarly, Figure 4.5 shows contour plots of the velocity magnitude on a vertical plane, located at the centre of the domain. As in Figure 4.4, the general pattern is very similar for the four domains. There is a low velocity region located at about $H/2$ downstream and at mid–height of the building for the four domains, which corresponds to the centre of the major recirculation behind the building. Again, for the small domain the flow does not fully recover to the freestream near the top boundary as it does for the two medium and the large domains.

The velocity profiles upstream and downstream the building, illustrated in Figure 4.6, exhibit very good agreement for the four domains. A slight decay in the velocity can be observed for the large domain, which can be attributed to the much longer fetch upstream the building. The velocity profiles downstream the building in the wake do not highlight any significant differences between the four domains. This tends to indicate that the four domains have their lateral boundaries located far enough from the building so as not to significantly influence the flow in the wake. In order to investigate this further, a "width of the wake", B_W, was computed on a horizontal plane at the mid–height of the building for the four cases. It is presented in non–dimensionalised form in Figure 4.7(a). The wake was defined to be the region in which the velocity is lower than $0.9U_{H/2}$, where $U_{H/2}$ is free stream velocity at a height $H/2$ as determined from Equation 4.3.1. Here, the small and medium domains have similarly sized wake widths, whereas the medium 2 and large domains form another group. It is not clear how the

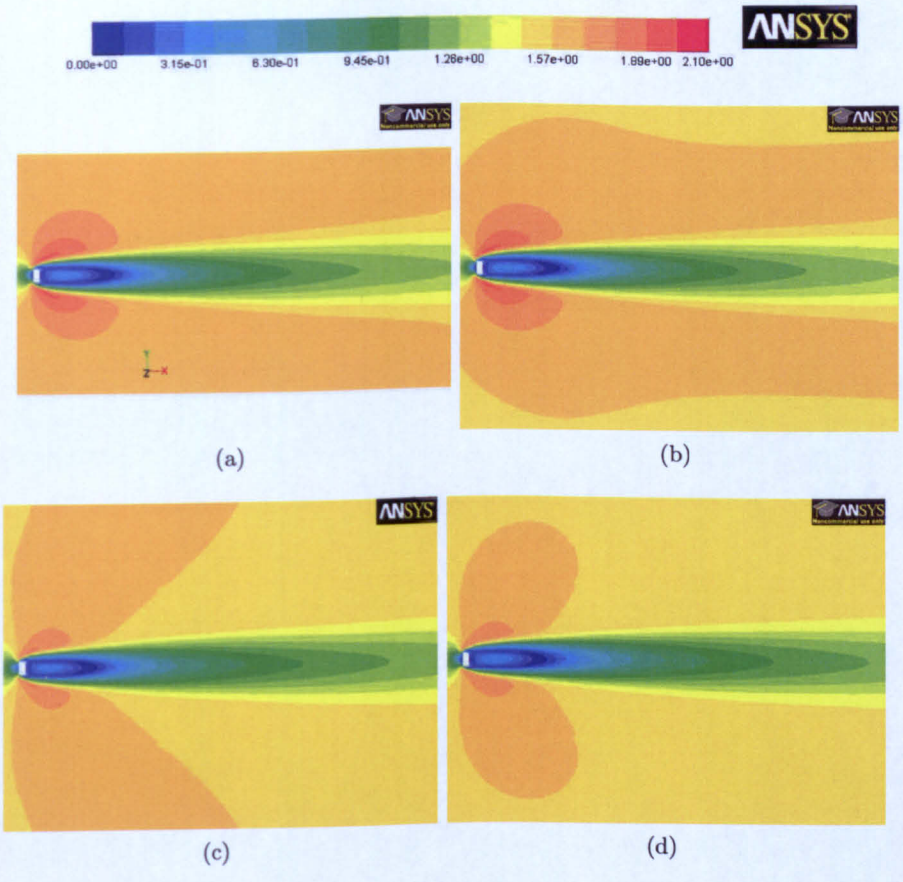

Figure 4.4: Contours of velocity magnitude on a horizontal plane at $z = H/2$ for the (a) small, (b) medium, (c) medium 2 and (d) large domains.

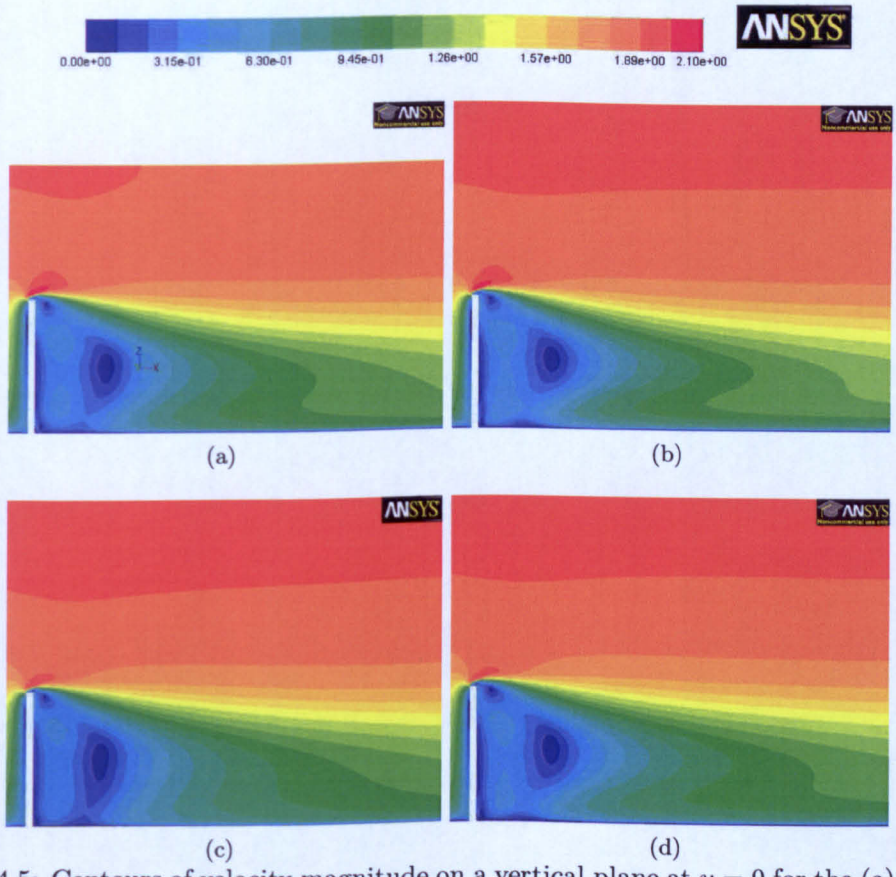

Figure 4.5: Contours of velocity magnitude on a vertical plane at $y = 0$ for the (a) small, (b) medium, (c) medium 2 and (d) large domains.

extra upwind fetch of the medium 2 domain (over the medium domain) should lead to a much wider wake, when it might be expected that the lateral boundaries would play more of a role. A more convincing argument is that the change in the velocity profile between the two medium domains is responsible for the difference.

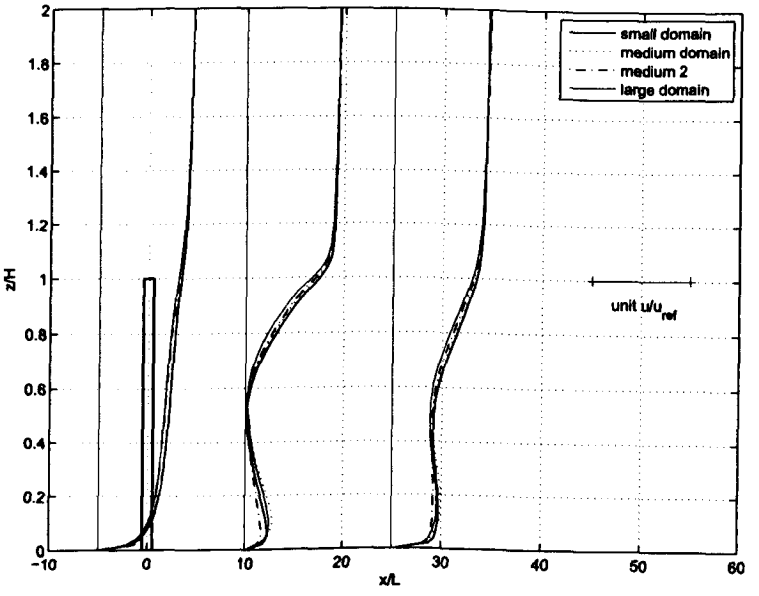

Figure 4.6: Comparison of velocity profiles on a vertical rake on $y = 0$ at $5L$ upstream, $10L$ downstream and $25L$ downstream of the building for the small, medium and large domains.

In addition, Figure 4.7(b) shows the behaviour of the so-called "wake depression", which is defined here as the $(U_{H/2} - U_{\min})/U_{H/2}$, where $U_{\min}$ is the minimum value of velocity on a horizontal line at right angles to the wind direction and $U_{H/2}$ is the wind speed at half the building height (shown as U_0 in the figure). So, a value of 1 for the wake depression equates to zero velocity magnitude, as can be seen for all domains at a distance $x \sim 10L = H/2$ downstream of the building, which corresponds well with the centre of the low velocity region seen in Figure 4.5. From this point, the velocity magnitude recovers back towards $U_{H/2}$. Far from the building, the trend that the smaller domains have a greater depression is clear. This can be explained by the higher blockage ratios in the smaller domains creating higher wind speeds around the building and a more intense wake, the strength of which is related to the free stream velocity. Evidence for this can be found in Eskridge and Hunt (1979), who look, theoretically, at

the development of a wake behind a moving vehicle.

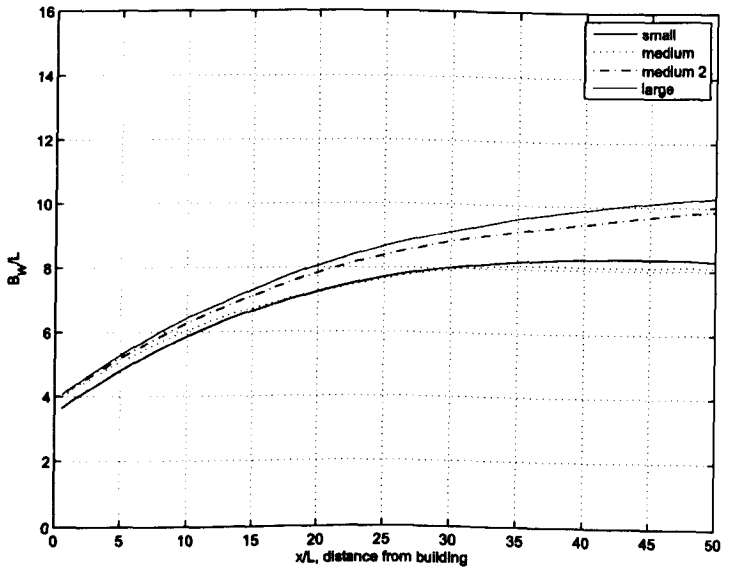

(a)

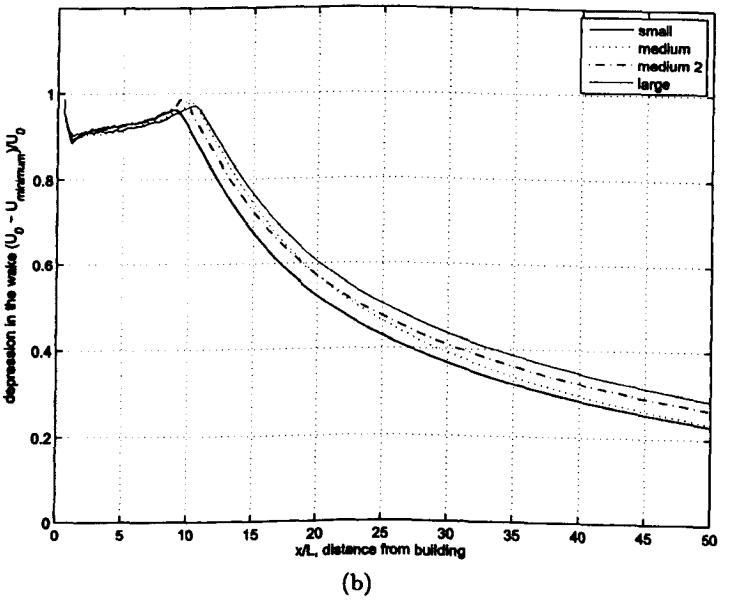

(b)

Figure 4.7: Comparison of (a) wake widths and (b) wake depressions for all domains.

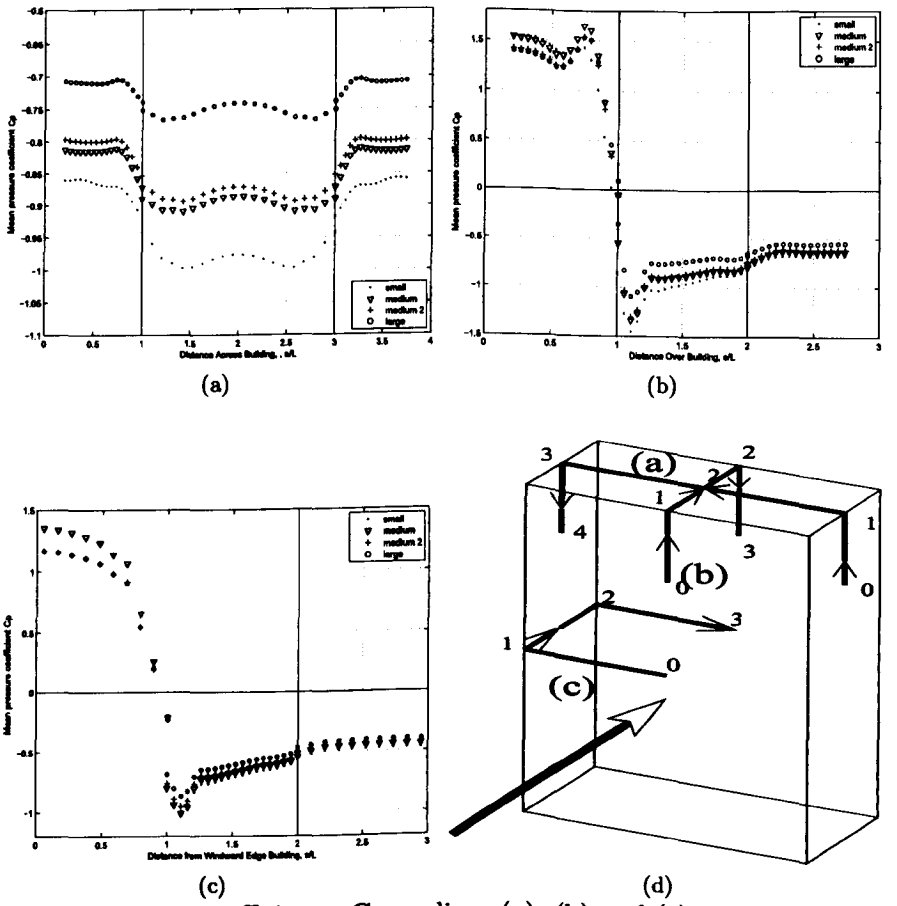

Figure 4.8: Pressure coefficients, C_p, on lines (a), (b) and (c), shown in plot (d).

Finally, and perhaps most significantly, pressure coefficients along several lines over the building are presented in Figure 4.8(a) to (c). The locations of the lines are shown in Figure 4.8(d) and on the plots, the non–dimensionalised distance along each line s/L is used, where s is the distance from the start of the line. The pressure coefficient, C_p, is defined as:

$$C_p = \frac{p - p_{\text{ref}}}{\frac{1}{2}\rho U_H^2},$$

where U_H is the wind speed at height H and p_{ref} is defined as the average pressure on the outlet, in this case 0 Pa relative. It should be noted that the pressure coefficients are deliberately not corrected by the free stream velocity in the domain, as this would be the equivalent of applying a blockage ratio correction to the results. The lines (a) and (b) shown in Figure 4.8(d) have been deliberately chosen to pass over the roof because this

is where much of the interest for low–rise buildings lies. Pressures on the roof are less of an issue when analysing the dynamic response of a tall building, which is often driven by pressure differences between the long, vertical walls of the building. Nonetheless, the pressures acting on the roof of a high–rise building are still important in terms of debris release during storms, for example.

The pressure coefficients appear to be more sensitive to the blockage ratio than the velocity is. The pressure coefficients on line (a) display higher suction on the roof for the smaller domains[1]. The difference between the two medium domains is negligible, while the difference between the small and large domains approaches 40% on the roof. As mentioned, on the roof, the two medium domains exhibit similar results, which can be explained by the fact that the domain height ($2H$ and $2.5H$) is roughly the same in each case. The large domain which has a top boundary located much higher ($5H$) shows lower suction on the roof. This would indicate that $2.5H$ is indeed too small to accurately resolve the pressure distribution on the roof, and that the $5H$ recommendation should be followed.

Figure 4.8(b) paints a less dramatic picture, but this is due to the much greater range of pressure coefficients seen on this line. At the mid-point of the roof, there is still the large discrepancy in C_p between the small and large domains. However, on the front face ($0 < s/L < 1$), the differences between the domains are, in percentage terms, less than 10%. The fact that the medium 2 and large domains agree more closely on the front face in both plots (b) and (c), indicates that the pressures here are very sensitive to any decay in the velocity profile for these slightly longer upwind fetches. However, the large domain still has an upwind fetch twice that of the medium 2 domain, but this would indicate that a shorter upwind fetch, here $20B$, than that suggested by Franke et al. (2004) is acceptable.

The pressure coefficients on the leeward face, in Figure 4.8(b) and (c) indicate that a much larger downstream distance is unlikely to greatly influence the results. Therefore,

[1]The traverse (a) in Figure 4.8 goes from one side of the building to the other and has been left like this to demonstrate the symmetry of the pressure field.

a downstream distance of $30B$ seems to be enough to let the wake develop, without any danger of the outlet boundary unduly influencing the results. The pressure coefficients on the side face at mid–height of the building, $1 < s/L < 2$, indicate that the medium 2 and large domains produce results that are within 5% of each other, except in the critical zone just downstream of the leading edge of the building.

4.5 Summary and new recommendations

The aim of this chapter was to provide some guidance as to what size of domain should be used when modelling tall buildings using CFD. It is intended as an extension of the admirable work of Franke et al. (2004) for low-rise buildings. It should be re-iterated that this was a parametric study with only one parameter; the domain size. Although the use of a steady RANS model in the context of wind engineering is flawed, that this modelling approach does give a satisfactory representation of the blockage effects supports its use here. With this in mind, from the discussion of the results in §4.4, the following conclusions can be drawn:

- Pressure coefficients and velocity fields are sensitive to domain size, which confirms observations from wind tunnel blockage ratio studies for many years.
- Assuming that the large domain provides the benchmarking data, under the premise that infinitely distant boundaries would be desirable, the small domain is simply too small to provide acceptable results: the relative errors of the small domain compared to the large domain are significantly larger than 5-10% as shown in Section 4.4 (the disagreement reaches 40% of the pressure coefficient on the roof). This suggests that the 3% blockage ratio suggested by VDI is not acceptable.
- The smaller differences between the medium 2 and large domains suggest that the following (tentative) guidelines for domain size with a tall building are appropriate:
  - Upwind fetch, l_u : $20B$ or $2H$, whichever is the greater.
  - Downwind fetch, l_d: $30B$ or $3H$, whichever is the greater.

- Top clearance, h_s: $4H$.
- Side clearances, b_d and b_g: $\geq 13B$, and such as the ratio $b/h \geq 1$

which can be compared with the corresponding recommendations of Franke et al. (2004), which are: $5H$, $15H$, $5H$ and $5H$ respectively.

Therefore, for the particular case presented here, this represents a reduction in the volume of the domain of approximately 90%. This constitutes a significant reduction in the number of cells required, even if the mesh can be coarsened away from the building/wake region.

4.6 Application of the new recommendations

Following these recommendations, a new mesh was created. The characteristics of the new mesh called the Final Recommendations (FR) domain are presented in Table 4.3. The new domain represents a saving of 88% in terms of volume, and a saving of 30% in number of cells, while still respecting a blockage ratio of less than 1% in the y-z plane. For the FR domain, the mesh was slightly refined in the outer region since a lot of the volume could be saved compared to the large domain. It shows that by applying the new recommendations, the mesh can be refined while still reducing the number of cells significantly.

Table 4.3: Characteristics of the mesh following the Final Recommendations (FR).

	Final Recommendations (FR)	COST recommendations
Length, l	20B + L + 30B	45B + L + 108B
Width, b	26B + B + 26B	62B + B + 62B
Height, h	5H	6H
Ratio b/h	1.2	2.78
B.R.[a] in yz-plane	0.75%	0.15%
B.R. in y-dir.	2%	0.8%
B.R. in z-dir.	20%	16%
Cell count	3.5×10^6	5×10^6

[a] Blockage ratio.

Figures 4.9 and 4.10 show the velocity magnitude for the FR and large domains. Similar

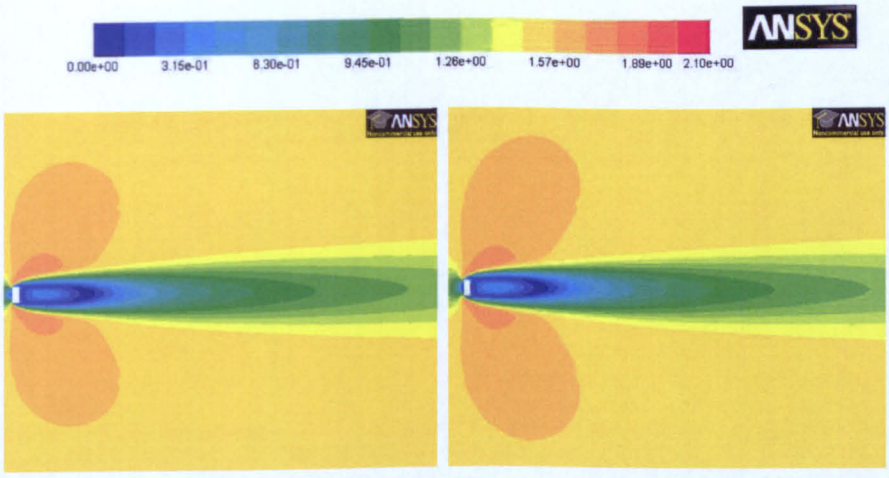

Figure 4.9: Contours of velocity magnitude on a horizontal plane at $z = H/2$ for the (a) FR ("optimum" in the legend), (b) large domains.

flow fields are obtained with both domains. It can be seen that the wake does not show dramatic differences in Figure 4.9 even though the large domain is more than twice as wide as the FR domain. Figure 4.10 shows that the flow fields in the x-z plane are again very similar for the large and FR domains. The point where the velocity reaches a minimum in the wake is located at approximatly $H/2$ downstream the building for both domains. The similarity is confirmed by the velocity profiles plotted upstream and downstream the building, presented in Figure 4.11.

Figure 4.12 (a) presents the width of the wake for all the domains (as defined previously). The FR domain has a similar wake of the width to the one exhibited by the large domain. The fact that the FR domain is wider than the medium and medium 2 domains could explain the slightly larger width of the wake, closer to the large domain. As for the velocity in the wake, shown in Figure 4.12 (b), the maximum depression occurs at the same location downstream the building for the FR and medium 2 domains, which may be explained by their similar downwind fetch.

The last results presented are the ones regarding the pressure distribution on the building, Figure 4.13. The largest differences are exhibited in (a) with a relative error of 11% but it must be noted that a smaller range of pressure is shown in this distribution

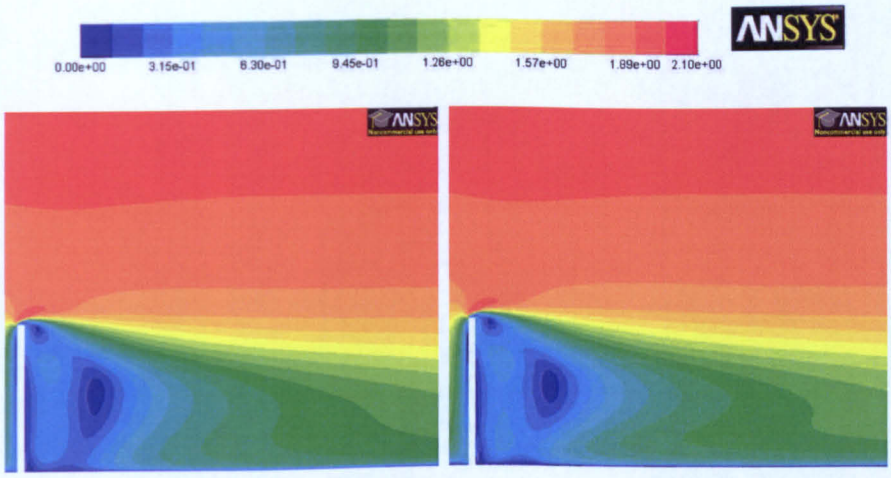

(a) (b)

Figure 4.10: Contours of velocity magnitude on a vertical plane at $y = 0$ for the (a) FR ("optimum" in the legend), (b) large domains.

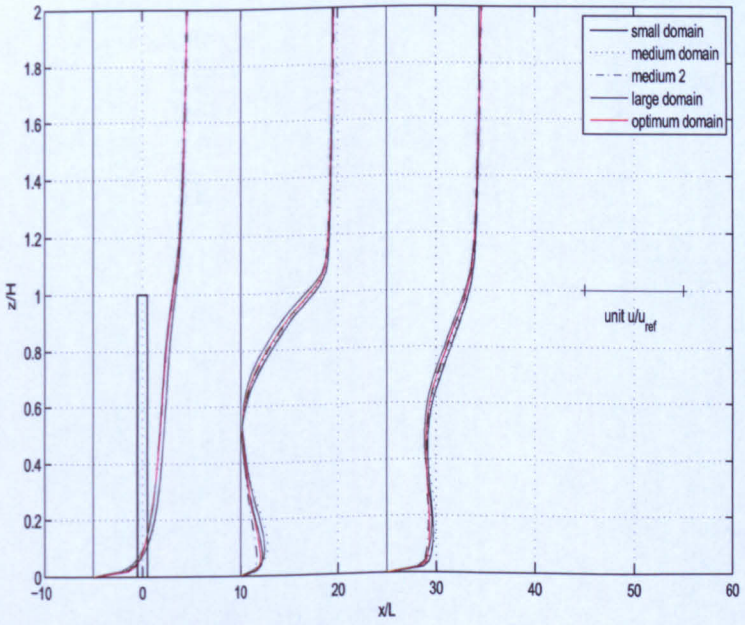

Figure 4.11: Comparison of velocity profiles on a vertical rake on $y = 0$ at $5L$ upstream, $10L$ downstream and $25L$ downstream of the building for the small, medium, large and FR ("optimum" in the legend) domains.

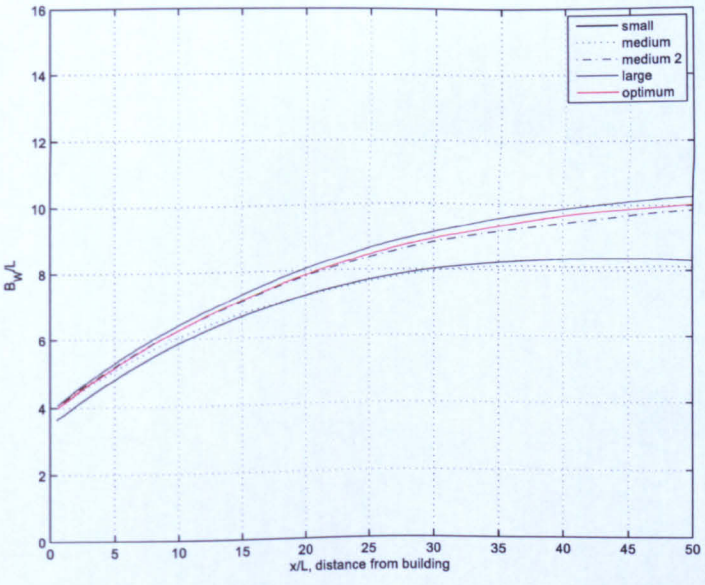

(a)

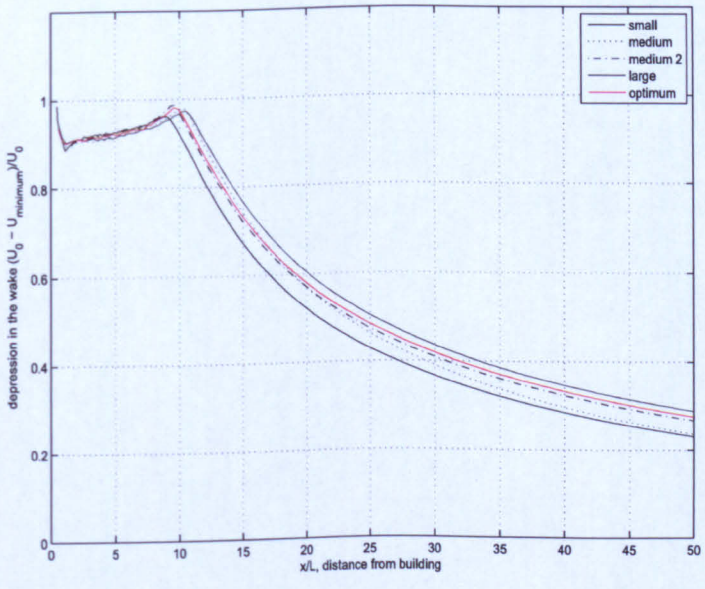

(b)

Figure 4.12: Comparison of (a) wake widths and (b) wake depressions for all domains including the FR domain ("optimum" in the legend).

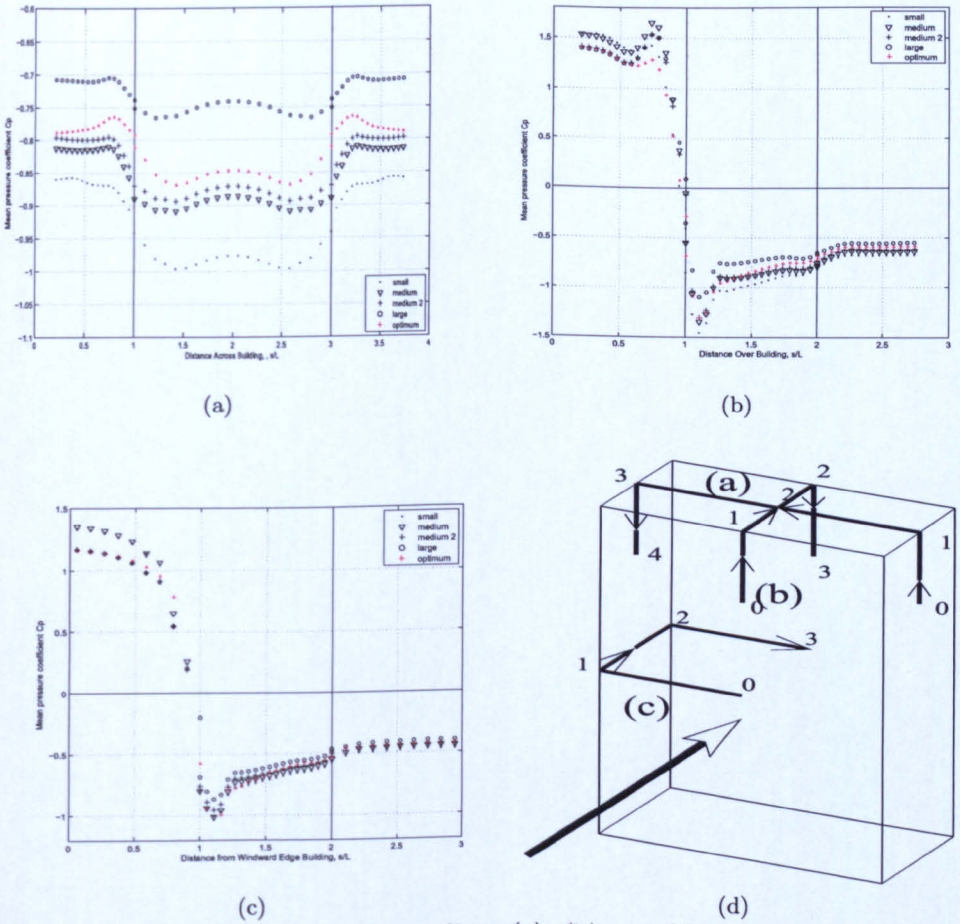

Figure 4.13: Pressure coefficients, C_p, on lines (a), (b) and (c), shown in plot (d) for all domains including the FR domain ("optimum" in the legend).

than in (b) and (c). The pressure distribution on the front face in the FR domain is similar to the large domain. On the side faces of the building, the pressure distribution in the FR domain is closer to the one in the medium 2 domain, although this is not clear in (c) where the results for the FR and the large domain appear to be very close. On the leeward face, as it was observed for the four domains in Figure 4.8, the results for the five domains are in very good agreement, which would tend to indicate that the downwind fetch for the FR is long enough.

Generally, the FR domain shows results that are very close to the one shown by the large domain, while saving a significant amount of computing resources allowing for a smaller domain to be used.

4.7 Conclusions

In this chapter, it was attempted to define new recommendations for the size of the computational domain for tall buildings. This study was motivated by the fact that the existing guidelines appear to have been defined for low to mid-rise buildings, leading to extremely large computational domains for high aspect ratio structures (height over width), such as slender and tall buildings. The study focused on the size of the domain solely, and not on other aspects such as mesh refinement, and turbulence models. The comparison of the results for domains of increasing sizes lead to the definition of new recommendations for this particular geometry that could be used for modelling the wind flow around tall buildings while maintaining an acceptable level of accuracy. These new recommendations were applied; the flow field and the pressure distribution on the building in this new domain were compared with the other domains. It was found that the new recommendations gave results that compared well with results obtained when following Franke et al. (2004). As a consequence, in the next chapters, the new recommendations are followed, sometimes with slight variations, in order to use the computing resources with better efficiency.

Chapter 5

Fluid-structure interactions

5.1 Introduction

This chapter aims to introduce a method for fluid-structure interactions (FSI), in order to address the first intermediate objective: to develop and evaluate a numerical tool in order to account for the dynamic response of the building to wind loading, and to assess the coupling of the building motion and the wind flow.

After a short review of the methods for FSI and their applications to wind engineering, the method developed for this work is described in detail. Then, the results of the application of the method to a 180 m building are presented.

5.2 Review of the method for modelling fluid-structure interactions

5.2.1 Introduction

Three elements are usually distinguished when solving fluid-structure interactions: the fluid, the structure and the mesh. The stresses and displacements of the structure are calculated from the fluid computation. The fluid mesh is then moved accordingly to the structure displacements, and the effects of such displacements are accounted for by the

fluid solver.

The governing equations are composed of the well-known Navier-Stokes equations for the fluid and the following equations for the structure:

$$\boldsymbol{M}\ddot{\boldsymbol{u}} + \boldsymbol{C}\dot{\boldsymbol{u}} + \boldsymbol{K}\boldsymbol{u} = \boldsymbol{F}_s(t) \tag{5.2.1}$$

where $\boldsymbol{u}$ is here the displacement vector of the structure, $\boldsymbol{M}$ the mass matrix per unit span, $\boldsymbol{C}$ the damping matrix, $\boldsymbol{K}$ the stiffness matrix, and $\boldsymbol{F}_s(t)$ the time-dependent force due to wind loading.

5.2.2 Fluid-mesh coupling

The third element to account for in FSI is the movement of the mesh. One sensitive part is how the motion of the fluid is handled within the moving mesh. The *Arbitrary Lagrangian Eulerian* (ALE) method is used in most cases to deal with that issue.

The idea for ALE is to combine Lagrangian and Eulerian approaches. The Lagrangian method is usually used in solid mechanics and also in fluid mechanics when one wants to follow individual particles: in such view, the grid is allowed to deform with the solid or the particle. In particular, this means that the displacement of each particle is calculated and the nodes of the mesh correspond to the particles, which limits the extend to which the particle can move. This approach becomes more difficult in fluid mechanics where the fluid is inherently not cohesive, which could lead to over distortion of the grid. In that case, the Eulerian approach is preferred. In an Eulerian approach, the grid is fixed in space, the fluid is allowed to flow through it and mean properties of the flow flowing through each cell are calculated. Conservation of mass then needs to be ensured.

In an ALE method the nodes may be moved with the continuum (fluid) in normal Lagrangian fashion, or they may remain fixed in Eulerian manner, or, and it is the point of the ALE method, the nodes may be moved in an arbitrary way to give a continuous rezoning capability (Donea et al., 2004). A comparison of the motion of the nodes in

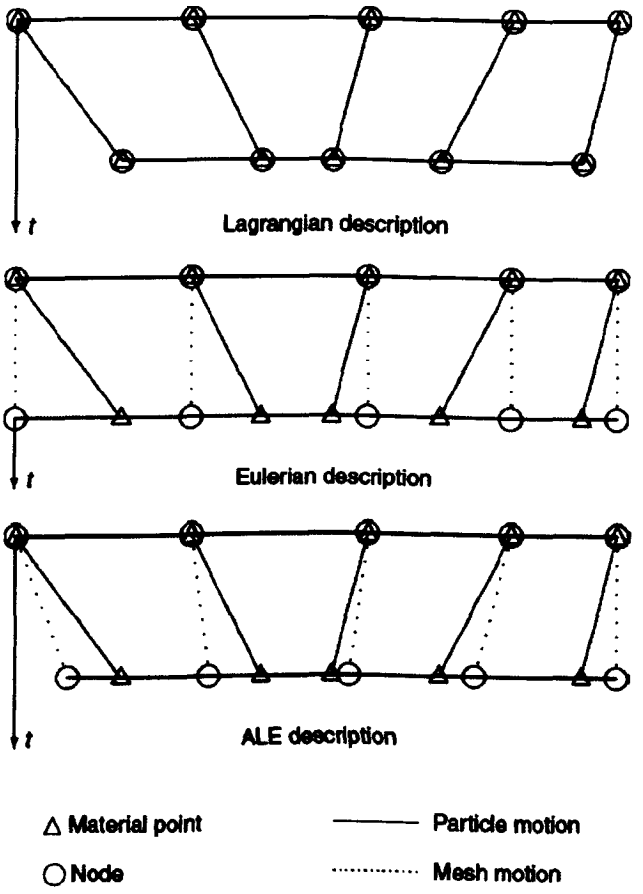

Figure 5.1: One-dimensional example of Lagrangian, Eulerian and ALE mesh and particle motion (after Donea et al. (2004)).

the Lagrangian, Eulerian and ALE method is shown in Figure 5.1: in a Lagrangian approach, the nodes of the mesh coincide with the material points, whereas the mesh nodes are fixed in the Eulerian description. In the ALE description, the mesh nodes are not fixed but do not move as much as the material points. In other words, the mesh is moved to a certain extent, and an Eulerian approach is employed to compute the flow through the faces of the elements.

The ALE method was developed in order to combine the advantages of the Lagrangian and Eulerian kinematical descriptions, while limiting their respective drawbacks (limited available motion in the Lagrangian approach and limited resolution in the Eulerian method). Details on the fundamental equations of the ALE approach can be found in Appendix A.

The ALE formulation, originally developed by Noh (1964) and Franck and Lazarus (1964), has been more recently implemented by several research groups (Longatte et al., 2005; Farhat and Lesoinne, 2000; Farhat et al., 2006; Küttler and Wall, 2006).

ALE methods are recommended for high Reynolds number simulations with the requirement of a high order of accuracy. In addition, they are limited to problems with moderate body deformation since the moving grid follows the deformable boundaries. As the wind flow around high-rise buildings is characterized by high Reynolds numbers and wind loading induces limited structural displacement, choosing the ALE formulation for modelling FSI in CWE is justifiable.

Another mesh update option is to remesh the whole computational domain at each time-step as opposed to partial remeshing used for ALE. In addition to being very demanding in terms of computer speed and memory, this method is believed to introduce discontinuities into the solution (Dale et al., 2002). Non-ALE methods, such as pure Lagrangian methods (Antoci et al., 2007) or the Immersed Boundary Method (IBM) exist but they are not used in CWE and hence are not presented here. Details on the Immersed Boundary Method can be found in Peskin (1977), and more recently Gilmanov and Acharya (2007) and Zhang and Gay (2007).

5.2.3 Fluid-structure coupling schemes

There are several manners of coupling the three elements of a FSI problem, depending on the application, and the resources available. The coupling methods can be classified in two general categories: *Sequential methods* and *Monolithic method*. A sequential approach consists in solving the flow equations and the structure equations sequentially, at staggered or non-staggered times, but always in two distinct steps. Whereas, in a monolithic or implicit approach, both the structure and the fluid are solved at the same time. This makes the monolithic approach more robust, but less flexible than sequential methods. This section reviews the two approaches, and compare them to each other.

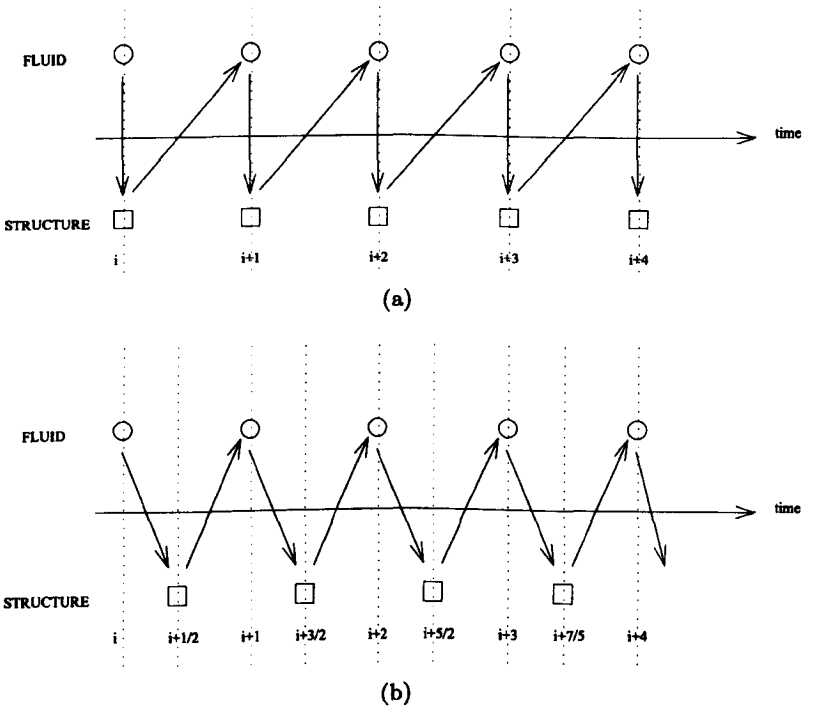

Figure 5.2: Illustration of the conventional (a) and staggered (b) sequential fluid-structure coupling.

Sequentially

The simplest way of coupling the fluid and the structure sequentially is to solve for the fluid, then to compute the forces on the structure, afterwards to solve for the structure motion and finally to move the mesh, at a certain time-step t_n. At the next time-step t_{n+1}, the fluid is solved on the mesh computed at the previous time-step. The method is illustrated in Figure 5.2 (a).

It is very popular among FSI practitioners because of its stability and acceptable performances Farhat and Lesoinne (2000); Farhat et al. (2006). Besides, because the flow field and structural displacements are not solved by the same solver, it is rather flexible in terms of the CFD code and CSD (Computational Structural Dynamics) codes that can be used.

The fact that the fluid is solved on the mesh computed at the previous time step causes the main disadvantage of such a method: structure velocity and displacement continuity cannot be simultaneously satisfied (Longatte et al., 2005), which can lead to numerical

errors. Besides, even if the solvers for the structure and the fluid are second-order time-accurate, the coupling of the whole system Fluid-Structure is only first-order time-accurate (Piperno et al., 1995). For these reasons monolithic schemes may be advised in particular cases.

A common improvement to the conventional sequential procedure is achieved by the use of sub-iterations for the fluid (Farhat and Lesoinne, 2000). This is justified by the fact that fluid and structure often require different time-step sizes: the fluid typically requires smaller time-step than the structure. Then, one can either choose the same time-step for both fluid and structure, or one can use sub-cycles for the fluid, which allow a larger time-step size to be allocated to the structure, while solving the fluid with the inevitably smaller time-step required for optimal accuracy. It allows savings in CPU time since the structure is advanced fewer times and also in communication costs between the fluid and the structure solvers [1]. (Piperno et al., 1995).

An improved method, based on the sequential method, allows the numerical errors to be reduced by staggering the fluid and structure solvers in time: the fluid computation is performed at $t_{n+\frac{1}{2}}$ and the structure is solved at t_{n+1}. This method has been developed by Farhat and Lesoinne (2000), who called it the *Improved Serial Staggered* procedure, and Longatte et al. (2005), who called the implementation of this principle *Explicit Asynchronous* as opposed to *Explicit Synchronous*, which is the equivalent of the sequential procedure.

Farhat et al. (2006) have recently developed the *Generalized Serial Staggered* (GSS) procedure, which is, in fact, the sequential procedure to which predictors are added. One structure displacement predictor is used when the the motion is transferred to the fluid. Another structure force predictor is applied when the forces exerted by the fluid on the structure are computed from the pressures. In short, the predictors allow the displacement at t_n computed from the pressures on the structure to be corrected by the displacement at two previous time-steps. This makes the GSS procedure second-order

[1] However, in the present development of a FSI tool, due to the simplicity of the structural solver, the CFD takes such a large proportion of the total compute time that savings on the structural solver time would be relatively small with staggered coupling scheme; for this reason, the coupling is non-staggered.

time-accurate, while keeping the advantage of the stability of the conventional sequential procedure over monolithic schemes (Farhat et al., 2006).

Monolithic scheme

In a monolithic method, also called *fully implicit* method, the three elements, fluid, structure and mesh, are solved as one single block. To achieve a monolithic coupling scheme, the flow equations and the structural equations may be written in a similar form to allow them to be solved by the same solver. Thus, Dale et al. (2002), who were using a finite volume based CFD code, had to rewrite the structural equations to solve both parts within a single solver. They used a monolithic approach with good results to predict stress fields and displacement in a simple square tube of one material filled with another. Longatte et al. (2005) conducted a comparison of explicit and implicit coupling schemes for a concentric moving mesh. Even if the implicit method gave more accurate results, they carried out the rest of their investigation using an explicit coupling to limit the computational cost.

The advantages of a monolithic coupling approach have been pointed out by Dale et al. (2002) and Longatte et al. (2005): it does inherently not face any numerical errors due to time-staggering. Furthermore, in a sequential coupling scheme, fluid and structure are solved by two distinct packages, special care must therefore be taken for the conservation of energy between the fluid and the structure. The fully implicit scheme does not face this issue.

However, authors have pointed out difficulties related to its use: Piperno et al. (1995) have qualified the monolithic scheme as "computationally challenging, software-wise unmanageable", Farhat and Lesoinne (2000) have restricted its use to "simple and small-scale structural problems" . Then, Farhat et al. (2006) describe the fully-implicit scheme as being only suitable for simple and academic problems because of the restriction previously quoted, and also because solving everything within a single block does not recognize the differences between the mathematical properties of the fluid and the structure.

This implies that explicit schemes are more accurate, as they use software specifically designed for the fluid or the structure as opposed to one solver for both elements. For these reasons, the conventional sequential fluid-structure coupling has been chosen for the present work.

5.2.4 Discretization

The flow equations are usually discretized using the finite volume method, while the structural equations can be discretized using the finite element method. This has been chosen by most authors although some groups have also used finite element discretization for the fluid equations, especially when using monolithic coupling methods, where the methods of discretization for the fluid and the structure have to be consistent (Piperno et al., 1995; Farhat et al., 1995; Farhat and Lesoinne, 2000; Farhat et al., 2006).

Concerns can arise from the fact that the fluid usually requires much finer grids than the structure, and more importantly, the grid for the fluid and the one for the structure do not need to be refined at the same locations. Thus, for the fluid, the grid should be very fine near the interface in the boundary layer, while the structure does not require such a fine mesh at the interface. From that observation several approaches can be adopted: either the fluid grid coincides with the structural grid, or the fluid grid is different from the structural grid and some kind of interpolation from the fluid to the structure must be defined or a node mapping scheme is needed (Dale et al., 2002).

5.2.5 Applications to CWE

As previously described, a lot of the fundamental work in FSI has been done by Farhat and his colleagues. One application of their theoretical work has been led by Slone et al. (2002, 2004). Slone et al. wrote a code (*PHYSICA*) handling fluid and structure based on finite volume discretization and the ALE formulation for unstructured meshes and applied it to model interactions between air flow and a three-dimensional fixed-free

cantilever. The characteristic Reynolds number was 2×10^5 based on the section of the structure. A good prediction of the flow field was obtained, the main flow features were reproduced. However, in the context of wind engineering, the main limitation was the absence of turbulence modelling and compressibility.

Because CWE typically deals with bluff bodies, wind-induced effects are largely three-dimensional, and appropriate turbulence modelling is needed. Numerical studies of the interaction between the wind and buildings are rather recent, following progress in computer speed and memory. A recent paper presents the numerical results of FSI for tension structures (Wu et al., 2008). This kind of structure is inherently flexible and is more likely to cause/undergo aeroelastic phenomena as a result. The authors have used finite-volume formulation for the fluid equations, and a finite-element based code for the structure. The mesh updating was handled by an ALE formulation. The main advance compared to Slone's work (2002) is the use of LES. The transient simulations were run for air flow around scale model buildings (0.3 meters high roof, rood span of 1.2 meters) with a Reynolds number of 2×10^5. Since the numerical outcomes could not be validated by experiments, no real quantitative conclusions could be draw.

Swaddiwudhipong and Khan (2002) presented a 2D study of wind flow around an aeroelastic tall structure. The turbulent inflow was generated using weighted amplitude wave superposition, but there is no evidence of a different treatment for each of the velocity components, and the authors admitted a simplified random number generation, with a single seed for all three components, likely to be the cause of the discrepancy between the expected and obtained energy spectrum.

More recently, Braun and Awruch (2009) presented results of a study of an aeroelastic tall building, comparing the LES results to experimental studies of the CAARC building. The CAARC is a standard building of simple design to be studied in wind tunnels in a given wind environment as a common problem for investigation. It was originally suggested by Wardlaw and Moss and detailed characteristics of the building can be found in Wardlaw and Moss (1971). The CAARC building is 180 m high, and its cross-

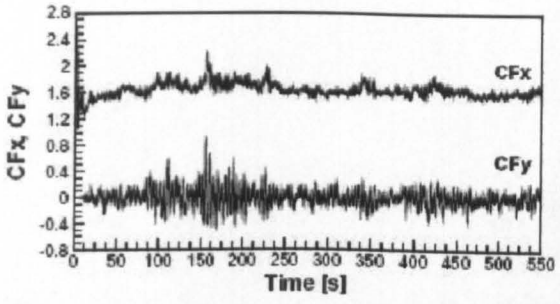

Figure 5.3: Time histories of the aerodynamic coefficients derived from the lift CF_y and derived from the drag CF_x from Braun and Awruch (2009).

section is 30 m by 45 m. Braun and Awruch developed their own CFD code, based on LES, and combined it with their originally developed structural solver. They presented extensive results of the building response for different velocities, but identified the need to use a truly turbulent inflow with fluctuating velocities. Figure 5.3 shows the time histories of the lift and drag coefficients presented by Braun and Awruch. Figure 5.4 shows the response of the building for two reduced velocities. For a reduced velocity of 11.1 (b), the "lock-in" phenomenon can be observed: the transversal building response is maximal.

Because most of the researchers interested in modelling FSI have designed their own code, they had to focus on the most difficult part of FSI: the mesh-fluid relationship. That is why it is interesting to demonstrate the coupling of a structural solver with a well-established CFD code, such as ANSYS-Fluent, that has been shown to handle the fluid flow and the remeshing well. The focus would then consistently be on the fluid-structure coupling. This is the purpose of the next section work to investigate the fluid-structure coupling using ANSYS-Fluent.

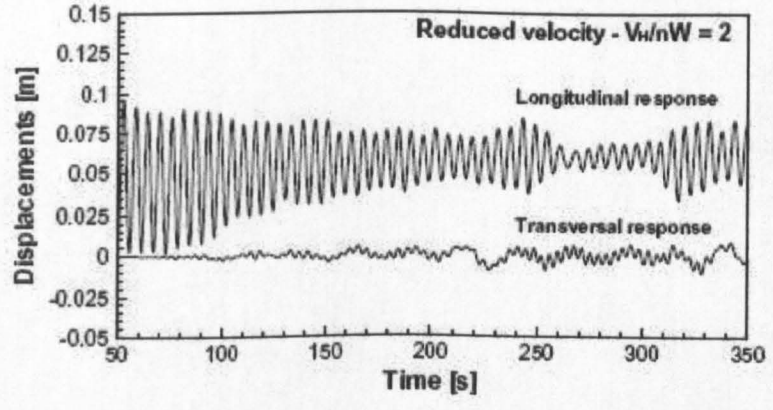

(a)

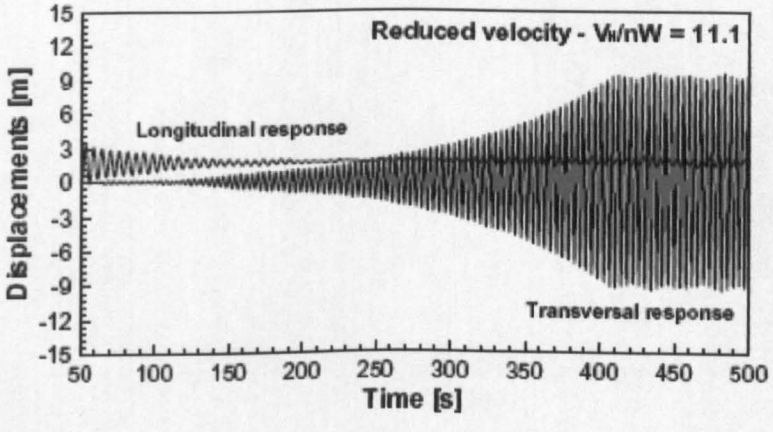

(b)

Figure 5.4: Time histories of longitudinal and transversal displacements computed at the top of the CAARC building (structural damping) by Braun and Awruch (2009).

5.3 The method for modelling fluid-structure interaction

5.3.1 Introduction

The objective of the present work is to model the response of a cantilever-like building to wind loading, and more precisely, the response of the cantilever to vortex shedding (transversal excitation) and buffeting (along-wind excitation). In this context, an approach based on modal superposition is chosen, combined with a non-staggered sequential fluid-structure coupling and an Arbitrary Lagrangian Eulerian mesh-fluid coupling.

The main objective is to demonstrate the relevance of this method to model the response of a building to vortex shedding, where turbulence is modelled with the DES method with the SST k-ω RANS model [2]. It is not the purpose of this chapter to consider buffeting.

In this context, the building is allowed to respond in the cross wind direction only, and mode shapes are determined just for this direction. The response in the along wind direction is not modelled as there are very limited fluctuations in the incoming wind: the LES region is in and around the wake of the building, where the mesh is fine enough, but near the inlet, and the other boundaries, the SST k-ω RANS model is used. Therefore, a constant turbulent kinetic energy profile is specified at the inlet, as for a RANS simulation (see section 3.3.4), since any fluctuating velocities would not be maintained in a simulation where the turbulent quantities are effectively time-averaged in some regions of the domain (in the RANS regions) even if the simulation is transient.

5.3.2 The structural solver: modal superposition approach

Dynamic properties and mode shapes of the structure

The mode shapes and dynamic properties of the cantilever are determined by means of a finite element analysis of the structure using an open source Finite Element package, OpenFEM (B.1).

[2] see section 3.5 for the DES method, and section 3.3.2 for details on the SST k-ω model

The first mode shape in the cross-wind direction is determined as well as the dynamic properties of the structure, necessary to solve the dynamic equation of motion.

Solving the dynamic equation

Equation (5.2.1) is applied to a single degree of freedom cantilever that is allowed to move in the cross-wind direction [3]. A modal superposition approach is adopted. The displacements in the Y direction at coordinate z, $g(z,t)$, are written as a product of the mode shape, ϕ_n , coordinate dependent only, and a time-dependent amplitude or modal amplitude $y_n(t)$, n being the mode considered:

$$g(z,t) = \sum_n \phi_n(z)\, y_n(t)$$

The equation of motion with generalized coordinates can then be rewritten as follows:

$$m^* \ddot{y}(t) + c^* \dot{y}(t) + k^* y(t) = f^*(t) \tag{5.3.1}$$

with:

$$m^* = \overline{m} \int_0^L \phi(x)^2 dx \tag{5.3.2}$$

$$c^* = a_1 EI \int_0^L \left(\phi''(x)\right)^2 dx \tag{5.3.3}$$

$$k^* = EI \int_0^L \left(\phi''(x)\right)^2 dx \tag{5.3.4}$$

$$f^*(t) = \int_0^L p(t)\phi(x) dx \tag{5.3.5}$$

where m^* is the generalised mass, c^* generalised damping in which a_1 is to be defined, k^* is the generalised flexural stiffness, and $f^*(t)$ is the generalised effective load, $m(x)$ mass per unit length and EI the product of the Young's modulus and the second moment of inertia.

[3] In this chapter, the building is allowed to only move in the cross-wind direction, but in Chapter 7, the building is allowed to move in its two main directions.

The simplest way to formulate the damping is to make it proportional to either the mass or the stiffness: $\xi = (a_1 w_n)/2$ for the n-th mode. Or it can be chosen to define the damping as a function of the mass and the stiffness $C_n = a_0 M_n + a_1 w_n^2 M_n$. In short, either the damping ratio ξ_n is defined and $C_n = 2\xi_n w_n M_n$ or the two constants a_1 and a_2 are defined.

A fourth order Adam-Bashforth algorithm is used to solve equation (5.3.1), which is rewritten in a simplified form as:

$$m\,\ddot{y}_n + c\,\dot{y}_n + k\,y_n = P_n$$

from which $\ddot{y}_{n+1}$ can be expressed as a function of P_n (the load), y and $\dot{y}$

$$\ddot{y}_{n+1} = F(P_{n+1}, y_{n+1}, \dot{y}_{n+1})$$

$$\ddot{y}_n = F(P_{n+1}, y_{n+1}, \dot{y}_{n+1}) \tag{5.3.6}$$

$$y_{n+1} = y_n + h\left[\dot{y}_n + \frac{1}{2}\Delta\dot{y}_n + \frac{5}{12}\Delta^2\dot{y}_n\right] \tag{5.3.7}$$

$$\dot{y}_{n+1} = \dot{y}_n + h\left[\ddot{y}_n + \frac{1}{2}\Delta\ddot{y}_n + \frac{5}{12}\Delta^2\ddot{y}_n\right] \tag{5.3.8}$$

The fourth order Adam-Bashforth algorithm is chosen because it offers more accuracy than a first order Euler algorithm, but it is still consistent with a sequential coupling method, where the fluid and the structure are solved distinctly. Because the fourth order algorithm requires storing the displacements at 3 previous time steps, the first order Euler algorithm is used for the first 3 time steps.

Verification: Response of the structural solver to harmonic loading

In order to achieve verification of the structural solver and the efficiency of the Adam-Bashforth algorithm, harmonic loading was imposed on a single degree of freedom cantilever (stiffness k, damping ξ, ω the natural frequency). The response y_n of the can-

tilever to harmonic loading $f_n = f_0 \, sin(\overline{\omega} \, t)$ with varying damping ratio and as a function of the applied loading frequency $\overline{\omega}$ is presented.

The algorithm is tested in Matlab and the post analysis is also done in Matlab[4].

The response can be expressed as $g(t) = \rho \, sin(\overline{\omega} \, t - \theta)$ where ρ is the amplitude of the displacement, and θ the phase angle of the response.

Results are presented in Figures 5.5 and 5.6. Figure 5.5 shows the variation of the dynamic magnification factor, $D = \frac{\rho}{p_0 k}$ with the dimensionless frequency $\beta = \overline{\omega}/\omega$. Figure 5.6 shows the variation of the phase angle of the response as a function of the dimensionless frequency for various damping ratios. Comparison of these results to textbook results (Clough and Penzien, 1993, p. 38) shows excellent agreement.

Having verified that the structural solver behaves in the expected way for a sinusoidal loading example, it can be used with more confidence in a fluid-structure interactions situation where harmonic loading is replaced by wind loading.

[4]At this point of verification, there is no fluid-structure interaction.

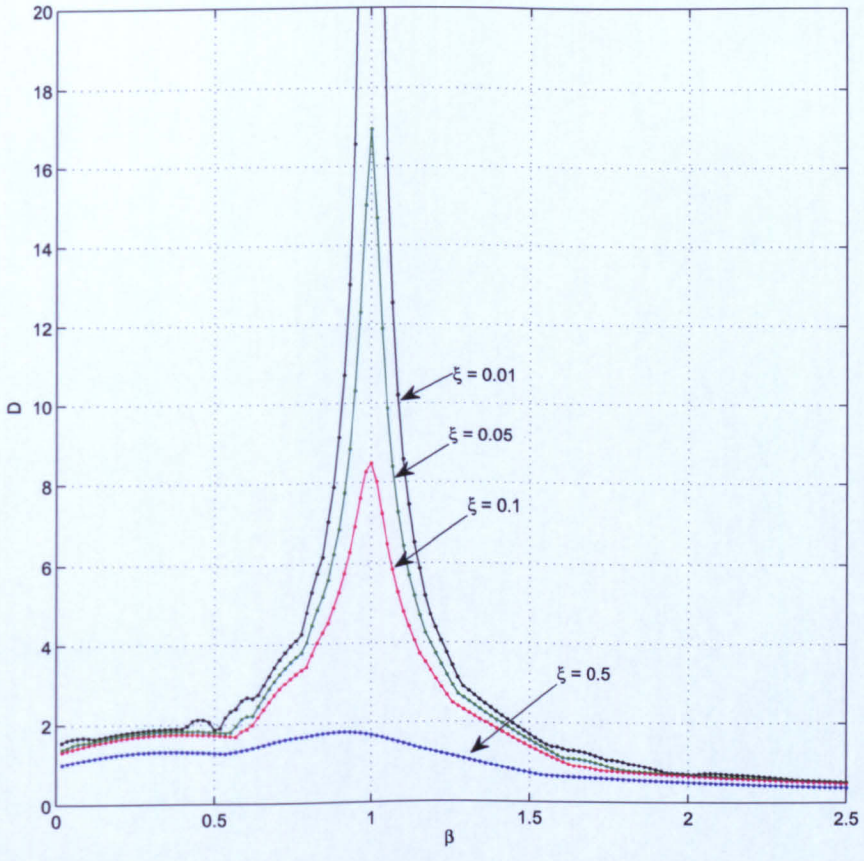

Figure 5.5: Response to harmonic loading: variation of dynamic magnification factor with damping and frequency

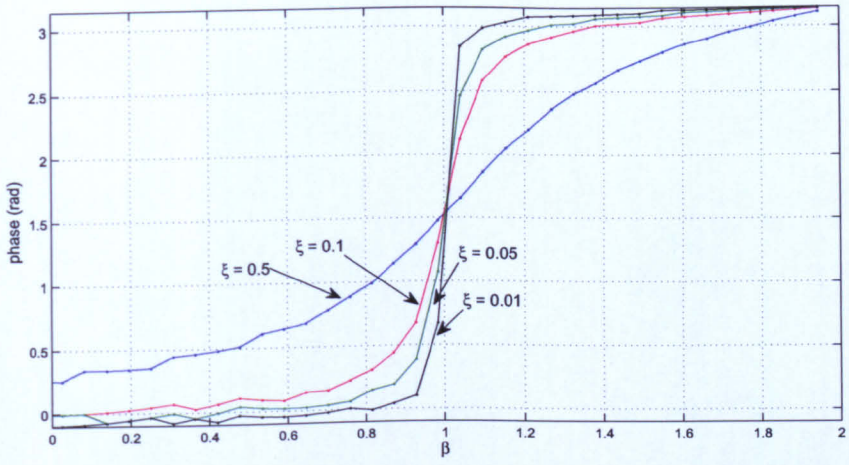

Figure 5.6: Response to harmonic loading: variation of phase angle with damping and frequency

5.3.3 Application of the method

ANSYS-Fluent offers the possibility of accessing and modifying solver variables through the utilisation of User Defined Functions (UDF), which are pieces of code written in C++. Predefined functions, called *Macros*, can be used in UDFs to simplify the communication between the solver and the user. For example, predefined macros exist to easily access parts of the mesh, or perhaps a velocity component in a cell. Some of these macros have been used in the present work. They will therefore be more specifically described later.

The code offers two main ways for achieving dynamic meshing. The first and simplest one allows the user to define the centre of gravity motion of an element. As the dynamic response of a cantilever cannot be written as a simple function of the motion of the centre of gravity of the element, another method is adopted here. The method that is used in the present work allows each node of the dynamic zone to be individually moved. The *macro* associated with this method is called `Define Grid Motion`.

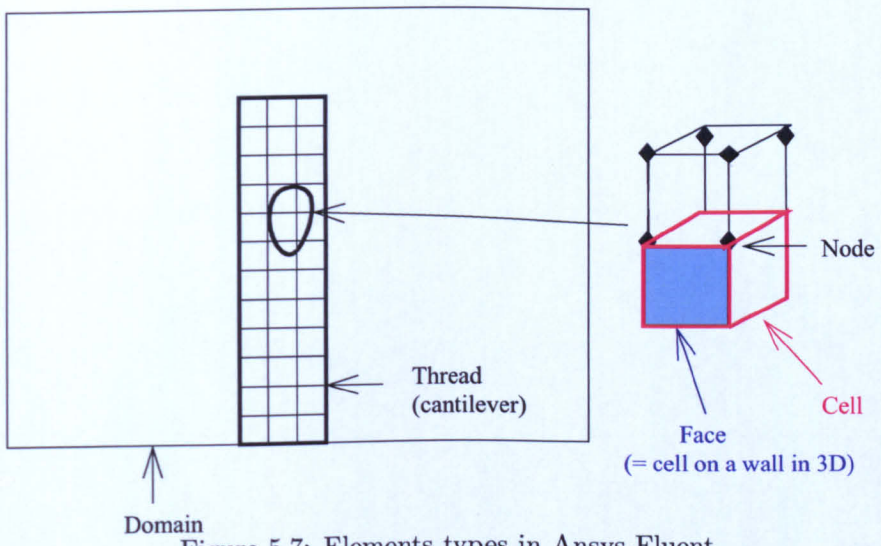

Figure 5.7: Elements types in Ansys-Fluent

General procedure for moving the mesh

Before explaining the procedure for moving the mesh, it is important to review the types of data that the code will have to handle. Generally speaking, the mesh can be seen as comprising a set of domains. In this study, there is only one domain. The domain is then composed of a number of threads. For example the surface of the cantilever forms a thread, the ground forms another one. As a result, a thread is a group of cells or faces. In 3D, walls are composed of faces, the rest of thread's elements are cells. In 3D, a cell is usually composed of either 4 nodes (tets) or 8 nodes (hex). Figure 5.7 summarizes the different types of entities that will be considered when moving the mesh.

The general procedure for moving the mesh is presented in Figure 5.8.

Initially, it is necessary to identify the nodes that will be moved. As shown on the Figure 5.8 and in Appendix B, the index of the nodes composing the cantilever are stored by looping over the nodes in the cantilever. This is achieved by using a *macro* that loops over the nodes in a specific thread (e.g. cantilever). In addition, the initial position of each of these nodes is stored.

Next, the solver starts iterating. First, the fluid solver starts computing the flow around the building; at the end of this second iteration, the structural solver is called by the

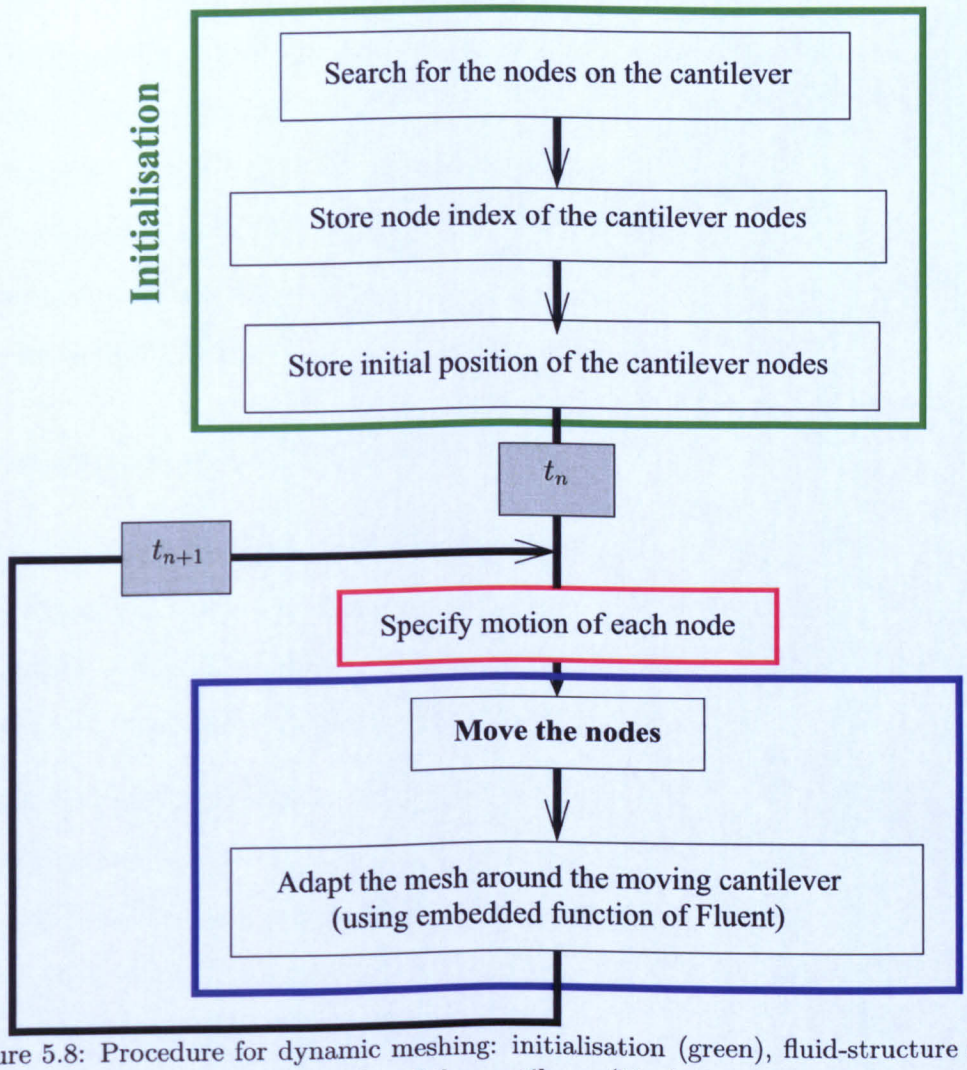

Figure 5.8: Procedure for dynamic meshing: initialisation (green), fluid-structure coupling (red) and motion of the nodes of the cantilever (blue)

macro `Execute at end` to compute the forces due to wind loading acting on the building. Then, the node displacement is computed accordingly.

Nodes are moved before the first iteration of each time step. In transient flow simulations, there are a number of iterations within each time step, and the process is repeated for all time steps. These two levels of looping can be seen in Figure 5.10.

At the beginning of each iteration, the motion of each node on the surface of the cantilever is specified, and the nodes are moved. The remeshing of the moving zone is processed by ANSYS-Fluent, using the spring-based scheme, in which the edges of the mesh elements are treated as a network of interconnected springs; their initial position is the state of equilibrium. Besides, the remeshing of the zone around the cantilever is handled by ANSYS-Fluent.

Introduction of the Rigid Zone around the cantilever

A comparison of the deformation of the cells near the cantilever walls is shown in Figure 5.9. The sketch on the left shows that if no deformation at all is specified, the mesh around the moving wall is fixed. This option is not acceptable as it could lead to negative volume cells. The second option is to use the embedded function in ANSYS-Fluent.

It has been found that using this second option for handling the mesh around the moving zone induces stretching of the cells in the near wall region of the cantilever. This had to be addressed because cell stretching prevents fine features of the flow to be captured, and we know that the near wall region is a key zone for the flow; separation occurs in that zone and vortices develop near the walls of the cantilever.

Stretching of the cells can be avoided by introducing a *rigid zone* around the cantilever in which the motion of each node is controlled by the user. This forces the cells in the rigid zone to move similarly to the cantilever. The shape of the near wall cells are then preserved from over-stretching.

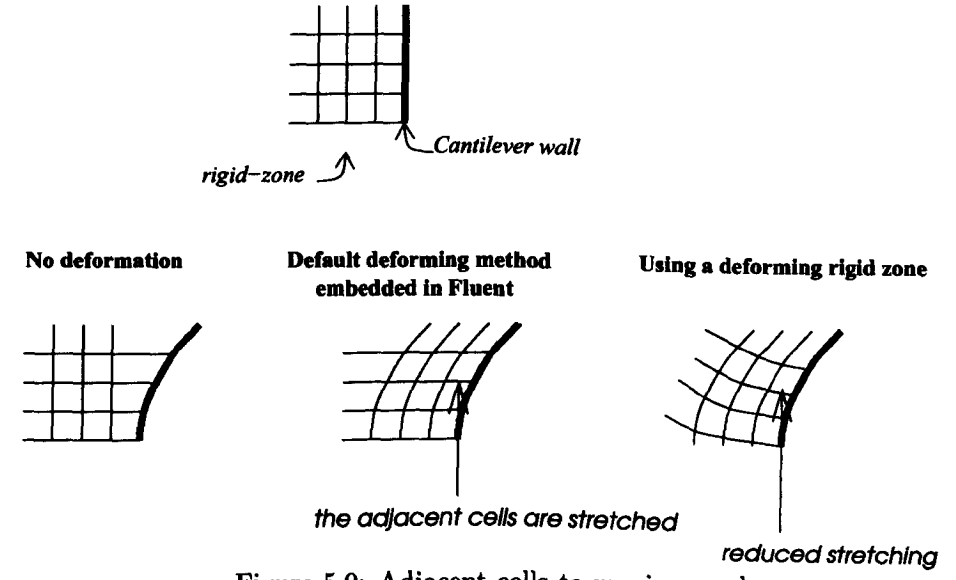

Figure 5.9: Adjacent cells to moving mesh

Parallelisation of the UDF

The UDF code was written for parallel computing, which means that the different operations had to be carefully excecuted on either the host or the compute nodes. Only the compute nodes contain information on the mesh, such as mesh node positions and face variables such as forces. Only the host can gather this information to compute the total force acting on a body, the building in the present case. [5]

5.3.4 Summary of the FSI coupling method

Figure 5.10 presents a diagram of the method to couple the structural solver with the fluid solver Ansys-Fluent.

Its summarizes the important steps of the fluid-structure coupling, including the initialisation detailed in section 5.3.3, the computation of the dynamic response, the motion of the nodes and the solver iterations. The colours applied to the boxes of the diagram are consistent with the colours used in the previous diagram 5.8. Macros used in the UDF are also included in the diagram, alongside the steps of the method to which they

[5]Details on the parallelisation of the code can be found in Appendix B

correspond. Referring to the terminology used in section 5.2 shows that the method used in here is a non-staggered sequential method, that is, the fluid is solved at t_n on the mesh computed at t_{n-1}.

As for the time stepping, theoretically, the structural solver would handle larger time step sizes than the fluid solver. But since the computational time involved by the structural solver was shown to be negligible compared to the computational time needed by the fluid solver, the time step size for the structural solver was chosen to be the same as the fluid time step.

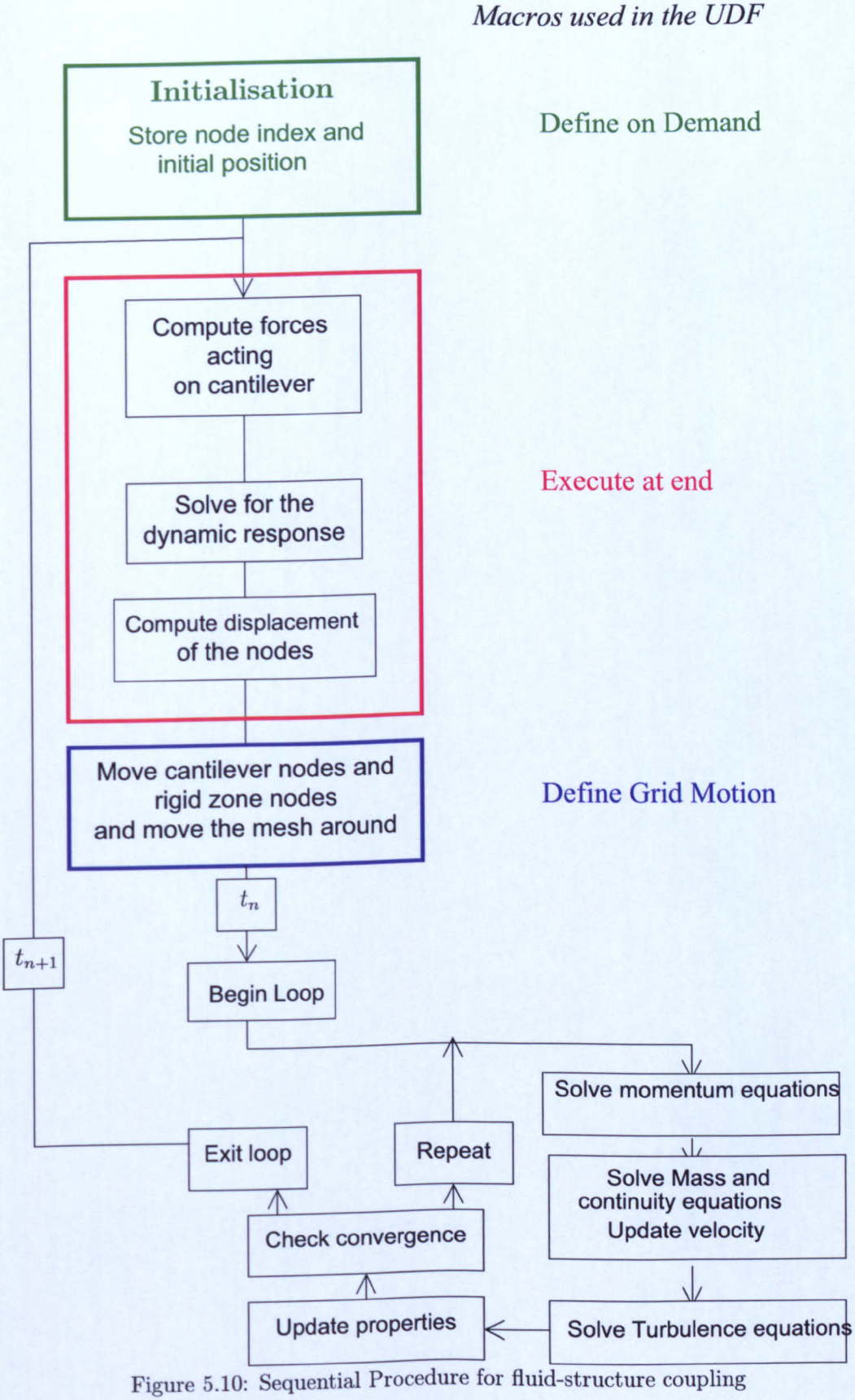

Figure 5.10: Sequential Procedure for fluid-structure coupling

5.4 Application of the FSI method to a 1 in 200 scale building

5.4.1 Introduction

The objective of this section is to apply the method for modelling fluid-structure interactions just described to a 180 m building, and to investigate its ability to resolve aeroelastic phenomena under specific conditions, such as the "lock-in" phenomenon. As presented in a previous section, "lock in" is an aeroelastic phenomenon linked to the presence of vortex shedding in the wake of the building, and that can occur when the vortex shedding frequency comes close to the natural frequency of the building: the vortex shedding frequency gets locked at a frequency close to the natural frequency of the building, and differs from the vortex shedding frequency of a static building defined by the Strouhal number.

This section will present the results of a DES simulation of a 180 m building. DES[6] with a SST k-ω RANS turbulence model[7] was chosen because of the unsteady nature of the flow studied. A transient flow simulation was done. Moreover, it was shown in previous studies that RANS based models, even used in an unsteady manner, were not able to capture vortex shedding while DES was able to capture and maintain these unsteady phenomena, which is essential to couple the flow with the dynamic response of the building (Revuz et al., 2009).

The DES approach allows vortex shedding to be predicted. It follows that an oscillation and transversal force acts on the building. The varying parameter is the vortex shedding frequency, which is modified by the incoming velocity (see section 2.2.1 and the definition of the Strouhal number). It is the purpose of this section to investigate the response of the building to wind loading with various incoming velocities.

[6] see section 3.5
[7] see section 3.3.2

5.4.2 Set-up

The approach described previously for modelling fluid-structure interactions is applied to a 180 m building, with plan dimensions of 20 m (along wind direction) by 10 m (across wind direction). As explained before, a rigid zone is defined around the building. Details on the geometry of the building and the rigid zone can be found in Figure 5.11(b). The size of the domain follows the findings of Chapter 4, namely the final dimensions of the domain corresponds to the "Medium 2" domain. The mesh (Figure 5.11(a)) is structured and refined around the building, in the rigid zone and in the wake region, and has 2.1×10^6 cells.

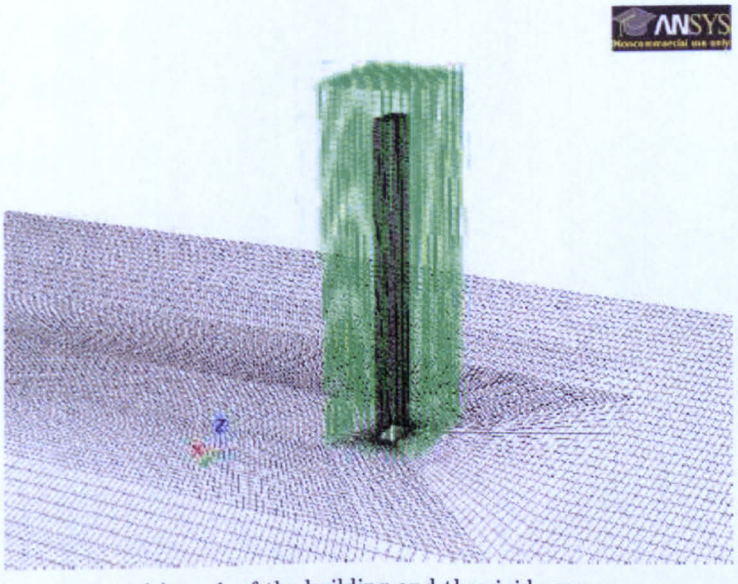

(a) mesh of the building and the rigid zone

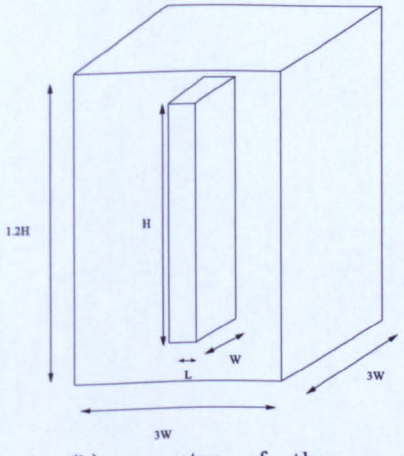

(b) geometry of the building and its rigid zone

Figure 5.11: Geometry and mesh of the 180 m building and its rigid rigid zone

A log-law velocity profile is implemented at the inlet as presented in section 3.3.4. A zero-pressure outlet is specified. The lateral and top boundaries are modelled as symmetry boundaries as recommended in Franke et al. (2007).

The domain is scaled down by 200 in order to save computing time and maintain reasonable $y+$ values.

A Finite Element Analysis (using openFEM) sets the dynamic properties of the cantilever, as well as the main mode shape of the building response in the transversal

direction. To reiterate, this is because the main objective of this chapter is to study the response of the building to vortex shedding.

The reference height was defined to be the top of the building and it was the velocity at this height which was varied in this investigation.

5.4.3 Methodology

As mentioned, the building is allowed to move in the transversal direction. However, in an initial simulation, the structure is treated as rigid to let the wake develop. From this initial static simulation, the Strouhal number is obtained. By equating the vortex shedding frequency and the natural frequency, $f_{vs} = f_n$, the critical wind speed at which the vortex shedding frequency reached the natural frequency is computed:$u_{cr} = f_n W/St$ (where f_{vs} is the vortex shedding frequency, f_n the natural frequency of the building, and W the width of the structure).

After the initial static simulation, the building is released and the fluid-structure interaction starts. The inlet velocity is increased incrementally until it reaches the critical velocity, and goes beyond.

Results are presented against reduced velocity, u/u_{cr}, and dimensionless frequency f_{vs}/f_n.

5.4.4 Results and discussion

Presence of vortex shedding is confirmed by the plot of the time series of the lift coefficient of the building in Figure 5.12 as well as the contours of the velocity magnitude at midheight of the domain in Figure 5.14.

The time varying component of the building response, $y_n(t)$, is plotted against time in Figure 5.13 for a couple of reduced velocity, around "'lock-in". It can be observed that the maximum amplitude is reached for an incoming velocity u close to the critical velocity, previously defined. The maximum response corresponds to the resonance of

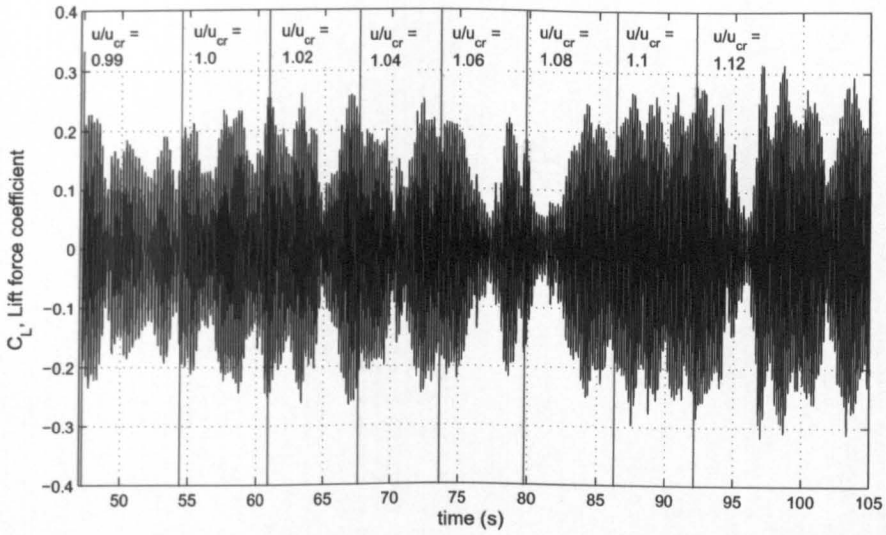

Figure 5.12: Time history of the lift coefficient on the building, for incoming velocities varying around u_{cr}

the structure to an oscillating transversal force, produced by vortex shedding.

To conclude the analysis, the time series were studied in the frequency domain by the mean of Fast Fourier Transforms (FFT). The FFT was performed in Matlab using the function fft and the time series of the response were padded with zeros so that the results was not dependent on the length of the time series. Figure 5.15 shows the resulting plot of the analysis of the lift coefficient in the frequency domain for various u/u_{cr} ratios. First, from the slope of the vortex shedding frequency in static conditions the Strouhal number is deduced, $St = 0.08$, which is consistent with the literature Sachs (1978, p. 141). It can be seen from the plot that for $u/u_{cr} <= 1.1$, the vortex shedding coincides with the vortex shedding frequency in the static case. But the vortex shedding frequency gets locked for $f_{vs}/f_n \approx 1.1$ and does not match the Strouhal number definition anymore (where f_{vs}/f_n is a constant ratio and is equal to u/u_{cr}): this is the "lock-in" phenomenon. This region, of "lock-in" phenomenon matches a region of large lift coefficients. After the reduced velocity has reached 1.5, the vortex shedding frequency coincides again with the vortex shedding frequency in static (indicated by the slope of the line before the plateau).

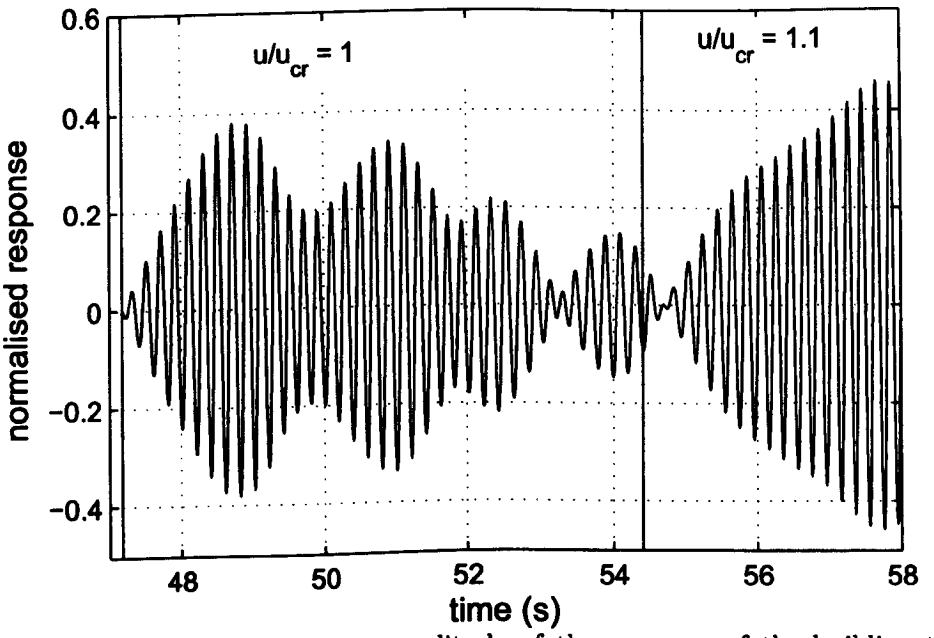

Figure 5.13: Time history of the amplitude of the response of the building to wind loading in the transversal direction ($y_n(t)$, time varying component of the response, normalised by L)

5.5 Summary and conclusions

In this Chapter, details on the method developed to model fluid-structure interactions were presented. The method involves the fluid solver Ansys-Fluent and a structural solver based on modal superposition.

The structural solver to be coupled with the fluid was verified with a classic test case (harmonic loading). Later on, the method was applied to a 180 m building whose characteristics were chosen arbitrarily in the absence of full-scale or wind tunnel data and successful coupling of the flow and the structure was achieved (prediction of the "lock-in" phenomenon).

Another important aeroelastic phenomenon related to the presence of wind gusts causes along-wind excitation to the building. To model this phenomenon, some sort of fluctuating velocity need to be input, which involves the generation of realistic time-varying turbulent inflow in a simulation of the flow able to maintain such small scale features,

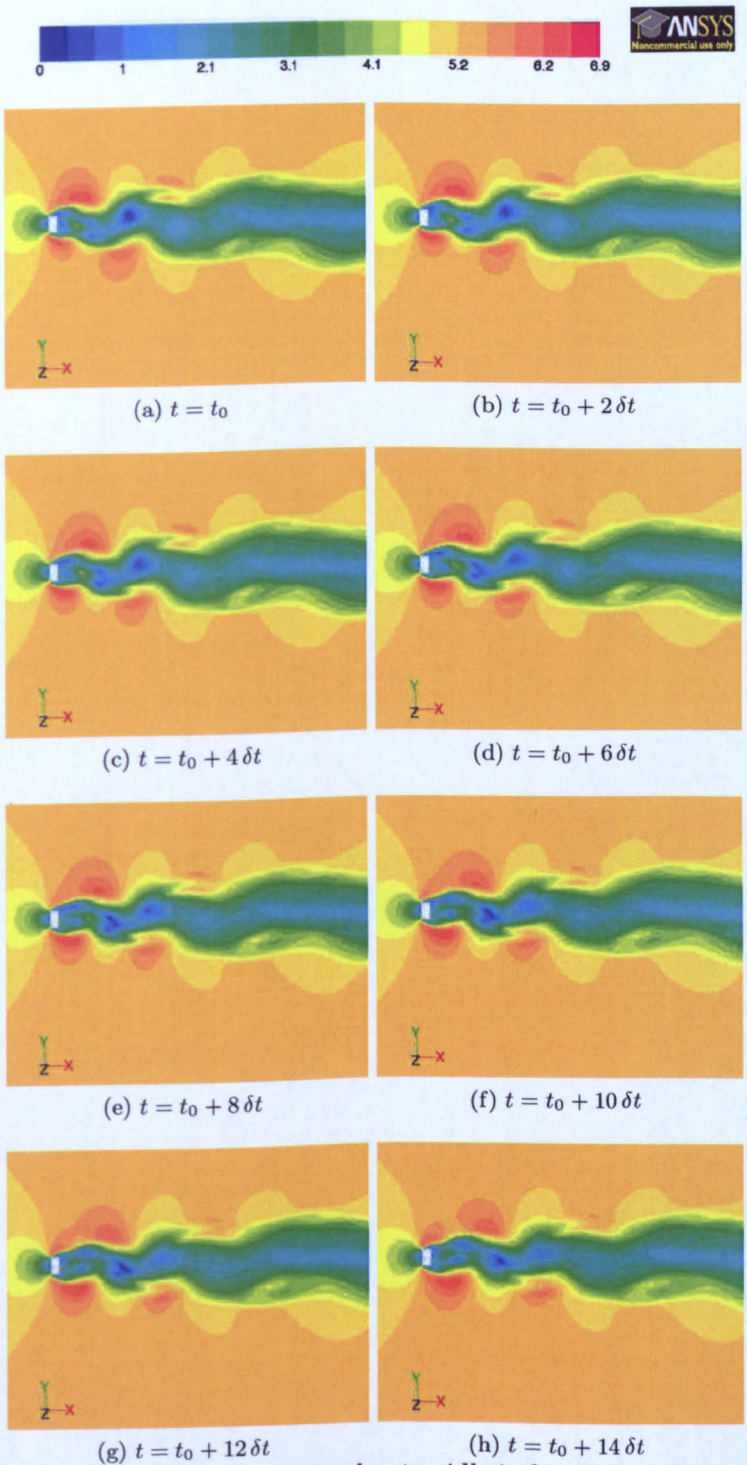

(a) $t = t_0$ (b) $t = t_0 + 2\,\delta t$

(c) $t = t_0 + 4\,\delta t$ (d) $t = t_0 + 6\,\delta t$

(e) $t = t_0 + 8\,\delta t$ (f) $t = t_0 + 10\,\delta t$

(g) $t = t_0 + 12\,\delta t$ (h) $t = t_0 + 14\,\delta t$

Figure 5.14: Flow field: velocity magnitude at midheigtht of the building, illustration of vortex shedding ($\delta t = 0.005s$, $Re = 3.5 \times 10^4$, velocity in m/s).

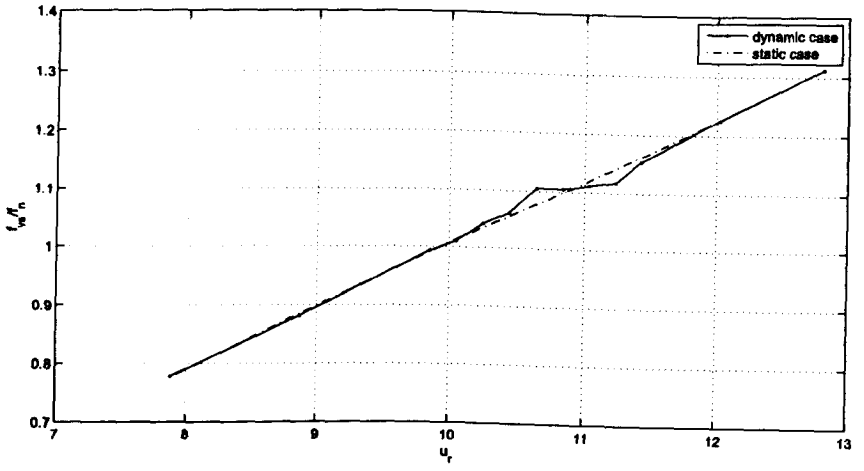

Figure 5.15: Vortex shedding frequency vs reduced velocity: "lock-in" phenomenon at $u/u_{cr} \approx 1.1$

namely LES. It is the object of the next Chapter to present the optimisation of a method for generating synthetic time-varying turbulent inflow for LES, that could be used in combination with the fluid-structure interactions tool in order to predict buffeting.

Chapter 6

Turbulent Inflow

6.1 Introduction

In computational wind engineering, accurate modelling of the turbulent Atmospheric Boundary Layer (ABL) is a key issue. When using a RANS model such as the k-ϵ turbulence model, the variables input at the inlet are either k or ϵ or other variables directly related to k and ϵ. This approach assumes turbulence isotropy and since it is a time-averaging method, any fluctuations of the velocity components are not maintained through the domain. The approach is very different when it comes to Large Eddy Simulation (LES). In LES, the equations for the flow are spatially averaged, and the Navier-Stokes equations are resolved for the length scales that are bigger than the grid size (or another prescribed filtering cutoff). The smaller eddies are believed to have a more isotropic nature and are therefore modelled. As a consequence, in this time-varying approach, it is important to properly define a field of fluctuating velocities at the inlet that reflects the characteristics of the turbulent flow within the ABL.

From the late nineties, when LES was first investigated for wind engineering, research groups pointed out the advantages of generating time-varying turbulent inflows Murakami (1998, 1997). Since then, several methods for producing velocity fluctuations at the inlet of the domain have arisen. The most widely used, and certainly the most costly,

is the method that uses a precursor simulation. The velocity field is stored at an appropriate downstream station of the precursor simulation in an empty domain with roughness elements. This field is then used as an inflow for the main simulation. This method is believed to reproduce coherent turbulent structures (Thomas and Williams, 1999). However, the nature of the method means that it is unsuitable for complex urban terrain due to the large costs in terms of computing and time.

The method employed in this work aims at generating a synthetic field of fluctuating velocities rather than generating it through a precursor simulation. This can be done using inverse Fourier transforms: Inverse Fourier transforms are applied to prescribed spectra to produce artificial turbulent inflows that respect given spatial and time correlations. This method was notably described and assessed by Lee et al. (1992), but some disadvantages of this technique were reported by Klein et al. (2003). Firstly it seems to be difficult to program; secondly the use of Fourier transforms restricts the application to Cartesian and equispaced meshes; and furthermore, it requires a 3D energy spectrum that is not easily obtainable experimentally. Finally, the major disadvantage appears to be the randomness in wave number space, that is, a realistic turbulence is only recovered after a long distance (Xie and Castro, 2008). For these reasons, Klein et al. developed another technique achieving the same goal and based on the method published by Lee et al. Klein et al. proposed a technique that consists of filtering a set of random data using a Gaussian filter. The filter is applied to three components of 3D random data ($2N_x \times N_y \times N_z$ with N_x, N_y and N_z being the longitudinal, lateral and vertical integral length scales respectively) to obtain a two dimensional turbulent time-varying inflow. Temporal (longitudinal) and spatial (vertical and lateral) correlations are ensured by a filter based on an exponential autocorrelation function. Later, Xie and Castro (2008) modified the method in order to make it less demanding in terms of computing power: instead of using three sets of 3D random data, their method only needs three sets of 2D random data ($N_y \times N_z$) and the temporal correlation is guaranteed by a second filtering operation, which consists of combining the fluctuating components at the current time step with those from the previous time step with weighting coefficients dependent on the

expected temporal correlation. The other major change is the form of the filter: instead of using a normal distribution their filter is based on a decaying exponential distribution for defining the autocorrelation function.

It is the objective of this chapter to present the optimization of an efficient method for generating turbulent inflow for LES.

6.2 Description of the method for generating turbulent inflow for LES

As previously stated, the filtering operations in the method developed by Xie and Castro (2008) is based on an autocorrelation function which takes the form of the following equation:

$$R_{uu}(k\Delta) = \frac{\overline{u(m)u(m+k)}}{\overline{u(m)u(m)}} = \exp^{-\frac{\pi k}{2n}} \tag{6.2.1}$$

where u is one of the fluctuating components of the velocity, R_{uu} the autocorrelation function (normalised) of u, n a wave number related to the expected length scale, and m is a repeating subscript used in the implicit summation. The same form of equation is used to define the autocorrelation in time and in space (in the vertical and horizontal direction), with three different length scales, for the temporal, vertical and horizontal autocorrelations respectively.

The method requires us to provide a **length scale**, n, for each spatial direction (Y and Z) and in the longitudinal direction (also called temporal length scale) for each component of the velocity. Based on the fact that the length scales do not vary significantly in the upper region of the ABL (ESDU 85020, 1985, revised in 1990) it was decided to define two zones: a lower region, in the *lower quarter* of the ABL, and an *upper region* in the rest of the ABL.

The **filter coefficients** that are used to filter the set of random data in order to produce

a spatially correlated (in Y and Z directions) field of data are derived from Equation (6.2.1). The form of the filter is illustrated in Figure 6.1.

Spatial correlation is ensured by the filtering operations done at steps 5 and 7, when the random data are filtered through the coefficients b_y and b_z, defined in equations (6.2.5), (6.2.6).

Temporal correlation is ensured by the operation executed at step 8 via the weighting coefficients used in equation (6.2.13). These weighting coefficients are also derived from (6.2.1).

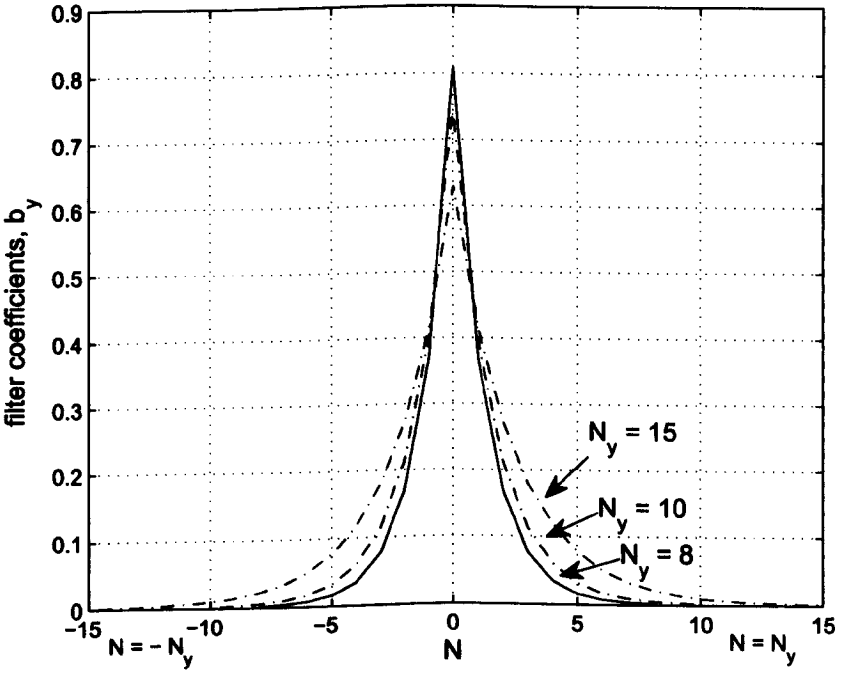

Figure 6.1: Filter coefficients b_y in Y direction. Illustration for three different filter sizes $N_y = 8$, 10, 15. The coefficients are defined for N $= -N_y$ to N_y

The fluctuating components of the velocity are computed on a virtual uniform mesh. However the mesh to be used in the CFD simulation is unlikely to be uniform, therefore, a **bilinear interpolation** scheme is used to interpolate the field of fluctuating velocities from the virtual uniform mesh to the non-uniform CFD mesh, Figure 6.4. The grid sizes of the virtual uniform mesh are chosen so that they are consistent with the smallest grid

sizes of the CFD non-uniform mesh, in order to limit the loss of information between the two meshes. The process is illustrated in Figure 6.4.

The method used to generate the field of fluctuating velocities is summarized below. It can be decomposed into 12 steps, the first step is an initialization step, steps 2 to 5 are called at the first iteration only, and from the step 6, the iterative process starts.

1. The first step is to determine the filter sizes:

   (a) Firstly, the vertical (z) and lateral (y) integral length scales are defined in the lower quarter region $^{(1)}$ and in the upper region $^{(2)}$.

   It is assumed that the lateral and vertical integral length scales do not vary from one component of the velocity to another (ESDU 85020, 1985, revised in 1990), but this is not a requirement from the method and it is possible to specify a different length scale for each component since the filtering operation is done on each component separatly.

$$L_u^{z^{(i)}} = L_v^{z^{(i)}} = L_w^{z^{(i)}}{}_{i=1,2}$$

$$L_u^{y^{(i)}} = L_v^{y^{(i)}} = L_w^{y^{(i)}}{}_{i=1,2}$$

   From these length scales, the filter sizes are computed:

$$N_y^{(i)} = \frac{2L_u^{y^{(i)}}}{\Delta y}{}_{i=1,2} \tag{6.2.2}$$

$$N_z^{(i)} = \frac{2L_u^{z^{(i)}}}{\Delta z}{}_{i=1,2} \tag{6.2.3}$$

   where Δy and Δz are the cell dimensions in Y and Z directions respectively of the virtual uniform mesh (cf. Figure 6.4).

   In effect the filter sizes reflect the size of the average wind gusts. For this reason, it will be ensured that the filter sizes do not exceed a quarter of the total number of cells in a given direction, i.e. $N_y <= \frac{M_y}{4}$ and $N_z <= \frac{M_z}{4}$, otherwise the wind gusts might exceed the inlet area in size.

(b) The longitudinal length scales are then defined:

$$L_u^{x^{(i)}}, L_v^{x^{(i)}}, L_w^{x^{(i)}}{}_{i=1,2}$$

From these, the filter size in the X-direction is defined:

$$N_x^{(i)} = \frac{2L_u^{x^{(i)}}}{u_{\text{mean}}\Delta t}_{i=1,2} \tag{6.2.4}$$

where u_{mean} is the time averaged velocity (averaged over space), and Δt is the time step size. It will be observed later in the empty fetch test case that this relationship between N_x and the longitudinal length scales is actually not accurate and must be redefined.

2. Once the filter sizes have been determined, the first iteration can be started: it starts with the generation of one set of random data of dimension $(2N_y + M_y) \times (2N_z + M_Z)$ where M_y and M_Z are the total grid dimensions in Y and Z directions respectively:

$$(r^{(0)}_{(1,j,k)}, r^{(0)}_{(2,j,k)}, r^{(0)}_{(3,j,k)})|_{j=-N_y+1\ldots M_y+N_y, k=-N_z+1\ldots M_z+N_z}$$

3. The next step is to calculate the filter coefficients $b_{jk} = b_j \times b_k$ where b_j and b_k are the filter coefficients in the Y and the Z direction respectively and are defined as follows:

$$b_j = \frac{\exp\frac{-\pi|j-N_y|}{N_y}}{\sqrt{\sum_{l=-N_y}^{N_y}\left(\exp(\frac{-\pi|l-N_y|}{N_y})\right)^2}} \tag{6.2.5}$$

$$b_k = \frac{\exp\frac{-\pi|k-N_z|}{N_z}}{\sqrt{\sum_{l=-N_z}^{N_z}\left(\exp(\frac{-\pi|l-N_z|}{N_z})\right)^2}} \tag{6.2.6}$$

4. Then, the following amplitude coefficients are defined based on the Reynolds stresses. Details on the derivation of the amplitude tensor can be found in Lund

(1998).

$$a_{11} = \sqrt{R_{11}} \tag{6.2.7}$$

$$a_{21} = R_{21}/a_{11} \tag{6.2.8}$$

$$a_{22} = \sqrt{R_{22} - a_{21}^2} \tag{6.2.9}$$

$$a_{33} = \sqrt{R_{33}} \tag{6.2.10}$$

where R_{ij} are the Reynolds stresses, derived from ESDU 85020 (1985, revised in 1990).

5. Finally the filter coefficients are applied to the random data in order to create a set of filtered (spatially correlated) data:

$$\phi_\beta^{(0)}(t_0, y, z)_{|\beta=x,y,z} = \sum_{j'=-N_y}^{N_y} \sum_{k'=-N_z}^{N_z} b_{j'k'} r_{\beta,j+j',k+k'}^{(0)} \tag{6.2.11}$$

for $j = 0 \ldots M_y$ and $k = 0 \ldots M_z$.

Figure 6.2 shows how the filter is applied to the random data and also clarifies the reason for the dimensions of the set of random data.

The filtering operation results in three scalars ($\beta = x, y, z$) of $\phi_\beta^{(0)}(t_0, y, z)$ for each point of the $Y \times Z$ plane of dimension $M_y \times M_z$. An illustration of this process is shown in Figure 6.3: (a) shows a plot of the raw random data on the inlet plane before filtering, and (b) shows the filtered data after step 5, it can be seen that this new set of filtered data has some degree of order.

6. In order to ensure temporal correlation, another set of random data is generated. This set has the same dimensions as the set of random data in step 2: $(r_{(1,j,k)}^{(1)}, r_{(2,j,k)}^{(1)}, r_{(3,j,k)}^{(1)})_{|j=-N_y+1 \ldots M_y+N_y, k=-N_z+1 \ldots M_z+N_z}$

7. A filter is applied to this second set of random data as in step 5:

$$\psi_\beta^{(1)}(t_0, y, z)_{|\beta=x,y,z} = \sum_{j'=-N_y}^{N_y} \sum_{k'=-N_z}^{N_z} b_{j'k'} r_{\beta,j+j',k+k'}^{1} \tag{6.2.12}$$

8. The following step is where the method developed by Xie and Castro (2008) differs from the one developed by Klein et al. (2003): instead of filtering the data in 3D as done by Klein, Xie and Castro (2008) filters the 2D set of data (step 5) and then combines the fluctuations at the previous time step $\phi_\beta^{(0)}$ with the fluctuations at the current time step $\psi_\beta^{(1)}$ to achieve the temporal correlation. Weighting factors are applied to the data from the previous time step, and to the data at the current time step. Xie and Castro defines these weighting factors as follows:

$$\phi_\beta^{(1)}(t_0+\Delta t,y,z)=\phi_\beta^{(0)}(t_0,y,z)\exp\frac{-\pi\Delta t}{2T}+\psi_\beta^{(1)}(t_0,y,z)\sqrt{1-\exp\frac{-\pi\Delta t}{T}}$$

However, when these factors were applied, the average amplitude of the fluctuations would be constantly increasing leading the process to instability. It should be noted that the instability that was observed as part of this work had also been reported by Ralph Evins at Buro Happold (Evins, 2007). In order to try and find the source of the instability, email were also exchanged with Zeng-Tong Xie, but without success.

This major modification to Xie and Castro method was therefore proposed: the weighting factors are normalised so that the summation of the two factors is always equal to one. The following shows how this was implemented:

$$\phi_\beta^{(1)}(t_0+\Delta t,y,z)=\phi_\beta^{(0)}(t_0,y,z)\left(\frac{\exp\frac{-\pi\Delta t}{2T}}{A_{\psi\phi}}\right)+\psi_\beta^{(1)}(t_0,y,z)\left(\frac{\sqrt{1-\exp\frac{-\pi\Delta t}{T}}}{A_{\psi\phi}}\right) \tag{6.2.13}$$

where

$$A_{\psi\phi}=\exp\frac{-\pi\Delta t}{2T}+\sqrt{1-\exp\frac{-\pi\Delta t}{T}}$$

It must be noted that the normalisation of these weighting coefficients leads the time series to yield a variance just below 1, where the implementation by Xie and Castro ensured a variance of one, which is formally correct. As a consequence, this modification of the weighting coefficients is formally incorrect. However, fur-

ther tests of this implementation proved that it achieved the correct temporal correlation, without leading an unstable system.

9. After a set of spatially and temporally correlated data have been produced, these can be combined with the amplitude coefficients a_{ij} to compute the fluctuating velocities for the time step $t + \Delta t$

$$u'_x(y,z) = a_{11} \times \phi^x_1(y,z) \tag{6.2.14}$$

$$u'_y(y,z) = a_{21} \times \phi^x_1(y,z) + a_{22} \times \phi^1_y(y,z) \tag{6.2.15}$$

$$u'_z(y,z) = a_{33} \times \phi^z_3(y,z) \tag{6.2.16}$$

10. A log-law velocity profile, $\overline{u}_x(z)$, is then superimposed on the X-component of the velocity:

$$u_x(y,z) = \overline{u}_x(y,z) + u'_x(y,z) \tag{6.2.17}$$

$$u_y(y,z) = u'_y(y,z) \tag{6.2.18}$$

$$u_z(y,z) = u'_z(y,z) \tag{6.2.19}$$

11. At this point, the fluctuating components of the velocity have been computed for the virtual uniform mesh, with cell size Δy and Δz (see step 1 of the method). A bilinear interpolation scheme is used to interpolate the fluctuating velocities from the virtual uniform mesh to the CFD non-uniform mesh; this process is illustrated in Figure 6.4.

The process is then iterated from step 6 to step 11 for each time step: that is, a new set of random data $r^{(n+1)}$ is generated at each time step and then filtered to give $\psi^{(n+1)}_\beta(t_{n+1})$. Then, $\phi^{(n)}_\beta(t_n)$ and $\psi^{(n+1)}_\beta(t_{n+1})$ are combined to get $\psi^{(n+2)}_\beta(t_{n+2})$ with $\beta = x, y, z$ for the three components of the velocity at each point of the inlet plane.

The key steps of the method are illustrated in Figure 6.5. The important points of the method are:

1. The generation of the random data.

2. The calculation of the Reynolds stress tensor.

3. The choice of the longitudinal, vertical and lateral integral length scales for the three components of the velocity.

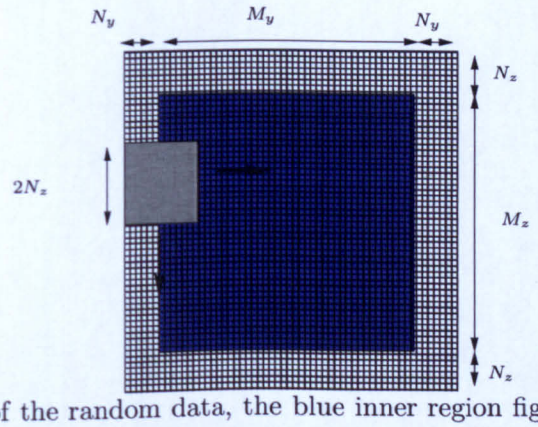

Figure 6.2: Filtering of the random data, the blue inner region figures the inlet plane, and the white outer region represents the size of the plane for which the random data need to be produced. The grey regions show the filtering process in both directions.

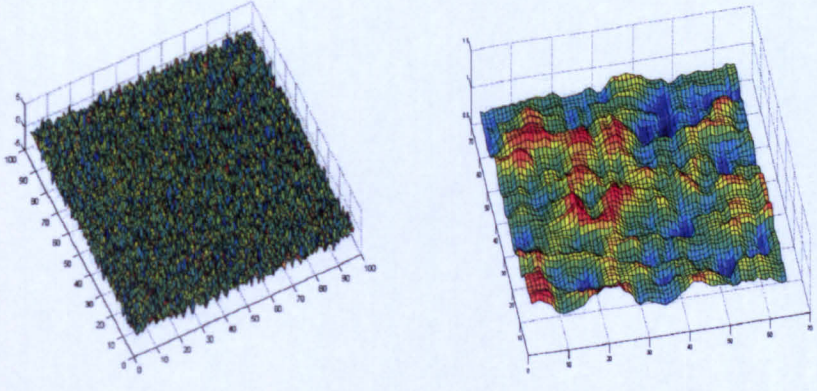

(a) Random data

(b) Filtered random data

Figure 6.3: 2D set of random data on the inlet plane, (a) shows the raw random data and (b) shows the filtered random data after step 5 of Xie and Castro's method, which are spatially correlated

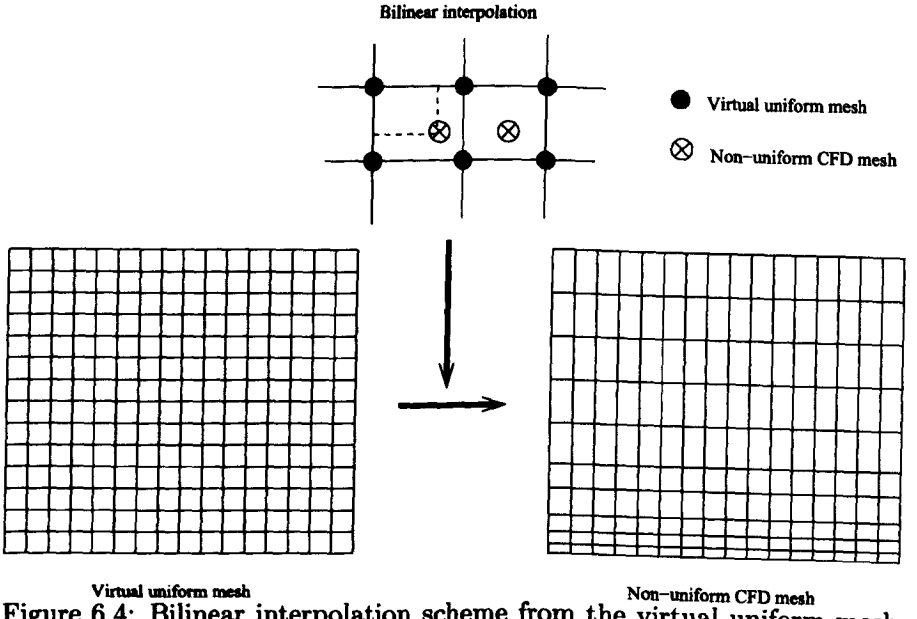

Figure 6.4: Bilinear interpolation scheme from the virtual uniform mesh on which the fluctuating velocities are generated onto the non-uniform CFD mesh.

Figure 6.5: Summary of the method for generating turbulent inflow (details in Section 6.2).

6.3 Application of the method: the UDF

6.3.1 Structure of the UDF

Ansys-Fluent allows the user to access and modify variables via User Defined Functions (UDF), which is code written in C. The annotated code of the UDF can be found in Appendix C. With the UDF, it is possible to access the variables of the fluid solver at any point of its execution. Figure 6.6 shows how and at what point the UDF interacts with the fluid solver. On the left side of the diagram a flow chart of the fluid solver and the steps of method for generating the turbulent inflow are included. On the right side, the types of the macros used in the UDF are shown. Macros work as functions, but each type of macro is called at a specific time in the solution of the fluid equations. For example, a "Define On Demand" macro is called at the initialisation stage; a "Define Adjust" macro is called before each iteration (in this case, this only needs to be called before the first iteration of each time step, this requires a few lines of code to detect which iteration the solver is handling); and, the "Define Profile" macro is called before each iteration, but after the 'Define Adjust'. The figure details the steps of the method for generating the turbulent inflow, as previously described, as well as the operation of the fluid solver.

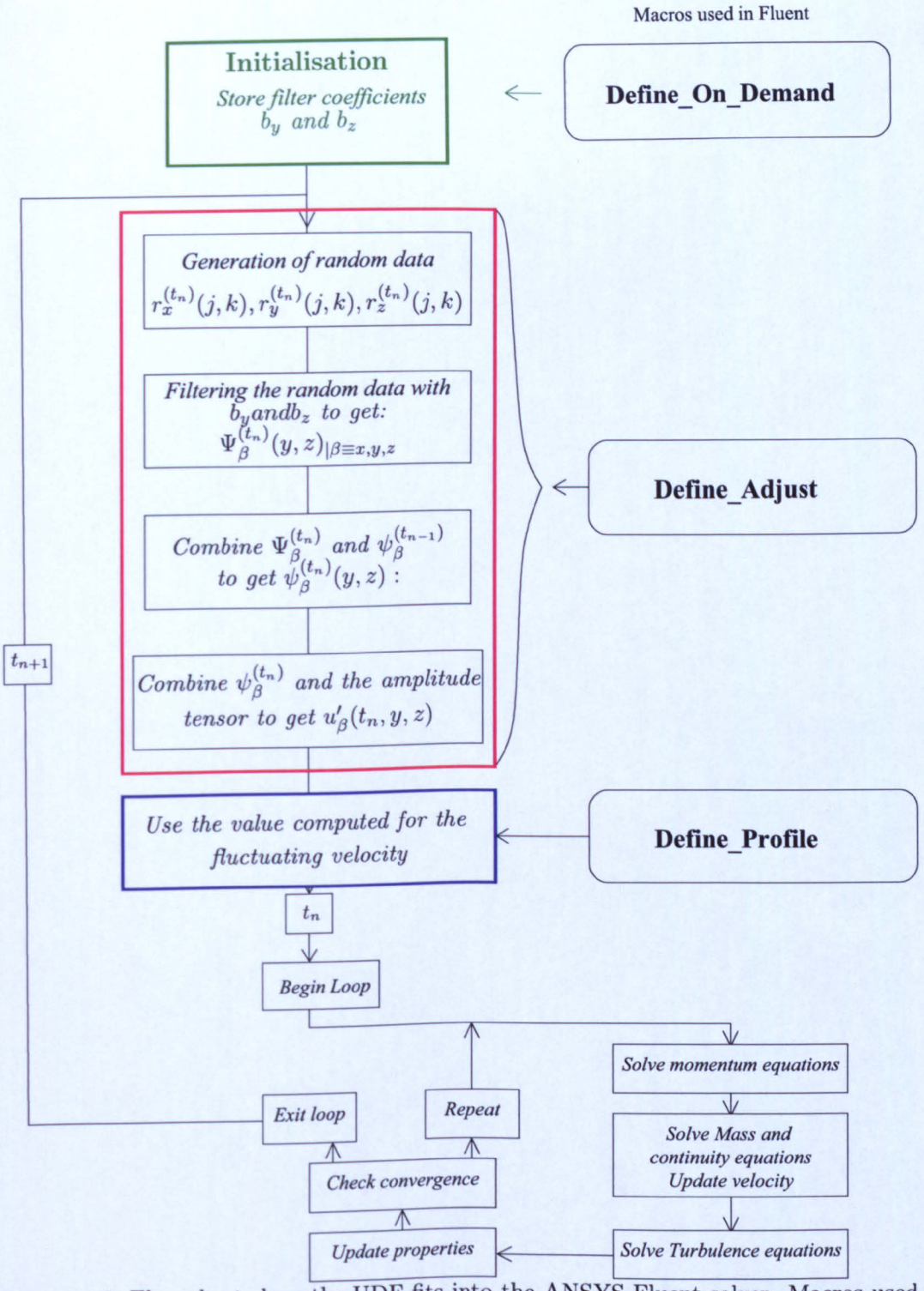

Figure 6.6: Flow chart: how the UDF fits into the ANSYS-Fluent solver. Macros used in the UDF are detailed in the right column.

6.3.2 Generation of the random data

As previously discussed in Section 6.2, step 2 of the method requires a set of random data whose dimension is $(2N_y + M_y) \times (2N_z + M_z)$ to be generated at each time step. In other words, the number of random numbers to be produced is high (typically > 8000), and this sequence of random numbers must produced at **each** time step. The method used by Xie and Castro (2008) to produce random numbers is the one embedded into C, the *rand* routine. `rand()` needs to be initialised by an arbitrary seed I_0. Each seed will give a different sequence of random numbers, but importantly, the same seed will produce the same sequence of random numbers. This routine is *linear congruential*, which means that the sequence of random numbers $I_1, I_2...$ follows the following relationship:

$$I_{j+1} = aI_j + c \quad [m] \tag{6.3.1}$$

where $m > 0$ is the modulus, $0 < a < m$ and $0 < c < m$ are the multiplier and the increment respectively, the initial increment (seed) I_0 respects $0 < I_0 < m$. Equation (6.3.1) can also be written as $I_{j+1} = (I_j \times a + c) - q \times m$ where q is the largest integer that satisfies this equation.

By definition, it is evident that the period of this random number generator cannot be larger than m. The greatest advantage of *linear congruential* generators is their speed, but their major drawback is that there is a degree of sequential correlation on successive calls, which means that they cannot be used where high quality randomness is critical. Another drawback is that their low-order (least significant) bits are much less random than their high-order bits. Details on these shortcomings of the routine `rand()` can be found in Press et al. (1992). Due to these shortcomings, which are particularly serious if a significant amount of random numbers is needed, the `rand()` routine is not used here. Instead, a method derived from L'Ecuyer (1988) is used; this combines two different sequences with different periods in order to obtain a new sequence whose period is the least common multiple of the two periods. The two sequences are added, modulo the modulus of either of them (Press et al., 1992). The method of producing these sets is

taken from Press et al. (1992) and passes all major statistical tests for randomness. The period of the random number generator is significantly long ($> 2 \times 10^{18}$). It returns random numbers that are in the specified range, 0.0 to 1.0. A second function is added to this random number generator to produce a set of random numbers whose mean is 0 and variance is 1.0. This second function is detailed in Appendix C from line 122.

6.3.3 The Reynolds stress tensor distribution

The Reynolds stresses are specified as previously discussed in Chapter 2 according to the specifications published by ESDU 85020 (1985, revised in 1990).

6.4 Verification: the empty fetch test case

6.4.1 Introduction

This section is concerned with the verification of the method for generating synthetic turbulent inflow, and more precisely the verification of the statistical characteristics of the synthetic inflow as well as how this inflow progresses through the domain. As a matter of fact, it is as important to know and control the characteristics of the field of fluctuating velocities produced at the inlet than to know how the fluctuations behave as they progress through the domain.

In short, this section aims to assess the following:

The main statistical characteristics of the field of fluctuating velocity at the inlet, namely the integral length scales in the three main directions, and the energy spectrum (reflect the size of the wind gusts produced).

The way the integral length scales of the synthetic turbulent inflow relate to the filter sizes input at stage 1 of the method.

The loss of energy and for what frequencies (or eddy sizes) it occurs as the flow progresses through the empty domain.

In order to achieve this verification, an empty fetch test case was used. The method for generating synthetic fluctuating velocities was used to produce various turbulent inflows, the varying parameters being the filter sizes, N_x ,N_y, N_z. The resulting inflows were compared with each other, as well as their behaviour across the empty fetch. The inflows were characterized in terms of longitudinal, vertical and horizontal auto-correlations, energy spectrum and co-spectrum. This way, the efficiency of the filtering operations at stages 5 and 8 could be assessed. Statistical characteristics were recorded across the empty fetch in order to quantify the loss of energy of the turbulent inflow across the empty fetch.

As mentioned before, the wind gusts – features of the turbulence in the wind – can be characterized by the Integral Length scales, see Section 2.1.5. These length scales are defined in the longitudinal, lateral and vertical directions for the three components of the velocity. The longitudinal length scales are derived from the temporal autocorrelation computed from the time series. The lateral and vertical length scales are obtained by performing a "spatial" autocorrelation. As far as the empty fetch test case is concerned, the same length scale is set in vertical and lateral directions since the filtering process in these two directions is done at the same stage. In the future, for a more realistic use of the turbulent inflow generator, a different length scale will be specified for each direction.

The definitions and details of the temporal and spatial autocorrelations can be found in Appendix D.

6.4.2 Empty fetch test case: set-up

Domain dimensions

The dimensions of the empty fetch are taken from the open channel test case presented by Xie and Castro (2008).

The domain used for the empty fetch case is shown schematically in Figure 6.7, the dimensions were chosen so they would match those chosen by Xie and Castro (2008):

$4\pi d$ in the X direction (streamwise), $2d$ in the Y-direction (vertical) and πd in the Z-direction (spanwise) where $d = 0.1$ m. The final dimensions of the domain are then: 1.26 m in the X direction (streamwise), 0.2 m in the Y-direction (height) and 0.314 m in the Z-direction (spanwise).

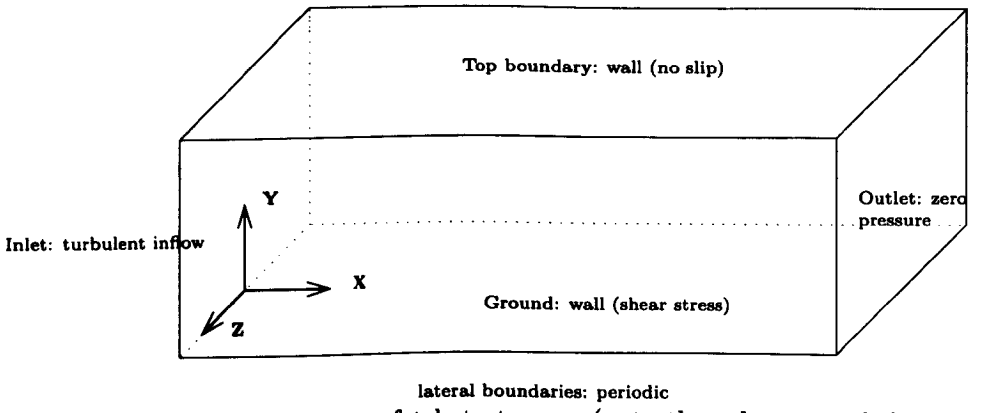

Figure 6.7: Domain for the empty fetch test case, (note that the vertical direction is indicated by the Y-axis)

Boundary Conditions

A zero pressure condition is specified at the outlet. The lateral boundaries are specified as periodic, and the ground and the top boundaries are defined as walls (Xie and Castro, 2008).

The set of fluctuating components of the velocity, produced as explained in Section 6.2 and superimposed on a log-law velocity profile , are specified at the inlet, as in equations (6.2.17) - (6.2.19).

A no slip wall condition is specified at the top (all velocities are equal to zeros, and so are the velocity gradients). Even if the log law velocity profile does not agree with the top boundary condition at the inlet, it gets adjusted to the top boundary condition as the wind flows through the domain.

As for the friction velocity, the Reynolds number used by Xie and Castro (2008) being $Re = 3300$, it follows that $U_{\text{mean}} = 0.495$ m/s, and $u_* = 0.027$ m/s from $Re_f = 180$ (Reynolds number computed with the friction velocity).

Table 6.1: Summary of the set up for the empty fetch test case

Dimensions in X, Y, Z	1.26 m × 0.20 m × 0.314 m
Mesh resolution $\Delta x, \Delta y, \Delta z$	0.021 m , 0.0026 m , 0.0052 m
Number of cells in X, Y, Z	60, 78, 60
u_*, U_{ref}, y_{ref}	0.027 m/s, 0.5 m/s, 0.1 m
Von Karman constant κ	0.42
Aerodynamic roughness length y_0	0.01 m
Time step size Δt	0.005 s

u_* is consistent with the definition presented by ESDU 85020 (1985, revised in 1990) in which

$$u_* = \frac{U_{z_{\text{ref}}}}{2.5ln(z_{\text{ref}}/y_0)}$$

Mesh

As discussed in section 3.4, the mesh for the Large Eddy Simulation needs to be fairly uniform and very fine. The following requirements for the cell sizes were applied: $\Delta x^+ = 38$, $2 < \Delta y^+ < 13$, $\Delta z^+ = 11$ where, for example, $\Delta x^+ = \Delta x \times \frac{u_*}{\nu}$, (Xie and Castro, 2008). Y being the vertical direction, the cell size in this direction is the finest in order to capture the boundary layer.

Since $d = 0.1$ m, the following minimum mesh resolution is achieved for the non-uniform mesh used: $\Delta x = 0.021$ m, 0.0011 m $< \Delta y < 0.0072$ m, $\Delta z = 0.0052$ m. The lower bounds of these cell sizes are used to build the virtual uniform mesh on which the turbulent inflow is generated. A linear interpolation scheme is used to interpolate the fluctuating velocities from the uniform virtual mesh onto the non-uniform mesh of the inlet plane.

A summary of the important points of the set up for the empty fetch test case is shown in Table 6.1.

6.5 Verification: the empty fetch test case, the results

The same set-up presented in the previous section is used for difference test cases, where the varying parameters are the filter sizes, N_x, N_y, N_z. Monitor points are places at different heights and at different location across the empty fetch. It is ensured that the fluctuating inflow reaches the end of the domain before recording the velocity at the monitor points as well as at the inlet. $y+$ values were checked and did not exceed 1.1, which was considered an acceptable level to model the near wall flow.

6.5.1 Characteristics of the generated synthetic turbulent inlet

Time series of the velocity at the inlet

Figure 6.8 shows a sample of the time history of the velocity magnitude at one particular point on the inlet plane. It can be noted that there is no apparent periodicity on the record.

Figure 6.9 shows the contours of the velocity on the inlet plane, and on a transverse plane across the empty fetch at two consecutive time steps. Some qualitative conclusions can be drawn from the observation of the contour plots. The wind gusts appear to be larger near the ground, this is due to the shape of the Reynolds stress distribution. Moreover, it can be seen that the turbulent structures are propagated in the along-wind direction.

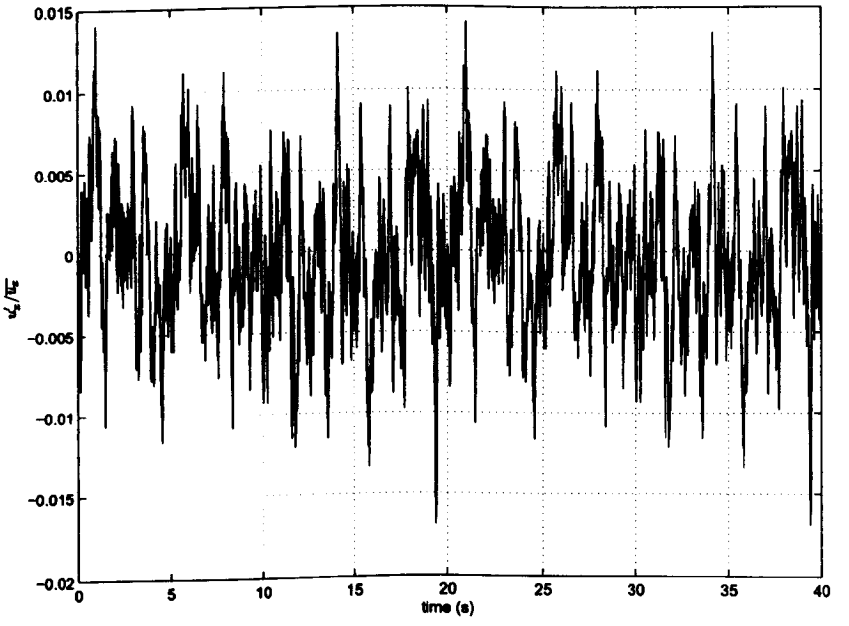

Figure 6.8: Empty fetch test case: Sample of time history of the velocity magnitude at a point at 0.06d height on the inlet plane

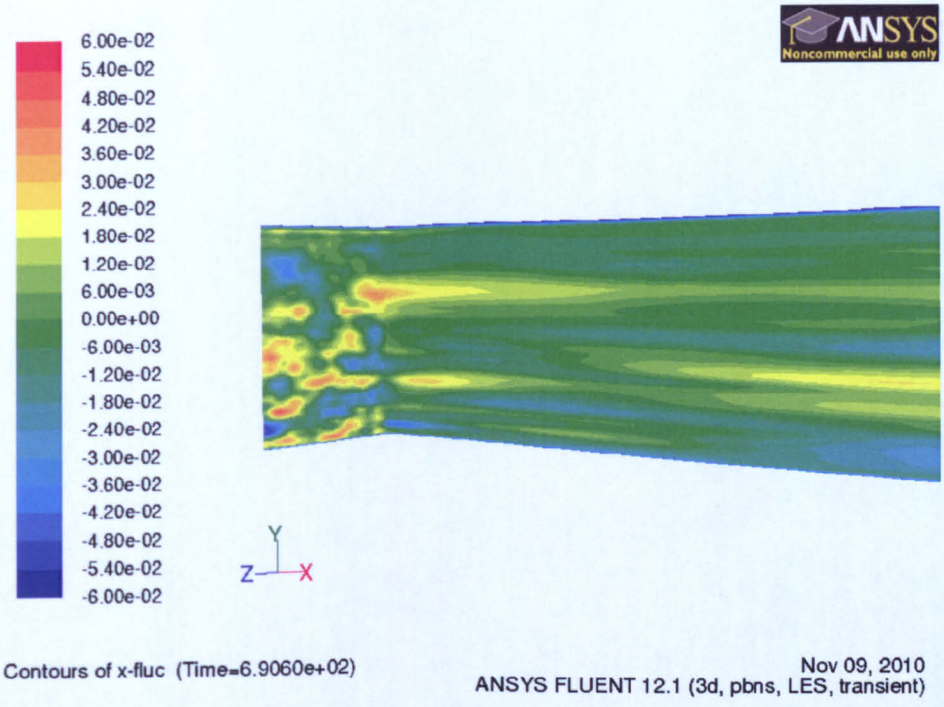

(a) at t

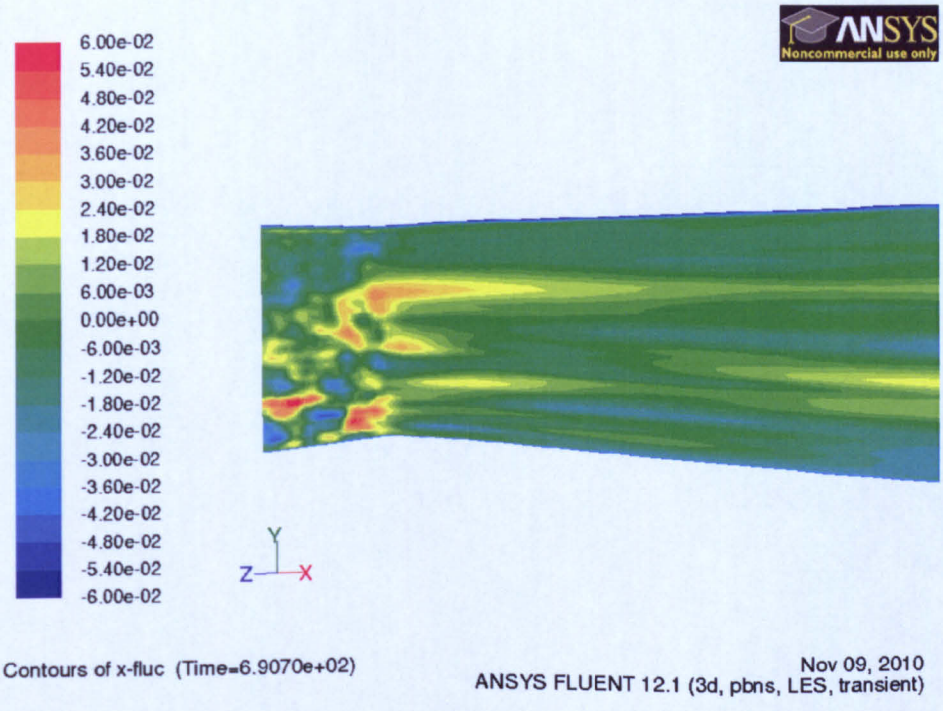

(b) at $t + \Delta t$

Figure 6.9: Empty fetch test case: Snapshots of the contours of the X-component of the velocity fluctuations on the inlet plane and on the middle transversal plane, at two consecutive time steps.

Length scales and autocorrelation coefficients of the turbulent inflow

In order to determine the integral length scales of the synthetically generated wind, the autocorrelation coefficients need to be computed from the time series of the velocity components on the inlet. [1]

Temporal autocorrelations [2]

Firstly, the temporal autocorrelation coefficients are computed; details on this procedure can be found in Appendix D.

Once the temporal autocorrelation coefficients have been computed, a decaying exponential, $e^{-\frac{-\pi\Delta t}{2T}}$, is fitted to the autocorrelation plots in order to determine the integral length scales. Figure 6.10 presents some plots of the normalised temporal autocorrelation coefficients, fitted to the decaying exponential. The comprehensive list of the resulting length scales is presented in Table 6.2.

The filter sizes can be plotted against the resulting length scales. It is possible to deduce a linear relationship between the specified filter sizes and the resulting time scales.

It was found that the relationship expressed in equation (6.2.4) does not appear to be true, namely if a filter size is used in the equation to find the resulting length scale, this length scale is different from the one obtained in the synthetic turbulent inflow. The difference between the specified filter size and the resulting length scale can be explained by the nature of the filtering operation. The filter is a first order operation, i.e. it only calls the data at the previous time step to combine them with a set of data at the current time step to produce the filtered data at the current time step. While this saves time in the computation by saving memory space, and make this operation of filtering in the longitudinal direction simpler, it is also likely to make it less accurate.

The linear relationship between N_x, used in equation (6.2.13) and the computed time

[1] the term length scale refer to the spatially averaged length scales, cf. Appendix D

[2] the following paragraph is concerned with the longitudinal length scale in the incoming flow which is equivalent to the time scale, therefore time scale and longitudinal length scale will be used interchangeably.

scale T_u (synthetic) from the synthetic generator, equation (6.5.1) will then be used to specify the filter size knowing the required longitudinal length scales. In this set-up, only one longitudinal length scale was specified, but in later work, three longitudinal length scales will be specified, one for each velocity component. Instead of having the same factor $\exp \frac{-\pi \Delta t}{2T}$ in equation (6.2.13) for u_x u_y and u_z, there will be three different factors, one for each component.

$$T_{(\text{synthetic})} = a_1 N_x + a_2 \tag{6.5.1}$$

where T refers to the time scale T used in equation (6.2.13), and $\overline{U}$ refers to the mean velocity. The constants a_1 and a_2 are equal to 0.0003 and 0.0445 respectively. The fact that the line does not cross the origin shows that there is a minimal length scale that the generator of synthetic turbulent inflow can achieve.

To sum up, even though there is a difference between the "expected" time scale and the resulting longitudinal length scale, it is possible to define a linear relationship between the two and this relationship is used in later work to set up the filter size depending on what length scale is required.

Spatial correlations [3] To compute the spatial correlation, namely the autocorrelation in the Y and Z directions, a Matlab program is written (details on the procedure can be found in Appendix D). In short, at a given time step, the correlation coefficients are computed for each distance interval r_k. The correlation coefficients are then averaged over time as described in section D.2. Figure 6.9 show a few examples of autocorrelation coefficients plotted against the distance intervals. A decaying exponential is then fitted to these plots in order to determine the associated integral length scales. The results are presented in Table 6.3.

From these results, it can be seen that there is an excellent agreement between the expected length scale and the resulting length scale computed from the spatial correlation

[3] refers to time-averaged spatial correlations, cf. D

Table 6.2: Empty fetch test case: Time scales, comparison of the input filter size and its equivalent time scale (expected) with the obtained time scales (synthetic) after filtering (see method in section 6.2). Expected time scales are computed from equation (6.2.4). Time scales (synthetic) are computed from the temporal autocorrelation coefficients.

N_X	31	31	47	110	141	189
Synthetic T_{u_x} (s)	0.0560	0.0560	0.0680	0.0900	0.1000	0.114
Synthetic T_{u_y} (s)	0.0560	0.0480	0.0540	0.0780	0.0860	0.094
Synthetic T_{u_z} (s)	0.0580	0.0520	0.0640	0.0860	0.0940	0.114
Synthetic $\overline{T}$ (s)	0.0560	0.0520	0.0620	0.0840	0.0940	0.108

Table 6.3: Empty fetch test case: Spatial Length scales, comparison of the input filter sizes and their equivalent length scales (expected) with the obtained length scales after filtering. Expected length scales are computed from equation (6.2.2). Length scales (synthetic) are computed from the spatial autocorrelation coefficients. Relative errors refers to relative errors between expected and synthetic L_u^r.

Input: N_y, N_z	4	8	8	12	16
Expected averaged L_u^r	0.0078	0.0156	0.0156	0.0234	0.0312
Synthetic $L_{u_x}^r$ (m)	0.0080	0.0162	0.0162	0.0240	0.0320
Synthetic $L_{u_y}^r$ (m)	0.0078	0.0158	0.0158	0.0240	0.0320
Synthetic $L_{u_z}^r$ (m)	0.0080	0.0164	0.0166	0.0240	0.0340
Synthetic $\overline{L_u^r}$(m)	0.0080	0.0162	0.0166	0.0240	0.0340
Relative errors	2%	4%	6%	3%	9%

plots, with a maximum relative error of 9%. This 9% error can be explained by the fact that for this larger filter size, 16, the total length of the filter represents about 40% of the height of the inlet plane (Y), and about 50% of the width (Z), which leads to large structures, hence fewer wind gusts generated.

Length scales in the Y direction only were also computed, Table 6.4. In this context, only the size of the gusts in the vertical direction is examined. The largest relative error is exhibited for the smallest filter size. The first possible reason for this large relative error would be numerical errors from the the linear interpolation step (see step 11 of the method) from the uniform mesh onto the non-uniform mesh. Another possible reason is that computing the length scales in both directions, Table 6.3 introduces an averaging step that is not present when computing length scale only in the vertical direction.

Table 6.4: Empty fetch test case: Spatial Length scales in the Y direction,: comparison of the input filter sizes and their equivalent length scales (expected) with the obtained length scales after filtering (see method in section 6.2). Expected length scales are computed from equation (6.2.2). Length scales (synthetic) are computed from the vertical (Y) autocorrelation coefficients. Relative errors refers to relative errors between expected and synthetic L_u^y.

Input N_y	4	8	12	16
Expected L_u^y	0.0052	0.0104	0.0156	0.0208
Synthetic $L_{u_x}^y$ (m)	0.0036	0.0092	0.0140	0.0220
Synthetic $L_{u_y}^y$ (m)	0.0036	0.0090	0.0170	0.0200
Synthetic $L_{u_z}^y$ (m)	0.0036	0.0096	0.0146	0.0220
Synthetic $\overline{L_u^r}$ (m)	0.0036	0.0092	0.0152	0.0214
Relative errors	30%	10%	3%	3%

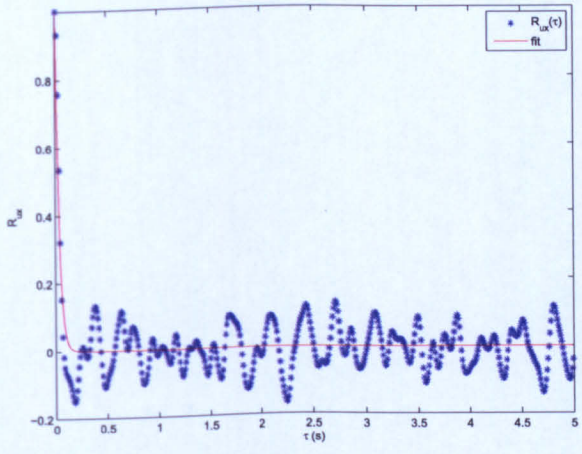

(a) $R_{u_x}(\tau)$, $N_x = 10$

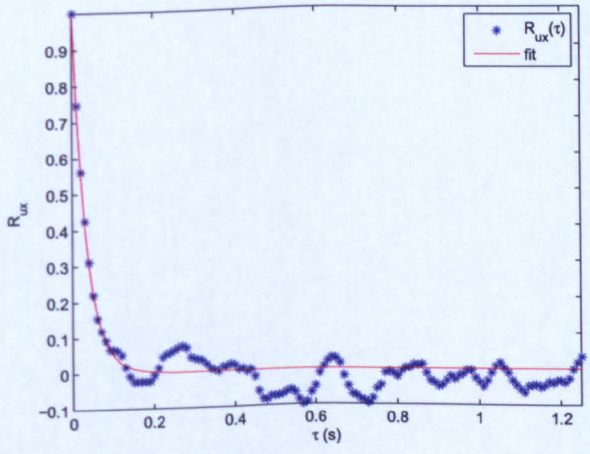

(b) $R_{u_y}(\tau)$, $N_x = 15$

Figure 6.10: Empty fetch test case: Autocorrelation plots of the longitudinal component of the velocity, and decaying exponential fit ($e^{-\frac{\tau\pi\Delta t}{2T}}$) for $N_x = 10$, 15, 35, 45, 60.

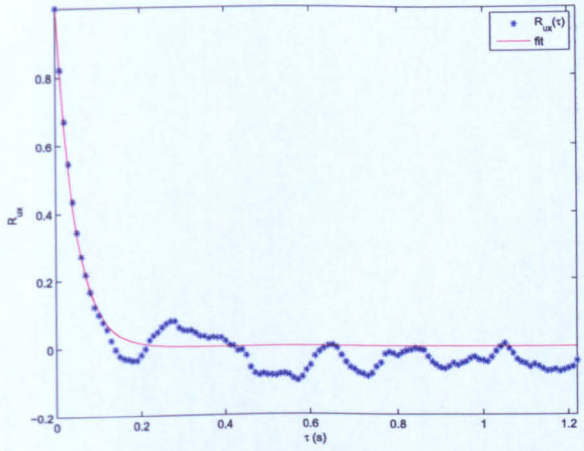

(c) $R_{u_x}(\tau)$, $N_x = 35$

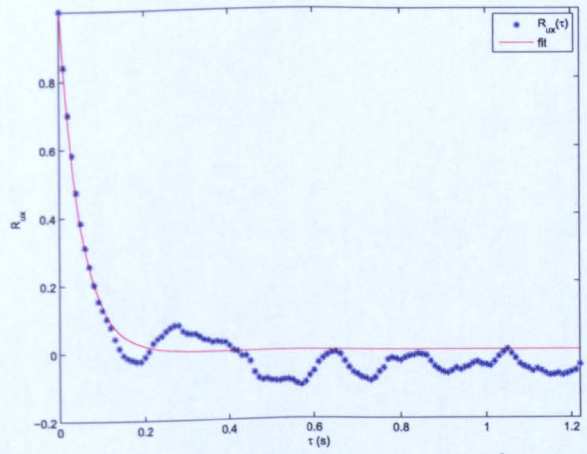

(d) $R_U(\tau)$, $N_x = 45$

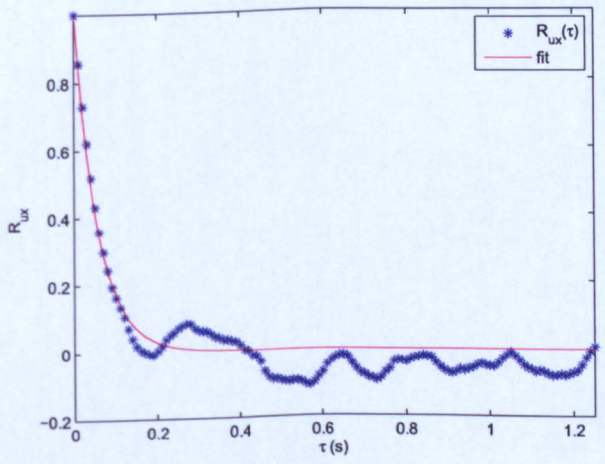

(e) $R_U(\tau)$, $N_x = 60$

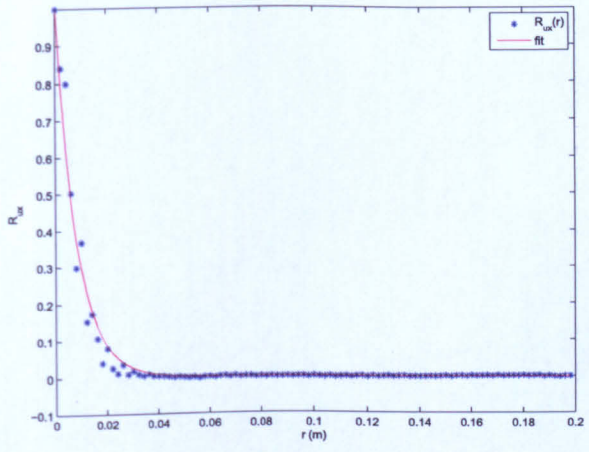

(f) $R_{u_x}(r)$, $N_y = N_z = 8$

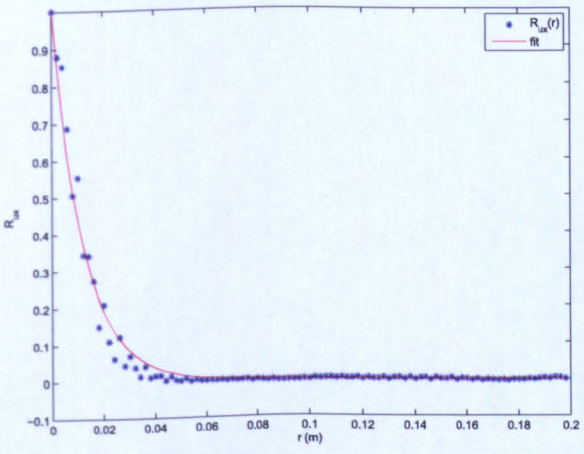

(g) $R_{u_x}(r)$, $N_y = N_z = 12$

Figure 6.9: Empty fetch test case: Spatial autocorrelation of the longitudinal component of the velocity, and exponential fit ($e^{-r/L}$), for $N_{y,z} = 8$, 12, 16.

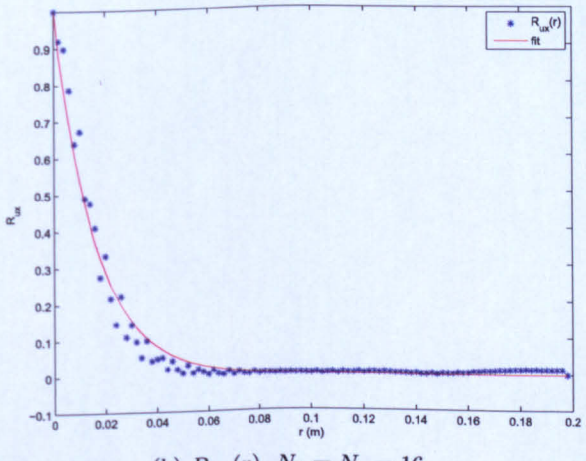

(h) $R_{u_x}(r)$, $N_y = N_z = 16$

Energy spectrum at the inlet

Figure 6.9 shows the longitudinal power spectrum for a given case. It can be seen that the expected $-5/3$ slope corresponding to the energy cascade at the higher frequencies is obtained.

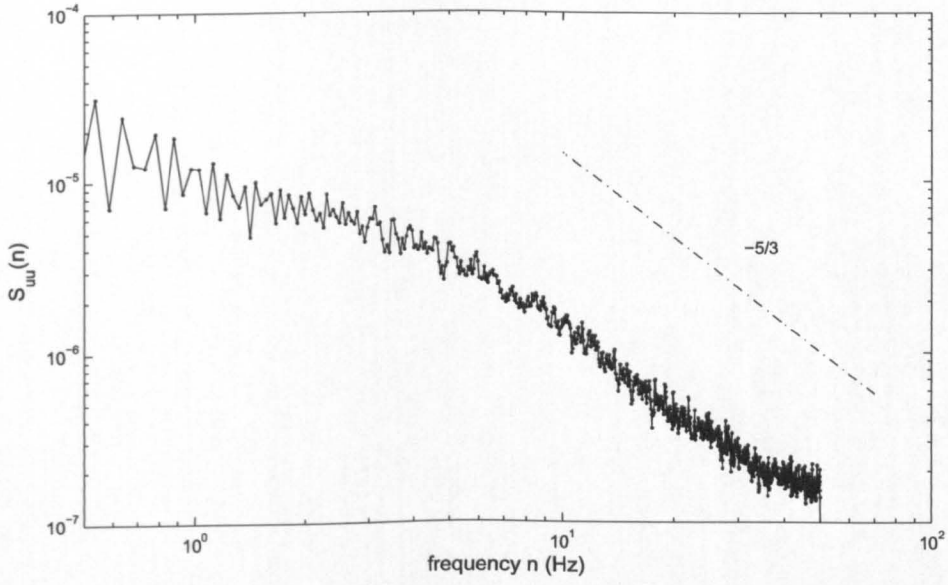

Figure 6.9: Empty fetch test case: Power spectrum of the longitudinal component of the velocity, at the inlet.

Cross spectra at the inlet

A cross-spectrum, or two points spectrum is computed on four pairs of points, chosen at the same height, along a horizontal line, Figure 6.10. The frequency is non-dimensionalised with the distance between each point of the pair of points, which gives a reduced frequency for the X-axis. A decaying exponential, e^{-f}, is then fitted to the cross spectra where:

$$f = \frac{n[C_{1z}^2(z_1 - z_2)]^{1/2}}{U_{\text{ref}}} \tag{6.5.2}$$

where C_{1z} is a constant to be parametrized, and U_{ref} is the reference velocity, taken at midheight in that case. It can be seen that although there is a good agreement with the data at high reduced frequencies, a lot of the data are below the fitted curve at the low

frequencies. It was noted by Dyrbye and Hansen (1997) that equation (6.5.2) contains some inconsistencies, one of them being that the normalised co-spectrum, equation (6.5.2), approaches unity at very small reduced frequencies, which is not true when the two points are separated by a distance of the same order of magnitude or even larger than the average size of gusts. In this zone, the wind structure is characterized by a lack of correlation even at low frequencies.

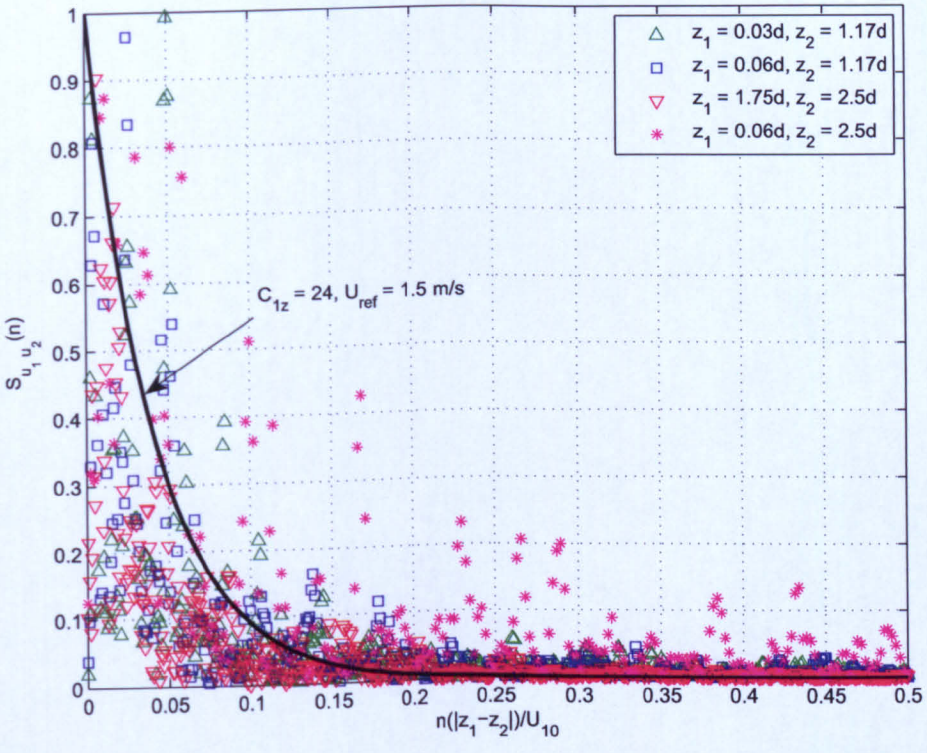

Figure 6.10: Empty fetch test case: Normalised two points cross-spectrum of the longitudinal component of the velocity at the inlet plane. Points are located on a horizontal line, at midheight. (In that test case, Y is the horizontal direction)

6.5.2 Behaviour of the turbulent inflow along the domain

Longitudinal, vertical and horizontal length scales

Figure 6.11 presents the auto-correlation (temporal) function computed in the centre of the domain section on the inlet, and at three points downstream, also located at the

centre of the domain section. The aim is to observe any decay in the correlation. It can be seen that the correlations are maintained along the X-axis, although they exhibit a slight decay which can be observed in Figure 6.11.

It is observed that along the empty fetch, the dominant length scale gets larger, which would tend to indicate that the high frequency turbulence is damped out. This is to be expected as there are no roughness elements in the domain to maintain turbulent structures. In ideal ABL modelling, roughness would be added to the ground in the form of buildings, or a roughness height, and the building would be placed near the inlet. This is the interesting aspect of this method: to provide a turbulent inflow quickly and accurately, without having to let the flow and the turbulent structures develop over a long period of time and over a long fetch containing roughness elements. The following is to be considered when modelling the ABL: accounting for the decay in the high frequencies, a smaller length scale can be specified at the inlet, so that the apparent length scale seen by the building is what is required.

In order to investigate this further, the length scales resulting from the correlation plots at different locations down the empty fetch are plotted against the longitudinal distance at three different heights, Figure 6.12. The time series on which these length scales are based contain more than 2000 times the averaged time scale. This figure shows how the length scales vary across the domain. From this plot, it is clear that the length scales get larger for $x < 1d$, which means that there is a loss in the high frequencies. However after $x = 1d$, the length scales do not seem to carry on increasing, which would suggest that there is an initial loss after the inlet, but that subsequently the average size of the eddies seems to be maintained. The length scales increase by about 20% between the inlet and $x = 1d$, which is not negligible. However, considering that there is not significant further loss for $x \geqslant 1d$,provided that the initial loss is accounted for in later work, the longitudinal length scale can still be controlled.

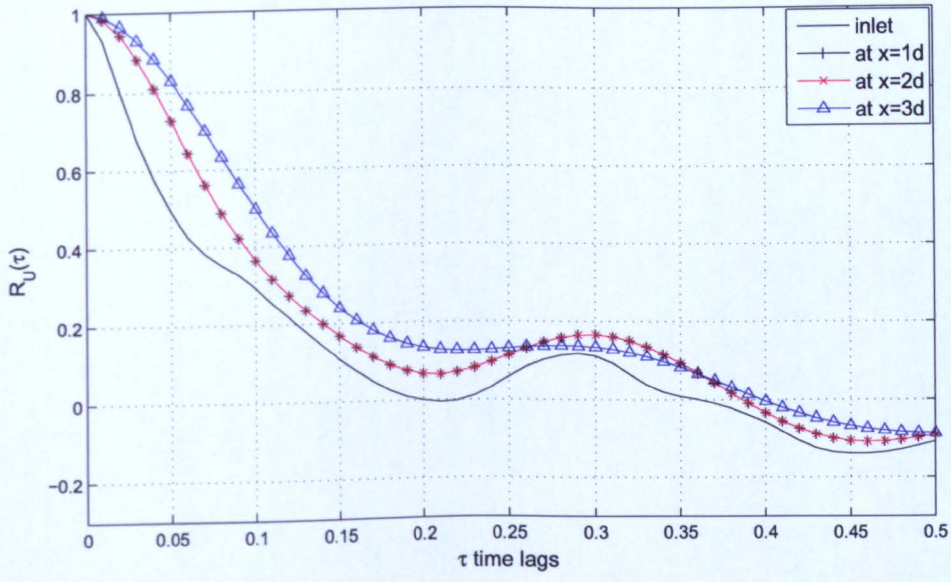

Figure 6.11: Empty fetch test case: Auto-correlation (temporal) in the middle of the inlet plane, and at $x = 1d, 2d, 3d$ downstream the inlet

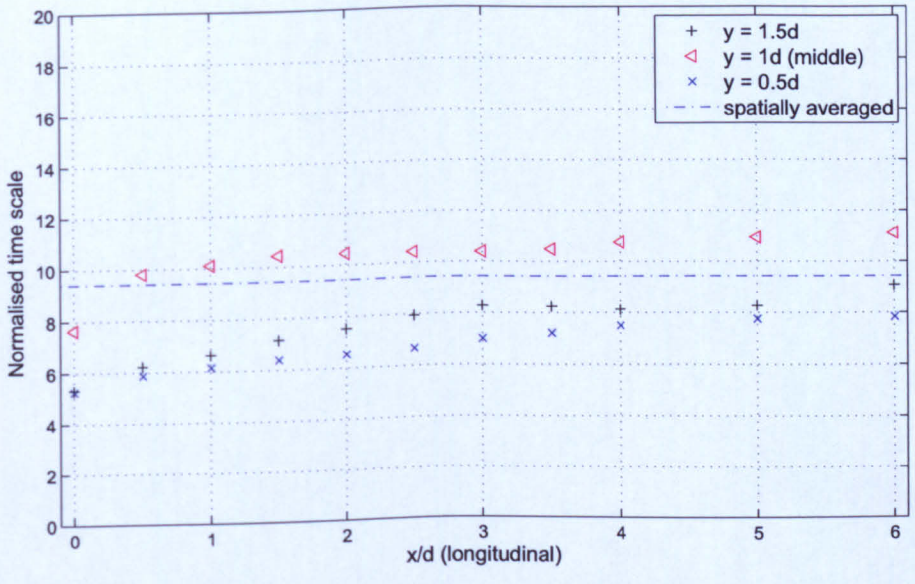

Figure 6.12: Empty fetch test case: Length scales at three height locations, across the empty fetch. Time scales are non dimensionalised with the time step size. "Spatially averaged" refers to the time scale averaged over the inlet plane.

Longitudinal spectrum of the velocity at various locations across the empty fetch

Figure 6.13 shows the longitudinal spectrum of the velocity at 5 locations across the empty domain. It can be seen from the figure that there is a loss of energy between the inlet and $x = 1d$, at around 10 Hz. However, for $x \geqslant 1d$, the spectra are very close to each other which would suggest that while there is an initial loss of energy in the high frequencies (also seen in the increase of the length scale between the inlet and $x >= 1d$ in Figure 6.12, the turbulent structures seem to be maintained across the fetch for $x \geqslant 1d$.

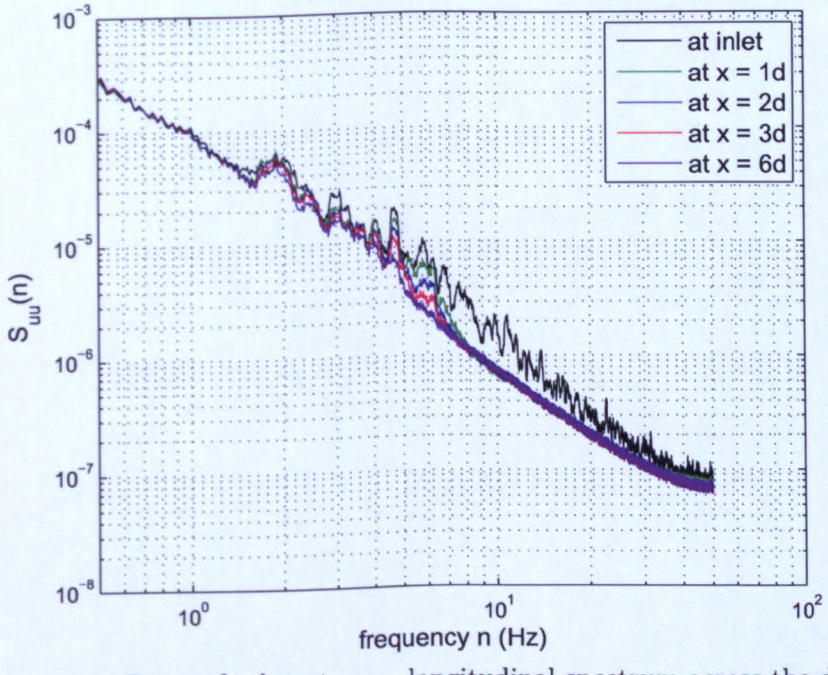

Figure 6.13: Empty fetch test case: longitudinal spectrum across the domain

Cross-covariance results

Figure 6.14 shows two points cross covariance between pairs of points of equal distance, d along the domain, Figure 6.14(d) details the point locations. The amplitude of the oscillations of the cross covariance function are larger for the points located in the lower quarter, near the ground than at midheight or in the higher quarter, and they are

larger at midheight than in the higher quarter: the shear stress applied at the bottom helps maintaining the turbulent eddies, while the no slip boundary condition at the top (zero velocity at the wall) contributes to a rapid decay of the turbulence near the top boundary. It can also be observed that the amplitude of the cross correlation at small time scales is smaller for the points located near the top than near the ground or at midheight; in other words, the cross covariance function crosses the X axis for a larger τ at midheight than in the lower quarter. This is due to the presence of the shear stress at the bottom wall, which is not present at the top boundary. These results show that a turbulent inflow put into a domain that does not contain roughness elements or roughness characteristics of some sort will not be maintained. Even though the runs can be sped up using a synthetic turbulent inflow via a smaller upstream fetch, it must be combined with roughness elements or a rough wall in order to maintain the eddies formed by the synthetic turbulent inflow.

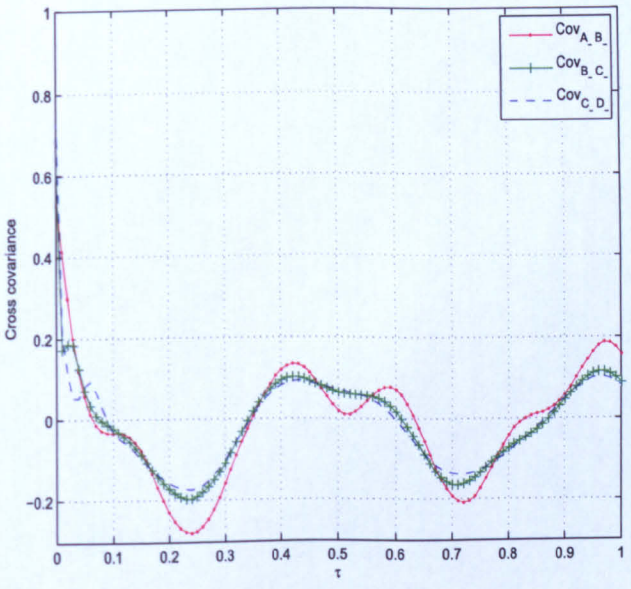

(a) Cross covariance in the lower quarter of the domain

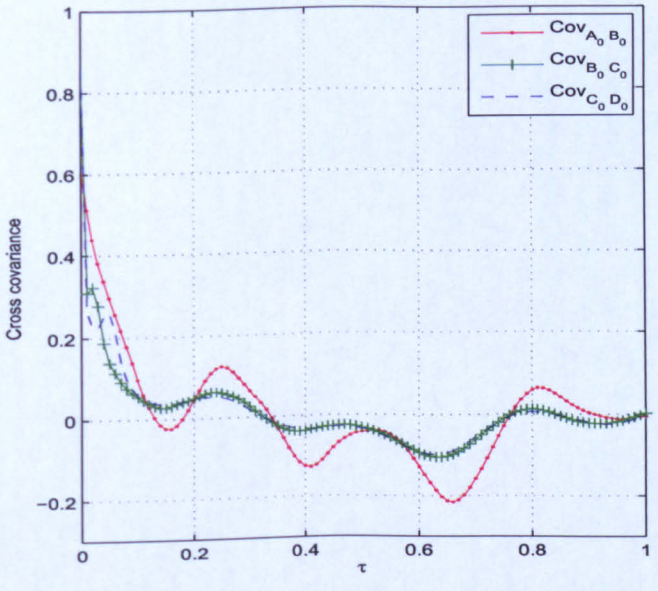

(b) Cross covariance at mid-height

Figure 6.14: Empty fetch test case: Cross covariance of the longitudinal component of the velocity at various heights along the empty fetch, the cross covariance is computed for pairs of points, equally distanced by d.

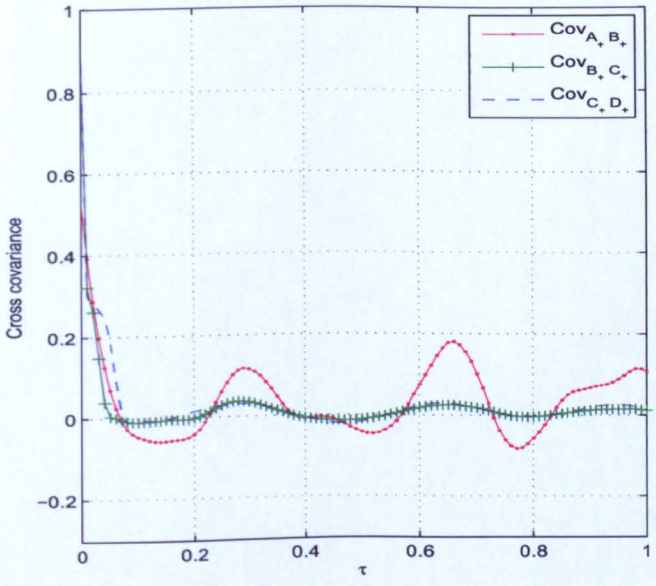

(c) Cross covariance in the higher quarter of the domain

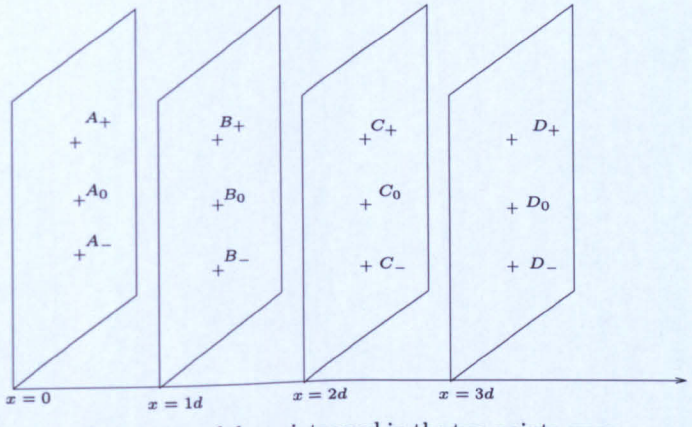

(d) Location of the points used in the two points cross covariance

6.6 Summary and conclusions

This section aimed to establish a means of generating artificial turbulence for LES. In order to achieve this, a method originally proposed by Xie and Castro (2008) to generate synthetic turbulent inflow for LES was investigated and optimized.

Initially, it was found that the method developed by Xie and Castro presented a major instability due to the choice of weighting factors in the filtering operation (ensuring the

longitudinal correlation); this was corrected accordingly.

The empty fetch test cases helped to determine both the main statistical properties of the synthetic turbulent inflow, as well as the way in which these properties are modified as the flow goes across the empty fetch.

As for the statistical properties of the synthetic turbulent inflow at the inlet, it was found that there is a clear understanding of the 2D filter, which ensures the spatial correlation. The expected length scales in the vertical and horizontal directions from the filter sizes were in very good agreement with the resulting length scales. On the contrary there was not such a good control over the longitudinal length scales: a serious discrepancy was found between the expected longitudinal length scales (from the specified filter size) and the resulting longitudinal length scale. It has been suggested that the nature of the filtering operation in the longitudinal direction may have contributed to the observed differences. However, since a linear relationship could be established between the filter size and the resulting length scale, a control over the resulting longitudinal length scale was ultimately achieved.

The synthetic turbulent inflow appears to loose some energy in the high frequencies, leading to an increase in the average length scale. However, it was shown that this loss of energy was confined to near the inlet, and after this initial loss, the flow maintained its statistical characteristics.

In conclusion, this section presents a method for generating synthetic turbulence inflow for LES and demonstrates the possibility of controlling the main statistical properties of the turbulent field, at the inlet but also further down the domain. It is therefore possible to use this method in order to generate an accurate ABL; this will be demonstrated in the following chapter.

Chapter 7

Combination of turbulent inflow for LES and FSI method

7.1 Introduction

The main objective of the present work was to assess the validity of commercial CFD codes for modelling the wind flow around a tall building, including the consideration of the coupled dynamic response of the building to turbulent wind loading. In order to achieve this, two objectives were identified: the first was to develop a numerical tool to account for the dynamic response of the building to wind loading, the second to identify and develop a suitable method for generating turbulent inflow for unsteady LES simulations. Chapter 5 addressed the former by presenting a method for modelling fluid-structure interactions and showed the successful coupling of the fluid and the structure, which was allowed to move in the transversal direction in response to vortex shedding in the wake. The second objective was addressed in Chapter 6, in which a method for generating fluctuating velocities was presented and modified from an original method by Xie and Castro (2008).

The present chapter shows how the combination of the tools developed in the last two chapters can be used to attempt to model buffeting, which is the response of the building

to turbulence in the oncoming wind flow. It must be noted that little work involving the numerical analysis of an aeroelastic building has been done and published so far whereas a fair amount of papers are concerned with the numerical analysis of rigid models. For example, Huang et al. (2007) studied the wind flow around a high-rise structure and the resulting aerodynamic coefficients. Very interesting results were presented, specifically those comparing RANS and LES. However, the structure was static and the turbulence in the ABL was modelled using the spectral synthesizer in the ANSYS-Fluent code, which allows for only one length scale to be specified for the three components of the velocity and the three main directions. The method used in the present work allows each of the nine length scales to be individually specified. Swaddiwudhipong and Khan (2002) presented a 2D study of wind flow around a tall aeroelastic building. The turbulent inflow was generated using weighted amplitude wave superposition, but there is no evidence of a different treatment for each of the velocity components. Further, the authors admitted the use of a simplified random number generator, with a single seed for all three components was likely to be the cause of the discrepancy between the expected and obtained energy spectrum. Since their study was 2D, the response mainly responded to vortex shedding. More recently, Braun and Awruch (2009) presented results of a study of an aeroelastic tall building, comparing the LES results to experimental studies of the CAARC building[1]. Braun and Awruch did not rely on an existing CFD code, but developed their own, based on LES, and combined it with their own structural solver. They presented extensive results of the building response for different wind speeds, but identified the need to use a truly turbulent inflow with meaningful fluctuating velocities.

In this chapter, the turbulent inflow and the FSI are combined in a LES simulation and the structure is allowed to bend in the two main directions. Results of the pressure distributions and the response of the building are presented, as well as velocity profiles upstream the building, and, for illustrative purposes only, contours of vorticity. Whenever it is possible, the results are compared to experimental results from the CAARC test case or ESDU.

[1]

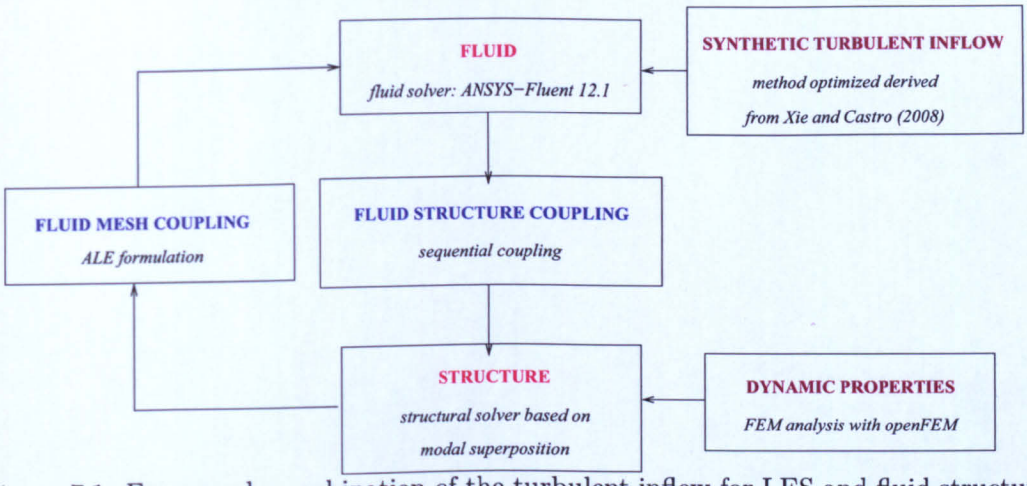

Figure 7.1: Framework, combination of the turbulent inflow for LES and fluid structure interactions tool.

7.2 Method

The methodology is presented schematically in Figure 7.1. The fluid is solved in ANSYS-Fluent, to which is attached the code for turbulent inflow with fluctuating velocities for LES. The dynamic properties of the structure, as well as the mode shapes are determined by a Finite Element analysis in openFEM. The fluid-structure coupling is done sequentially, and the fluid-mesh coupling is done in a ALE approach.

7.3 Set-up

The approach described previously for modelling the fluid-structure interactions is applied to a 180 m building, with plan dimensions of 20 m (along wind direction) by 10 m (across wind direction). The dimension of the domain follow the recommendations highlighted at the end of Chapter 4. A rigid zone is created around the building, as shown in Figure 7.2. The total number of cells is 15 million. The mesh is greatly refined near the walls, so that $y+ < 5$.

The flow is resolved in ANSYS-Fluent, using LES with the Smagorinsky subgrid scale model. At the inlet, the fluctuating components of the velocity are generated with the method described in Chapter 6. The integral length scales are taken from ESDU.

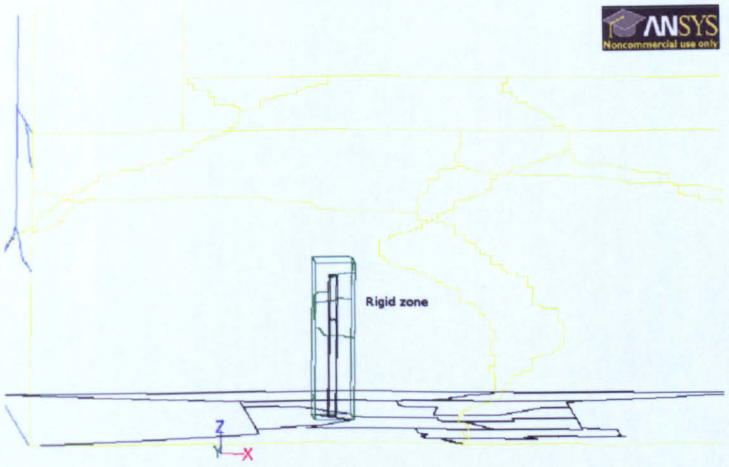

Figure 7.2: Domain for the LES run with turbulent inflow and fluid-structure interactions modelling. The black cantilever is the building, the green zone outlines the rigid zone, and the yellow lines shows the limits of the domain in the y direction. The irregular lined across the edges of the domain figure the partitions.

The maximum amplitude of the fluctuations are chosen to be about 10% of the mean velocity magnitude. The gust wind speed factor, computed from the time series, was $G = \frac{U_{gust}}{U_{hourly}} = 1.25$. The fluctuating components are superimposed on a log-law velocity profile, as per Equation 2.1.15. The 15 millions cell mesh is partitioned over 32 CPUs. Time integration of the flow governing equations is carried out with a time step of 1×10^{-4} s.

The building is allowed to move in the two main directions, along-wind and across-wind: The displacements in the X and Y directions at coordinate z, $g_x(z,t)$ and $g_y(z,t)$ respectively, are written as a product of the mode shape, ϕ_n , coordinate dependent only, and a time-dependent amplitude or modal amplitude $y_n(t)$, n being the mode considered:

$$g_x(z,t) = \sum_n \psi_n(z)\, x_n(t)$$

$$g_y(z,t) = \sum_n \phi_n(z)\, y_n(t)$$

The mode shapes are imported from the Finite Element analysis and the structural solver solves for $x_n(t)$ and $y_n(t)$. The time stepping for the time integration of the structure governing equations is the same as the one for the flow governing equations.

Damping in the two main directions is 1%.

The wind flow is first solved for a static building in a RANS simulation. This RANS solution is then used as an initial solution for LES. The building is released dynamically when the flow from the LES simulation has passed through the domain twice[2].

7.4 Results and Discussion

This section presents results of the LES simulation with the dynamic building.

Figure 7.3 shows the profile of the statistically averaged velocity at $x = 20L$ upstream the building. The velocity profile is plotted alongside the theoretical log-law and shows good agreement with the target log-law profile.

Figure 7.4 shows the rms velocities from the LES simulation compared with the distributions experimentally derived presented in ESDU 85020 (1985, revised in 1990). The vertical coordinate is normalised by the height of the building, h. It can be seen that there is a really good agreement between the CFD results and ESDU for the longitudinal rms velocity. The lateral rms velocity shows more discrepancy, especially near the ground, for $z < h/2$, where CFD under-predicts the rms velocity. The amplitude of the fluctuations of the lateral velocity seem to be damped near the ground. Since the ESDU distribution is used as a final filtering operation in the generation of the synthetic turbulent inflow, it may be suggested that the loss is due to the mesh not being fine enough near the ground. The CFD prediction becomes a lot better as z reaches the top of the building and the error remains below 10% for $z > h/2$ and $z < 2h$. The third graph of Figure 7.4 shows the rms vertical velocity. As for the lateral velocity, the CFD underpredicts the turbulence of the vertical velocity near the ground, but there is a very good agreement between CFD and ESDU for $h/2 < z < 2.5h$. For both the lateral and the vertical velocity, the CFD overpredicts the rms for $z > 2.5h$, but for $< z < 1.5h$, the rms velocities are relatively well reproduced, the relative errors are maintained below 10%. It could be argued that it is relatively more important to reproduce accurate rms

[2]The total duration of the simulation, static and dynamic stages included, was about 2 months long.

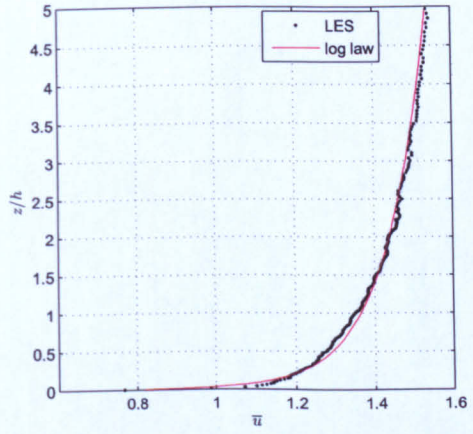

Figure 7.3: Velocity profile at $x = 20L$ upstream the building.

velocity for $z > 0.5h$ as the moment acting on the building is larger further away from its fixed end. Furthermore, the flow near the ground is very much subjected to large zones of recirculation, such as the horseshoe vortex, which are dominant compared with fluctuations in the wind.

Figure 7.5 shows the isosurface of vorticity for two levels of vorticity, coloured by instantaneous velocity. These figures show the large turbulent structures that are present in the wake of the building. Figure 7.6 shows the isosurface of a topological vortex indicator II. This indicator was suggested by Lim et al. (2009) and is defined as: $\mathrm{II} = -L_{ij}L_{ji}$ where $L_{ij} \equiv \frac{\partial u_i}{\partial x_j}$, and it is a measure of the regions of flow dominated by rotation rather than shear or stretching. The isosurface of this indicator clearly show the vertical tubular structures near the front edges of the building. Figure 7.7 shows contours of the instantaneous vorticity, on an horizontal plane near the ground. The figure shows the main rotational structures at this location, including the horse shoe vortex at the front of the building.

To summarize on these results, the reproduction of the ABL is considered to be acceptable, with a rather accurate reproduction of the turbulence levels along most of the height of the building. The qualitative assessment of the wind flow around the building showed that the main features are reproduced.

Figure 7.8 shows the distribution of the coefficient of pressure C_p at two heights $z = h/3$

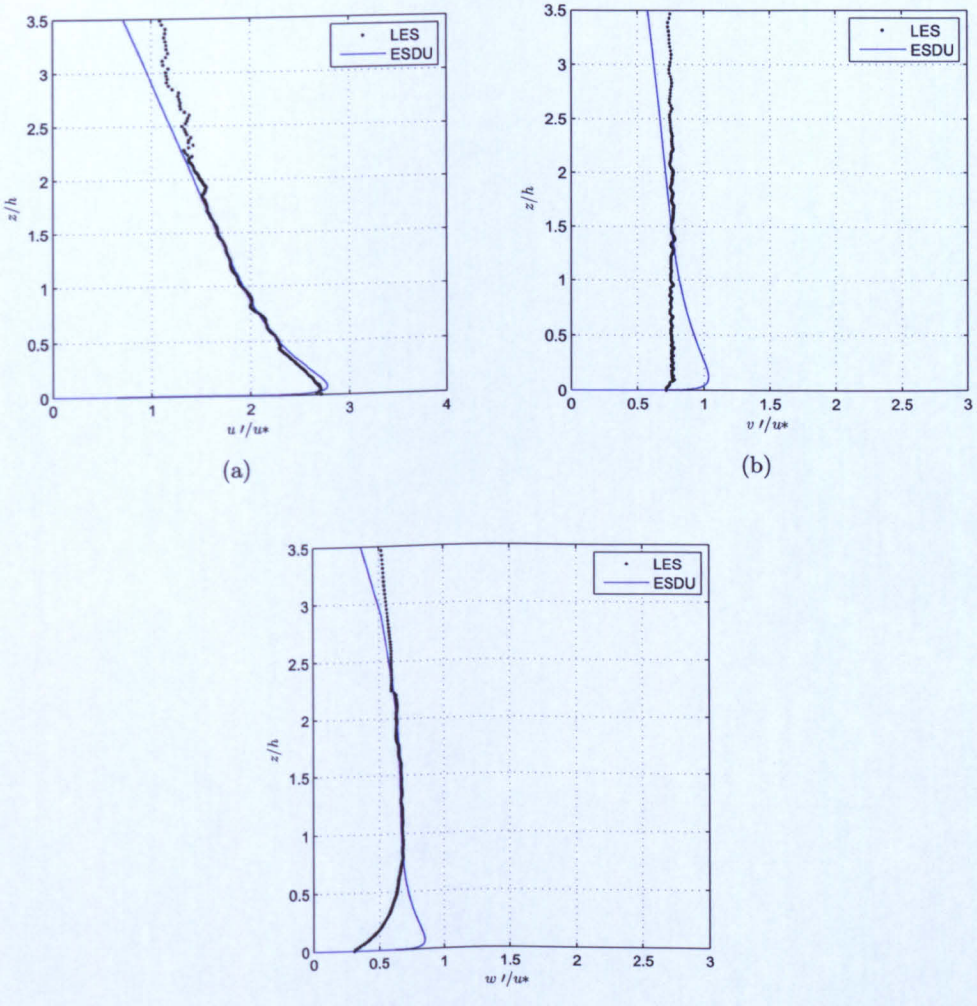

(a) (b)

(c)

Figure 7.4: Profiles of the rms of the u-component of the velocity (a), the v-component (b) and the w-component at $x = 20L$ upstream the building. The results of the LES with turbulent inflow simulation are plotted along side the distribution assumed by ESDU 85020 (1985, revised in 1990). The height is normalised by h, the height of the building.

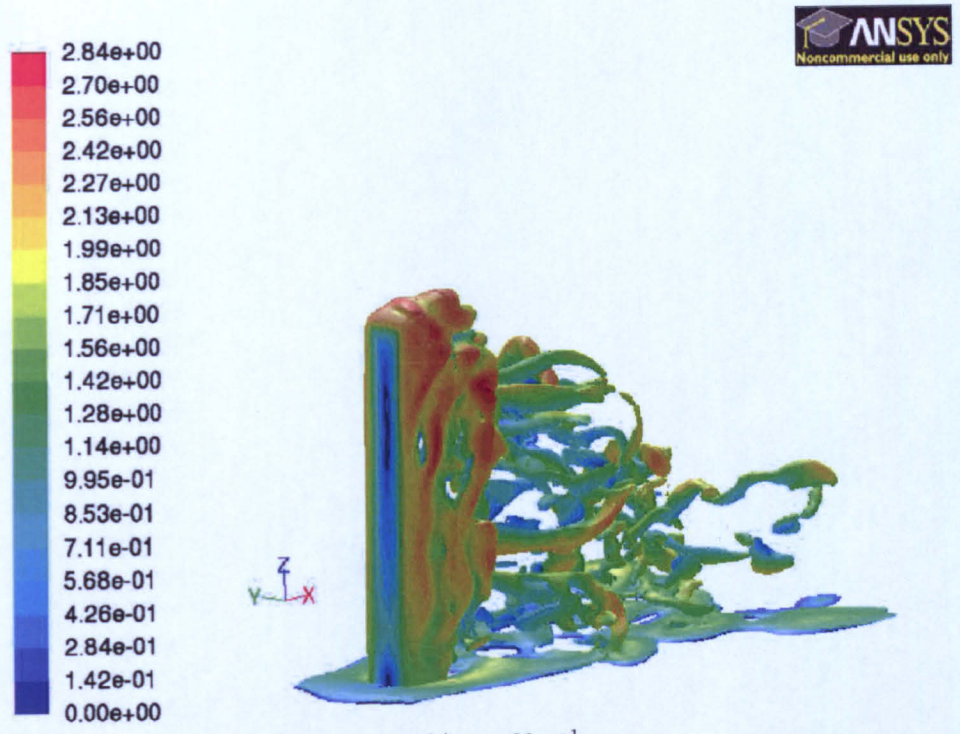

(a) $\omega = 20\ s^{-1}$

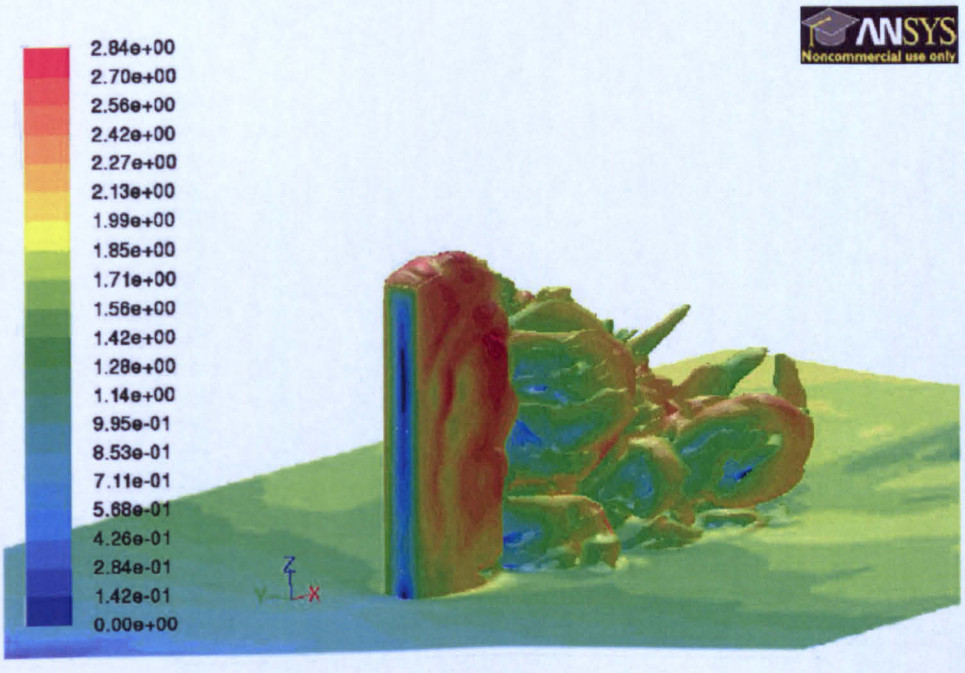

(b) $\omega = 50\ s^{-1}$

Figure 7.5: Iso surfaces of instantaneous vorticity magnitude 20 s^{-1} (a) and 50 s^{-1} (b) coloured by instantaneous velocity.

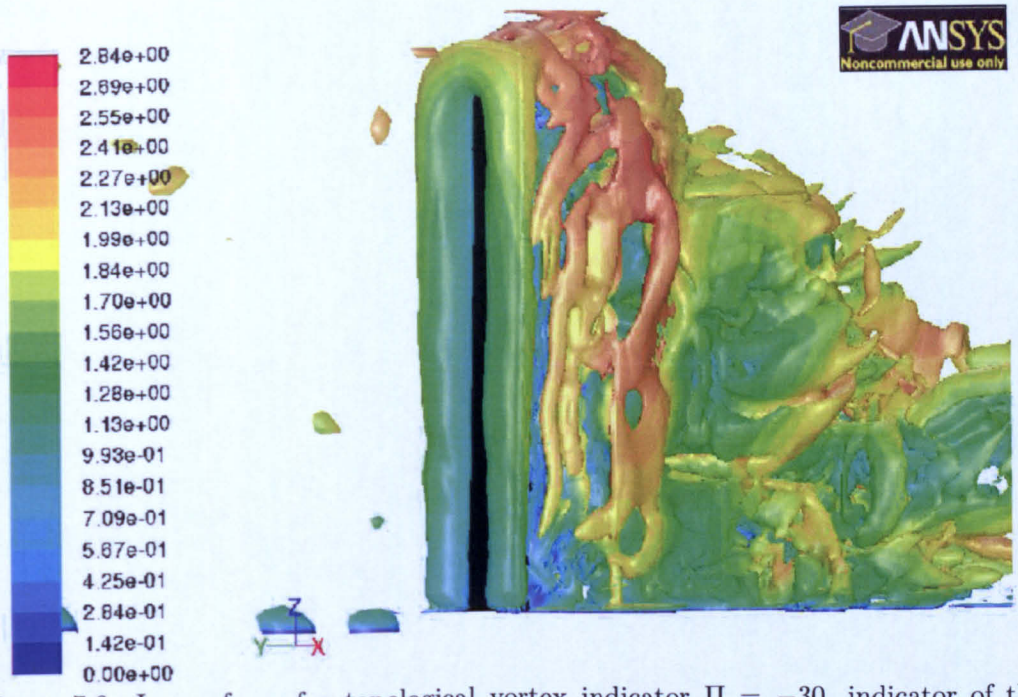

Figure 7.6: Iso surface of a topological vortex indicator $\mathrm{II} = -30$, indicator of the rotational structures in the flow. The tubular structures by the front edges of the building can be observed.

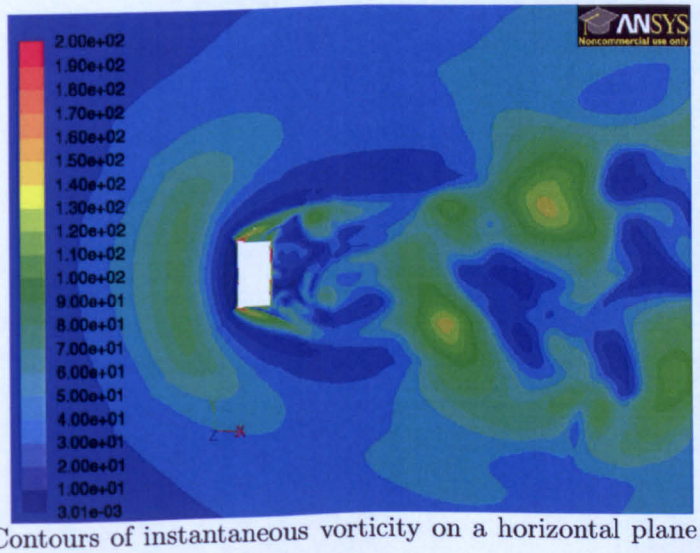

Figure 7.7: Contours of instantaneous vorticity on a horizontal plane near the ground at $z = L/10$.

and $z = 2h/3$ on a horizontal line. These coefficients of pressure are mean values obtained from statistical averaging (definition in Section 4.4, p.105). The reference velocity used to compute the pressure coefficients is the velocity at $z = h/3$ for (a), and $z = 2h/3$ for (b) far from the building. The reference pressure is taken to be the operating pressure far from the building. The results are compared to experimental data published for the CAARC building. For the results at $z = h/3$, the CFD results are compared to wind tunnel results from Goliger and Milford (1988), who tested two levels of longitudinal turbulence. The results at $z = 2h/3$ are compared to experimental results from Melbourne (1980) (City University and Monash University) and to results from Tanaka and Lawen (1986) (University of Ottawa). Since the width to length ratio is 1.5 for the CAARC building and 2 for the building of interest here, the experimental results are scaled. The first graph compares the CFD results to experimental results done in "low" and "high" turbulence wind tunnels. From the comparison, C_p is overpredicted on the front face, giving even larger values than the lowest turbulent case of the experimental data. This would tend to indicate that the "low" turbulent flow in the experiments was still more turbulent than the present simulation. The same reason can explain the underprediction of C_p on the back face. The predictions are better on the side face, which could be explained by the fact that the flow on the side face is dominated by the recirculation zone after the front edge of the building, so the flow is less dependent on the oncoming turbulence. The second graph compares the CFD results of C_p at $z = 2h/3$ with experimental data from various research groups (CAARC). Generally, the pressure coefficient is larger on the front face at $z = 2h/3$ than at $z = h/3$, which is confirmed by the contours of the static pressure in Figure 7.9. The maximal pressure can be observed at about $z = 4h/5$. On the front face, the maximum relative error is reached in the middle of the section and is equal to about 11%. The results are in good agreement with experiments on the side and back faces. On the side and back faces, C_p is over predicted by about 11%.

The longitudinal and transversal response of the top of the building is shown in Figure 7.10 for the reduced velocity $u/(nW) = 2.2$. The amplitude of longitudinal response

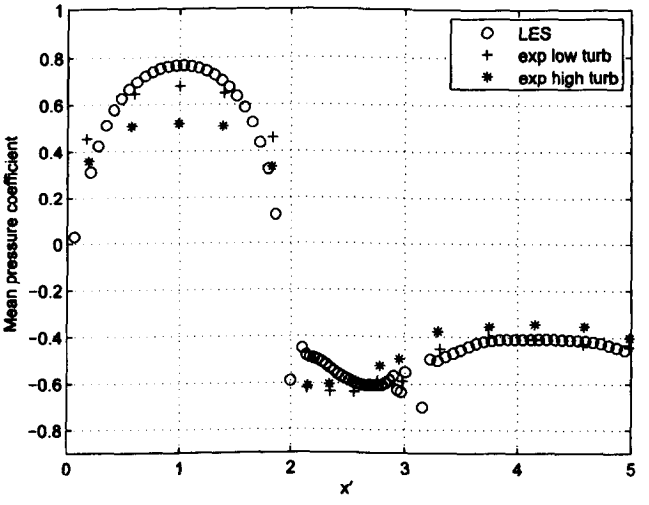

(a) "exp" refers to experimental results from Goliger and Milford (1988)

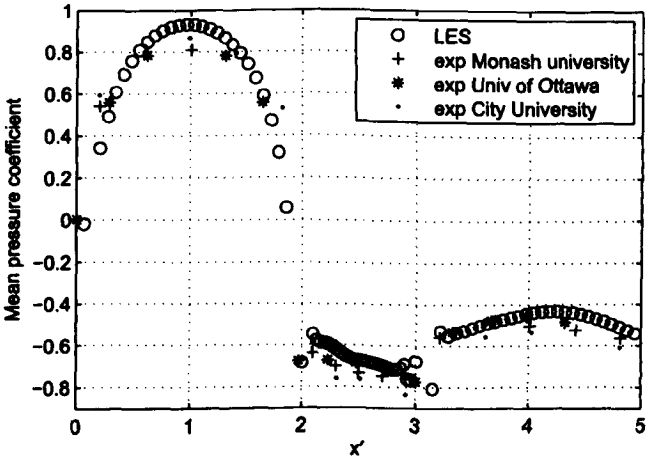

(b) "exp" refers to experimental results from Melbourne (1980); Tanaka and Lawen (1986)

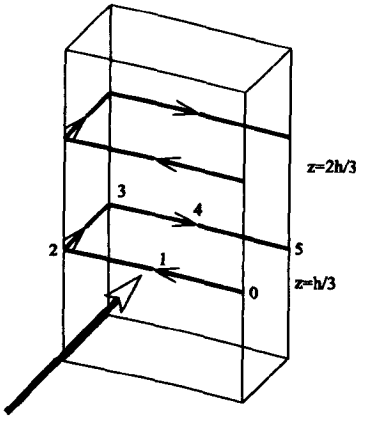

(c)

Figure 7.8: Distribution of pressure coefficient along an horizontal line at $z = h/3$ (a) and $z = 2h/3$ (b) as shown in (c). LES results compared to experimental data extracted from Braun and Awruch (2009).

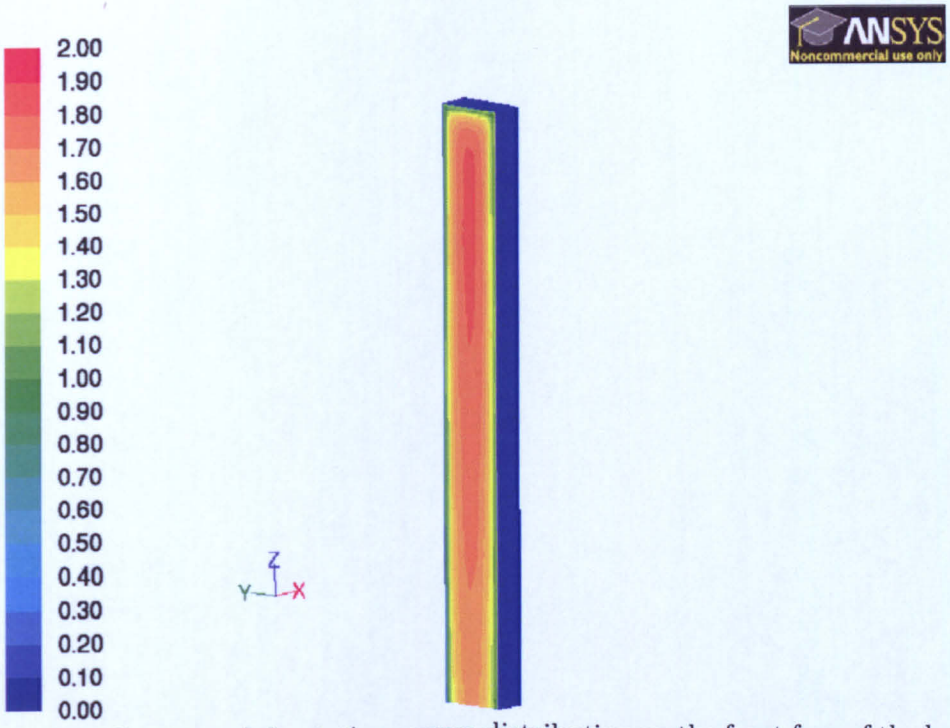

Figure 7.9: Contours of the static pressure distribution on the front face of the building.

is about 10 times larger than the amplitude of the transversal response. Structural damping causes the longitudinal response to decrease with time.

The transversal response is relatively small, which can be explained by the fact the reduced velocity is far from the region of "lock-in", or in other words, the frequency of the oscillating lift acting on the building remains far from the natural frequency of the building, for which the building response would be maximal. The transversal response is expected to be larger if the reduced velocity reaches 1.1 as seen in Chapter 5.

Figure 7.11 shows the trajectory covered by the roof center point of the building. The reduced velocity being far from the critical reduced velocity, the trajectory does not exhibit a predominant direction of motion.

7.5 Conclusions

This Chapter presented the results of a simulation combining the two tools developed in previous chapters. The turbulent inflow generator and the fluid-structure coupling are

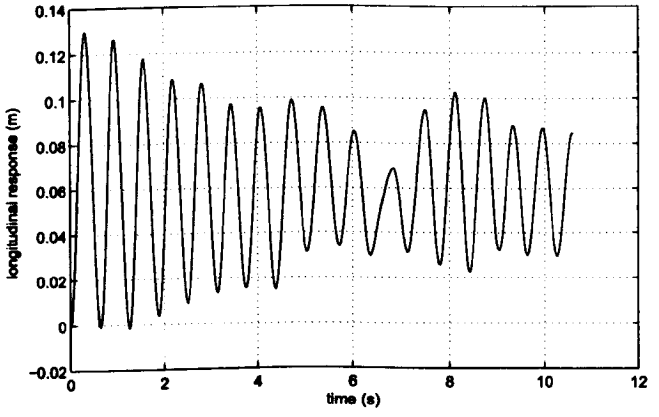

(a)

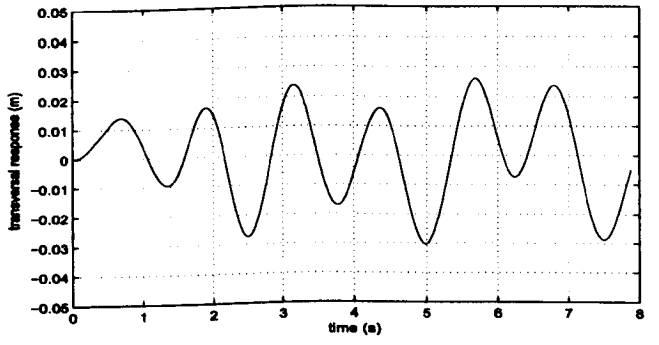

(b)

Figure 7.10: Response of the building (a) longitudinal response (b) transversal response.

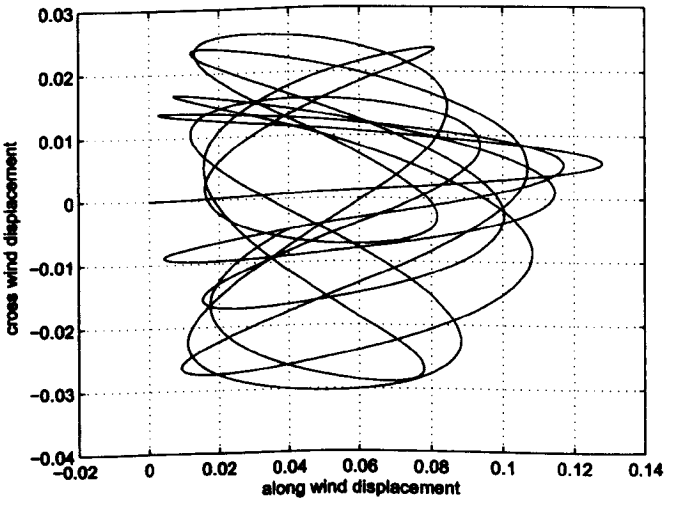

Figure 7.11: Trajectory covered by the roof center point.

used in combination in a fairly heavy simulation, which involves a very large number of cells to reach the minimum level of refinement required by LES. The mesh had also to be fine enough to maintain the turbulent structures that were injected at the inlet with the turbulent inflow generator.

The results, in terms of mean and rms velocities, showed good agreement with ESDU. Integral length scales in the ABL were reproduced with confidence. The 3D features of the wind flow, shown with iso surfaces of vorticity and contours of vorticity, presented a good qualitative picture of the wind flow. The quantitative comparisons of the pressure coefficients on the building showed good agreement with wind tunnel testing of the CAARC building. In terms of the response, since only one reduced velocity could be tested, only qualitative conclusions could be drawn. Chapter 5 demonstrated that the code could successfully couple fluid and structure's motion in the transversal direction, but the results of this chapter show that the structure can also be coupled with the wind flow in the longitudinal direction.

To conclude this chapter, a framework has been established to numerically study the wind flow around tall buildings and their response to wind loading. If more computing resources become available, the framework could be used to produce a more systematic numerical study of the response of a tall building to wind loading, by testing a range of reduced velocity.

Chapter 8

Conclusions and Recommendations

8.1 Summary

The main goal was to assess the the ability of commercial CFD codes to model the wind flow around a high-rise building – specifically the coupled dynamic response of the building to turbulent wind loading – by bringing together existing tools, thus establishing a framework for modelling of building response to wind loading within a turbulent ABL.

In order to meet the main objective three intermediate objectives were set. The first was to develop a tool for coupling the fluid and the structure, within the framework of the FLUENT code. The structural solver was contained in code attached to the CFD code in the form of user-defined functions. The fluid-structure coupling was then used to model a cantilever allowed to move in the transversal direction only. Turbulence modelling here was by means of an unsteady hybrid RANS-LES model that could reproduce small scale wake effects and large scale features, such as vortex shedding. The structure's response to vortex shedding in the wake was seen through the aeroelastic phenomenon of "lock-in", which occurs when the vortex shedding frequency is close to the natural frequency of the building. More precisely, "lock-in" was found to occur for a reduced

velocity of about 1.1, in agreement with the literature on "lock-in" phenomenon for rectangular cylinders and more recent publications on tall buildings.

The second intermediate objective was to investigate and apply a method for generating turbulent inflow for LES. It was shown in Chapter 2 that not only are wake effects of importance when predicting the response of tall buildings to wind loading, but also that the turbulence in the oncoming wind is of great importance. Upstream turbulence can produce a significant response of the structure if the natural frequency of the building is in the range of the dominant frequencies in the wind spectrum. For this reason, it was decided to adopt LES instead of the hybrid RANS-LES. However, LES requires a realistic turbulent inflow at the inlet of the domain. The option to use a precursor simulation to produce the appropriate turbulent inflow was considered too computationally expensive, and it was decided to produce a turbulent inflow synthetically, using a method developed by Xie and Castro (2008). The method for generating synthetic turbulent inflow was tested in an empty domain to determine the main statistical properties of the generated inflow, both on the inlet plane and as the flow moves through the fetch. It was found that it was possible to generate turbulent inflow at the inlet with predetermined statistical properties and that these properties were maintained throughout the domain.

Finally, in order to meet the third intermediate objective, the turbulent inflow generator and the fluid-structure coupling tool were brought together. In this final stage, the building was allowed to bend in both the along-wind and transversal directions. The structure was found to respond to wake effects (vortex shedding) but also to the wind gusts. In addition, results of the LES simulation in terms of the pressure distribution on the building, velocity profiles, turbulence, flow field around the building, and more particularly in the wake were shown to be in good agreement with experimental data. The main achievement of Chapter 7 was to establish a framework to numerically study the wind flow around tall buildings and their response to wind loading, and to demonstrate the ability of commercial CFD to model the wind flow around a high-rise building, addressing the main objective of this thesis.

In addition, a complementary study was done to challenge the current recommendations for the size of the computational domain for studying the wind flow around tall buildings. It was found that the size of the domain could be greatly reduced. This finding was then used in the later parts of the work, allowing us to achieve more efficient simulations in which the overall domain size could be reduced and the number of cells could be increased in key regions, such as the wake of the building.

8.2 Critical appraisal

Firstly, the framework that has been developed requires more testing. In the first instance, the sensitivity of the model to changes in inlet velocity, turbulence intensity, structural stiffness and damping and many other variables needs to be investigated. Secondly, it needs to be validated against full scale or wind tunnel experiments on an aeroelastic building. Both these investigations will require large amounts of computational time, which were beyond the scope of the present work.

Secondly, the structural solver was shown to work for individual modes, and it would be a trivial exercise to extend it to secondary and torsional modes.

Then, in order to make the method directly applicable to civil engineering, the region containing the building would need to be able to rotate to test a number of wind directions, as suggested by Morvan et al. (2007).

As for the method to generate turbulent inflow, it is not computationally expensive, at least for the applications concerned by this thesis. However, if the computational cost becomes an issue (for larger inlets, longer periods of time...), the method could be linked to methods such as wavelet reconstruction, which is a method that allows the reproduction of non-linearity in the wind. For example, one could produce the turbulent inflow with the method presented here, run it once or twice though the domain, and use the wavelet reconstruction method to reproduce and extend the wind outflow, that could then be used as a new inflow. The combination could potentially be more computationally efficient.

Finally, it was demonstrated that given an input of Reynolds stresses and integral length scales, it was possible to generate turbulent inflow for LES. However, more and more work seems to be done in linking micro scale models to larger scale meteorological scale models, which could be of interest in further work (Mochida et al., 2010).

8.3 Conclusions

The first conclusion that can be drawn from this thesis is that commercial CFD can be suitably adapted to model the wind flow around a high-rise building, and more specifically, it can be applied to model the coupled dynamic response of the building to turbulent wind loading. The second conclusion addresses the issue of computational domain sizes. The work that has been done as part of this thesis demonstrated that the current recommendations on domain sizes are inappropriate for tall buildings, and new recommendations were defined. Finally, it was shown that a synthetic method based on inverse Fourier transforms can be successfully used to generate turbulent inflow.

8.4 Further work

- Test the sensitivity of the model to change in inlet velocity, turbulent intensity, structural stiffness and damping.
- Include secondary modes and torsional modes.
- Modify the FSI code so it can be restarted at anytime (if it crashes for example). At the moment, if the run crashes for any reason, it has to be restarted from when the building is released.
- Define a cylindrical zone around the rigid zone already defined around the building. This cylindrical zone could then be rotated, allowing a range of wind directions to be tested.

- Use the synthetic turbulent inflow generator in combination with a wavelet reconstruction approach.
- Linking to larger scale meteorogical models.

Bibliography

ANSYS. *ANSYS-Fluent 12.0 User Manual, ANSYS Inc. Fluent.* Southpointe, Canonsburg PA, USA, 2009.

Carla Antoci, Mario Gallati, and Stephano Sibilla. Numerical simulation of fluid-structure interaction by sph. *Computers and Structures*, 85:879–890, 2007.

J. Baldyga and J.R. Bourne. Fluid mechanical approach to turbulent mixing and chemical reaction. *Chemical Engineering Communications*, 28:231–281, 1984.

P.W. Bearman. Vortex shedding from oscillating bluff bodies. *Annu. Rev. Fluid Mech.*, 16:195–222, 1984.

Prof. A. A. Becker. *Finite Element Analysis for Engineers, Course Lecture Notes.* University of Nottingham, 2008.

Girma Bitsuamlak and Emil Simiu. Cfd's potential applications: a wind engineering perspective. In *Proceedings of the Fifth International Symposium on Computational Wind Engineering, Chapel Hill, North Carolina, USA*, 2010.

Bert Blocken, Ted Stathopoulos, and Jan Carmeliet. Cfd simulation of the atmospheric boundary layer: wall function problems. *Atmospheric Environment*, 41:238–252, 2007.

Alexdrandre Luis Braun and Armando Miguel Awruch. Aerodynamic and aeroelastic analysis on the caarc standard tall building model using numerical simulation. *Computers and Structures*, 87:564–581, march 2009.

M. Breuer, B. Kniazev, and M. Abel. Development of wall models for les of separated flows using statistical evaluations. *Computers and Fluids*, 36:817–837, 2007.

M. Breuer, B. Jaffrézic, and K. Arora. Hybrid les-rans technique based on a one-equation near wall model. *Theor. Comput. Fluid Dyn.*, 22:157–187, 2008.

R. Buccolieri and S. Di Sabatino. Flow and pollutant dispersion in urban arrays for the standardization of CFD modelling practise. In *Proceedings of the 11th Conference on Harmonisation within Atmospheric Dispersion Modelling for Regulatory Purposes, Cambridge, July*, 2007.

Tony Burton, David Sharpe, Nick Jenkins, and Ervin Bossanyi. *Wind Energy Handbook.* John Wiley & Sons, 2002.

Ian P. Castro and J.M.R. Graham. Numerical wind engineering: the way ahead? In *Proceedings of The Institution of Civil Engineering Structures & Buidlings*, pages 275–277, August 1999.

Ray W. Clough and Joseph Penzien. *Dynamics of Structures, Second Edition.* McGraw-Hill book Co., 1993.

N.J. Cook. *The designer's guide to wind loading of building structures, Part 1.* Butterworth, 1992.

J. Counihan. Adiabatic atmospheric boundary layers: A review and analysis of data from the period 1880-1972. *Atmos. Env.*, 9:871–905, 1975.

Jason J. Dale, D.B. Spalding, A.E. Hold, and M.G. Armstrong. Fluid structure interaction through simultaneous calculation of velocity and displacement. *PVP, Emerging Technologies in Fluids, Structures, and Fluid/Structures Interactions*, 446-2:129–139, 2002.

A.G. Davenport. How can we simplify and generalize wind loads. *Journal of Wind Engineering and Industrial Aerodynamics*, 54/55:657–669, 1995.

Alan Garnett Davenport. The application of statistical concepts to the wind loading of structures. In *Proceedings of The Institution of Civil Engineers.* The Institution of Civil Engineers, August 1961.

L. Davidson and M. Billson. Hybrid les-rans using synthesized turbulent fluctuations for forcing in the interface region. *Int. J. of Heat and Fluid Flow*, 27:1028–1042, 2006.

L. Davidson and S.H. Peng. Hybrid les-rans modelling: a one equation sgs model combined with a k-ω model for predicting recirculating flows. *Int. J. Numer. Meth. Fluids*, 43:1003–1018, 2003.

J. Donea, Antonio Huerta, H-Ph. Ponthot, and A. Rodriguez-Ferran. *Arbitrary Lagrangian - Eulerian Methods*, chapter 14, pages 1–25. John Wiley & Sons, 2004.

P. Duchêne-Marullaz. Effects of high roughness on the characteristics of turbulence in the case of strong winds. In *Proceedings of the Fifth International Conference on Wind Engineering*, 1980.

Clas Dyrbye and Svend Ole Hansen. *Wind loads on structures.* John Wiley & Sons, 1997.

ESDU 85020. Esdu 85020: Characteristics of atmospheric turbulence near the ground, part ii: single point data for strong winds (neutral atmosphere). Technical report, 1985, revised in 1990.

ESDU 86010. Characterisation of atmospheric turbulence near the ground, part iii: Variations in space and time for strong winds (neutral atmosphere). Technical report, 1986, revised in 2001.

Robert E. Eskridge and J.C.R. Hunt. Highway modeling. part i: Prediction of velocity and turbulence fields in the wake of vehicles. *Journal of Applied Meteorology*, 18: 387–400, 1979.

Ralph Evins. Fds assessment. Technical report, Buro Happold, 2007.

C. Farhat and M. Lesoinne. Two efficient staggered algorithms for the serial and parallel solution of three-dimensional nonlinear transient aeroelastic problems. *Computer methods in applied mechanics and engineering*, 182:499–515, 2000.

C. Farhat, M. Lesoinne, and N. Maman. Mixed explicit/implicit time integration of coupled aeroelastic problems: three field formulation, geometric conservation and distributed solution. *Int. J. Numer. Meth. Fluids*, 21:807–35, 1995.

C. Farhat, G. van der Zee Kristoffer, and P. Geuzaine. Provably second-order time-accurate loosely-coupled solution algorithms for transient nonlinear computational aeroelasticity. *Computers methods in applied mechanics and engineering*, 195:1973–2001, 2006.

A.A. Fediw, M. Nakayama, K.R. Cooper, Y. Sasaki, S. Resende-Ide, and S.J. Zan. Wind tunnel study of an oscillating tall building. *Journal of Wind Engineering and Industrial Aerodynamics*, 57:249–260, 1995.

R.M. Franck and R.B. Lazarus. Mixed eulerian-lagrangian method: vol.3: Fundamental methods in hydrodynamics. In B. Alder, S. Fernbach, and M. Rotenberg, editors, *Methods in Computational Physics*, pages 47–67, 1964.

J. Franke. Introduction to the prediction of wind loads on buildings by computational wind engineering (CWE). In T. Stathopoulos and C.C. Baniotopoulos, editors, *Wind Effects on Buildings and Design of Wind-sensitive Structures*, chapter 3, pages 67–103. SpringerWien, New York, 2007.

J. Franke, C. Hirsch, A.G. Jensen, H.W. Krüs, M. Schatzmann, P.S. Westbury, S.D. Miles, J.A. Wisse, and N.G. Wright. Recommendations on the use of CFD in wind engineering. In J.P.A.J. van Beeck, editor, *COST Action C14: Impact of Wind and Storm on City Life and Built Environment*, pages C.1.1–C.1.11. von Karman Insitute for Fluid Dynamics, 2004.

J. Franke, A. Hellsten, Schlünzen, and B. Carissimo. Best practice guide for the CFD

simulation of flows in the urban environment. In *COST Action 732: Quality assurance and improvement of microscale meteorological models*, 2007.

S. Fu, B.E. Launder, and D.P. Tselepidakis. Accomodating the effects of high strain rates in modelling the pressure-strain correlation. Technical report, UMIST Mech. Eng. Dept. Report. TFD/87/5, 1987.

J.R Garrat. *The Atmospheric Boundary Layer.* Cambridge University Press, 1992.

M. Germano, U. Piomelli, P. Moin, and W.H. Cabot. A dynamic subgrid scale eddy viscosity model. *Phys. Fluids A*, 3:1760–1765, 1991.

J.H. Gerrard. The mechanics of the formation region of vortices behind bluff bodies. *J. Fluid Mech.*, 25:401–413, 1966.

Anvar Gilmanov and Sumanta Acharya. A hybrid immersed boundary and material point method for simulating 3d fuid-structure interaction problems. *International Journal for Numerical Methods in Fluids*, 56:2151–2177, 2007.

AM Goliger and RV Milford. Sensitivity of the CAARC standard building model to geometric scale and turbulence. *Journal of Wind Engineering and Industrial Aerodynamics*, 31(1):105–123, 1988. ISSN 0167-6105.

C. Gorle, J. van Beeck, P. Rambaud, and G. Tendeloo. Cfd modelling of small particle dispersion: The influence of the turbulence of the turbulence kinetic energy in the atmospheric boundary layer. *Atmospheric Environment*, 43:673–681, 2009.

Kemal Hanjalić and Saša Kenjereš. Some developments in turbulence modelling for wind and environmental engineering. *Journal of Wind Engineering and Industrial Aerodynamics*, 96:1537–1570, 2008.

D.M. Hargreaves and N. Wright. On the use of the k-ϵ model in commercial cfd software to model the neutral atmospheric boundary layer. *Journal of Wind Engineering and Industrial Aerodynamics*, 95:355–369, 2007.

R.I. Harris. The macrometeorological spectrum – a preliminary study. *Journal of Wind Engineering and Industrial Aerodynamics*, 96:2294–2307, 2008.

R.I. Harris and D.M. Deaves. The structure of strong winds. In *Proceedings of the Seminar on Wind Engineering in the Eighties*, 1980.

E.L. Houghton and N.B. Carruthers. *Wind forces on buildings and structures: an introduction.* Edward Arnold, 1976. ISBN 0713133619.

R.P. Hoxey, P.J. Richards, and J.L. Short. A 6 m cube in an atmospheric boundary layer flow part 1. full-scale and wind-tunnel results. *Wind and Structures*, 5(2-4):165–176, 2002.

S. Huang, Q.S. Li, and S. Xu. Numerical evaluation of wind effects on a tall steel building by cfd. *Journal of Constructional Steel Research*, 63:612–627, 2007.

T. Ishihara and K. Hibi. Turbulent measurements of the flow field around a high–rise building. *J. Wind Eng. Japan*, 76:55–64, 1998.

M. Kato and B.E. Launder. The modeling of turbulent flow around stationary and vibrating square cylinders. *Prep. of 9th Symp. On Turbulent shear flow*, 157:10–4–1–6, 1993.

W.-W. Kim and S. Menon. Application of the localized dynamic subgrid-scale model to turbulent wall-bounded flows. Technical Report AIAA-97-0210, American Institute of Aeronautics and Astronautics, 35th Aerospace Sciences Meeting, Reno, NV,, January 1997.

M. Klein, A. Sadiki, and J. Janicka. A digital filter based generation of inflow data for spatially developing direct numerical simulation or large eddy simulation. *J. Comp. Phys.*, 186:652–665, 2003.

A.N. Kolmogorov. The local structure of turbulence in incompressible viscous fluid for very large reynolds numbers. In *Dokl. Akad. Nauk SSSR*, volume 30, pages 9–13, 1941.

Ulrich Küttler and Wolfgang A. Wall. An approach for parallel fluid-structure interaction on unstructured meshes. In *Proceedings of the 13th European PVM/MPI user's group meeting, Bonn, Germany*, September 2006.

B.E. Launder and D.B. Spalding. The numerical computation of turbulent flows. *Comput. Methods Appl. Mech. Eng.*, 3:269–289, 1974.

P. L'Ecuyer. Efficient and portable combined random number generators. *Communication of the ACM*, 31:742–774, 1988.

S. Lee, S.K. Lele, and P. Moin. Simulation of spatially evolving turbulence and the applicability of taylors hypothesis in compressible flow. *Phys. Fluids A*, 4:1521–1530, 1992.

Hee Chang Lim, T.G. Thomas, and Ian P. Castro. Flow around a cube in a turbulent boundary layer: Les and experiment. *Journal of Wind Engineering and Industrial Aerodynamics*, 97:96–109, 2009.

E. Longatte, Z. Bendjeddou, V. Verreman, and M. Souli. Comparison of strong and partitioned fluid structure code coupling methods. In *Proceedings of ASME 2005 Pressure Vessels and Piping Division Conference, Denver, Colorado, USA*, July 2005.

Thomas S. Lund. Generation of turbulent inflow data for spatially-seveloping boundary layer simulations. *Journal of Computational Physics*, 140:233–258, 1998.

WH Melbourne. Comparison of measurements on the CAARC standard tall building model in simulated model wind flows. *Journal of Wind Engineering and Industrial Aerodynamics*, 6(1-2):73–88, 1980. ISSN 0167-6105.

P. Mendis, T. Ngo, N. Haritos, A. Hira, B. Samali, and J. Cheung. Wind loading on tall buidlings. *EJSE Special Issue: Loading on Structures*, pages 41–54, 2007.

A. Mochida, S. Murakami, M. Shoji, and Y. Ishida. Numerical simulation of flowfield around texas tech building by large-eddy simulation. *Journal of Wind Engineering and Industrial Aerodynamics*, 46/47:455–460, 1993.

A. Mochida, Y. Tominaga, S. Murakami, R. Yoshie, T. Ishihara, and R. Ooka. Comparison of various k-epsilon models and dsm applied to flow around a high-rise building - report on aij cooperative project for cfd prediction of wind environment -. *Wind and Structures*, 5(2-4):227–244, 2002.

A. Mochida, S. Iizuka, Y. Tominaga, and I. Yu-Fat Lun. Up-scaling cwe models to include mesoscale meteorological influences. In *In: the Fifth International Symposium on Computational Wind Engineering, Chapel Hill, North Carolina, USA, May 23-27*, 2010.

H.P. Morvan, P. Stangroom, and N.G. Wright. Automated CFD analysis for multiple directions of wind flow over terrain. *Wind and Structures*, 10(2):99–120, 2007. ISSN 1226-6116.

S. Murakami. Current status and future trends in computational wind engineering. *Journal of Wind Engineering and Industrial Aerodynamics*, 67&68:3–34, 1997.

S. Murakami. Overview of turbulence models applied in cwe-1997. *Journal of Wind Engineering and Industrial Aerodynamics*, 74-76:1–24, 1998.

S. Murakami and A. Mochida. On turbulent vortex shedding flow past 2d square cylinder predicted by cfd. *Journal of Wind Engineering and Industrial Aerodynamics*, 54-55: 191–211, 1995.

S. Murakami, A. Mochida, K. Kondo, Y. Ishida, and Tsuchiya. Development of new k-epsilon model for flow and pressure fields around bluff body. *Journal of Wind Engineering and Industrial Aerodynamics*, 67&68:169–182, 1994.

B. Neammanee, S. Sirisumrannukul, and S. Chatratana. Development of a wind turbine simulator for wind generator testing. *International Energy Journal*, 8:21–28, 2007.

N.V. Nikitin, F. Nocaud, B. Wasistho, K.D. Squires, and P.R. Spalart. An approach to wall modelling in large-eddy simulations. *Phys. Fluids*, 12:1629–1632, 2000.

W.F. Noh. Cel: a time dependent two space-dimensional, coupled eulerian lagrangian code. In *Methods in Computational Physics*, volume 3, page 117. Academic Press. New York, 1964.

Atsushi Okajima. Strouhal numbers of rectangualr cylinders. *Journal of Fluid Mechanics*, 123:379–398, 1982.

S.V. Patankar and D.B. Spalding. A calculation procedure for heat, mass and momentum transfer in three-dimensional parabolic flows. *Int. J. Heat Mass Transfer*, 15:1787, 1972.

C.S. Peskin. Numerical analysis of blood flow in the heart. *Journal of computational physics*, 25(3):220–252, 1977.

S. Piperno, C. Farhat, and B. Larrouturou. Partitioned procedures for the transient solution of coupled aeroelastic problems. *Comput. Methods Appl. Mech. Eng.*, 124: 79–711, 1995.

Stephen B. Pope. *Turbulent Flows.* Cambridge University Press, 2000.

F. Porte-Agel, C. Meneveau, and M.B. Parlange. A scale-dependent dynamic model for large edd simulation: application to a neutral atmospheric boundary layer. *Journal of Fluid Mechanics*, 415:261–284, 2000.

Willian H. Press, Saul A. Teukolsky, Willian T. Vetterling, and Brian P. Flannery. *Numerical Recipes in C: The art of Scientific Computing, Second Edition*, volume Chapter 7. Random Numbers. Cambridge University Press, 1992.

T. Prevezer, J. Holding, A. Gaylard, and R. Palin. Bluff body asymmetric flow phenomenon - real effect or solver artefact? *Wind & Structures*, 5:359–368, 2002.

J. Revuz, DM Hargreaves, and J. Owen. Numerical simulation of the dynamic wind loading on and response of tall buildings. In *Proceedings of the Proceedings of the fifth European and African Conference on Wind Engineering, Florence, Italy*, 2009.

G.M. Richards, R.P. Hoxey, and L.J. Short. Wind pressures on a 6 m cube. *Journal of wind Engineering and Industrial Aerodynamics*, 89:1553–1564, 2001.

P.J. Richards and R. Hoxey. Appropriate boundary conditions for computational wind engineering models using the k-ε turbulence model. *J. Wind Eng. Ind. Aerodyn*, 46 & 47:145–153, 1993.

P.J. Richards and A.D Quinn. A 6 m cube in an atmospheric boundary layer flow part 2. computational solutions. *Wind and Structures*, 5(2-4):177–192, 2002.

Silvana Di Sabatino, Alexander Baklanov, John Bartzis, Ruwim Berkowicz, Riccardo Buccolieri, Ana Margarida Costa, George Efthimiou, Jrg Franke, Matthias Ketzel, Bernd Leitl, Roman Nuterman, Helge Rrdam Olesen, and Richard Tavares. Analyses, critical issues and outcome from cost732 cfd evaluation exercise. In *Proceedings of the Fifth International Symposium on Computational Wind Engineering, Chapel Hill, North Carolina, USA*, 2010.

Peter Sachs. *Wind forces in Engineering.* Pergamon press, 1978.

R. Sankaran and D.A. Paterson. Computation of rain falling on a tall rectangular building. *J. Wind Eng. Ind. Aerodyn.*, 72:127–136, 1997.

Inanc Senocak, Andrew S. Ackerman, Michael P. Kirkpatrick, David E. Stevens, and Nagi N. Mansour. Study of near-surface models for large-eddy simulations of a neutrally stratified atmospheric boundary layer. *JBoundary-Layer Meteorology*, 124:405–424, 2007.

E. Simiu and R.H. Scanlan. *Wind effects on structures.* Wiley-Interscience, 1986.

A.K. Slone, K. Pericleous, C. Bailey, and M. Cross. Dynamic fluid-structure interaction using finite volume unstructured mesh procedures. *Computers and Structures*, 80: 371–390, 2002.

A.K. Slone, K. Pericleous, C. Bailey, M. Cross, and C. Bennett. A finite volume unstructured mesh approach to dynamic fluid-structure interaction: an assessment of

the challenge of predicting the onset of flutter. *Applied Mathematical Modelling*, 28: 211–239, 2004.

J. Smagorinsky. General circulation experiments with the primitive equations. i. the basic experiment. *Month. Wea. Rev.*, 91:99–164, 1963.

E.S.P. So, A.T.Y. Chan, and A.Y.T. Wong. Large–eddy simulations of wind flow and pollutant dispersion in a street canyon. *Atmos. Env.*, 39:3573–3582, 2005.

P. Spalart. Young-person's guide to detached-eddy simulation grids. Technical Report CR-2001-211032, NASA, July 2001.

C.G. Speziale, , S. Sarkar, and T.B. Gatski. Modelling the pressure-strain correlation of turbulence: and invariant dynamical system approach. *J. Fluid Mech.*, 227:245–272, 1991.

Theodore Stathopoulos. Computational wind engineering: Past achievements and future challenges. *Journal of Wind Engineering and Industrial Aerodynamics*, 67-68:509–532, 1997.

S. Swaddiwudhipong and M.S. Khan. Dynamic response of wind-excited building using cfd. *Journal of Sound and Vibration*, 253(4):735–754, 2002.

GR Tabor and MH Baba-Ahmadi. Inlet conditions for large eddy simulation: A review. *Computers & Fluids*, 39(4):553–567, 2010. ISSN 0045-7930.

H. Tanaka and N. Lawen. Test on the CAARC standard tall building model with a length scale of 1: 1000. *Journal of Wind Engineering and Industrial Aerodynamics*, 25(1):15–29, 1986. ISSN 0167-6105.

L. Temmerman, M.A. Leschziner, C.P. Mellen, and J. Fr'ohlich. Investigation of wall-function approximations and subgrid-scale models in large eddy simulation of separated flow in a channel with streamwise periodic constrictions. *Int. J. of Heat and Fluid Flow, Turbulence and Combustion*, 24:157–180, 2003.

L. Temmerman, M. Hadžiabdić, M.A. Leschziner, and K. Hanjalić. A hybrid two-layer urans-les approach for large eddy simulation at high reynolds numbers. *Int. J. of Heat and Fluid Flow*, 26:173–190, 2005.

F. Tessicini, L. Temmerman, and M.A. Leschziner. Approximate near-wall treatments based on zonal and hybrid rans-les methods for les and high reynolds numbers. *Int. J. of Heat and Fluid Flow*, 27:789–799, 2006.

F. Tessicini, N. Li, and M.A. Leschziner. Large-eddy simulation of three-dimensional flow around a hill-shaped obstruction with a zonal near-wall approximation. *Int. J. of Heat and Fluid Flow*, 28:894–908, 2007.

T.G. Thomas and J.J.R. Williams. Generating a wind environment for large eddy simulation of bluff body flows. *Journal of Wind Engineering and Industrial Aerodynamics*, 82:189–208, 1999.

Y. Tominaga, A. Mochida, R. Yoshie, H. Kataoke, T. Nozu, M. Yoshikawa, and T. Shirasawa. AIJ guidelines for practical applications of CFD to pedestrian wind environment around buildings. *J. Wind. Eng. Ind. Aerodyn.*, 96:1749–1761, 2008.

Isaac van der Hoven. Power spectrum of horizontal wind speed in the frequency range from 0.0007 to 900 cycles per hour. *J. Meteor.*, 14:160–164, 1957.

H.K. Versteeg and W. Malalasekera. *An Introduction to Computational fluid dynamics, The Finite Volume Method.* Pearson Education, 2007.

R.L. Wardlaw and G.F. Moss. A standard tall building model for the comparison of simulated natural winds in wind tunnels. Technical report, Supplement by Commonwealth Advisory Aeronautical Research Council, 1971.

M. Watakabe, M. Ohashi, H. Okada, Y. Okuda, Y. Okuda, H. Kikitsu, S. Ito, Y. Sasaki, K. Yasui, K. Yoshikawa, and M. Tonagi. Comparison of wind pressure measurements on tower-like structure obtained from full–scale observation, wind tunnel test, and the CFD technology. *J. Wind Eng. Ind. Aerodyn.*, 90:1817–1829, 2002.

C.H.K. Williamson and R. Govardhan. A brief review of recent results in vortex-induced vibrations. *Journal of Wind Engineering and Industrial Aerodynamics*, 96:713–735, 2008.

N.G. Wright and G.J. Easom. Non-linear $k-\epsilon$ turbulence model results for flow over a building at full scale. *Apl. Math. Modelling*, 27:1013–1033, 2003.

Y. Wu, X. Sun, and S. Shen. Computation wind-structure interaction on tension structures. *Journal of Wind Engineering and Industrial Aerodynamics*, page doi: 10.1016/j.jweia.2008.02.043, 2008.

W. Xiang and H. Wang. Discussion on grid size and computational domain in CFD modelling of pedestrian wind environment around buildings. *J. Civ. Eng. Arch.*, 2(1): 8–14, 2008.

Zhenh-Tong Xie and Ian P. Castro. Efficient generation of inflow conditions for large eddy simulation of street-scale flows. *Flow, Turbulence and Combustion*, 81(3):449–470, October 2008.

V Yakhot, S.A. Orszag, S. Thangam, T.B. Gatski, and C.G. Speziale. Development of turbulence models for shear flows by a double expansion technique. *Physics of Fluids A*, 4:1510–1520, 1992.

W. Yang, H. Jin, M. Gu, and S. Chen. Applicationof new inflow boundary conditions for modelling equilibrium atmosphere boundary layer in rans-based turbulence models. In *Proceedings of International Conference on Wind Engineering*, 2007.

Yi Yang, Ming Gu, Suqin Chen, and Xinyang Jin. New inflow boundary conditions for modelling the neutral equilibrium atmospheric boundary layer in computational wind engineering. *Journal of Wind Engineering and Industrial Aerodynamics*, 97:88–95, 2009.

L.T. Zhang and M. Gay. Immersed finite element method for fluid-structure interaction. *Journal of Fluids and Structures*, 23:839–857, 2007.

Appendices

Appendix A

The Arbitrary Lagrangian Eulerian formulation for mesh-fluid coupling

This appendix presents a kinematical description of the Arbitrary Lagrangian Eulerian formulation, based on Donea et al. (2004).

Figure A.1 illustrates the three frames of reference: $R_{\boldsymbol{X}}$ is the material configuration ($\boldsymbol{X}$ is the material coordinate in the Lagrangian description), $R_{\boldsymbol{x}}$ the spatial configuration ($\boldsymbol{x}$ is the spatial coordinate in the Eulerian description) and $R_{\boldsymbol{\chi}}$ is the referential configuration. Theoretically, the referential configuration could be any configuration, but it is usually seen as the mesh configuration. Therefore $\boldsymbol{\chi}$ is the computational coordinate.

One can express the mapping application from the computational to the spatial configuration:

$$\begin{aligned} \boldsymbol{\Phi} \; : \; R_{\boldsymbol{\chi}} \times [t_0, t_{\text{final}}[\quad &\longrightarrow \quad R_{\boldsymbol{\chi}} \times [t_0, t_{\text{final}}[\\ (\boldsymbol{\chi}, t) \quad &\longmapsto \quad \boldsymbol{\Phi}(\boldsymbol{\chi}, t) = (\boldsymbol{x}, t) \end{aligned}$$

the transformation from the material configuration to the spatial configuration:

$$\begin{aligned} \boldsymbol{\varphi} \; : \; R_{\boldsymbol{X}} \times [t_0, t_{\text{final}}[\quad &\longrightarrow \quad R_{\boldsymbol{x}} \times [t_0, t_{\text{final}}[\\ (\boldsymbol{X}, t) \quad &\longmapsto \quad \boldsymbol{\varphi}(\boldsymbol{X}, t) = (\boldsymbol{x}, t) \end{aligned}$$

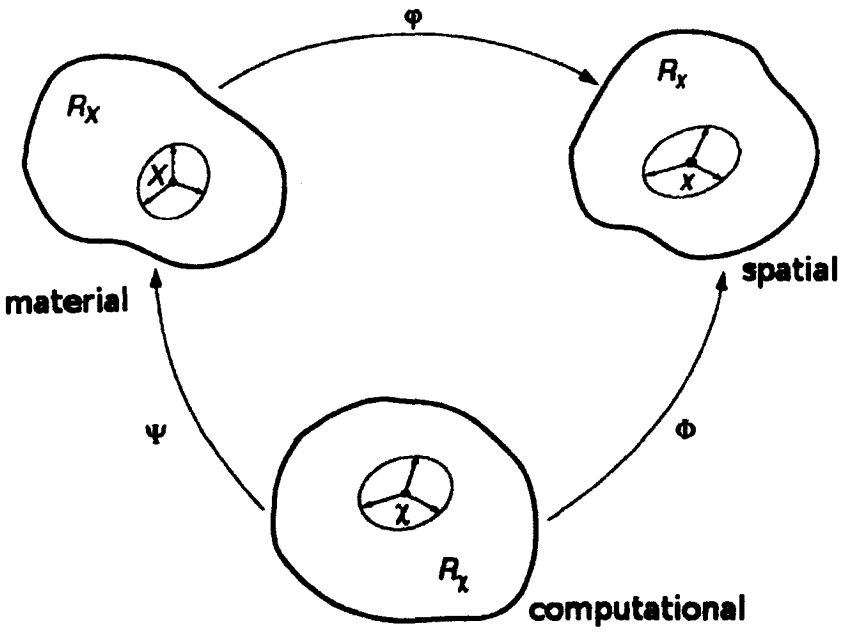

Figure A.1: Material, spatial and computational frames of reference and mapping transformations of the ALE method (after Donea et al. (2004)).

and the transformation from the computational domain to the material configuration:

$$\begin{aligned} \Psi^{-1} : R_X \times [t_0, t_{\text{final}}[&\longrightarrow R_\chi \times [t_0, t_{\text{final}}[\\ (\boldsymbol{X}, t) &\longmapsto \Psi^{-1}(\boldsymbol{X}, t) = (\boldsymbol{\chi}, t) \end{aligned}$$

The three applications are not independently defined, and the following composition of mapping exists: (illustrated in Figure A.1):

$$\boldsymbol{\varphi} = \boldsymbol{\Phi} \circ \boldsymbol{\Psi}^{-1} \tag{A.0.1}$$

The gradients of each transformation can be expressed as matrices:

$$\frac{\partial \boldsymbol{\varphi}(\boldsymbol{X}, t)}{\partial (\boldsymbol{X}, t)} = \begin{pmatrix} \frac{\partial \boldsymbol{x}}{\partial \boldsymbol{X}} & \boldsymbol{v} \\ 0^T & 1 \end{pmatrix}, \quad \frac{\partial \boldsymbol{\Phi}(\boldsymbol{\chi}, t)}{\partial (\boldsymbol{\chi}, t)} = \begin{pmatrix} \frac{\partial \boldsymbol{x}}{\partial \boldsymbol{\chi}} & \hat{\boldsymbol{v}} \\ 0^T & 1 \end{pmatrix}, \quad \frac{\partial \boldsymbol{\Psi}^{-1}(\boldsymbol{\chi}, t)}{\partial (\boldsymbol{\chi}, t)} = \begin{pmatrix} \frac{\partial \boldsymbol{X}}{\partial \boldsymbol{\chi}} & \boldsymbol{w} \\ 0^T & 1 \end{pmatrix} \tag{A.0.2}$$

where $\boldsymbol{v}$ is the material velocity, which is the velocity of the particles evaluated in the spatial frame of reference, $\hat{\boldsymbol{v}}$ expresses the mesh velocity (the velocity of the computational frame evaluated in the spatial frame of reference) and $\boldsymbol{w}$ is the velocity of particle

evaluates in the computational frame of reference.

$$\boldsymbol{v} = \frac{\partial \boldsymbol{x}}{\partial t}|_{\boldsymbol{X}}, \quad \hat{\boldsymbol{v}} = \frac{\partial \boldsymbol{x}}{\partial t}|_{\boldsymbol{\chi}}, \quad \boldsymbol{w} = \frac{\partial \boldsymbol{\chi}}{\partial t}|_{\boldsymbol{X}} \tag{A.0.3}$$

In a fully Lagrangian approach, there is no relative motion between the particles and the mesh, which translated into:$\boldsymbol{w} = 0$ and $\boldsymbol{v} = \hat{\boldsymbol{v}}$. Whereas in a fully Eulerian approach, the computational frame of reference and the spatial frame of reference coincide: $\hat{\boldsymbol{v}} = 0$ and $\boldsymbol{v} = \boldsymbol{w}$

The differentiation of Equation (A.0.1) leads to:

$$\frac{\partial \varphi(\boldsymbol{X}, t)}{\partial(\boldsymbol{X}, t)} = \frac{\partial \Phi(\boldsymbol{\chi}, t)}{\partial(\boldsymbol{\chi}, t)} \frac{\partial \Psi^{-1}(\boldsymbol{\chi}, t)}{\partial(\boldsymbol{\chi}, t)} \tag{A.0.4}$$

If each terms is replaced by its definition (Equations (A.0.2)), it leads to the definition of the convective velocity $\boldsymbol{c}$, which is the velocity between the material and the mesh:

$$\boldsymbol{c} = \boldsymbol{v} - \hat{\boldsymbol{v}} = \frac{\partial \boldsymbol{x}}{\partial \boldsymbol{\chi}} \cdot \boldsymbol{w} \tag{A.0.5}$$

The fundamental ALE equations are then obtained by replacing the velocity in the spatial frame of reference $\boldsymbol{v}$ by the convective velocity $\boldsymbol{c}$ in the convective terms of the continuity and momentum equations:

$$\frac{\partial \rho}{\partial t}|_{\boldsymbol{\chi}} + \boldsymbol{c} \cdot \boldsymbol{\nabla} \rho = 0 \tag{A.0.6}$$

$$\rho \left(\frac{\partial \boldsymbol{v}}{\partial t}|_{\boldsymbol{\chi}} + (\boldsymbol{c} \cdot \boldsymbol{\nabla}) \boldsymbol{v} \right) = \boldsymbol{\nabla} \cdot \boldsymbol{\sigma} + \rho \boldsymbol{g} \tag{A.0.7}$$

where ρ is the density, σ the Cauchy stress tensor and $\boldsymbol{g}$ the gravity force vector. It must be noted that in both equation the derivatives in the spatial frame of reference are replaced by derivatives in the computational frame of reference. New terms related to the mesh velocity $\hat{\boldsymbol{v}}$ appear in the left hand side of each equation.

Finally, when considering fluid-structure interactions, the following boundary conditions are applied at the interface: the velocity of the fluid and the structure (subscript s) must

coincide along the interface for a viscous fluid:

$$u = u_s \text{ continuity of displacement}$$

$$v = v_s \text{ continuity of velocities}$$

The integral forms of the equations of the ALE formulation can be found in Donea et al. (2004)

Appendix B

UDF for fluid structure interactions

B.1 Finite Element Method: openFEM

The FEM analysis is done using the open-source package openFEM[1], which runs within Matlab. The underlying ideas of Finite Element Analysis is to divide the domain into small finite segments, and the behaviour of each of these elements is described by the displacements of the elements and the material laws. All elements are assembled together and the requirements of continuity and equilibrium are satisfied between the neighbouring elements. Provided that the boundary conditions of the actual problem are satisfied, a unique solution can be obtained to the overall system of linear algebraic equations. (Becker, 2008)

B.2 Running the flow solver ANSYS-Fluent with fluid-structure interactions

The structural properties and the mode shapes of the cantilever are obtained from the FEM analysis. Two files are output at the end of the FEM analysis:

1. "*dyn_properties.txt*": contains the structural properties of the structure:

    - l, A, rho: the height, the cross section and the density of the material respec-

[1]The documentation about openFEM can be found at `http://www.sdtools.com/openfem/`, it is distributed under the LGPL license.

tively,

- EIx, EIy: the flexural stiffness in the along-wind and the cross-wind directions respectively,
- Mnx, Mny: the generalised mass in the along-wind and the cross-wind directions respectively,
- Knx, Kny: the generalised stiffness in the along-wind and the cross-wind directions respectively, and
- wnx, wny: the natural frequency in the along-wind and the cross-wind directions respectively.

2. "*mode_shapes.txt*": contains the mode shapes information of the first mode in each direction.

B.3 The FSI program (the UDF): functions and Macros

As explained in section 5.3.3, the FSI program is a User-Defined Function that is called by the flow solver. The UDF is composed of a number of auxiliary functions, and MACROS, which allow the user to access and modify solver data.

B.3.1 Auxiliary functions in the UDF

The following auxiliary functions are used in the UDF:

1. Functions that store the initial position of the nodes:

   find_Index_C: stores the initial position of the nodes of the cantilever,

   find_Index_RZ: stores the initial position of the nodes in the rigid zone.

2. Functions that describe that the mode shapes:

   phi_x: first mode in the along-wind direction,

   phi_y: first mode in the cross-wind direction.

3. Functions that describe the schemes to discretisize the equation of the structure motion:

   Euler scheme (1^{st} order): euler_y_npl and euler_ydot_npl,

   4^{th} order Adam Bashforth[2]: AB4_y_npl[3] and AB4_ydot_npl[4].

   F_ydotdot_npl: discretizes Equation (5.3.6) and computes $\ddot{y}$.

4. Functions that move the nodes on the cantilever and in the rigid zone:

   new_position_C: moves the nodes of the cantilever in the along-wind and across-wind directions,

   new_position_RZ: moves the nodes in the rigid zone in the along-wind and across-wind directions.

B.3.2 Main body of the UDF

The rest of the UDF is composed of MACROS functions, that are specifically designed to interact with the flow solver.

Macros called once at the beginning of the calculation:

1. Define_On_Demand(Load_FEData): effectively read the files produced by the Finite Element Analysis.

2. Define_On_Demand(Store_Cantilever): store the initial position of the nodes of the cantilever.

3. Define_On_Demand(Store_rigid_zone): store the initial position of the nodes in the rigid zone (zone surrounding the cantilever).

4. Define_On_Demand(close_files) and Define_On_Demand(open_files): open and close the files in which the forces coefficients and the response of the building are written.

[2]The scheme is described in section 5.3.2.
[3]Refers to Equation (5.3.7)
[4]Refers to Equation (5.3.8)

Macros called at each time step:

1. Define_execute_at_end(calc_F): this macro is called at the last iteration of each time step, it computes the forces acting on the structure and solves the equation of motion for the structure.

2. Define_Grid_Motion(cantilever,...): this macro is attached to the building, and calls the function new_position_C that moves the nodes of the cantilever (it receives the time-dependant part of the response from Define_execute_at_end(calc_F)).

3. Define_Grid_Motion(rigidzone,...): this macro is attached to the nodes in the rigid zone and calls the function new_position_RZ that moves the nodes in the rigid zone (it also receives the time-dependant part of the response from Define_execute_at_end(calc_F)).

The types of data are real (double) and integers.

B.4 The UDF for FSI

B.4.1 Parallelisation of the code

The code is parallelised as all the runs have to be run in parallel due to the large number of cells involved. The domain is split into a number of partition, and each data partition is assigned to a different compute process (compute-node). The compute-nodes hold all the mesh information while the host does not contain any information about mesh cells, faces, or nodes. The host sends commands to the compute-nodes, and more importantly gather the data when needed. Figure B.1 shows when and in what order the operations are called on the host, the compute node 0 and the rest of the compute nodes.

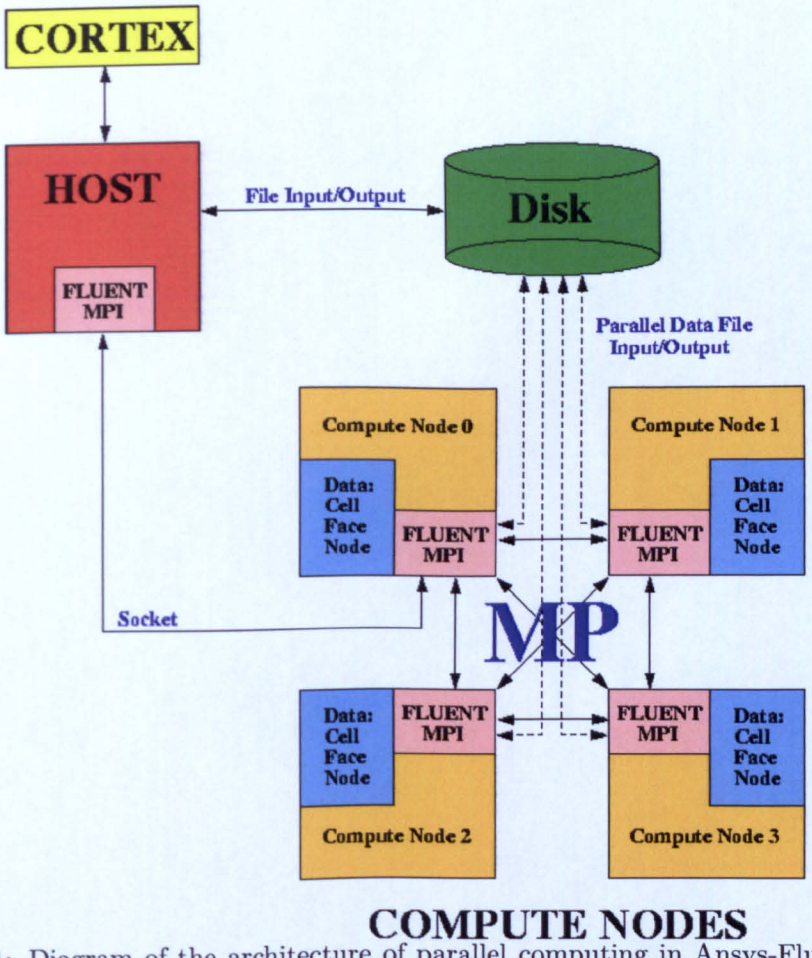

Figure B.1: Diagram of the architecture of parallel computing in Ansys-Fluent: host, and compute-node zero and other compute nodes (ANSYS, 2009).

In the UDF, the parts that computes the forces acting on the building are called on the compute-nodes and these parts are indicated by "if #if ! RP_HOST". The part that computes the response of the building is called on the host (indicated by "if #if ! RP_NODE"), and finally the nodes of the mesh are moved from the compute-nodes only.

B.4.2 The UDF

```
1
  /************************************************************
   UDF to move the nodes of a cantilever, dynamic response to
   wind loading
   ************************************************************/
6 #include "udf.h"
  #include "math.h"
```

```
#include "unsteady.h"

#define DEBUG 0

#define MAX_NODES_C 5000      /* Number of nodes of the cantilever*/
#define MAX_NODES_RZ 160000 /* Number of nodes in the rigid zone */

int nodeIndex_C[MAX_NODES_C]; /* Vector listing the local node index
    of the cantilever nodes */
int nodeIndex_RZ[MAX_NODES_RZ];/* Vector listing the local node index
    of the nodes in the rigid zone */
int ID_C = 4;       /*This is the index of the cantilever thread,
   filled with non-sense value, to be defined at the beginning of
   each simulation*/
int ID_RZ = 3;      /* This is the index of the rigid zone thread, to
   be defined at the beginning of each simulation */
int ID_moving = 2;/* This is the index of the zone around the rigid
   zone, to be defined before each simulation*/

/* Parameters for the equation defining the mode shape:*/
real a[7];          /* coefficients of the polynomial expression for
   first mode shape in X direction */
real b[7];     /* coefficients of the polynomial expression for first
   mode shape in Y direction */

real L;             /* Height of the cantilever (in meters)*/
real rho;           /* solid material density */
real A;             /* core section (1m x 2m) of the structure */
real wnx, wny;      /* first natural frequency X dir, second mode
   frequency Y dir*/
real quix = 0.01; /*damping ratio*/
real quiy = 0.01; /*damping ratio */
real EIx, EIy;      /* flexural stiffness in each direction */


/* Parameters for solving the differential equation for dynamic
   response*/
real Mnx, Mny;      /* Mass per unit length of the structure */
real Knx, Kny;          /* Generalized stiffness matrix*/


real P_lift, P_drag;  /* Lift and drag force acting on the building
   */

real real_time = 0;

/* Vector containing the coordinates of the cantilever nodes, in the
   same order as in nodeIndex_C */
real init_C_X[MAX_NODES_C];
real init_C_Y[MAX_NODES_C];
real init_C_Z[MAX_NODES_C];
/* Vector containing the coordinates of the rigid zone nodes, in the
   same order as in nodeIndex_RZ */
real init_RZ_X[MAX_NODES_RZ];
real init_RZ_Y[MAX_NODES_RZ];
```

```
real init_RZ_Z[MAX_NODES_RZ];

real tol = 0.001; /* Tolerance: means that the first node of the
    cantilever to be moved is at 0.001m above the ground */
real dts = 0.005; /* Time step size, updated later */
count = 0;/* variable that is incremented at each time step: ensures
    that the mesh is not moved at the first and second time step */

/*Time-dependent component of the mode shape */
real Zt_x = 0.0 ;
real Zt_x_1 = 0.0;
real Zt_x_2 = 0.0;
real Zt_y = 0.0 ;
real Zt_y_1 = 0.0;
real Zt_y_2 = 0.0;

/*Time-dependent component of the mode shape Y direction */
real y_npl, y_n, y_nml, y_nm2, y_nm3;
real ydot_npl, ydot_n, ydot_nml, ydot_nm2, ydot_nm3;
real ydotdot_npl, ydotdot_n, ydotdot_nml, ydotdot_nm2, ydotdot_nm3;

/*Time-dependent component of the mode shape X direction */
real x_npl, x_n, x_nml, x_nm2, x_nm3;
real xdot_npl, xdot_n, xdot_nml, xdot_nm2, xdot_nm3;
real xdotdot_npl, xdotdot_n, xdotdot_nml, xdotdot_nm2, xdotdot_nm3;

/* define another Z for X motion */

FILE *file_forces,*file_zt, *file_dynpro, *file_modeshape;
int newfileN = 1;

/*FILE *file_forces; file containing values of lift, drag, the total
    wind loading at each time step*/
/*FILE *file_Z; file with values of Zt, the time-dependent component
    of the mode shape*/

/*=============================================================*/
/*=============AUXILIARY FUNCTIONS=============================*/
/*=============================================================*/
/*This function returns the position of a node in the list
    nodeIndex_C, knowing its global index*/
int findIndex_C(int index)
{
  int i;
  for(i=0;i<MAX_NODES_C;i++)
    {
      if ( nodeIndex_C[i] == index )
 break;
    }
  return (i);
}
/*=============================================================*/
/*This function returns the position of a node in the list
    nodeIndex_RZ, knowing its global index*/
int findIndex_RZ(int index)
```

```
{
  int i;
101  for(i=0;i<MAX_NODES_RZ; i++)
    {
      if ( nodeIndex_RZ[i] == index )
 break;
    }
106  return (i);

}
/*=============================================================*/
/*===Spatial-dependent component of the mode shape============*/
111 /*Mode shape in X direction */
real phi_x(real z)
{
    return 1*(a[6]*z*z*z*z*z*z*z + a[5]*z*z*z*z*z*z + a[4]*z*z*z*z + a
        [3]*z*z*z + a[2]*z*z + a[1]*z + a[0]);

116 }

/*Mode shape in Y direction */
real phi_y(real z)
{
121     return 1*(b[6]*z*z*z*z*z*z*z + b[5]*z*z*z*z*z*z + b[4]*z*z*z*z + b
        [3]*z*z*z + b[2]*z*z + b[1]*z + b[0]);

}

/*=============================================================*/
126 /*Calc of time-dependent compononent of the mode shape Y*/
real F_ydotdot_npl(real Fy_Pnpl, real Ydot_npl, real Y_npl)
{
 real Cn2 = 2*wny*quiy*Mny; /*damping*/
   return (1/Mny)*( Fy_Pnpl - Cn2*Ydot_npl - Kny*Y_npl );
131 }

/* Euler differencing (1st order) */
real euler_y_npl(real Y_n, real Ydot_n, real h)
{
136  real A;
 A = Y_n + h*(Ydot_n);
 return A;
}
real euler_ydot_npl(real Ydot_n, real Ydotdot_n, real h)
141 {
 real A;
 A = Ydot_n + h*(Ydotdot_n);
 return A;
}
146
/* Adam Bashforth differencing four-step (4th order) */
real AB4_y_npl(real Y_n, real Ydot_n, real Ydot_nm1, real Ydot_nm2,
    real Ydot_nm3, real h)
{
 real A;
```

```
151  A = Y_n + h*( Ydot_n + 0.5*( Ydot_n - Ydot_nm1 ) + (5/12)*( Ydot_n -
         2*Ydot_nm1 + Ydot_nm2 ) + (3/8)*( Ydot_n - 3*Ydot_nm1 + 3*
         Ydot_nm2 - Ydot_nm3 ));
     return A;
     }
     real AB4_ydot_np1(real Ydot_n, real Ydotdot_n, real Ydotdot_nm1, real
         Ydotdot_nm2, real Ydotdot_nm3, real h)
     {
156  real A;
     A = Ydot_n + h*( Ydotdot_n + 0.5*( Ydotdot_n - Ydotdot_nm1 ) +
         (5/12)*( Ydotdot_n - 2*Ydotdot_nm1 + Ydotdot_nm2 ) + (3/8)*(
         Ydotdot_n - 3*Ydotdot_nm1 + 3*Ydotdot_nm2 - Ydotdot_nm3 ));
     return A;
     }

161

     /*=============================================================*/
     /* Calculation of the new position of nodes on cantilever=====*/
     void new_position_C(Node *v, real t, real Y, real X)
166  {
       int index;
       real yc0, zc0, yc, zc, zp, dl;
       real xc;
       real alpha, delta_y, delta_z;
171
       index = findIndex_C(NODE_INDEX(v)); /* Find node index in
           nodeIndex_C to know its initial position*/

       yc0 = 0.0;
       zc0 = init_C_Z[index];/*init_C_Z is the Z component of the initial
           position of the node */
176    zc = zc0; /* Initial height */

       dl = init_C_Y[index];/*init_C_Y is the Y component of the initial
           position of the node */

       yc = phi_y(zc)*Y;
181    xc = phi_x(zc)*X;

       if (DEBUG == 1)
       {Message("yc=%g\n",yc);}

186    /* The node is moved: */
       NODE_X(v) = init_C_X[index] + xc;
       NODE_Y(v) = init_C_Y[index] + yc;
       NODE_Z(v) = init_C_Z[index];

191  }
     /*=============================================================*/
     /* Calculation of new position of nodes on rigid zone=========*/
     void new_position_RZ(Node *v, real t, real Y, real X)
     {
196    int index;
       real yc0, zc0, yc, zc, zp, dl;
```

```
    real alpha, delta_y, delta_z;
    real xc;

    index = findIndex_RZ(NODE_INDEX(v)); /*Find node index in
        nodeIndex_C to know its initial position*/

    yc0 = 0.0;
    zc0 = init_RZ_Z[index];/*init_C_Z is the Z component of the initial
        position of the node */

    dl = init_RZ_Y[index];/*init_C_Z is the Y component of the initial
        position of the node */
    zc = zc0;

    yc = phi_y(zc)*Y;
    xc = phi_x(zc)*X;

    /*The node is moved: */
    NODE_X(v) = init_RZ_X[index] + xc;
    NODE_Y(v) = init_RZ_Y[index] + yc;
    NODE_Z(v) = init_RZ_Z[index];
}

/*=============================================================*/
/*=================MAIN BODY===================================*/
/*=================DEFINE MACROS===============================*/

/*===DEFINE ON DEMAND MACROS===================================*/

/*===Load data from finite element analysis====================*/
DEFINE_ON_DEMAND(Load_FEData)
{

 #if !RP_NODE
 if (DEBUG == 1)
 {
  Message("define on demand Load_FEData started\n");
 }
 /* load L, A, rho, EIx EIy Mnx Mny Knx Kny wnx wny */
 file_dynpro = fopen("dyn_properties.txt","r");
 fscanf (file_dynpro, "%g\n", &L);
 fscanf (file_dynpro, "%g\n", &A);
 fscanf (file_dynpro, "%g\n", &rho);

 Message("L=%g, A=%g, rho=%g",L,A,rho);

 fscanf (file_dynpro, "%g\n", &EIx);
 fscanf (file_dynpro, "%g\n", &EIy);
 fscanf (file_dynpro, "%g\n", &Mnx);
 fscanf (file_dynpro, "%g\n", &Mny);
 fscanf (file_dynpro, "%g\n", &Knx);
 fscanf (file_dynpro, "%g\n", &Kny);
 fscanf (file_dynpro, "%g\n", &wnx);
 fscanf (file_dynpro, "%g\n", &wny);
 Message("EIx=%g, EIy=%g\n",EIx,EIy);
```

```
    Message("Mnx=%g, Mny=%g\n",Mnx,Mny);
    Message("Knx=%g, Kny=%g\n",Knx,Kny);
    Message("wnx=%g, wny=%g\n",wnx,wny);
      fclose (file_dynpro);

    /* ------------------------------------------------------*/
    Kny = Kny_forced;
    wny = wny_forced;
    /* ------------------------------------------------------*/

      file_modeshape = fopen("fem_analysis.txt","r");
      fscanf (file_modeshape,"%g %g %g %g %g %g %g\n", &a[6], &a[5], &a
          [4], &a[3], &a[2], &a[1], &a[0]);
      Message("a6=%g, a5=%g, a4=%g, a3=%g, a2=%g, a1=%g, a0=%g\n",a[6],a
          [5],a[4],a[3],a[2],a[1],a[0]);
      fscanf (file_modeshape,"%g %g %g %g %g %g %g\n", &b[6], &b[5], &b
          [4], &b[3], &b[2], &b[1], &b[0]);
      Message("b6=%g, b5=%g, b4=%g, b3=%g, b2=%g, b1=%g,b0=%g\n",b[6],b
          [5],b[4],b[3],b[2],b[1],b[0]);
      fclose (file_modeshape);

      /*Initialize time-dependent components of the mode shape */
      y_np1 = 0.0; y_n = 0.0; y_nm1 = 0.0; y_nm2 = 0.0; y_nm3 = 0.0;
    ydot_np1 = 0.0; ydot_n = 0.0; ydot_nm1 = 0.0; ydot_nm2 = 0.0;
       ydot_nm3 = 0.0;
    ydotdot_np1 = 0.0; ydotdot_n = 0.0; ydotdot_nm1 = 0.0; ydotdot_nm2 =
        0.0; ydotdot_nm3 = 0.0;

    #endif
    }


    /*===Store the index of the cantilever nodes and store their initial
        position*/
    DEFINE_ON_DEMAND(Store_Cantilever)
    {

    #if !RP_HOST   /* Compile this section for computing processes only (
        serial
                       and node)  since these variables are not available
                       on the host */

        Domain *d;
        Thread *ft_C ;
        face_t f;
        Node *v;
        int i, n, ml, found, v_index;

    #endif /* !RP_HOST */


    host_to_node_int_1(ID_C);/* Send the ID value to all the nodes */

    #if RP_NODE /*Does nothing in serial, on compute nodes in parallel*/
     Message("\nNode %d is calculating on thread # %d\n",myid,ID_C); /*OK
          !!! */
```

```
#endif /* RP_NODE */

#if !RP_HOST /* SERIAL or compute nodes in parallel */

    d = Get_Domain(1); /* d defines the domain in which one works,
       here there is only one domain containing the entire mesh */
    ft_C = Lookup_Thread(d,ID_C); /* ID_C identifies the cantilever
       within the mesh, so ct_C will be used to loop over the
       cantilever nodes*/

    /* Initialisation of the lists with non-sense*/
    for(i=0;i<MAX_NODES_C;i++)
      {
  nodeIndex_C[i] = -99;
  init_C_X[i] = 0;
  init_C_Y[i] = 0;
  init_C_Z[i] = 0;
      }

    ml = 0;
/* Loop over the nodes of the cantilever in order to store their
   index and position: */

    /* loop over the faces of the cantilever identified by ft_C, at
       each loop f identifies another face:*/
    begin_f_loop(f,ft_C)
      {
  if PRINCIPAL_FACE_P(f,ft_C) /* Always TRUE in serial version, in
     parallel, check that the face is the principal one on the
     compute node so that the face is not computed twice */
  {
   /* loop over the nodes within the face f, at each loop n
      identifies another node of the face f*/
   f_node_loop(f,ft_C,n)
   {
        v = F_NODE(f,ft_C,n);/* return the global node index of n in
            v */
        v_index = NODE_INDEX(v);/* store the global node number of v
           into v_index */

        /* only for the first loop, the first node index found
           v_index is put as first scalar in the vector nodeIndex_C
           [0] and its coordinates are stored init_C[0][x..z]*/
         if ( ml == 0 )
          {
           nodeIndex_C[ml] = v_index;
           /*Message("\nNode # %d",v_index);*/
           init_C_X[ml] = NODE_X(v);
           init_C_Y[ml] = NODE_Y(v);
           init_C_Z[ml] = NODE_Z(v);
           ml++;/*ml is now strictly superior to 0, nodeIndex_C[1]
              and init_C[1][x..z] can be filled */
          }
         else /* applied from second loop */
          {
```

```
                found = 0; /* true if the node index has not been already
                    stored in the vector nodeIndex[] */
                for (i=0;i<ml;i++) /* search for the node in the vector
                   nodeIndex */
        {
341       if ( v_index == nodeIndex_C[i] )
            {
              found = 1;
              break; /* if node index already stored, then break and
                  loop over another node */
            }
346      }
            if ( found == 0 ) /* if node has not been found, then the
                 node index is stored in the vector nodeIndex[ml] and
                 its coordinates are stored in init_C[ml]x..z]*/
        {
          nodeIndex_C[ml] = v_index;
          init_C_X[ml] = NODE_X(v);
351       init_C_Y[ml] = NODE_Y(v);
          init_C_Z[ml] = NODE_Z(v);
          ml++;
        }
           }
356
     }
    }
       }
      end_f_loop(f,ft_C);
361
      Message("\n %d nodes stored", ml);

  #endif

366 /* Open the files to store the lift and drag and the response
      amplitude*/
  # if !RP_NODE

     char *filename_forces;
     char * filename_response;
371
     filename_forces="forces.txt";
     filename_response="zt.txt";

     file_forces = fopen(filename_forces,"w");
376  file_response = fopen(filename_response,"w");
  #endif


  }
381
  /*===Store the position of the nodes in the rigid zone=====*/
  DEFINE_ON_DEMAND(Store_rigidzone)
  {
  #if !RP_HOST   /* Compile this section for computing processes only (
      serial
```

```
                    and node)  since these variables are not available
                    on the host */
      Domain *d;
      Thread *ct_RZ ;
      cell_t c;
      Node *v;
      int i, n, ml, p, found_in_RZ, v_index, found_in_C;

#endif /* !RP_HOST */

 host_to_node_int_1(ID_RZ);/* Send the ID value to all the nodes */

#if RP_NODE /*Nothing in serial, compute nodes in parallel*/
 Message("\nNode %d is calculating on thread # %d\n",myid,ID_RZ);
#endif /* RP_NODE */

#if !RP_HOST /* SERIAL or Compute NODE in parallel*/

      d = Get_Domain(1);
      ct_RZ = Lookup_Thread(d,ID_RZ);

      for(i=0;i<MAX_NODES_C;i++)
        {
    nodeIndex_RZ[i] = -99;
    init_RZ_X[i] = 0;
    init_RZ_Y[i] = 0;
    init_RZ_Z[i] = 0;
      }

      ml = 0;

   Message("\nNode %d has done the initialisation",myid);

      begin_c_loop(c,ct_RZ)
        {
   c_node_loop(c,ct_RZ,n)
   {
    v = C_NODE(c,ct_RZ,n);
    v_index = NODE_INDEX(v);
    found_in_C = 0;
    /*Message("\nNode # %d inves",v_index);*/
    for(p=0;p<MAX_NODES_C;p++)
        {
            if ( v_index == nodeIndex_C[p])
     {
        found_in_C = 1;
        break;
     }
        }

        if(found_in_C == 0)
        {
     if ( ml == 0 )
     {
      nodeIndex_RZ[ml] = v_index;
```

```
441           Message("\nFirst Node # %d stored in RZ\n",v_index);
          init_RZ_X[ml] = NODE_X(v);
          init_RZ_Y[ml] = NODE_Y(v);
          init_RZ_Z[ml] = NODE_Z(v);
          ml++;
446       }
          else
          {
           found_in_RZ = 0;

451        for (i=0;i<ml;i++)
           {
           if ( v_index == nodeIndex_RZ[i] )
            {
            found_in_RZ = 1;
456         break;
            }
           }
           if ( found_in_RZ == 0 )
            {
461         nodeIndex_RZ[ml] = v_index;

            init_RZ_X[ml] = NODE_X(v);
            init_RZ_Y[ml] = NODE_Y(v);
            init_RZ_Z[ml] = NODE_Z(v);
466         ml++;
            }
         }
        }

471   }

          }
        end_c_loop(c,ct_RZ);

476     Message("\n %d nodes stored", ml);

  #endif

  }
481
  /*===Close and open new files in case of restart=========*/
  DEFINE_ON_DEMAND(close_files)
  {
  #if !RP_NODE
486

   fclose(file_forces);
   fclose(file_response);
  #endif
491 }

  DEFINE_ON_DEMAND(open_files)
  {
  #if !RP_NODE
```

```
496  /*append file names with time step*/

     file_forces = fopen("forces2.txt","w");
     file_response = fopen("Zt2.txt","w");
    #endif
501 }

    /*=============EXECUTE AT END MACRO=============================*/
    /*===Calculation of the forces acting on the building ===*/
    DEFINE_EXECUTE_AT_END(calc_F)
506 {
     if (DEBUG == 1)
     {
      Message("\ndefine execute at end started\n");
     }
511  #if !RP_HOST
     Domain *d;
     Thread *ft_C;
     face_t f;
       Node *v;
516    d = Get_Domain(1);

       real x[ND_ND],NV_VEC(f_A);


521  if(DEBUG == 1)
     { Message("d has been defined\n");}

     ft_C = Lookup_Thread(d,ID_C);

526    P_lift = 0.0;
       P_drag = 0.0;
       test_shear_x = 0.0;
       test_shear_y = 0.0;


531
     begin_f_loop(f,ft_C)
     {
        if PRINCIPAL_FACE_P(f,ft_C)
       {
536       F_CENTROID(x,f,ft_C);
          F_AREA(f_A,f,ft_C);
          P_lift += F_P(f,ft_C)*f_A[1] ;
       /*f_A[1] = Y component of the vector normal to the face, will be
           positive if face on the sides*/
          P_drag += F_P(f,ft_C)*f_A[0] ;

541
       }
     }
     end_f_loop(f,ft_C);


546
     # if RP_NODE /* Perform node synchronized actions here, Does
         nothing in Serial */
     /*Sum over the compute nodes for the value of Fm_X[i], Fm_Y[i],
```

```
      Fm_Z[i] */
    P_lift = PRF_GRSUM1(P_lift);
    P_drag = PRF_GRSUM1(P_drag);
    Message("lift=%g\n",P_lift); /*Display on screen the lift acting on
        the building */
    Message("drag=%g\n",P_drag); /*Display on screen the drag acting on
        the building */
    # endif /* RP_NODE */

  #endif  /*!RP_HOST */

  /* Pass the node's total area and pressure to the Host for averaging
      */
  /* Does nothing in SERIAL */
  node_to_host_real_1(P_lift);
  node_to_host_real_1(P_drag);


  #if !RP_NODE /* SERIAL or HOST in parallel*/

    real curr_ts;
    curr_ts = N_TIME; /*Current iteration */
    char *filename_forces;
    char *filename_response;
    real integral_phi_y = 0.0;
    real integral_phi_x = 0.0;
    int i;

    if(curr_ts!=0){
    dts = CURRENT_TIMESTEP ;} /*time step size */
    else
    { dts=0.5;}

    real_time = CURRENT_TIME;

    /* Get integral of phi_y */
    for(i=0; i<20; i++)
    {
     integral_phi_y += (L/20) * (phi_y(L*i/20) - phi_y(L*(i+1)/20) );
    }
    /* Get integral of phi_x */
    for(i=0; i<20; i++)
    {
     integral_phi_x += (L/20) * (phi_x(L*i/20) - phi_x(L*(i+1)/20) );
    }

    P_lift = P_lift*integral_phi_y;
    P_drag = P_drag*integral_phi_x;

    fprintf(file_forces,"%f %f %f %f %f\n",real_time,P_lift, P_drag,
       test_shear_x, test_shear_y);/*Print lift in a file */

     /*For the first three time steps, do nothing: */
     if((count == 0) || (count == 1) || (count == 2) || (count == 3))
     {
```

```
        /* Response to lift */
601     y_nm3 = y_nm2;
        ydot_nm3 = ydot_nm2;
        ydotdot_nm3 = ydotdot_nm2;

        y_nm2 = y_nm1;
606     ydot_nm2 = ydot_nm1;
        ydotdot_nm2 = ydotdot_nm1;

        y_nm1 = y_n;
        ydot_nm1 = ydot_n;
611     ydotdot_nm1 = ydotdot_n;

        y_n = y_np1;
        ydot_n = ydot_np1;
        ydotdot_n = ydotdot_np1;
616
      /*Solve the temporal-dependent component of the mode shape */
        y_np1 = euler_y_np1(y_n, ydot_n, dts);
        ydot_np1 = euler_ydot_np1(ydot_n, ydotdot_n, dts);
        ydotdot_np1 = F_ydotdot_np1(P_lift, ydot_np1, y_np1);
621
      /* Response to drag */
        x_nm3 = x_nm2;
        xdot_nm3 = xdot_nm2;
        xdotdot_nm3 = xdotdot_nm2;
626
        x_nm2 = x_nm1;
        xdot_nm2 = xdot_nm1;
        xdotdot_nm2 = xdotdot_nm1;

631     x_nm1 = x_n;
        xdot_nm1 = xdot_n;
        xdotdot_nm1 = xdotdot_n;

        x_n = x_np1;
636     xdot_n = xdot_np1;
        xdotdot_n = xdotdot_np1;

      /*Solve the temporal-dependent component of the mode shape */
        x_np1 = euler_y_np1(x_n, xdot_n, dts);
641     xdot_np1 = euler_ydot_np1(xdot_n, xdotdot_n, dts);
        xdotdot_np1 = F_xdotdot_np1(P_drag, xdot_np1, x_np1);

          count += 1;
      }
646
      else
      {
        y_nm3 = y_nm2;
        ydot_nm3 = ydot_nm2;
651     ydotdot_nm3 = ydotdot_nm2;

        y_nm2 = y_nm1;
```

```
        ydot_nm2 = ydot_nm1;
        ydotdot_nm2 = ydotdot_nm1;
656
      y_nm1 = y_n;
      ydot_nm1 = ydot_n;
      ydotdot_nm1 = ydotdot_n;

661   y_n = y_npl;
      ydot_n = ydot_npl;
      ydotdot_n = ydotdot_npl;

     /* Solve the temporal-dependent component of the mode shape */
666   y_npl = AB4_y_npl(y_n, ydot_n, ydot_nm1, ydot_nm2, ydot_nm3, dts)
          ;
      ydot_npl = AB4_ydot_npl(ydot_n, ydotdot_n, ydotdot_nm1,
         ydotdot_nm2, ydotdot_nm3, dts);
      ydotdot_npl = F_ydotdot_npl(P_lift, ydot_npl, y_npl);

      /* Response to drag */
671   x_nm3 = x_nm2;
        xdot_nm3 = xdot_nm2;
        xdotdot_nm3 = xdotdot_nm2;

        x_nm2 = x_nm1;
676     xdot_nm2 = xdot_nm1;
        xdotdot_nm2 = xdotdot_nm1;

      x_nm1 = x_n;
      xdot_nm1 = xdot_n;
681   xdotdot_nm1 = xdotdot_n;

      x_n = x_npl;
      xdot_n = xdot_npl;
      xdotdot_n = xdotdot_npl;
686
     /* Solve the temporal-dependent component of the mode shape */
      x_npl = AB4_y_npl(x_n, xdot_n, xdot_nm1, xdot_nm2, xdot_nm3, dts)
          ;
      xdot_npl = AB4_ydot_npl(xdot_n, xdotdot_n, xdotdot_nm1,
         xdotdot_nm2, xdotdot_nm3, dts);
      xdotdot_npl = F_xdotdot_npl(P_drag, xdot_npl, x_npl);
691
        Message("y(t)=%g\n",y_npl); /* Display value of Zt computed */
        fprintf(file_response,"%f %f\n",real_time,y_npl); /* Also print
           Zt into a file */

     count += 1;
696   }

   #endif /* !RP_NODE */

    host_to_node_real_2(y_npl,x_npl);/* passes the value of Zt computed
        on the HOST to the compute nodes*/
701
  }
```

```
   /*==========DEFINE GRID MOTION MACROS==========*/
   /*===Move the node of the building===========*/
DEFINE_GRID_MOTION(cantilever,domain,dt,time,dtime)
   {

    if(DEBUG==1)
    {Message("DGM on C started");}
   /* Variables declared on the master node and the compute nodes */
   # if RP_NODE
     Message("\nNode %d is calculating on its part of the cantilever",
        myid);
   # endif /* RP_NODE */


   #if !RP_HOST /*serial or compute nodes in parallel*/

     Thread *ft;
     face_t f;
     Node *v;
     int n;
     real x[ND_ND],NV_VEC(f_A);

     ft = DT_THREAD(dt);

   #endif

   #if !RP_HOST /* SERIAL or compute nodes in parallel */

     begin_f_loop(f,ft)/*Loop over the nodes of the cantilever */
     {
     if PRINCIPAL_FACE_P(f,ft) /*Ensures that if a node belongs to two
        partitions, it is moved only once (by the partition that "owns"
        the node*/
     {
          f_node_loop(f,ft,n)
     {
       v = F_NODE(f,ft,n);

       if ((NODE_Z(v) > 0.003) && (NODE_POS_NEED_UPDATE (v))) /*
          Ensures that the nodes are moved only once*/
         {
          NODE_POS_UPDATED(v); /*NODE_POS_UPDATED turns true when
              the node is moved, which turns NODE_POS_NEED_UPDATE to
              false */
          new_position_C(v,time, y_npl, x_npl); /* Move the nodes of
              the cantilever */

         }
     }
   }
   }
     end_f_loop(f,ft);
   #endif
```

```
751 }

    /*===Move the node in the rigid zone, surrounding the building*/
    DEFINE_GRID_MOTION(rigidzone,domain,dt,time,dtime)
    {
756
     /*int i;*/
    if(DEBUG==1)
    {Message("DGM on RZ started");}
   # if RP_NODE
761   Message("\nNode
      d is calculating on its part of the cantilever",myid);
   # endif /* RP_NODE */


766 #if !RP_HOST /*serial or compute nodes in parallel*/

      Thread *frz,*fc, *moving;
      cell_t cl;
      face_t fl;
771   Node *vl;
      int nl, found,p;
      real y_npl_scaled;

      frz = DT_THREAD(dt);
776   fc = Lookup_Thread(domain,ID_C);

      /* set deforming flag on adjacent cell zone, this allow the mesh
         around the cantilever to deform. If this is not specified,
         negative cells appear and the run cannot carry on. But this MUST
          be commented if the motion of the nodes in the rigid zone
         around the cantilever is already specified*/
     moving = Lookup_Thread(domain,ID_moving);
     SET_DEFORMING_THREAD_FLAG(moving);
781
   #endif  /*!RP_HOST */


   #if !RP_HOST /* SERIAL or compute nodes in parallel */
786
       begin_c_loop(cl,frz)
       {

            c_node_loop(cl,frz,nl)
791       {
          vl = C_NODE(cl,frz,nl);
          found =0;
          for(p=0;p<MAX_NODES_C;p++)
          {
796        if(NODE_INDEX(vl) == nodeIndex_C[p])
           {
            found = 1;
            break;
           }
801       }
```

```
        if(found == 0)
        {

806         if (NODE_Z(v1) > 0.003 && NODE_POS_NEED_UPDATE (v1))
              {
                NODE_POS_UPDATED(v1);
                new_position_RZ(v1, time, y_np1, x_np1);

811           }
            }
          }

    }
816   end_c_loop(c1,frz);
  #endif

  }
```

Appendix C

UDF for turbulent Inflow

As in the UDF for FSI, this UDF is composed of a number of auxiliary functions, and MACROS, which allow the user to access and modify solver data.

C.1 Auxiliary functions in the UDF

The following auxiliary functions are used in the UDF:

1. Functions to generate the random data:

   ran2: generate the random data,

   rnd_gen2: sets the mean of the random data to 0, and variance to 1.

2. Functions to define the integral length scales:

   L_u_x, ...

C.2 Scheme

Through the definition of a scheme file, Fluent allows the user to define new interactive menus. A scheme is used to allow the user to define the length scales for both regions, and the important constants to help define the velocity profile from the graphical interface. Figure C.1 shows the new menus in ANSYS-Fluent.

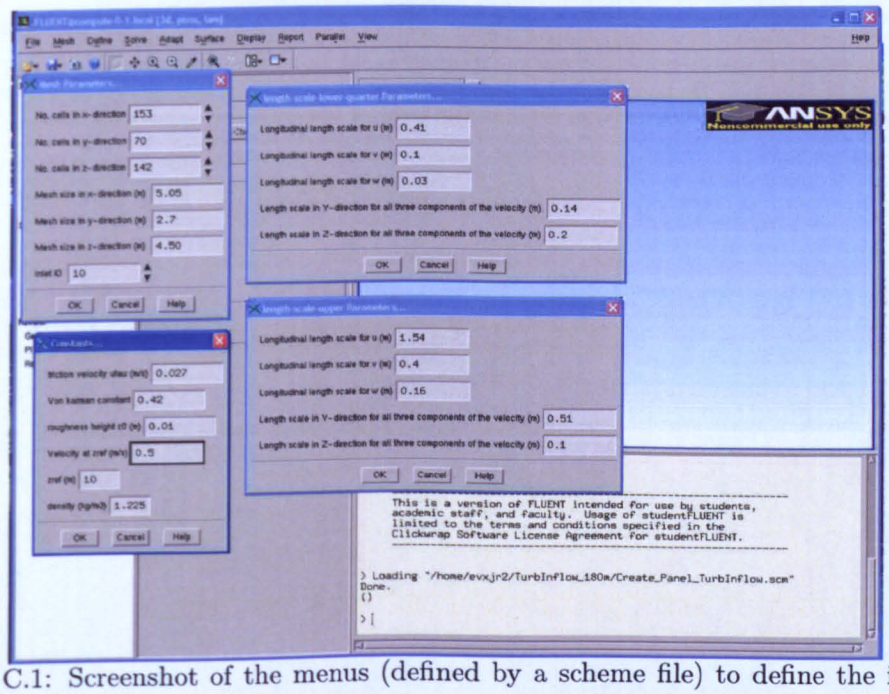

Figure C.1: Screenshot of the menus (defined by a scheme file) to define the integral lengths scales, and constants for the generation of the turbulent inflow.

C.2.1 Main body of the UDF

The rest of the UDF is composed of MACROS functions, that are specifically designed to interact with the flow solver.

Macros called once at the beginning of the calculation:

1. Define_On_Demand(update_variable_scheme): reads in the information entered via the graphical interface (scheme).

2. Define_On_Demand(reset): defines the filtering coefficients.

3. Define_On_Demand(mapping_interpolation): defines the mapping coefficient from the uniform virtual inlet mesh to the real non-uniform inlet mesh.

Macros called at each time step:

1. Define_adjust(update): computes the turbulent inflow (spatial filtering, temporal ...ng, and amplitude tensor).

2. Define_profile(...): these macros are defined for each of the component of the velocity, and call the turbulent inflow computed by Define_adjust(update).

C.3 The UDF

```
#include "udf.h"
#include "time.h"
#include "models.h"
#include "stdlib.h"
#include "stdio.h"
#include "math.h"
#include "sg.h"
#include "unsteady.h"

/* Constants for random number generator*/
#define IM1 2147483563
#define IM2 2147483399
#define AM (1.0/IM1)
#define IMM1 (IM1-1)
#define IA1 40014
#define IA2 40692
#define IQ1 53668
#define IQ2 52774
#define IR1 12211
#define IR2 3791
#define NTAB 32
#define NDIV (1+IMM1/NTAB)
#define EPS 1.2e-7
#define RNMX (1.0-EPS)

#define UDM_J 0   /* mapping, y direction vertical */
#define UDM_K 1 /* mapping, z direction horizontal */
#define UDM_Um  2 /* Umean */
#define UDM_U 3 /* u' */
#define UDM_V 4 /* v' */
#define UDM_W 5 /* w' */
#define NUM_OF_USED_UDM 6
#define MAX 4600

static int INLET_ID; /* Inlet thread ID from boundary conditions
    panel */

/* Constant (user-modifiable values) */
static int MX;      /* No. cells in x- (streamwise) direction*/
static int MY;       /* No. cells in y- (lateral) direction  */
static int MZ;       /* No. cells in z- (vertical) direction */

static real GX;      /* Mesh size in x- (streamwise) direction (m) */
static real GY;      /* Mesh size in y- (lateral)  direction (m)   */
static real GZ;      /* Mesh size in z- (vertical) direction (m)   */

static real UTAU;    /* Friction velocity (m/s)  0.285 */
static real Ka ; /* Von Karman constant */
```

```
static real z0 ; /* Aerodynamic roughness length (m)*/
static real Uref; /* Reference velocity (m/s)*/
static real zref; /* Reference height (m) */
static real rho ; /* Air density (kg/m3)*/

/*Integral Length Scales to be defined by the scheme*/
static real Lux_lower;
static real Lvx_lower;
static real Lwx_lower;
static real Luy_lower;
static real Luz_lower;

static real Lux_upper;
static real Lvx_upper;
static real Lwx_upper;
static real Luy_upper;
static real Luz_upper;

/*Filter sizes to be defined from the integral length scales */
static int NX = 100;     /*       Max Filter size in x-direction  */
static int NY_1;  /*       Max Filter size in y-direction  */
static int NY_2;  /*       Max Filter size in y-direction  */
static int NZ_1;  /*       Max Filter size in z-direction  */
static int NZ_2;  /*      Max Filter size in z-direction  */

/* Derived values from the filter sizes*/
static int NY2_1;  /* 2*NY_1     Twice the filter size in y-direction
   */
static int NY2_2;  /* 2*NY_2     Twice the filter size in y-direction
   */
static int NZ2_1;  /* 2*NZ_1     Twice the filter size in z-direction
   */
static int NZ2_2;  /* 2*NZ_2     Twice the filter size in z-direction
   */

static int NY2P1_1;  /* 2*(NY_1)+1   Twice filter size plus 1 in y-
   dir */
static int NY2P1_2;  /* 2*(NY_2)+1   Twice filter size plus 1 in y-
   dir */
static int NZ2P1_1;  /* 2*(NZ_1)+1   Twice filter size plus 1 in z-
   dir */
static int NZ2P1_2;  /* 2*(NZ_2)+1   Twice filter size plus 1 in z-
   dir */

/*Size of random number arrays */
static int NYRND;  /* MY+1+NY2_1                */
static int NZRND;  /* MZ+1+NZ2_1                */

/*cell size in all directions*/
static real dx;    /* GX/(real)MX;     Cell size in x-direction (m) */
static real dy;    /* GY/(real)MY;     Cell size in y-direction (m) */
static real dz;    /* GZ/(real)MZ;     Cell size in z-direction (m) */

static int MYMZ;  /* (MZ+1) * (MY+1)            */
```

```
static real utausq;  /* UTAU*UTAU    UTAU squared      */

/* For execution only at the start of the timestep */
static int lastTimeStep = -1;

/*seeds for the generation of the random numbers */
static long seed1 = 25; /* seed for rnd_ux   Cell size in x-direction
    (m) */
static long seed2 = 12; /* seed for rnd_uy   Cell size in x-direction
    (m) */
static long seed3 = 60; /* seed for rnd_uz   Cell size in x-direction
    (m) */

static real deltaT = 0.0005;/* */

/*filter coefficients for first filtering (spatial filtering)      */
real *by_1;     /*in zone 1 (lower quarter), in Y-dir, dimension:
   NY2P1_1 */
real *by_2;     /*in zone 2 (upper region) , in Y-dir, dimension:
   NY2P1_2 */
real *bz_1;     /*in zone 1 (lower quarter), in Z-dir, dimension:
   NZ2P1_1 */
real *bz_2;     /*in zone 2 (upper region) , in Z-dir, dimension:
   NZ2P1_2 */

/*2D arrays to store fluctuating components of the velocity at
   previous time step */
real **ux_m1;    /*dimensions [MZ+1][MY+1]          */
real **uy_m1;    /*dimensions [MZ+1][MY+1]          */
real **uz_m1;    /*dimensions [MZ+1][MY+1]          */


/*************************************************/
/* Function to generate random numbers     */
/*************************************************/
real ran2(long *idum)
{
 int j;
    long k;
    static long idum2=123456789;
    static long iy=0;
    static long iv[NTAB];
    real temp;

    if (*idum <= 0) /* Initialise */
    {
      if (-(*idum) < 1) *idum=1;
      else *idum = -(*idum);
      idum2=(*idum);
      for (j=NTAB+7;j>=0;j--) /* Load the shuffle table */
      {
        k=(*idum)/IQ1;
        *idum=IA1*(*idum-k*IQ1)-k*IR1;
        if (*idum < 0) *idum += IM1;
        if (j < NTAB) iv[j] = *idum;
```

```
        }
        iy=iv[0];
      }

      k=(*idum)/IQ1;
      *idum=IA1*(*idum-k*IQ1)-k*IR1;
      if (*idum < 0) *idum += IM1;
      k=idum2/IQ2;
      idum2=IA2*(idum2-k*IQ2)-k*IR2;
      if (idum2 < 0) idum2 += IM2;
      j=iy/NDIV;
      iy = iv[j]-idum2;
      iv[j] = *idum;
      if (iy < 1) iy += IMM1;
      if ((temp=AM*iy) > RNMX) return RNMX;
      else return temp;

  }

  /*************************************************/
  /* Function to generate random numbers of mean = 0, variance = 1*/
  /*************************************************/
  real rnd_gen2(long *seed)
  {
   int p;
      real sum=0;

      for (p=0; p<12; p++)
      {
    sum += ran2(seed);
      }

      sum -= 6;
      return sum;
  }


  /*************************************************/
  /* Function to define the reynolds stresses distribution*/
  /*************************************************/
  real reynolds(int i,        /* Row in Reynolds Stress Tensor */
          int j,        /* Column in Reynolds Stress Tensor */
          real zDash)   /* Non-dimensional height in domain */
  {
   int test = 0;
   /*real ufriction = Ka*Uref/(log(zref/y0));*/
   /*utausq = ufriction*ufriction;*/

      /* Use the switch...case construct to choose elements of tensor
         */
      switch (i)
      {
   case 1:
       switch (j)
       {
```

```
    case 1:
    test = 0; /* R11*/
     if(zDash<0.025)
     {
200                  test=1;
                     /*return ( (297*zDash+0.44)*utausq );*/
         return utausq*(213.713*zDash+2.317);
         break;
     }
205  if((zDash>=0.025) && (zDash<0.4))
     {
      test=1;
      /*return ( (1.91*pow(zDash,(-0.363)))*utausq );*/
      return utausq*(-6.215*zDash+12.133);
210   break;
        }
              if((zDash>=0.4) && (zDash<0.82))
     { test=1;
      /*return ( (-4.8*zDash+4.6)*utausq );*/
215   return utausq*(-15.940*zDash+16.393);
      break;
     }
     if((zDash>=0.82) && (zDash<=1.0))
     { test=1;
220   /*return ( (4.2*zDash*zDash-9.2*zDash+5.5)*utausq );*/
      return utausq*(-7.1037*zDash+9.0886);
      break;
     }
     if(test == 0)
225  {
      return (0.0);
      break;
     }

230  default:
        return ( 0.0 );
        break;
       }
       break;
235 case 2: /*R21 and R22 */
       switch (j)
       {
     case 1:/*R21 */
     test =0;
240   if(zDash<0.25)
      {
       test=1;
          /*return ( (-32*zDash + 0.1)*utausq );*/
          return utausq*(-4.698*zDash-1.3633);
245       break;
      }
      if((zDash>=0.25) && (zDash<0.5))
      {
       test=1;
250    return utausq*(7.4292*zDash*zDash-5.644*zDash-1.551);
```

```
        break;
      }
      if((zDash>=0.5) && (zDash<=1.0))
      {
255    test=1;
       return utausq*( 4.215*zDash-4.725 );
       break;
      }

260   if(test == 0)
      {
       return (0.0);
       break;
      }
265

    case 2: /* R22*/
    test =0;
          if(zDash<0.04)
270   {
       test=1;
       /*return (  (-32*zDash + 0.1)*utausq );*/
       return utausq*(156.314*zDash+1.227);
       break;
275   }
      if((zDash>=0.04) && (zDash<0.29))
      {
       test=1;
       return utausq*(-0.7451*zDash+7.0496);
280    break;
      }
      if((zDash>=0.29) && (zDash<0.92))
      {
       test=1;
285    return utausq*( -8.780*zDash+9.489 );
       break;
      }
      if((zDash>=0.92) && (zDash<=1.0))
      {
290    test=1;
       return utausq*( -13.390*zDash+13.884 );
       break;
      }

295   if(test == 0)
      {
       return (0.0);
       break;
      }
300
    default:
        return ( 0.0 );
        break;
       }
305
```

```
      case 3:
          switch (j)
          {
       case 3: /* R33*/
310    test = 0;
        if(zDash<0.04)
        {
         test=1;
            return utausq*( 61.173*zDash+0.369 );
315         break;
          }
        if((zDash>=0.04) && (zDash<0.49))
        {
         test=1;
320      return utausq*( -18.969*zDash*zDash+13.2711*zDash+1.9815 );
                    break;
        }
        if((zDash>=0.49) && (zDash<0.91))
        {
325      test=1;
         return utausq*( 1.4532*zDash*zDash - 7.9452*zDash + 7.630 );
                    break;
        }
        if((zDash>=0.91) && (zDash<=1.0))
330     {
         test=1;
         return utausq*( -9.862*zDash+10.621 );
                    break;
        }
335     if(test == 0)
        {
         return 0.0;
         break;
        }
340
      default:
          return ( 0.0 );
          break;
         }
345
     default:
         return ( 0.0 );
         break;
        }
350 }


   /*****************************************************/
   /* Function to define the longitudinal integral length scale for ux,
      L_(ux)^x*/
355 /*****************************************************/
   real L_u_x(int i)
   {
    if (i==0 || i==1)
    {
```

```
360     if (i==0) return  Lux_lower;
        if (i==1) return  Lux_upper;
      }
      else
      {
365    return 1;
      }

    }

370 /*****************************************************/
    /* Function to define the longitudinal integral length scale for uy,
       L_(uy)^x*/
    /*****************************************************/
    real L_v_x(int i)
    {
375  if (i==0)
     {
      return Lvx_lower;
     }

380  if (i==1)
     {
      return  Lvx_upper;
     }
    }
385
    /*****************************************************/
    /* Function to define the longitudinal integral length scale for uz,
       L_(uz)^x*/
    /*****************************************************/
    real L_w_x(int i)
390 {
     if (i==0)
     {
      return Lwx_lower;
     }
395
     if (i==1)
     {
      return  Lwx_upper;
     }
400 }

    /*****************************************************/
    /* Function to define the size of the filter for for ux in Y-dir: L_(
       ux)^y  */
    /*****************************************************/
405 int N_u_y(int i)
    {

     if (i==0)
     {
410   return NY_1; /* Luy=0.135*/
     }
```

```
    if (i==1)
    {
415  return NY_2; /* Luy=0.514*/
    }

   }

420 /*****************************************************/
   /* Function to define the size of the filter for for uy in Y-dir: L_(
      uy)^y  */
   /*****************************************************/
   int N_v_y(int z)
   {
425  return N_u_y(z);
   }
   /*****************************************************/
   /* Function to define the size of the filter for for uz in Y-dir: L_(
      uz)^y  */
   /*****************************************************/
430 int N_w_y(int z)
   {
    return N_u_y(z);
   }
   /*****************************************************/
435 /* Function to define the size of the filter for for ux in Z-dir: L_(
      ux)^z  */
   /*****************************************************/
   int N_u_z(int i)
   {
    if (i==0)
440  {
     return NZ_1; /* Luz=0.202*/
    }
    if (i==1)
    {
445  return NZ_2; /* Luz=0.771*/
    }

   }
   /*****************************************************/
450 /* Function to define the size of the filter for for uy in Z-dir: L_(
      uy)^z  */
   /*****************************************************/
   int N_v_z(int z)
   {
    return N_u_z(z);
455 }
   /*****************************************************/
   /* Function to define the size of the filter for for uz in Z-dir: L_(
      uz)^z  */
   /*****************************************************/
   int N_w_z(int z)
460 {
    return N_u_z(z);
```

```
}

/*************************************************/
/* UDF to update user-defined scheme variables   */
/*************************************************/
DEFINE_ON_DEMAND(update_variable_scheme)
{
#if !RP_NODE

  int temp, mypl, mzpl, i, j;
  real *uxptr;
  real *uyptr;
  real *uzptr;

  Message("Export data from Scheme...");

  INLET_ID = RP_Get_Integer("mesh/inlet-id");
  MX = RP_Get_Integer("mesh/mx");
  MY = RP_Get_Integer("mesh/my");
  MZ = RP_Get_Integer("mesh/mz");
    GX = RP_Get_Real("mesh/meshsize-x");
  GY = RP_Get_Real("mesh/meshsize-y");
  GZ = RP_Get_Real("mesh/meshsize-z");

  Lux_lower = RP_Get_Real("length-scale-lower-quarter/lux");
  Lvx_lower = RP_Get_Real("length-scale-lower-quarter/lvx");
  Lwx_lower = RP_Get_Real("length-scale-lower-quarter/lwx");
  Luy_lower = RP_Get_Real("length-scale-lower-quarter/luy");
  Luz_lower = RP_Get_Real("length-scale-lower-quarter/luz");

  Lux_upper = RP_Get_Real("length-scale-upper/lux");
  Lvx_upper = RP_Get_Real("length-scale-upper/lvx");
  Lwx_upper = RP_Get_Real("length-scale-upper/lwx");
  Luy_upper = RP_Get_Real("length-scale-upper/luy");
  Luz_upper = RP_Get_Real("length-scale-upper/luz");

  UTAU = RP_Get_Real("constants/utau");
  Ka = RP_Get_Real("constants/ka");
  z0 = RP_Get_Real("constants/z0");
  Uref = RP_Get_Real("constants/uref");
  zref = RP_Get_Real("constants/zref");
  rho = RP_Get_Real("constants/rho");

  dx = GX/(real)MX;  /* Cell size in x-direction (m)      */
  dy = GY/(real)MY;  /* Cell size in y-direction (m)      */
  dz = GZ/(real)MZ;  /* Cell size in z-direction (m)      */

  temp = floor(Luy_lower/dy);
  NY_1 = (int)(temp);
  temp = floor(Luy_upper/dy);
  NY_2 = (int)(temp);

  temp = floor(Luz_lower/dz);
  NZ_1 = (int)(temp);
  temp = floor(Luz_upper/dz);
```

```
    NZ_2 = (int)(temp);

    /*NY_lower computed from Luy: NY_lower = int(Luy_lower/dy)*/
    NY2_1 = 2*NY_1;
    NY2_2 = 2*NY_2;

    NZ2_1 = 2*NZ_1;
    NZ2_2 = 2*NZ_2;

    NY2P1_1 = 2*NY_1+1;      /* Twice filter size plus 1 in y-dir      */
    NY2P1_2 = 2*NY_2+1;      /* Twice filter size plus 1 in y-dir      */

    NZ2P1_1 = 2*NZ_1+1;      /* Twice filter size plus 1 in z-dir      */
    NZ2P1_2 = 2*NZ_2+1;      /* Twice filter size plus 1 in z-dir      */

    /* Size of random number arrays */
    NYRND = MY+1+NY2_2;
    NZRND = MZ+1+NZ2_2;

    utausq = UTAU*UTAU;

    MYMZ = (MZ+1) * (MY+1);
    mypl = MY+1;
    mzpl = MZ+1;

    /*Allocate memory for by_1 (lower) by_2 (upper) bz_1 (lower) bz_2 (
       upper)*/
    by_1 = malloc(NY2P1_1 * sizeof(real));
    by_2 = malloc(NY2P1_2 * sizeof(real));

    bz_1 = malloc(NZ2P1_1 * sizeof(real));
    bz_2 = malloc(NZ2P1_2 * sizeof(real));

    /*Allocate memory for ux_m1, uy_m1 and uz_m1 */
    uxptr = malloc(mzpl * mypl * sizeof(real));
    uyptr = malloc(mzpl * mypl * sizeof(real));
    uzptr = malloc(mzpl * mypl * sizeof(real));
    if (uxptr == NULL || uyptr == NULL || uzptr == NULL)
          {
              printf("\nFailure to allocate room for array\n");
          }

    ux_m1 = malloc(mzpl * sizeof(real *));
    uy_m1 = malloc(mzpl * sizeof(real *));
    uz_m1 = malloc(mzpl * sizeof(real *));
    if (ux_m1 == NULL || uy_m1 == NULL || uz_m1 == NULL)
          {
              printf("\nFailure to allocate room for array\n");
          }
    /* and now we point the pointers*/
    for (i=0; i<mzpl; i++)
    {
     ux_m1[i] = uxptr + (i * mypl);
     uy_m1[i] = uyptr + (i * mypl);
     uz_m1[i] = uzptr + (i * mypl);
```

```
    }
    Message("...done \n");
  #endif

    host_to_node_real_3(GX,GY,GZ);
    host_to_node_real_3(z0, UTAU, Ka);
    host_to_node_real_3(Lux_lower,Lvx_lower,Lwx_lower);
    host_to_node_real_3(Lux_upper,Lvx_upper,Lwx_upper);
    host_to_node_real_4(Luy_lower,Luy_upper,Luz_lower,Luz_upper);
    host_to_node_int_7(MX,MY,MZ,NY_1,NY_2,NZ_1,NZ_2);
    host_to_node_int_2(INLET_ID,MYMZ);
    host_to_node_int_6(NY2_1,NY2_2,NZ2_1,NZ2_2,NY2P1_1,NY2P1_2);
    host_to_node_int_4(NZ2P1_1,NZ2P1_2,NYRND,NZRND);
    host_to_node_real_4(dx,dy,dz,utausq);

  }

  /*****************************************************/
  /* MACRO to run before each calculation: get data from scheme and
     compute filter coefficients */
  /*****************************************************/
  DEFINE_ON_DEMAND(reset)
  {

  #if !RP_NODE
    int i, j, k, index;   /* Indices for looping */
        real fy;
        real fz;
    real zDash;
    real sumy[2];   /* Temporary sums */
        real sumz[2];
    real temp;

    /* Calculate the non-normalised filter coefficients */
    /*initialize temporary sums */
    sumy[0] = sumy[1] = 0.0;
    sumz[0] = sumz[1] = 0.0;

    /* filter coefficients in zone 1*/
    for (k=0; k<=2*N_u_y(0); k++)
    {
     fy = 2.0*M_PI/(real)N_u_y(0);
     by_1[k] = exp(-fabs(fy*(real)(k-N_u_y(0))));

    }
    for (k=0; k<=2*N_u_z(0); k++)
    {
     fz = 2.0*M_PI/(real)N_u_z(0);
     bz_1[k] = exp(-fabs(fz*(real)(k-N_u_z(0))));
    }
    /* filter coefficients in zone 2*/
    for (k=0; k<=2*N_u_y(1); k++)
    {
     fy = 2.0*M_PI/(real)N_u_y(1);
     by_2[k] = exp(-fabs(fy*(real)(k-N_u_y(1))));
```

```
625  }
     for (k=0; k<=2*N_u_z(1); k++)
     {
      fz = 2.0*M_PI/(real)N_u_z(1);
      bz_2[k] = exp(-fabs(fz*(real)(k-N_u_z(1))));
630  }
     /* Calculate the normalizing factors */
     /*filter coeffs in zone 1 */
     for (k=0; k<=2*N_u_y(0); k++)
     {
635   sumy[0] += by_1[k]*by_1[k];
     }
     if (sumy[0] == 0) Message("sumy[0] = 0\n");
     for (k=0; k<=2*N_u_z(0); k++)
     {
640   sumz[0] += bz_1[k]*bz_1[k];
     }
     if (sumz[0] == 0) Message("sumz[0] = 0\n");

     /*filter coeffs in zone 2 */
645  for (k=0; k<=2*N_u_y(1); k++)
     {
      sumy[1] += by_2[k]*by_2[k];
     }
     if (sumy[1] == 0) Message("sumy[1] = 0\n");
650  for (k=0; k<=2*N_u_z(1); k++)
     {
      sumz[1] += bz_2[k]*bz_2[k];
     }
     if (sumz[1] == 0) Message("sumy[1] = 0\n");
655
        /* And normalise the filter coefficients in zone 1*/
     /* Filter coefficients in y-dir */
     sumy[0] = sqrt(sumy[0]);
     i = 0;
660  for (k=0; k<=2*N_u_y(0); k++)
     {
      by_1[k] /= sumy[0];
     }
     /* Filter coefficients in z-dir */
665  sumz[0] = sqrt(sumz[0]);
     for (k=0; k<=2*N_u_z(0); k++)
     {
      bz_1[k] /= sumz[0];
     }
670     /* And normalise the filter coefficients in zone 2*/
     /*Filter coefficients in y-dir*/
     sumy[1] = sqrt(sumy[1]);
     i = 1;
     for (k=0; k<=2*N_u_y(1); k++)
675  {
      by_2[k] /= sumy[1];
     }
     Message("Filter coefficients in z-dir:");
     sumz[1] = sqrt(sumz[1]);
```

```
680   for (k=0; k<=2*N_u_z(1); k++)
      {
       bz_2[k] /= sumz[1];
      }
      Message("\n Filter coefficients computed and stored");
685      /* Reset the components of velocity arrays from previous time
            step*/
      Message("Iinitialisation of ux_m1, uy_m1 and uz_m1...");
         for (j=0; j<=MZ; j++)
         {
       for (k=0; k<=MY; k++)
690    {
        ux_m1[j][k] = 0.0;
        uy_m1[j][k] = 0.0;
        uz_m1[j][k] = 0.0;
       }
695       }
      Message("done\n");
    #endif
    }

700 /*************************************************/
    /* UDF to get coefficients for the interpolation from the uniform
       mesh to
    the real non uniform mesh*/
    /*************************************************/
    DEFINE_ON_DEMAND(mapping_interpolation)
705 {
    #if !RP_HOST
     Domain *d;
     Thread *ft, *ct0;
     face_t f;
710  cell_t c0;
        real xCen[3], jr, kr, y, z;/* y and z coordinate in [m] on the
            uniform mesh of the inlet */
        int jj, kk;
     d = Get_Domain(1);
     ft = Lookup_Thread(d, INLET_ID);
715 #endif

    #if !RP_NODE
     /*Loop over the faces of the inlet, non-uniform */
        if (N_UDM<6)
720  {
     printf("YOU MUST DEFINE 6 UDFM's!!");
     Internal_Error("YOU MUST DEFINE more UDFM's!!");
     }
    #endif
725
    #if !RP_HOST
        begin_f_loop(f,ft)
         {
       /* Get the centroid of the face*/
730    F_CENTROID(xCen,f,ft);
       ct0 = THREAD_T0(ft);
```

```
      c0 = F_C0(f,ft);

      for (jj=0; jj<=MZ; jj++) /* vertical*/
      {
       z = (real)(jj)*dz; /* z vertical coordinate on the uniform mesh,
           from 0 to MZ*/

       if((xCen[2]>=z) && (xCen[2]<=z+dz))
       {
        C_UDMI(c0,ct0,UDM_J) = (real)(jj);
        break;
       }

      }
      for (kk=0; kk<=MY; kk++)
      {
       y = (real)(kk)*dy;  /* y horizontal coordinate on the uniform
           mesh*/
       if( (xCen[1]+(real)(GY/2)>=y) && (xCen[1]+(real)(GY/2)<=y+dy) )
       {
        C_UDMI(c0,ct0,UDM_K) = (real)(kk);

        break;
       }

      }

      /* Initialise other C_UDMIs*/
      C_UDMI(c0,ct0,UDM_Um) = 0;
      C_UDMI(c0,ct0,UDM_U) = 0;
      C_UDMI(c0,ct0,UDM_V) = 0;
      C_UDMI(c0,ct0,UDM_W) = 0;

     }
     end_f_loop(f,ft);
     Message("Coefficients for linear interpolation computed and stored
         .\n");
   #endif
   }

   /************************************************/
   /* UDF to compute fluctuating components of the velocity at the start
       of each
   time step on a virtual uniform mesh, and then interpolate them onto
       the
   non-uniform mesh                */
   /************************************************/
   DEFINE_ADJUST(update, domain)
   {

   int currentTimeStep = N_TIME;
   real ux_uni[MYMZ], uy_uni[MYMZ], uz_uni[MYMZ]; /*arrays of the
       components of the velocity on the uniform mesh, to be passed from
       the host to the nodes -> only one dimension*/
```

```
780 if ( lastTimeStep != currentTimeStep )
      {
    /* Calculating new inlet velocity at current time step */

    lastTimeStep = currentTimeStep;
785 Message("\nDefine adjust started\n");

    int i, j, k, jj, kk; /* Indices for looping          */
       int iy, iz;     /* Location of face on inlet thread     */

790 #if !RP_NODE   /* execute this on the host        */
     long* a1;
     long* a2;
     long* a3;
     real rndx[NZRND][NYRND], rndy[NZRND][NYRND], rndz[NZRND][NYRND];
795  real ux_uniform[MZ+1][MY+1], uy_uniform[MZ+1][MY+1], uz_uniform[MZ
        +1][MY+1];
     real tmpx, tmpy, tmpz;
     real factor_U[2], factor_V[2], factor_W[2];
     real sfactor_U[2], sfactor_V[2], sfactor_W[2];
     real temp, Umean, MZreal, znonDim;
800  int zone, index, mypl, mzpl;
     MZreal = (real)(MZ);
     mypl = (int)(MY+1);
     mzpl = (int)(MZ+1);

805 #endif

    #if !RP_HOST
     Thread *ft = Lookup_Thread(domain, INLET_ID);
     face_t f;
810  Thread *ct0 ;
     cell_t c0;
     int indexjk, indexjkplus1, indexjp1kp1, indexjp1k;
    #endif

815 #if !RP_NODE /*on the HOST */

     /* Seed the random number generator */
     Message("Setting the random number seed...");
     /*seed1 = currentTimeStep;*/  /*%1000*/
820  /*seed2 = currentTimeStep;*/  /*%1500*/
     /*seed3 = currentTimeStep;*/  /*%2000*/
     /*seed3 = currentTimeStep - 2000*floor(currentTimeStep/2000);*/
     a1 = &seed1;
     a2 = &seed2;
825  a3 = &seed3;
     Message("done.\n");

     /* Generate three fields of random numbers */
     Message("Generating the random number fields...");
830  for (j=0; j<NZRND; j++)
     {
      for (k=0; k<NYRND; k++)
      {
```

```
      rndx[j][k] = rnd_gen2(a1);
      rndy[j][k] = rnd_gen2(a2);
      rndz[j][k] = rnd_gen2(a3);
     }
    }
    Message("done.\n");

    deltaT = CURRENT_TIMESTEP;

    Message("Computing the factor for temporal corr...");
    /* factors for longitudinal length scales Lux Lvx Lwx*/
    for (i=0; i<2; i++)
    {
     factor_U[i] = exp(-1.0*M_PI*deltaT/(2*L_u_x(i)));
     factor_V[i] = exp(-1.0*M_PI*deltaT/(2*L_v_x(i)));
     factor_W[i] = exp(-1.0*M_PI*deltaT/(2*L_w_x(i)));
     sfactor_U[i] = sqrt(1.0-factor_U[i]*factor_U[i]);
     sfactor_V[i] = sqrt(1.0-factor_V[i]*factor_V[i]);
     sfactor_W[i] = sqrt(1.0-factor_W[i]*factor_W[i]);
    }
    Message("done.\n");

    Message("Loop over uniform mesh...\n");
    /* Loop over the UNIFORM mesh of the inlet, on the HOST      */
    for(j=0; j<=MZ; j++)  /* vertical coordinate        */
    {
     for (k=0; k<=MY; k++) /* horizontal coordinate      */
     {
      real y,z;   /* real coordinates on the UNIFORM inlet  */
      real a11, a21, a22, a33;
      z = (real)(j)*dz; /* Vertical coordinate        */
      y = (real)(k)*dy; /* Horizontal coordinate      */
      ux_uniform[j][k] = uy_uniform[j][k] = uz_uniform[j][k] = 0.0;
      index = j*(MY+1) + k; /*index to store velocity components on
          uniform mesh
              to be passed from host to nodes (1D array)*/

      if (j>=0 && j<(int)(MZ/4)) /*ZONE 0 */
      {
       zone = 0;
       for (jj=0; jj<=2*N_u_z(zone); jj++)
        {
         for (kk=0; kk<=2*N_u_y(zone); kk++)
          {
           real byz = bz_1[jj]*by_1[kk];
           ux_uniform[j][k] += byz*(rndx[jj+j][kk+k]);
           uy_uniform[j][k] += byz*(rndy[jj+j][kk+k]);
           uz_uniform[j][k] += byz*(rndz[jj+j][kk+k]);
          }
        }
       if ( currentTimeStep > 1 )
       {
        tmpx = (ux_m1[j][k]*factor_U[zone]+ux_uniform[j][k]*sfactor_U[
            zone])/(factor_U[zone] + sfactor_U[zone]);
```

```
        tmpy = (uy_m1[j][k]*factor_V[zone]+uy_uniform[j][k]*sfactor_V[
            zone])/(factor_V[zone] + sfactor_V[zone]);
        tmpz = (uz_m1[j][k]*factor_W[zone]+uz_uniform[j][k]*sfactor_W[
            zone])/(factor_W[zone] + sfactor_W[zone]);
      }
      else
890   {
        tmpx = ux_uniform[j][k];
        tmpy = uy_uniform[j][k];
        tmpz = uz_uniform[j][k];
      }
895
      /* Save velocity for next time step*/
      ux_m1[j][k] = tmpx;
      uy_m1[j][k] = tmpy;
      uz_m1[j][k] = tmpz;
900   }
      else
      {
      zone = 1; /*if (j>=(int)(MZ/4) && j<=MZ)*/ /*ZONE 1 */
      for (jj=0; jj<=2*N_u_z(zone); jj++)
905    {
        for (kk=0; kk<=2*N_u_y(zone); kk++)
          {
            real byz = bz_2[jj]*by_2[kk];
            ux_uniform[j][k] += byz*rndx[jj+j][kk+k];
910         uy_uniform[j][k] += byz*rndy[jj+j][kk+k];
            uz_uniform[j][k] += byz*rndz[jj+j][kk+k];
          }
      }
      if ( currentTimeStep > 1 )
915   {
        tmpx = (ux_m1[j][k]*factor_U[zone]+ux_uniform[j][k]*sfactor_U[
            zone])/(factor_U[zone] + sfactor_U[zone]);
        tmpy = (uy_m1[j][k]*factor_V[zone]+uy_uniform[j][k]*sfactor_V[
            zone])/(factor_V[zone] + sfactor_V[zone]);
        tmpz = (uz_m1[j][k]*factor_W[zone]+uz_uniform[j][k]*sfactor_W[
            zone])/(factor_W[zone] + sfactor_W[zone]);
      }
920   else
      {
        tmpx = ux_uniform[j][k];
        tmpy = uy_uniform[j][k];
        tmpz = uz_uniform[j][k];
925
      }
      /* Save velocity for next time step*/
      ux_m1[j][k] = tmpx;
      uy_m1[j][k] = tmpy;
930   uz_m1[j][k] = tmpz;
    } /*end of if j second zone */

    /* Now calculate velocity components for use in
       DEFINE_PROFILES */
```

```
      znonDim = (real)(j)/MZreal;
      a11 = sqrt(reynolds(1,1,znonDim));
      a21 = reynolds(2,1,znonDim)/a11;
      temp=reynolds(2,2,znonDim)-a21*a21;
      if (temp>=0) a22 = sqrt(temp);
      else a22 =0;
      a33 = sqrt(reynolds(3,3,znonDim));

      ux_uniform[j][k] = (a11*tmpx);
      uy_uniform[j][k] = (a21*tmpx + a22*tmpy);
      uz_uniform[j][k] = (a33*tmpz);

      ux_uni[index] = ux_uniform[j][k];
      uy_uni[index] = uy_uniform[j][k];
      uz_uni[index] = uz_uniform[j][k];
    } /*end of k */
  } /* end of j*/
  Message("done.\n");

#endif

host_to_node_real(ux_uni, MYMZ);
host_to_node_real(uy_uni, MYMZ);
host_to_node_real(uz_uni, MYMZ);


/* Loop over the faces of the thread */
#if !RP_HOST /*on the NODES */

 begin_f_loop(f,ft)
 {
 real xCen[ND_ND], z_nonDim, t, u;

 ct0 = THREAD_T0(ft);
 c0 = F_C0(f,ft);

 /* Get the centroid of the face*/
 F_CENTROID(xCen,f,ft);

 /* define the square in which the face centre belongs */
 j = C_UDMI(c0,ct0,UDM_J); /* z vertical direction */
 k = C_UDMI(c0,ct0,UDM_K); /* y horizontal direction */

 indexjk  = j*(MY+1) + k;
 indexjkplus1= j*(MY+1) + k +1;
 indexjp1kp1 = (j+1)*(MY+1) + k+1;
 indexjp1k = (j+1)*(MY+1) + k;

 t = ((xCen[1]+(real)(GY/2))-(real)(k)*dy)/(dy); /* lies between 0
    and 1*/
 if((t>1) || (t<0)) Message("problem with interpolation t");
 u = (xCen[2]-(real)(j)*dz)/(dz); /* lies between 0 and 1*/
 if((u>1) || (u<0)) Message("problem with interpolation u");

 C_UDMI(c0,ct0,UDM_Um) = ((UTAU/Ka) *log((xCen[2]+z0)/z0));
```

```
990     C_UDMI(c0,ct0,UDM_U) = ((1-t)*(1-u)*ux_uni[indexjk] + t*(1-u)*
            ux_uni[indexjkplus1] + t*u*ux_uni[indexjp1kp1] + (1-t)*u*ux_uni
            [indexjp1k]);
        C_UDMI(c0,ct0,UDM_V) = ((1-t)*(1-u)*uy_uni[indexjk] + t*(1-u)*
            uy_uni[indexjkplus1] + t*u*uy_uni[indexjp1kp1] + (1-t)*u*uy_uni
            [indexjp1k]);
        C_UDMI(c0,ct0,UDM_W) = ((1-t)*(1-u)*uz_uni[indexjk] + t*(1-u)*
            uz_uni[indexjkplus1] + t*u*uz_uni[indexjp1kp1] + (1-t)*u*uz_uni
            [indexjp1k]);

        }
995   end_f_loop(f,ft);
      #endif

      } /*end of :if fist iteration of time step do...*/

1000 }

     /*************************************************/
     /* UDF to define the X component of the velocity */
     /*************************************************/
1005 DEFINE_PROFILE(unsteady_inlet_x_vel, thread, position)
     {
      #if !RP_HOST
      face_t f;
      cell_t c0;
1010  Thread *ct0;
      ct0 = THREAD_T0(thread);

      begin_f_loop(f,thread)
         {
1015    c0 = F_C0(f,thread);
        F_PROFILE(f,thread,position) = C_UDMI(c0,ct0,UDM_Um) + C_UDMI(c0,
            ct0,UDM_U);

       }
      end_f_loop(f,thread)
1020  #endif
     }

     /*************************************************/
     /* UDF to define the Y component of the velocity */
1025 /*************************************************/
     DEFINE_PROFILE(unsteady_inlet_y_vel, thread, position)
     {
      #if !RP_HOST
      face_t f;
1030  cell_t c0;
      Thread *ct0;
      ct0 = THREAD_T0(thread);

      begin_f_loop(f,thread)
1035     {
        c0 = F_C0(f,thread);
```

```
      F_PROFILE(f,thread,position) = C_UDMI(c0,ct0,UDM_V);
        }
      end_f_loop(f,thread)
1040
    #endif

  }

1045 /*************************************************/
  /* UDF to define the Z component of the velocity  */
  /*************************************************/
  DEFINE_PROFILE(unsteady_inlet_z_vel, thread, position)
  {
1050 #if !RP_HOST
    face_t f;
    cell_t c0;
    Thread *ct0;
    ct0 = THREAD_T0(thread);
1055
    begin_f_loop(f,thread)
        {
      c0 = F_C0(f,thread);
      F_PROFILE(f,thread,position) = C_UDMI(c0,ct0,UDM_W);
1060    }
    end_f_loop(f,thread)

  #endif

1065 }
```

Appendix D

Statistics: temporal and spatial correlations

This appendix introduces and define the key terms used in the statistical analysis of the synthetic turbulent inflow.

D.1 Temporal autocorrelation

The temporal autocorrelation of a second order stationary signal $X(t)$ is defined as:

$$R_t(\tau) = \frac{E[(X(t) - \mu)(E(X(t+\tau) - \mu)]}{\sigma^2}$$

where E is the expected value operator, σ^2 is the variance of the signal and μ the mean value of $X(t)$. The three fluctuating components of the velocity, u_x, u_y, u_z are being treated as second order stationary signals. If T is the total duration of the time series, and Δt the time step, then N_t, as in $N_t = T/\Delta t$, is the number of records and the discretized form of the non-normalised temporal autocorrelation coefficients (or autocovariance) at a given location $P(y, z)$ can be written as follows:

$$C_{t_{u_x}}(\tau_k = 0) = \frac{1}{N_t} \sum_{i=1}^{N_t} u_x(y, z, t_i)^2 \tag{D.1.1}$$

$$C_{t_{u_x}}(\tau_k \neq 0) = \frac{1}{N_t} \sum_{i=1}^{N_t - \tau_k} u_x(y, z, t) \times u_x(y, z, t + \tau_k) \tag{D.1.2}$$

The normalised temporal autocorrelation coefficients are then computed as follows:

$$R_{t_{u_x}}(\tau_k) = \frac{C_{t_{u_x}}(\tau_k)}{C_{t_{u_x}}(0)} \tag{D.1.3}$$

These autocorrelation coefficients are then averaged over the distance over which the longitudinal length scale is constant. For the empty fetch test case, since constant longitudinal length scales are specified over the height of the domain, it is sensible to spatially average the coefficients: $\widetilde{R}t_{u_x}(r_k)$, $\widetilde{R}t_{u_y}(r_k)$, $\widetilde{R}t_{u_z}(r_k)$ and $\widetilde{R}t_U(r_k)$, are therefore spatially averaged (over the inlet plane) temporal autocorrelation coefficients.

D.2 Spatial autocorrelation

The spatial autocorrelation gives an indication of the length scales in the plane transverse to the main direction of the flow. It measures how much the signal is correlated in space at a given time step. It is therefore equivalent to a temporal correlations where the time lag is replaced by distance.

Since the length scales do not vary in time, the resulting spatial autocorrelation coefficients can be averaged over time, which can be expressed:

$$R_{s_u}(r_k) = \lim_{T\to\infty} \frac{1}{T} \int_0^T u(P,t) \times u(P',t)\Delta t \tag{D.2.1}$$

where r_k is a distance interval, $u(P,t)$ is a fluctuating component of the velocity at location $P(x,y)$ and at time t, T the length of the signal, and P and P' are defined such as $||\vec{PP'}|| = r_k$.

The discretized form of the spatial autocorrelation coefficients are then derived: let N be the total number of points on the YZ plane (inlet plane), and N_{r_k} the number of pairs of points $P_i(y_i,z_i), P_j(y_j,z_j)$ such as $||\vec{P_iP_j}|| = r_k$ where $r_k = k\Delta r$ and $k \in [1;m]$, Δr being the minimal distance interval (typically the smallest cell size), m is defined so as $m\Delta r < \frac{1}{4}D$, D being defined as the maximum distance between two cells (the diagonal of the inlet plane). The non-normalised spatial correlation coefficients for a zero distance interval at a **given time** is defined for each component, which gives the

following expression for the X-component of the velocity:

$$C_{s_{u_x}}(r_k = 0) = \frac{1}{N}\sum_{1}^{N} u_x(y_i, z_i)^2 \tag{D.2.2}$$

For the two other components of the velocity and the velocity magnitude, the coefficients $C_{s_{u_y}}(r_k = 0)$, $C_{s_{u_z}}(r_k = 0)$ and $C_{s_U}(r_k = 0)$ are defined in the same manner. For $r_k > 0$:

$$C_{s_{u_x}}(r_k \neq 0) = \frac{1}{N_{r_k}}\sum_{1}^{N_{r_k}} u_x(y_i, z_i) \times u_x(y_j, z_j) \tag{D.2.3}$$

where $||\vec{P_iP_j}|| = r_k$. For the two other components of the velocity and the velocity magnitude, the coefficients $C_{s_{u_y}}(r_k \neq 0)$, $C_{s_{u_z}}(r_k \neq 0)$ and $Cs_U(r_k \neq 0)$ are defined in the same manner. Finally, the normalised spatial correlation coefficients are defined as follows:

$$R_{s_{u_x}}(r_k) = \frac{C_{s_{u_x}}(r_k)}{C_{s_{u_x}}(0)} \tag{D.2.4}$$

These coefficients are computed at each time step, and then averaged over time as in equation (D.2.1) to give $\overline{Rs}_{u_x}(r_k)$, $\overline{R}_{s_{u_y}}(r_k)$, $\overline{R}_{s_{u_z}}(r_k)$ and $\overline{R}_{s_U}(r_k)$.

The principles used to compute the spatial autocorrelation coefficients can be applied to obtain autocorrelations with respect to the distance in the Y-direction and the Z-direction, the distance intervals r_k are replaced by distance intervals in the Y and Z directions respectively. This way, the **vertical autocorrelation coefficients** are computed as follows:

$$C_{y_{u_x}}(y_k) = \frac{1}{N_{y_k}}\sum_{1}^{N_{y_k}} u_x(y_i, z_i) \times u_x(y_j, z_j) \tag{D.2.5}$$

where $P(y_i, z_i)$ and $P(y_j, z_j)$ satisfy $||\vec{P_iP_j} \cdot \vec{y}|| = y_k$, and N_{y_k} the number of pairs of points that satisfies this equation. The normalised vertical autocorrelation coefficients can then be expressed:

$$R_{y_{u_x}}(y_k) = \frac{C_{y_{u_x}}(y_k)}{C_{y_{u_x}}(0)} \tag{D.2.6}$$

And the normalised **horizontal autocorrelation coefficients**, $Rz_{u_x}(z_k)$, are calculated in the same manner (refer to Figure 6.7 for the main directions of the domain for the empty fetch test case).